

Search for sterile neutrinos at colliders

By

Sanjoy Mandal

PHYS10201304005

The Institute of Mathematical Sciences, Chennai

A thesis submitted to the

Board of Studies in Physical Sciences

In partial fulfillment of requirements

For the Degree of

DOCTOR OF PHILOSOPHY

of

HOMI BHABHA NATIONAL INSTITUTE



April, 2019

Homi Bhabha National Institute

Recommendations of the Viva Voce Committee

As members of the Viva Voce Committee, we certify that we have read the dissertation prepared by Sanjoy Mandal entitled “Search for sterile neutrinos at colliders” and recommend that it may be accepted as fulfilling the thesis requirement for the award of Degree of Doctor of Philosophy.

_____ Date:
Chairman - V. Ravindran

_____ Date:
Guide/Convener - Nita Sinha

_____ Date:
Examiner - S. Uma Sankar

_____ Date:
Member 1 - Shrihari Gopalakrishna

_____ Date:
Member 2 - Sitabhra Sinha

_____ Date:
Member 3 - Sibasish Ghosh

Final approval and acceptance of this thesis is contingent upon the candidate’s submission of the final copies of the thesis to HBNI.

I hereby certify that I have read this thesis prepared under my direction and recommend that it may be accepted as fulfilling the thesis requirement.

Date:

Place: IMSc, Chennai

Guide- Nita Sinha

STATEMENT BY AUTHOR

This dissertation has been submitted in partial fulfillment of requirements for an advanced degree at Homi Bhabha National Institute (HBNI) and is deposited in the Library to be made available to borrowers under rules of the HBNI.

Brief quotations from this dissertation are allowable without special permission, provided that accurate acknowledgement of source is made. Requests for permission for extended quotation from or reproduction of this manuscript in whole or in part may be granted by the Competent Authority of HBNI when in his or her judgment the proposed use of the material is in the interests of scholarship. In all other instances, however, permission must be obtained from the author.

Sanjoy Mandal

DECLARATION

I, hereby declare that the investigation presented in the thesis has been carried out by me.
The work is original and has not been submitted earlier as a whole or in part for a degree
/ diploma at this or any other Institution / University.

Sanjoy Mandal

List of Publications arising from the thesis

1. **“Favoured B_c Decay modes to search for a Majorana neutrino”**
Sanjoy Mandal and Nita Sinha
[Phys.Rev. D94 \(2016\) no.3, 033001](#)
2. **“Constraining the right-handed gauge boson mass from lepton number violating meson decays in a low scale left-right model”**
Sanjoy Mandal, Manimala Mitra and Nita Sinha
[Phys.Rev. D96 \(2017\) no.3, 035023](#)
3. **“Probing leptoquarks and heavy neutrinos at the LHeC”**
Sanjoy Mandal, Manimala Mitra and Nita Sinha
[Phys.Rev. D98 \(2018\) no.9, 095004](#)
4. **“Probing right handed neutrinos at the LHeC and lepton colliders using fat jet signatures”**
Arindam Das, Sudip Jana, Sanjoy Mandal and S. Nandi
[Phys.Rev. D99 \(2019\) no.5, 055030](#)

Sanjoy Mandal

List of publications (not included in this thesis)

1. **“Searching for New physics in Charm Radiative decays”**

Aritra Biswas, Sanjoy Mandal and Nita Sinha

[Int.J.Mod.Phys. A33 \(2018\) no.32, 1850194](#)

2. **“New physics in neutral $D \rightarrow VV$ decay modes”**

Aritra Biswas and Sanjoy Mandal

[Int.J.Mod.Phys. A31 \(2016\) no.34, 1650180](#)

3. **“Neutrino oscillations in discrete-time quantum walk framework”**

Arindam Mallick, Sanjoy Mandal and C. M. Chandrashekar

[Eur.Phys.J. C77 \(2017\) no.2, 85](#)

4. **“Simulating Dirac Hamiltonian in Curved Space-time by Split-step Quantum Walk”**

Arindam Mallick, Sanjoy Mandal, Anirban Karan and C. M. Chandrashekar

[J.Phys.Comm. 3 \(2019\) 1](#)

Sanjoy Mandal

Seminars presented

1. Talk on “**Constraining Right Handed Gauge Boson Mass from Lepton Number Violating Meson Decays in a Low Scale Left Right Model**”, at [39th International Conference on High Energy Physics](#), 4-11 July 2018, COEX, Seoul, Korea.
2. Talk on “**Favored B_c decay modes to search for Majorana neutrino**”, at [XXII DAE-BRNS High Energy Physics Symposium 2016](#), 12-16 December 2016, University of Delhi, India.
3. Talk on “**Sterile Neutrinos and Lepton Number Violating Meson Decays**”, at [Workshop on High Energy Physics Phenomenology XV](#), 14-23 December 2017, IISER Bhopal, Bhopal, India.
4. Talk on “**Right Handed Neutrino Search at Colliders**”, at [International Meeting on High Energy Physics](#), 17-22 Jan, 2019, Institute of Physics, Bhubaneswar, India.
5. Talk on “**Constraining Right Handed Gauge Boson Mass from Lepton Number Violating Meson Decays in Left Right Model**”, at [Korea Institute for Advanced Study](#), 18 th July,2018.
6. Talk on “**Favored B_c decay modes to search for Majorana neutrino**”, at [Post-CKM School](#), 3-7 December, 2016.

Sanjoy Mandal

Conferences and workshops attended

1. **39th International Conference on High Energy Physics**, held at COEX, Seoul, Korea from 4-11 July 2018.
2. **XXII DAE-BRNS High Energy Physics Symposium 2016**, held at University of Delhi, Delhi, India from 12-16 December, 2016.
3. **Workshop on High Energy Physics Phenomenology XV**, held at IISER Bhopal, Bhopal, India from 14-23 December, 2017.
4. **Post-CKM School**, held at Tata Institute of Fundamental Research, Mumbai, India from 3-7 December, 2016.
5. **9th International Workshop on the CKM Unitarity Triangle (CKM2016)**, held at Tata Institute of Fundamental Research, Mumbai, India from Nov.28-Dec.2, 2016.
6. **SANGAM@HRI-2016**, held at Harish-Chandra Research Institute, Allahabad, India from 15-19 February, 2016.
7. **International Neutrino Summer School (INSS 2016)**, held in Quy Nhon, Vietnam from 21-27 August 2016.
8. **International Meeting on High Energy Physics**, held at Institute of Physics, Bhubaneswar, India from 17-22 January, 2019.
9. **IITB-ICTP Workshop on Neutrino Physics**, held at IIT Bombay, Mumbai, India from 14-18 December, 2018.

Dedicated To
My Parents,
Wife and Brother

ACKNOWLEDGEMENTS

I would like to express my sincere gratitude for my supervisor Prof. Nita Sinha for not only academically guiding me, but also supporting me in the highs and lows of my PhD life. I am grateful to her for helping me to learn the subject in the way I wanted. She will have an everlasting impact on me.

I am thankful to my senior Dr. Aritra Biswas for helping me to learn a completely new field and for supporting me in my bad times. I am thankful to Prof. C. M. Chandrashekar for letting me work with him and learn a completely new area of research field.

I am thankful to Prof. Manimala Mitra, Prof. José W. F. Valle, Dr. Rahul Srivastava, Dr. Arindam Das and Prof. S. Nandi for allowing me the opportunity to work with them and learn from their experience and insight. I am also thankful to my friends and collaborators Arindam Mallick, Anirban Karan and Sudip Jana.

I am blessed to have found many close friends in every stage of my life. It is impossible to list them all and their impact on my life in this short Phd acknowledgement. Spending time, chatting, going for dinner at various places with Sagnik, Dipanjan, Pulak, Arnab, Anirban, Arindam and Dhani was the best part of my IMSc life. Special thanks to Sagnik and Dipanjan for tolerating a short temper person like me.

A special thanks to my wife Parijat Ghosh for showing faith in my capabilities, motivating me and for spending many quality times with me.

Finally, I would not have reached this far if there has not been the support and faith parents and my brother have shown in me. I am thankful to my parents and brother for always supporting me and respect my choices.

Contents

Synopsis	1
1 Introduction	9
1.1 Standard Model	12
1.2 Neutrino Mass	17
1.2.1 Formalism for heavy neutrino mixing	19
1.2.2 Left-Right Symmetric Model	21
1.3 Existing bounds on mixing angles	24
1.4 Outline of the thesis	28
2 Favoured B_c Decay modes to search for a Majorana neutrino	31
2.1 Model	32
2.2 $B_c^- \rightarrow \bar{B}_s^0 \ell_1^- \ell_2^- \pi^+$ Decays	33
2.3 Other B_c Decay Modes	42
2.3.1 $B_c^- \rightarrow J/\psi \ell_1^- \ell_2^- \pi^+$	43
2.3.2 $B_c^- \rightarrow \pi^+ \ell_1^- \ell_2^-$	44

2.4	Summary	47
3	Constraints on Right Handed Gauge Boson Mass from LNV meson decays	49
3.1	Imprint of Majorana Signature in Meson Decays	50
3.2	Total Decay Width of the heavy Majorana neutrino N	53
3.3	Limit on M_{W_R} from ongoing and future experiments in presence of heavy Majorana neutrinos	55
3.4	Comparison with Existing constraints from other experiments	63
3.5	Summary	64
4	Probing Leptoquark and Heavy Neutrino at LHeC	65
4.1	Model	66
4.2	Constraints on Leptoquark Couplings	68
4.3	Leptoquark Production and Its Decays	71
4.4	Collider Analysis	74
4.5	Signals and Background	75
4.6	Signal Strength for Higher LQ Mass	83
4.7	Results	85
4.8	Summary	86
5	Probing right handed neutrinos using fat jet signatures	89
5.1	Heavy neutrino production	92
5.1.1	Production cross section at LHeC	92

5.1.2	Production cross section at linear collider	94
5.2	Collider Analysis	95
5.2.1	LHeC analysis for the signal $e^- p \rightarrow j N_1 \rightarrow e^\pm + J + j_1$	97
5.2.2	Linear collider analysis for the signal $e^\pm + J + p_T^{miss}$	102
5.2.3	Linear collider analysis for the signal $J_b + p_T^{miss}$	107
5.3	Current bounds	110
5.4	Summary	113
6	Conclusions and Outlook	117
	Appendices	121
A	Kinematics of four-body decay $B_c^- \rightarrow \bar{B}_s^0 \ell_1^- \ell_2^- \pi^+$	123
B	Partial decay widths of RH neutrino N_i in LRSM	127
	Bibliography	131

List of Figures

- 1.1 Left: Bounds on the mixing angle $|V_{eN}|^2$ as a function of RH neutrino mass M_N in the mass range 10 MeV-100 GeV. The bounds are from peak searches ($K \rightarrow e\nu, \pi \rightarrow e\nu$) and from the following experiments: PS191, NA3, CHARM, DELPHI, L3. The region above the contour lines are excluded. The dotted maroon contour is for neutrinoless double beta decay experiment. Right: Excluded region on $|V_{eN}|^2$ versus M_N from meson decays $M_1 \rightarrow ee\pi$. The thin black line is for $K \rightarrow ee\pi$ meson decay with including N decay probability inside the detector. 25
- 1.2 Left: Bounds on the mixing angle $|V_{\mu N}|^2$ as a function of RH neutrino mass M_N in the mass range 10 MeV-100 GeV. Again the bounds are from peak searches ($\pi \rightarrow \mu\nu, K \rightarrow \mu\nu$) and from the visible decay products in N decays in PS191, NA3, BEBC, FMMF, NuTeV. We have also shown the bounds from DELPHI and L3 data analysis. Right: Excluded region on $|V_{\mu N}|^2$ versus M_N from meson decays $M_1 \rightarrow \mu\mu\pi$. The thin black line is for $K \rightarrow \mu\mu\pi$ meson decay with including N decay probability inside the detector. 26
- 1.3 Bounds on $|V_{\tau N}|^2$ as a function of RH neutrino mass M_N from the decays of heavy neutrinos in CHARM, NOMAD and DELPHI. 26
- 1.4 The bounds on the mixing angle $|V_{eN}V_{\mu N}|$ versus M_N from the meson decays $M_1 \rightarrow \mu\pi$. The thin black line is for $K \rightarrow e\mu\pi$ meson decay with including N decay probability inside the detector 27

1.5	Bounds on $ V_{eN}V_{\tau N} $ and $ V_{\mu N}V_{\tau N} $ versus M_N from $\tau \rightarrow e(\mu)\pi\pi$, $\tau \rightarrow e(\mu)\pi K$ and $\tau \rightarrow e(\mu)KK$ decays. The effect of the probability of N decay inside the detector is shown by thin black line.	28
2.1	Feynman diagrams for the decay $B_c^- \rightarrow \bar{B}_s^0 \ell_1^- \ell_2^- \pi^+$	33
2.2	Heavy neutrino decay width, Γ_N as a function of the mass m_N when the magnitude of all the mixing angles $ V_{\ell N} = 1$ ($\ell = e, \mu, \tau$). A bigger range for m_N is chosen than that which allows a resonant enhancement of the $B_c^- \rightarrow \bar{B}_s^0 \ell_1^- \ell_2^- \pi^+$ decay, so as to include the larger values of m_N that will be permitted by the other B_c decay modes to be discussed in Sec. 2.3.	36
2.3	$\frac{\mathcal{B}(B_c^- \rightarrow \bar{B}_s^0 \ell_1^- \ell_2^- \pi^+)}{ V_{\ell N} ^2}$, where, $\ell = e, \mu$. The theoretical calculation uses Γ_N obtained with the assumption $ V_{eN} \sim V_{\mu N} \sim V_{\tau N} $	38
2.4	Exclusion curves for the mixing element $ V_{eN} ^2$, $ V_{\mu N} ^2$ and $ V_{eN}V_{\mu N} $ corresponding to the different expected upper limits for branching ratio of the decay modes $B_c^- \rightarrow \bar{B}_s^0 e^- e^- \pi^+$, $\bar{B}_s^0 \mu^- \mu^- \pi^+$, $\bar{B}_s^0 e^- e \mu^- \pi^+$. In Γ_N , we are using the assumption, $ V_{eN} \sim V_{\mu N} \sim V_{\tau N} $	41
2.5	Feynman diagrams for the decay $B_c^- \rightarrow J/\psi \ell_1^- \ell_2^- \pi^+$	43
2.6	Feynman diagrams for the decay $B_c^- \rightarrow \pi^+ \ell_1^- \ell_2^-$	45
2.7	Exclusion curves for the mixing element $ V_{\ell_1 N}V_{\ell_2 N} $ from upper limits for the branching fraction $\mathcal{B}(B_c^- \rightarrow J/\psi \ell_1^- \ell_2^- \pi^+) \sim 10^{-7}$ and $\mathcal{B}(B_c^- \rightarrow \pi^+ \ell_1^- \ell_2^-) \sim 10^{-9}$. Notation regarding the ordering of the leptons is the same as that described in Sec. 2.2	46

2.8	Exclusion curves for the mixing element $ V_{\ell_1 N} V_{\ell_2 N} $. For (a), one of the leptons is an electron while the second one is a tau; the upper limits used are: $\mathcal{B}(B_c^- \rightarrow J/\psi \ell_1^- \ell_2^- \pi^+) \sim 10^{-6}$, $\mathcal{B}(B_c^- \rightarrow \pi^+ \ell_1^- \ell_2^-) \sim 10^{-8}$, (b) corresponds to the case of one muon and one tau, again using the upper limits: $\mathcal{B}(B_c^- \rightarrow J/\psi \ell_1^- \ell_2^- \pi^+) \sim 10^{-6}$, $\mathcal{B}(B_c^- \rightarrow \pi^+ \ell_1^- \ell_2^-) \sim 10^{-8}$ and for (c), both final leptons are taus and the expected upper limit for $\mathcal{B}(B_c^- \rightarrow \pi^+ \ell_1^- \ell_2^-) \sim 10^{-7}$	47
3.1	The Feynman diagrams for the lepton number violating meson decays. These processes produce resonance enhancement. See text for details.	51
3.2	The t-channel diagram for the lepton number violating meson decay. See text for details.	51
3.3	The total decay width of the heavy neutrino N_1	54
3.4	Constraints on the RH gauge boson M_{W_R} mass, corresponding to a heavy neutrino M_N , that could be resonantly produced in lepton number violating decays of (a) K , (b) D, D_s and (c) B mesons. The shaded region to the left of the curves corresponding to expected limits from searches at different ongoing and future experiments will be ruled out in the absence of LNV meson decays with like sign di-electrons.	58
3.5	Same as Fig. 3.4, except that the limits corresponding to searches at different ongoing and future experiments with like sign dimuons are shown.	62
4.1	Left panel: Feynman diagram for the gluon-initiated LQ pair-production process at LHC. Right panel: the same, but for the quark-initiated processes.	69

4.2	Left panel: variation of the production cross-section with Yukawa coupling for $\sqrt{s} = 13$ TeV. Right panel: limit on scalar LQ pair-production time branching fraction to eq final state as a function of mass for first-generation LQs. The yellow and green bands represent the 2σ and 1σ expected limits. The NLO prediction is shown in blue curve with uncertainty due to choice of PDF set and renormalisation/factorisation scale [1].	70
4.3	Feynman diagram for $e^-p \rightarrow \ell j$	71
4.4	Comparison of the cross section for LQ production at LHC and at LHeC. The c.m.energy for LHC is $\sqrt{s} = 13$ TeV. For LHeC, we use electron beam of 150 GeV and proton beam of 7 TeV, respectively. The coupling Y_{de} has been varied as $0.3 \frac{M_{LQ}}{1\text{TeV}}$, in agreement with the APV constraints.	72
4.5	Production cross-section for $\ell j, jN_1$ and $\bar{\tau}N_3$ at LHeC with varying coupling Z_{11} . We have considered 150 GeV electron beam colliding with 7 TeV Proton beam. The LQ mass has been set to 1.1 TeV. For l^-j, jN_1 , the coupling $Y_{11} = 0.3$, Z_{11} is varying and for $\bar{\tau}N_3$ production, the coupling $Y_{11} = 0.3$, Z_{33} is varying, rest of the Yukawa couplings have been set to zero.	74
4.6	Distribution of transverse momentum p_T of leading lepton, leading and sub leading jet p_T distribution, and invariant mass distribution of leading lepton and leading jet for the final state $\ell^- + n$ -jets ($1 \leq n \leq 2$).	76
4.7	Feynman diagram for various final states from $e^-p \rightarrow jN$. For this case, t-channel LQ mediated diagram can also contribute.	77
4.8	Invariant Mass distribution of LQ, p_T distribution of leading, sub leading jet, and of leading lepton. We also show the invariant mass distribution of N for the final state $\ell^- + n$ -jets ($n \geq 3$).	79
4.9	Missing transverse energy distribution, M_{EFF} distribution, p_T distribution of leading jet, and leading lepton for the final state $\ell^- \ell^+ + n$ -jets ($n \geq 1$) + \cancel{E}_T	80

4.10	Feynman diagram for various final states from $e^-p \rightarrow \bar{t}N_3$. For this case also, the t-channel mediated diagram with gauge boson and LQ will contribute.	81
4.11	Signal cross-section as a function of LQ mass for different final states.	84
4.12	Left panel: The signal cross-section as a function of LQ mass for different final states. Right panel: the significance with 100 fb^{-1} luminosity.	85
4.13	The required luminosity to achieve 3σ (left panel) and 5σ (right panel) for different final states.	86
5.1	Production process, $ep \rightarrow N_1 j_1$, of the RHN at the LHeC through a t channel W boson exchange.	92
5.2	RHN production cross section at the LHeC considering $e p \rightarrow N_1 j$ process for the $e p$ collider at $\sqrt{s} = 1.3 \text{ TeV}$ (LHeC, left panel) and $\sqrt{s} = 1.8 \text{ TeV}$ (HE-LHeC, right panel).	93
5.3	RHN production processes at the linear collider. The left panel is the dominant t channel process and the right panel is s channel process to produce the $e^+e^- \rightarrow N_1 \nu_1$. To produce $N_2 \nu_2$ and $N_3 \nu_3$, the Z mediated s channel process will act.	93
5.4	RHN production cross section at the linear collider considering $e^+e^- \rightarrow N_1 \nu_1$ process at the different center of mass energies.	95
5.5	RHN production cross section at the linear collider considering $e^+e^- \rightarrow N_2 \nu_2$ ($N_3 \nu_3$) process at the different center of mass energies from the s channel Z boson exchange.	95
5.6	$e + J + j_1$ final state at the LHeC and HE-LHeC.	96
5.7	$e + J + p_T^{miss}$ and $J_b + p_T^{miss}$ final states at the linear colliders.	97

5.8	Transverse momentum distribution of the associated jet (p_T^j) from the signal and background events for $M_N = 600$ GeV and 700 GeV at the $\sqrt{s} = 1.3$ TeV LHeC (left panel) and $M_N = 900$ GeV and 1 TeV at the $\sqrt{s} = 1.8$ TeV LHeC (right panel).	98
5.9	Transverse momentum distribution of the electron (p_T^e) from the signal and background events for $M_N = 600$ GeV and 700 GeV at the $\sqrt{s} = 1.3$ TeV LHeC (left panel) and $M_N = 900$ GeV and 1 TeV at the $\sqrt{s} = 1.8$ TeV HE-LHeC (right panel).	98
5.10	Transverse momentum distribution of the fat jet (p_T^J) from the signal and background events for $M_N = 600$ GeV and 700 GeV at the $\sqrt{s} = 1.3$ TeV LHeC (left panel) and $M_N = 900$ GeV and 1 TeV at the $\sqrt{s} = 1.8$ TeV HE-LHeC (right panel).	99
5.11	Jet mass (M_J) distribution of the fat jet from the signal and background events for $M_N = 600$ GeV and 700 GeV at the $\sqrt{s} = 1.3$ TeV LHeC (left panel) and $M_N = 900$ GeV and 1 TeV at the $\sqrt{s} = 1.8$ TeV HE-LHeC (right panel).	99
5.12	Invariant mass distribution of the fat jet and electron system (M_{eJ}) from the signal and background events for $M_N = 600$ GeV and 700 GeV at the $\sqrt{s} = 1.3$ TeV LHeC (left panel) and $M_N = 900$ GeV and 1 TeV at the $\sqrt{s} = 1.8$ TeV HE-LHeC (right panel).	100
5.13	Missing momentum distribution of the signal and background events for $M_N = 500$ GeV and 800 GeV at the $\sqrt{s} = 1$ TeV (left panel) and $M_N = 800$ GeV and 2 TeV at the $\sqrt{s} = 3$ TeV (right panel) linear colliders.	102
5.14	Transverse momentum distribution of the electron (p_T^e) from the signal and background events for $M_N = 500$ GeV and 800 GeV at the $\sqrt{s} = 1$ TeV (left panel) and $M_N = 800$ GeV and 2 TeV at the $\sqrt{s} = 3$ TeV (right panel) linear colliders.	103

5.15	Transverse momentum distribution of the fat jet (p_T^J) from the signal and background events for $M_N = 500$ GeV and 800 GeV at the $\sqrt{s} = 1$ TeV (left panel) and $M_N = 800$ GeV and 2 TeV at the $\sqrt{s} = 3$ TeV linear colliders.	103
5.16	Jet mass (M_J) distribution of the fat jet from the signal and background events for $M_N = 500$ GeV and 800 GeV at the $\sqrt{s} = 1$ TeV (left panel) and $M_N = 800$ GeV and 2 TeV at the $\sqrt{s} = 3$ TeV (right panel) linear colliders.	104
5.17	$\cos \theta_{J(e)}$ distributions for the $J(e)$ in the first row (second row) for the 1 TeV (left column) and 3 TeV (right column) linear colliders.	104
5.18	p_T^{miss} distribution of the signal and background events for $M_N = 700$ GeV and 800 GeV at the $\sqrt{s} = 1$ TeV (left panel) and $M_N = 1.5$ TeV and 2 TeV at the $\sqrt{s} = 3$ TeV (right panel) linear colliders.	107
5.19	Transverse momentum distribution of J_b ($p_T^{J_b}$) from the signal and background events for $M_N = 700$ GeV and 800 GeV at the $\sqrt{s} = 1$ TeV (left panel) and $M_N = 1.5$ TeV and 2 TeV at the $\sqrt{s} = 3$ TeV (right panel) linear colliders.	108
5.20	Fat b-Jet mass (M_{J_b}) distribution from the signal and background events for $M_N = 700$ GeV and 800 GeV at the $\sqrt{s} = 1$ TeV (left panel) and $M_N = 1.5$ TeV and 2 TeV at the $\sqrt{s} = 3$ TeV (right panel) linear colliders.	108
5.21	The prospective upper limits on $ V_{eN} ^2$ at the 1.3 TeV LHeC (blue band) and 1.8 TeV HE-LHeC (red band) at the 1 ab^{-1} luminosity compared to EWPD, LEP2, GERDA, ATLAS (ATLAS8- ee), CMS (CMS8 - ee) at the 8 TeV LHC, 13 TeV CMS search for $e^\pm e^\pm + 2j$ (CMS13- ee) and 13 TeV CMS search for 3ℓ (CMS13- ee) respectively.	111
5.22	Same as Fig. 5.21 with 3 ab^{-1} luminosity at the 1.3 TeV LHeC and 1.8 TeV HE-LHeC.	112

5.23	The prospective upper limits on $ V_{eN} ^2$ at the 1 TeV (red band) and 3 TeV (blue band) linear colliders at the 1 ab^{-1} luminosity for $e + J + p_T^{miss}$ signal compared to EWPD, LEP2, GERDA, ATLAS (ATLAS8- ee), CMS (CMS8 - ee) at the 8 TeV LHC, 13 TeV CMS search for $e^\pm e^\pm + 2j$ (CMS13- ee) and 13 TeV CMS search for 3ℓ (CMS13- ee) respectively.	113
5.24	Same as Fig. 5.23 with 3(5) ab^{-1} luminosity at the 1(3) TeV linear collider. . . .	114
5.25	The prospective upper limits on $ V_{eN} ^2$ at the 1 TeV (red band) and 3 TeV (blue band) linear colliders at the 1 ab^{-1} luminosity for $J_b + p_T^{miss}$ signal compared to EWPD, LEP2, GERDA, ATLAS (ATLAS8- ee), CMS (CMS8 - ee) at the 8 TeV LHC, 13 TeV CMS search for $e^\pm e^\pm + 2j$ (CMS13- ee) and 13 TeV CMS search for 3ℓ (CMS13- ee) respectively.	114
5.26	Same as Fig. 5.25 with 3(5) ab^{-1} luminosity at the 1(3) TeV linear collider. . . .	115
A.1	Kinematics of four-body decays $B_c^- \rightarrow \bar{B}_s^0 \ell_1^- \ell_2^- \pi^+$ in the B_c rest frame.	124

List of Tables

1.1	The SM particle contents and $i = 1, 2, 3$ is the generation index.	12
4.1	Benchmark parameters and production cross-section for $\ell j, jN_1$ and $\bar{i}N_3$ at LHeC with electron and proton beam energy 150 GeV and 7 TeV respectively. LQ mass is considered as 1.1 TeV.	72
4.2	Signal and Background cross-sections for the final state $\ell^- + n$ -jets ($1 \leq n \leq 2$) after different cuts. BP1 has been used for this final state.	76
4.3	Signal and Background cross-sections for the final state $\ell^- + n$ -jets ($n \geq 3$) with cuts. BP2 has been used for this final state.	78
4.4	Signal and Background cross-section after various cuts for the final state $\ell^- \ell^+ + n$ -jets ($n \geq 1$) + \cancel{E}_T . BP2 has been used for this final state.	80
4.5	Signal and Background cross-section after various cuts for the final state $\bar{b} \ell^- \tau^- \ell^+ + \cancel{E}_T$. BP3 has been used for this final state.	82
4.6	Signal and Background cross-section after various cuts for the final state $\bar{b} \ell^- \tau^- + n$ -jets ($n \geq 2$) + \cancel{E}_T . BP3 has been used for this final state.	82
4.7	Signal and Background cross-section after various cuts for the final state $\bar{b} \ell^+ \tau^- + n$ -jets ($n \geq 2$) + \cancel{E}_T . BP3 has been used for this final state.	83
4.8	Cross-sections (in fb) after all the cuts as a function of LQ mass.	83

4.9	Cross-sections in fb, after all the cuts (except invariant LQ and right handed neutrinos mass cut) as a function of LQ mass. Backgrounds are same as for 1.1 TeV, as the beam energies are same.	85
4.10	Significance for different final states with integrated luminosity $\mathcal{L} = 100 \text{ fb}^{-1}$ (1st column corresponding to each LQ mass) and $\mathcal{L} = 1000 \text{ fb}^{-1}$ (2nd column corresponding to each LQ mass) respectively for the LQ mass range [1.1-1.7]TeV.	86
5.1	Cut flow of the signal and background events for the final state $e^\pm + J + j_1$ for $M_N = 600 \text{ GeV}$ and 700 GeV with $\sqrt{s} = 1.3 \text{ TeV}$ LHeC where the signal events are normalized by the square of the mixing.	101
5.2	Cut flow of the signal and background events for the final state $e^\pm + J + j_1$ for $M_N = 900 \text{ GeV}$ and 1.0 TeV with $\sqrt{s} = 1.8 \text{ TeV}$ HE-LHeC where the signal events are normalized by the square of the mixing.	101
5.3	Cut flow for the signal and background events for the final state $e^\pm + J + p_T^{miss}$ for $M_N = 500 \text{ GeV}$ at the $\sqrt{s} = 1 \text{ TeV}$ linear collider. The signal events are normalized by the square of the mixing.	105
5.4	Cut flow for the signal and background events for the final state $e^\pm + J + p_T^{miss}$ for $M_N = 800 \text{ GeV}$ at the $\sqrt{s} = 1 \text{ TeV}$ linear collider. The signal events are normalized by the square of the mixing.	105
5.5	Cut flow for the signal and background events for the final state $e^\pm + J + p_T^{miss}$ for $M_N = 800 \text{ GeV}$ at the $\sqrt{s} = 3 \text{ TeV}$ linear collider. The signal events are normalized by the square of the mixing.	106
5.6	Cut flow for the signal and background events for the final state $e^\pm + J + p_T^{miss}$ for $M_N = 2 \text{ TeV}$ at the $\sqrt{s} = 3 \text{ TeV}$ linear collider. The signal events are normalized by the square of the mixing.	107

5.7	Cut flow for the signal and background events for the final state $J_b + p_T^{miss}$ for $M_N = 700$ GeV and 800 GeV at the $\sqrt{s} = 1$ TeV linear collider. The signal events are normalized by the square of the mixing.	109
5.8	Cut flow for the signal and background events for the final state $J_b + p_T^{miss}$ for $M_N = 1.5$ TeV and 2 TeV at the $\sqrt{s} = 3$ TeV linear collider. The signal events are normalized by the square of the mixing.	110

Synopsis

Introduction and Motivation

Neutrino oscillations have clearly established the fact that at least two out of three active neutrinos are massive. The immediate question one can then ask is, are neutrinos Majorana or Dirac particles? Lepton number conservation (LNC) would imply that neutrinos are Dirac particles, but there is no reason to have LNC as it is not a fundamental quantity like electric charge. From theorist's point of view, almost all extensions of standard model (SM) predict Majorana neutrinos. From experimental side, the most promising process to explore Majorana nature of neutrino is neutrinoless double beta decay, which may be feasible due to large sample of the decaying nuclei.

From neutrino oscillations and cosmological observations, we know that neutrino masses are very small. In various seesaw models, the inclusion of SM singlet heavy right handed neutrinos (sterile neutrinos)¹ to the Standard Model (SM) particle content is one of the best motivated way to account for the observed neutrino masses and flavor mixing. The modification of the charged and neutral currents from active-sterile mixing of the neutral leptons can provide novel signatures which can be tested at the future collider experiments. Sterile neutrino mass scale can lie in a wide range depending upon the models. In particular, in low energy seesaw models sterile neutrinos may have masses between 100 MeV to few GeV. On the theoretical and phenomenological side as well, considerable

¹We will be using the names sterile neutrinos or RHNs interchangeably.

effort has been made in proposing possible modes that could probe SM singlet Majorana neutrinos in various mass ranges and constrain their mixing parameters. Search strategy varies depending on the mass scale. For example, for the sterile neutrino mass of few GeV, various three and four body LNV meson decays $M_1^- \rightarrow \ell_1^- \ell^- M_2^+$ and $M_1^- \rightarrow M_2 \ell_1^- \ell_2^- M_3^+$ can be used as a probe to test their existence [2]. For mass range 100 GeV or beyond, best way to search for these heavy neutrinos is at e^+e^- , $e\gamma$, pp and $p\bar{p}$ colliders, as well as in top quark and W-boson rare decays. For very heavy RHNs, the production cross section of the RHNs decreases as the mass of RHN increases. But for very heavy RHN, gauge boson produced from heavy neutrino decay is highly boosted, leading to a fatjet. Hence, for very heavy RHN, even if the production cross section is small, using fatjet technique, one can significantly reduce the SM background. One common problem with the RHNs extensions of SM is that RHNs production is very small due to small mixing angle. Hence, prospects of discovering RHNs at colliders greatly improve if RHN production is independent of the mixing angle.

This thesis deals with three and four body LNV meson decays to search for Majorana neutrinos in the mass range of few GeV, RHNs search of orders of 100 GeV through Lep-toquark productions and very heavy RHNs search through fatjet signature. We describe each of these studies in the following sections.

Favoured B_c Decay modes to search for a Majorana neutrino

In this work [3], we propose a search for a few lepton-number violating ($\Delta L = 2$) decay modes of B_c which can only be induced by Majorana neutrinos. We extend the SM to include n right-handed SM singlets along with the three generation of left-handed SM SU(2) doublets: $L_{aL} = \begin{pmatrix} \nu_{aL} & \ell_{aL} \end{pmatrix}^T$, N_{bR} , where $a=1,2,3$ and $b=1,2,3,\dots,n$. In this model, flavor eigenstates $\nu_{\ell L}$ can be written in terms of the mass eigenstates as, $\nu_{\ell L} =$

$\sum_{m=1}^3 U_{\ell m} \nu_{mL} + \sum_{m'=4}^{3+n} V_{\ell m'} N_{m'L}^c$, with $UU^\dagger + VV^\dagger = 1$. In this work, we consider a minimal scenario in which a single RH neutrino is added to the SM field content. We take a phenomenological approach regarding the mass and mixing elements of the heavy singlet neutrino, taking them to be free parameters, constrained only by experimental observations. We denote by $V_{\ell N}$ the mixing angle between the standard flavour neutrino $\nu_\ell (\ell = e, \mu, \tau)$ and the heavy mass eigenstate N .

Since the lepton number violating modes are expected to be rare, when using meson decay modes for these searches one expects CKM favoured modes to be the preferred ones; $B_c \rightarrow B_s$ is one such transition. In the proton-proton collisions at the Large Hadron Collider, B_c mesons are expected to be mainly produced through the gluon-gluon fusion process $gg \rightarrow B_c^- + \bar{b} + c$. The expected number of B_c mesons at LHC with $\sqrt{s} = 13/14$ TeV and luminosity 10 fb^{-1} is $\mathcal{O}(10^9 - 10^{10})$. With this large number of B_c events, along with the resonance enhancement of the Majorana neutrino mediating the $B_c^- \rightarrow \bar{B}_s^0 \ell_1^- \ell_2^- \pi^+$ modes, one can hope to observe these rare modes, or, even their non-observation can be used to obtain tight constraints on the mixing angles from upper limits of the branching fractions. Using these modes we obtain exclusion curves for the mixing angles which are tighter or compatible with results from earlier studies. However, we find that the relatively suppressed mode $B_c^- \rightarrow J/\psi \ell_1^- \ell_2^- \pi^+$ can provide even tighter constraints on $|V_{eN}|^2$, $|V_{\mu N}|^2$, $|V_{eN}V_{\mu N}|$, and in a larger range of the heavy neutrino mass. Further, exclusion regions for $|V_{eN}V_{\tau N}|$, $|V_{\mu N}V_{\tau N}|$ can also be obtained for masses larger than those accessible in tau decays. Upper limits on $\mathcal{B}(B_c^- \rightarrow \pi^+ \ell_1^- \ell_2^-)$ can also result in stringent exclusion curves for all the mixing elements, including that for $|V_{\tau N}|^2$ in a mass range where it is unconstrained thus far.

Constraints on Right Handed Gauge Boson Mass from Lepton Number Violating Meson Decays

In this work [4], we analyze the three body lepton number violating (LNV) meson decays $M_1^+ \rightarrow \ell^+ \ell^+ \pi^-$, that arise in a TeV scale Left Right Symmetry model (LRSM). The LRSM is based on the gauge group $SU(3)_c \times SU(2)_L \times SU(2)_R \times U(1)_{B-L}$ [5]. In addition to the particle content of the Standard Model (SM), the model contains three right handed Majorana neutrinos N_R , and the additional gauge bosons W_R and Z' .

Right handed Majorana neutrinos with mass in the hundreds of MeV-few GeV range can be produced as an intermediate on mass shell state, resulting in a resonance enhancement of the LNV meson decay rates. We follow a most generic approach taking into account all the contributions arising from right handed, left handed currents as well as their combinations. When calculating signal events we have taken care of the velocity of the decaying meson and also the probability of RH neutrino to decay inside the detector. The theoretical estimates of the number of events are functions of the mass parameters M_N and M_{W_R} . Hence, equating the numerical upper limit on the number of events to the theoretical expressions, results in constraints on M_{W_R} , corresponding to specific M_N values. Using this method we calculated the number of events for the LNV decay modes $M_1^+ \rightarrow \ell^+ \ell^+ \pi^-$ ($M_1 = B, D, D_s, K$) and derive constraints plausible on the mass of the right handed charged gauge boson W_R by future searches at the ongoing NA62 and LHCb experiments at CERN, the upcoming Belle II at SuperKEK, as well as at the proposed future experiments, SHiP and FCC-ee. These bounds are complimentary to the limits from same-sign dilepton search at the Large Hadron Collider (LHC). The very high intensity of charmed mesons expected to be produced at SHiP will result in a far more stringent bound, $M_{W_R} > 18.4$ TeV (corresponding to $M_N = 1.46$ GeV), than the other existing bounds from collider and neutrinoless double beta decay searches.

Probing Leptoquark and Heavy Neutrino at LHeC

In this work [6], we explore leptoquark (LQ) production and decay for the \tilde{R}_2 class of models at the proposed Large Hadron electron Collider (LHeC), planned to operate with 150 GeV electron and 7 TeV proton beams. Leptoquarks (LQs) are hypothetical particles, which carry both lepton number and baryon number and couple directly to quarks and leptons. In the Pati-Salam model, they emerge from the unification of quarks and leptons [7]. Using the SM representation of quarks and leptons, all possible LQ states can be classified, with six scalar and six vector LQ multiplets under the SM gauge group. Among the different classes, the scalar LQ \tilde{R}_2 is interesting, as it is one of the multiplets that allows for matter stability. Moreover, it also couples to right handed neutrinos (RH neutrinos). The relevant Lagrangian is given by,

$$\mathcal{L} = -Y_{ij} \bar{d}_R^i e_L^j \tilde{R}_2^{2/3} + (Y_{UPMNS})_{ij} \bar{d}_R^i \nu_L^j \tilde{R}_2^{-1/3} + (V_{CKMZ})_{ij} \bar{u}_L^i N_R^j \tilde{R}_2^{2/3} + Z_{ij} \bar{d}_L^i N_R^j \tilde{R}_2^{-1/3} + h.c.,$$

where the superscript of LQ fields denotes electric charge. For the RH neutrino, we adopt a model independent framework as we are interested in frameworks that can lead to large active-sterile mixing, so that the heavy neutrinos decay inside the detector.

At e^-p colliders like LHeC, LQ can be resonantly produced and the production cross-section is larger than that at LHC. One more advantage is that unlike seesaw models the RH neutrino production through resonant LQ production does not depend on active-heavy neutrino mixing angle. Hence, the RH neutrino production will be enhanced compared to seesaw models. We analyse the collider signatures of a number of final states that can originate from LQ decay into the standard model particles, as well as the final states that originate from further decay of the heavy neutrinos produced from LQ: (1). $e^-p \rightarrow \ell j$, (2). $e^-p \rightarrow j N_1, N_1 \rightarrow \ell^- W^+$, (3). $e^-p \rightarrow \bar{i} N_3, \bar{i} \rightarrow \bar{b} W^-, N_3 \rightarrow \tau^- W^+$. We consider both leptonic and hadronic decays of W boson. We find that the final state $\ell^- + n\text{-jets}$ ($1 \leq n \leq 2$) has the largest discovery prospect, more than 5σ with only few fb^{-1} of data

to probe a LQ of mass 1.1 TeV, even with a generic set of cuts. The significance falls sharply with increasing LQ mass. However, with 100 fb^{-1} of data, a 5σ discovery for LQs of mass upto 1.4 TeV is still achievable. Also for the same luminosity, final state $\bar{b}\ell^+\tau^- + n\text{-jets } (n \geq 2) + \cancel{E}_T$, resulting from the cascade decay of the LQ to a \bar{t} and right handed neutrino, followed by further decays of \bar{t} and the neutrino, is expected to yield a rather large number of events (≈ 180).

Probing right handed neutrinos at the LHeC and lepton colliders using fat jet signatures

In this work [8], we explore the discovery prospect of a very heavy right handed neutrino in Type-I seesaw at the future collider experiments like LHeC and linear collider. We consider the production of the heavy neutrino via the t and s -channel processes and its subsequent decays into the semi-leptonic final states. We specifically focus on the scenario where the gauge boson produced from heavy neutrino decay is highly boosted, leading to a fat-jet. For both of the colliders we consider the luminosity at 1000 fb^{-1} . In our analysis we consider the following things:

- (1). We study the prospect of discovery of RHNs at LHeC considering the boosted objects for the first time. In the LHeC we concentrate on the lepton number violating (LNV) and lepton number conserving (LNC) channels to produce the RHN in association with a jet (j_1). Hence the RHN will decay into the dominant ℓW and the W will decay into a pair of jets. The daughter W coming from the heavy RHN will be boosted and its hadronic decay products, jets, of the W will be collimated such that they can form a fat jet (J). Hence a signal sample of $\ell + j_1 + J$ can be studied thoroughly at this collider. We consider two scenarios at the LHeC where the electron and proton beams will have 60 GeV and 7 (13.5) TeV energies where the center of mass energy becomes $\sqrt{s} = 1.3$ (1.8) TeV.

(2). At the linear collider the leading production of the RHNs is occurring from the t -channel process in association with a SM light neutrino (ν). We consider the linear collider at two different center of mass energies, such as $\sqrt{s} = 1$ TeV and $\sqrt{s} = 3$ TeV which can probe up to a high mass of the RHNs such as 900 GeV (at the 1 TeV linear collider) and 2.9 TeV (at the 3 TeV linear collider) due to the almost constant cross section for the $N\nu$ production. At this mass scale, the RHNs will be produced at rest, however, the daughter particles can be sufficiently boosted. We consider $N \rightarrow \ell W, W \rightarrow jj$ and $N \rightarrow h\nu, h \rightarrow b\bar{b}$ modes at the linear collider where h is the SM Higgs boson. If the RHN is sufficiently heavy, such the, $M_N \geq 400$ GeV, the W and h can be boosted because M_W and $M_h \ll \frac{M_N}{2}$. As a result W and h will produce a fat jet (J) and a fat b jet (J_b) respectively. Therefore the signal will be $\ell + J$ plus missing momentum and J_b plus missing momentum in the W and h modes respectively at the linear collider. Hence studying the signals and the backgrounds for each process we put the bounds in the mass-mixing plane of the RHNs.

Conclusion

We propose several LNV B_c decay modes to search for sterile neutrinos in the context of sterile neutrino extension of SM. We also evaluate the LNV meson decays $M_1^+ \rightarrow \ell^+ \ell^+ \pi^-$ within the framework of Left-Right Symmetric model. For both the above cases, from non-observations of these decay modes, we put bound on mixing angle and M_{W_R} corresponding to specific M_N values. We also study the discovery prospect of \tilde{R}_2 class of LQ model at LHeC. We study the production and its decay to different final states including a lepton and a jet, a jet and a RHN and RHN and a top quark. We have also explored the discovery prospect of a very heavy RHN at LHeC and linear collider. A massive RHN can sufficiently boost the W and h , such that its hadronic decay modes can form a fat jet. Therefore, we study $e + j_1 + J$ and $e + J + p_T^{miss}$, $J_b + p_T^{miss}$ at the LHeC and linear collider respectively.

1 Introduction

The SM is an outstanding theoretical framework of elementary particles. With the discovery of Higgs boson-the last missing piece, the SM is now complete. Though the current data so far indicates that this is the SM Higgs boson, further work is still needed to be certain. Even if one consider this as the SM Higgs, the SM can not be the final theory, as the SM predicts massless neutrinos, there is no viable dark matter candidate and it can not explain the matter-antimatter asymmetry. There are also several other issues like unification of forces, hierarchy, fine-tuning and naturalness problem which can not be explained in SM. A number of beyond Standard Model (BSM) extensions (minimal supersymmetric standard model, large extra dimensions, seesaw models of neutrino mass generation, leptoquarks, grand unified theories etc) have been proposed in the literature to address some of these issues. All the BSM extensions includes new particles, hence to experimentally verify a new model, one of the most advantageous paths might be to discover new states at various ongoing and future collider experiments. In this thesis, we are mostly dealing with models which can explain the observed neutrino masses in presence of heavy right-handed neutrinos¹ and how we can discover them from direct searches at colliders, as well as through indirect searches from meson decays.

The discovery of neutrino oscillations [9–19] confirms the existence of at least two non-vanishing neutrino mass-squared differences. So far, the solar and atmospheric mass square differences Δm_{12}^2 , $|\Delta m_{13}^2|$ and the mixing angles θ_{12} , θ_{23} and θ_{13} have been mea-

¹We will be using the names sterile neutrinos, RH neutrino or RHNs interchangeably.

sured with reasonable accuracy [20]. On the other hand, the cosmological constraints on the sum of light neutrino masses [21] guarantees the SM neutrino masses to be less than $\mathcal{O}(\text{eV})$. In principle, neutrino mass could be simply generated by addition of right-handed (RH) neutrinos through the Higgs mechanism, but to get neutrino masses less than 1 eV, the neutrino Yukawa coupling has to be extremely small $\sim \mathcal{O}(10^{-12})$. Hence alternate mechanisms for neutrino mass have been proposed. Among these the seesaw mechanism [22–28] provides a natural explanation of the smallness of neutrino mass. The simplest realization of the seesaw, the so-called type-I seesaw, requires the existence of a set of heavy electroweak singlet (sterile) lepton number violating (LNV) Majorana fermions, N . A typical scale for the Majorana mass m_N in grand unified theories (GUTs) [24] is of the order of the GUT scale, but in general, in various other scenarios, sterile neutrinos can lie in a wide range of masses. In particular, in low energy seesaw models [29–32] sterile neutrinos may have mass between ~ 100 MeV to few GeV. eV sterile neutrinos have also been invoked to explain the LSND [33, 34], Miniboone [35–37] and reactor [38–40] anomalies. A viable dark matter candidate is a KeV sterile neutrino [41–58]. Other astrophysical observations including supernovae explosions [59] permit sterile neutrinos mixed with active ones. While cosmological/astrophysical constraints on sterile neutrinos are strong, they are model dependent and hence laboratory searches and constraints on sterile neutrinos, particularly Majorana sterile neutrinos are rather important. On the theoretical and phenomenological side as well, considerable effort has been made in proposing possible observables or modes that could probe SM singlet Majorana neutrinos in various mass ranges and constrain their mixing parameters. Sterile neutrinos have been searched for in the laboratory through peak searches in leptonic decays of pions and kaons [60]. The lepton spectrum would show a monochromatic line at a lower energy in presence of a heavy neutrino. These have provided tight constraints on the mixing angle of the sterile neutrino with the active ones.

One of the promising processes to explore Majorana neutrinos is through neutrinoless double beta decay which may be experimentally feasible due to the large samples of the

decaying nuclei, however, on the theoretical side this involves large uncertainties coming from the nuclear matrix elements making it harder to extract information on neutrino properties. The rare LNV meson and tau decays can be more accurately evaluated [2, 61–63] and although their decay rates may be extremely small, they may be accessible with current and future high luminosity machines. In the last decade or so, many experimental collaborations, CLEO [64–66], FOCUS [67], BaBar [68], Belle and more recently LHCb [69], have searched for such LNV processes. For mass range of m_N (100 MeV–6 GeV), right handed Majorana neutrinos can be produced as an intermediate on mass shell state, resulting in a resonance enhancement of these LNV meson and tau decay rates. For mass range 100 GeV or beyond, sterile neutrinos have also been looked for through searches of their visible decay products. This includes proposals to search for heavier neutrinos at accelerator and collider experiments such as, e^+e^- [70–75], $e\gamma$ [71, 76], pp and $p\bar{p}$ [71, 74, 75, 77–86], e^-e^- [75, 87, 88], as well as in top quark and W-boson rare decays [89, 90]. For very heavy neutrinos, gauge boson produced from heavy neutrino decay is highly boosted, leading to a fatjet and this strategy can be very effective. One common problem with the right-handed neutrino extensions of SM is that their production rate is very small due to a small mixing angle. Hence, prospects of discovering them at colliders greatly improve if the production is independent of the mixing angle. We address some of these issues in this thesis.

This chapter is organized as follows: we first review briefly the basic features of SM, following which we describe the neutrino mass models. We briefly describe two such models like type-I seesaw and left right symmetric model. We present the existing bounds on the sterile-active neutrino mixing angles as a function of sterile neutrino mass. Finally, we give the outline of this thesis.

1.1 Standard Model

The SM [91, 92] is a renormalizable, Lorentz-invariant quantum field theory based on the gauge group $SU(3)_c \otimes SU(2)_L \otimes U(1)_Y$ which contains the fundamental set of particles, the leptons, quarks, gauge bosons and the Higgs.

	$SU(3)_C$	$SU(2)_L$	$U(1)_Y$				
q_L^i	3	2	$\frac{1}{6}$	Gauge bosons	Force		
u_R^i	3	1	$\frac{2}{3}$			G_μ^a	Strong
d_R^i	3	1	$-\frac{1}{3}$			W_μ^\pm, Z_μ^0	Weak
ℓ_L^i	1	2	$-\frac{1}{2}$	A_μ	Electromagnetic		
e_R^i	1	1	-1				
H	1	2	$\frac{1}{2}$				

Table 1.1: The SM particle contents and $i = 1, 2, 3$ is the generation index.

We have listed the particle content of the SM in Table. 1.1. q_L^i and ℓ_L^i are the left handed quark and lepton doublets respectively. u_R^i and d_R^i are the right handed up and down type singlet quarks. ℓ_R^i is the right handed lepton. H is the Higgs field. The SM fermions and gauge bosons (W^\pm, Z^0) are forced to be massless due to the exact $SU(2)_L \otimes U(1)_Y$ symmetry. We need to break this gauge symmetry somehow to generate masses for fermions and gauge bosons. This is achieved by the spontaneous symmetry breaking: the electroweak symmetry $SU(2)_L \otimes U(1)_Y$ is spontaneously broken to the electromagnetic $U(1)_Q$ through the non-zero vacuum expectation value (VEV) of the Higgs field. The Lagrangian for the SM can be written as

$$\mathcal{L}_{\text{SM}} = \mathcal{L}_{\text{kinetic}} + \mathcal{L}_{\text{Higgs}} + \mathcal{L}_{\text{Yukawa}} \quad (1.1)$$

In the following section we describe each part of this Lagrangian.

Kinetic Term for Leptons and Quarks

The kinetic term for the lepton and quark sector is given by

$$\begin{aligned} \mathcal{L}_{\text{kinetic}}^{\text{lepton+quarks}} &= \bar{\ell}_L \gamma^\mu \left(D^{\mu \ell_L} \ell_L \right) + \bar{e}_R \gamma^\mu \left(D_\mu^{e_R} e_R \right) + \bar{q}_L \gamma^\mu \left(D_\mu^{q_L} q_L \right) \\ &+ \bar{u}_R \gamma^\mu \left(D_\mu^{u_R} u_R \right) + \bar{d}_R \gamma^\mu \left(D_\mu^{d_R} d_R \right). \end{aligned} \quad (1.2)$$

The covariant derivative for the lepton doublet is given by

$$\mathcal{D}_\mu^{\ell_L} = \partial_\mu - i \frac{g}{2} \begin{pmatrix} 0 & \sqrt{2} W_\mu^+ \\ \sqrt{2} W_\mu^- & 0 \end{pmatrix} - i \frac{g}{2} W_\mu^3 \begin{pmatrix} 1 & 0 \\ 0 & -1 \end{pmatrix} - i g' Y_{\ell_L} B_\mu \quad (1.3)$$

where g and g' are the $SU(2)_L$ and $U(1)_Y$ gauge couplings. W_μ^\pm is defined as, $W_\mu^\pm = \frac{W_\mu^1 \mp i W_\mu^2}{\sqrt{2}}$. W_μ^1 , W_μ^2 and W_μ^3 are the gauge bosons of the $SU(2)_L$ generators $T^a = \frac{\sigma^a}{2}$. B_μ is the gauge boson corresponding to $U(1)_Y$ hypercharge generator. We can write the W_3 and B field in terms of physical gauge field A and Z as

$$\begin{pmatrix} W_\mu^3 \\ B_\mu \end{pmatrix} = \begin{pmatrix} \cos \theta_w & \sin \theta_w \\ -\sin \theta_w & \cos \theta_w \end{pmatrix} \begin{pmatrix} Z_\mu \\ A_\mu \end{pmatrix}. \quad (1.4)$$

where θ_w is the weak mixing angle which can be defined as

$$\tan \theta_w = \frac{g'}{g}. \quad (1.5)$$

Using Eq. 1.4 we can write Eqs.(1.3) as

$$\mathcal{D}_\mu^{\ell_L} = \partial_\mu - i \frac{g}{2} \begin{pmatrix} 0 & \sqrt{2} W_\mu^+ \\ \sqrt{2} W_\mu^- & 0 \end{pmatrix} - i \frac{g}{\cos \theta_w} (T^3 - Q_\ell \sin^2 \theta_w) Z_\mu - i e Q_\ell A_\mu \quad (1.6)$$

and the covariant derivative for e_R is given by

$$\mathcal{D}_\mu^{e_R} = \partial_\mu - i g' Y_{e_R} B_\mu = \partial_\mu - i \frac{g}{\cos \theta_w} (-Q_{e_R} \sin^2 \theta_w) Z_\mu - i e Q_{e_R} A_\mu. \quad (1.7)$$

Similarly for quark doublet q_L we can write the covariant derivative as

$$\mathcal{D}_\mu^{q_L} = \partial_\mu - ig_s G_\mu - ig W_\mu - iY_{q_L} B_\mu, \quad (1.8)$$

where $G_\mu = G_\mu^a \lambda^a$ is the gluon field and λ^a ($a = 1, 2, \dots, 8$) are the generator of $SU(3)_c$. g_s is the $SU(3)_c$ gauge coupling constant. The covariant derivative for u_R and d_R are given by

$$\begin{aligned} \mathcal{D}_\mu^{u_R} &= \partial_\mu - ig_s G_\mu - ig' Y_{u_R} B_\mu, \\ \mathcal{D}_\mu^{d_R} &= \partial_\mu - ig_s G_\mu - ig' Y_{d_R} B_\mu. \end{aligned} \quad (1.9)$$

The kinetic term for $SU(2)_L \otimes U(1)_Y$ and $SU(3)_c$ gauge sector

The kinetic term for the $SU(2)_L \otimes U(1)_Y$ gauge sector can be written as

$$\mathcal{L}_{kinetic}^{gauge} = -\frac{1}{4} F_{\mu\nu}^a F^{a\mu\nu} - \frac{1}{4} B_{\mu\nu} B^{\mu\nu} \quad (1.10)$$

where $F_{\mu\nu}^a = \partial_\mu A_\nu^a - \partial_\nu A_\mu^a + g \epsilon^{abc} A_\mu^b A_\nu^c$ and $B_{\mu\nu} = \partial_\mu B_\nu - \partial_\nu B_\mu$. This Lagrangian includes 3-point and 4-point interactions like $W^+ W^- \gamma$, $W^+ W^- Z$ and the 4-point interactions like $W^+ W^- \gamma \gamma$, $W^+ W^- Z Z$, $W^+ W^- \gamma Z$ and $W^+ W^- W^+ W^-$. The kinetic term for the gluon in the $SU(3)_c$ gauge sector can be written as

$$\mathcal{L}_{kinetic}^{gluon} = -\frac{1}{4} G_{\mu\nu}^a G^{a\mu\nu}, \quad (1.11)$$

where $G_{\mu\nu}^a = \partial_\mu G_\nu^a - \partial_\nu G_\mu^a + g_0 f^{abc} G_\mu^b G_\nu^c$, which includes 3-point and 4-point gluon-self interactions.

Spontaneous symmetry breaking: Higgs mechanism

In SM, the masses of all the fermions and $SU(2)_L$ gauge bosons are generated through the spontaneous symmetry breaking (SSB). The Lagrangian for the Higgs sector is given by

$$\mathcal{L}_{\text{Higgs}} = (D_\mu^H H) (D^{H\mu} H) - V(H^\dagger H) \quad (1.12)$$

where, the Higgs potential is $V(H^\dagger H) = -\mu^2 H^\dagger H + \lambda (H^\dagger H)^2$. After the SSB, the Higgs field develops its VEV and can be expanded around its classical minimum as

$$H(x) = \frac{1}{\sqrt{2}} \begin{pmatrix} H^+ \\ v + h(x) + iH^0 \end{pmatrix} \quad (1.13)$$

Now the covariant derivative can be written as

$$\mathcal{D}_\mu^H = \partial_\mu - i \frac{g}{2} \begin{pmatrix} A_\mu^3 + \tan \theta_w B_\mu & \sqrt{2} W_\mu^+ \\ \sqrt{2} W_\mu^- & -\frac{Z_\mu}{\cos \theta_w} \end{pmatrix}. \quad (1.14)$$

Three gauge bosons W^\pm and Z^0 gets masses by eating up the three Goldstone bosons H^\pm and H^0 . The photon field remain massless as $U(1)_Q$ is unbroken. The masses of these gauge bosons are given as

$$m_{W^\pm}^2 = \frac{1}{4} g^2 v^2, \quad m_Z^2 = \frac{1}{4} \frac{g^2 v^2}{\cos^2 \theta_w}, \quad m_A^2 = 0. \quad (1.15)$$

Replacing the Higgs field of Eq. 1.13 in Higgs potential we can derive the Higgs mass as

$$V = \lambda v^2 h^2 + \lambda v h^3 + \frac{\lambda}{4} h^4, \quad (1.16)$$

where the Higgs mass is $m_h = \sqrt{2\lambda}v$ and was measured to be 125 GeV in 2012 at LHC.

Yukawa Lagrangian for leptons and quarks

The Yukawa interactions for the lepton and quark sector are given by

$$\begin{aligned}\mathcal{L}_{\text{Yukawa}}^{\text{lepton}} &= Y_e \bar{\ell}_L H e_R + H.c., \\ \mathcal{L}_{\text{Yukawa}}^{\text{quark}} &= Y_u \bar{q}_L \tilde{H} u_R + Y_d \bar{q}_L H d_R + H.c.\end{aligned}\quad (1.17)$$

After the SSB, the Dirac mass terms for the leptons and quarks are generated as

$$\begin{aligned}\mathcal{L}_{\text{mass}}^{\text{lepton}} &= m_e \left(1 + \frac{h}{v}\right) [\bar{e}_L e_R + \bar{e}_R e_L], \\ \mathcal{L}_{\text{mass}}^{\text{quark}} &= m_{ij}^u \left(1 + \frac{h}{v}\right) \bar{u}_L^i u_R^j + m_{ij}^d \left(1 + \frac{h}{v}\right) \bar{d}_L^i d_R^j + H.c.\end{aligned}\quad (1.18)$$

where $m_e = \frac{Y_e v}{\sqrt{2}}$, $m_u^{ij} = \frac{Y_u^{ij} v}{\sqrt{2}}$ and $m_d^{ij} = \frac{Y_d^{ij} v}{\sqrt{2}}$. In the absence of right handed neutrinos we can not write such mass term for neutrinos, hence in SM, neutrinos are massless. m_u^{ij} , m_d^{ij} are 3×3 mass matrices that one needs to diagonalize to get the mass of the quarks. This can be done by a unitary transformation which connects the gauge eigenstate and mass eigenstate as

$$\begin{pmatrix} u_1 \\ u_2 \\ u_3 \end{pmatrix}_{L,R} = U_{L,R} \begin{pmatrix} u \\ c \\ t \end{pmatrix}_{L,R}, \quad \begin{pmatrix} d_1 \\ d_2 \\ d_3 \end{pmatrix}_{L,R} = D_{L,R} \begin{pmatrix} d \\ s \\ b \end{pmatrix}_{L,R}.\quad (1.19)$$

We encounter bilinear terms in charged current interactions like $\bar{u}_{1L} \gamma^\mu d_{1L}$, $\bar{u}_{2L} \gamma^\mu d_{2L}$, $\bar{u}_{3L} \gamma^\mu d_{3L}$ which can be written as inner product of vectors in generation space as

$$\overline{(u_1 \ u_2 \ u_3)}_L \gamma^\mu \begin{pmatrix} d_1 \\ d_2 \\ d_3 \end{pmatrix}_L = \overline{(u \ c \ t)}_L U_L^\dagger D_L \gamma^\mu \begin{pmatrix} d \\ s \\ b \end{pmatrix}_L\quad (1.20)$$

where $V_{CKM} = U_L^\dagger D_L$ is the Cabbibo- Kobayashi- Maskawa matrix and can be parameterized as

$$V_{CKM} = \begin{pmatrix} c_{12}c_{13} & s_{12}c_{13} & s_{13}e^{-i\delta} \\ -s_{12}c_{23} - c_{12}s_{23}s_{13}e^{i\delta} & c_{12}c_{23} - s_{12}s_{23}s_{13}e^{i\delta} & s_{23}c_{13} \\ s_{12}s_{23} - c_{12}c_{23}s_{13}e^{i\delta} & -c_{12}s_{23} - s_{12}c_{23}s_{13}e^{i\delta} & c_{23}c_{13} \end{pmatrix} \quad (1.21)$$

For the sake of completeness, we have given the neutral, electromagnetic and charged interactions of quarks. The neutral current interaction is given by

$$\begin{aligned} \mathcal{L}_{NC}^q = & -\frac{g}{\cos \theta_w} \left[\left(\overline{u_L^i} \quad \overline{d_L^i} \right) \gamma^\mu (T^3 - Q_{qL} \sin^2 \theta_w) \begin{pmatrix} u_L^i \\ d_L^i \end{pmatrix} + \frac{g}{\cos \theta_w} \overline{u_R^i} \gamma^\mu (-Q_{uR} \sin^2 \theta_w) u_R^i \right. \\ & \left. + \frac{g}{\cos \theta_w} \overline{d_R^i} \gamma^\mu (-Q_{dR} \sin^2 \theta_w) d_R^i \right] Z_\mu^0, \end{aligned} \quad (1.22)$$

where for up and down type quark $T^3 = \frac{1}{2}$ and $-\frac{1}{2}$. The electromagnetic interaction of quarks is given by

$$\mathcal{L}_{em}^q = -eQ_u \left[\overline{u_L^i} \gamma^\mu u_L^i + \overline{u_R^i} \gamma^\mu u_R^i \right] A^\mu - eQ_d \left[\overline{d_L^i} \gamma^\mu d_L^i + \overline{d_R^i} \gamma^\mu d_R^i \right] A^\mu \quad (1.23)$$

Finally the charged current interaction for quarks is given as

$$\mathcal{L}_{CC}^q = \frac{g}{\sqrt{2}} \sum_{i,j=1}^3 \overline{u_L^i} \gamma^\mu V_{CKM}^{ij} d_L^j W_\mu^+ + H.c., \quad (1.24)$$

1.2 Neutrino Mass

Neutrinos are massive, yet we do not know the exact mechanism by which they get mass. There are various models proposed in the literature which explain the small active neutrino masses. These includes variants of seesaw mechanism like type-I, II, III seesaw [22–26], inverse seesaw [93, 94], linear seesaw [95, 96], double seesaw [97] etc. In seesaw, light

neutrino masses are generated through $d = 5$ lepton number violating operator [98] once heavy states are integrated out. In the case of type-I seesaw, the light neutrinos acquire mass through mixings with additional Majorana RH neutrino fields N^c . To account for the tiny neutrino mass, the mass scale of these Majorana neutrinos has to be very close to the gauge coupling unification scale, in which case these massive RH neutrinos will remain inaccessible at LHC as well as, at other near future colliders. TeV scale RH neutrinos with substantially large active-sterile mixings are however possible to accommodate in type-I seesaw if cancellation exists in the light neutrino mass matrix [99]. In the case of type-III seesaw, one replace the singlet fermions N^c with $SU(2)$ triplet field Σ with zero hypercharge. The neutrino phenomenology is identical to that of type-I seesaw. In the case of type-II seesaw, one adds a new scalar field ξ , an $SU(2)_L$ triplet with hypercharge -1 and it couples to lepton doublet fields L^i as

$$\mathcal{L}_\xi = \frac{f_{ij}}{2} L^i L_j \xi + \text{H.c.} \quad (1.25)$$

This leads to Majorana neutrino masses $m_\nu = f \langle \xi \rangle$ after the neutral component of ξ acquire a vacuum expectation value $\langle \xi \rangle$. For the case of inverse seesaw mechanism, TeV scale or even smaller RH neutrino masses can exist. In this scheme, in addition to the SM particles there are gauge singlet neutrinos, with opposite lepton numbers (+1 and -1). The light neutrino mass matrix is given in terms of the Dirac neutrino mass term, $m_D \sim Y_\nu v$ (with v being the electroweak vev and Y_ν , a generic Yukawa coupling), the heavy neutrino mass scale M_R and, a small lepton number violating ($\Delta L = 2$) mass term μ , which ensures that M_R scale remains close to TeV or less, with order one Yukawa coupling. The light neutrino mass matrix in this case is: $m_\nu \sim (m_D^2/M_R^2)\mu$. Left right symmetric model is one another interesting model which can also explain light neutrino masses. As in this thesis we predominantly deal with type-I seesaw and left right symmetric model, we briefly describe these two models in the following sections.

1.2.1 Formalism for heavy neutrino mixing

In the most general “type-I seesaw” mechanism, one extends the SM to include arbitrary number of singlet “right-handed neutrinos” along with the three generation of left-handed SM SU(2) doublets [2, 27]:

$$L_{aL} = \begin{pmatrix} \nu_a \\ \ell_a \end{pmatrix}_L, \quad N_{bR},$$

where $a = 1, 2, 3$ and $b = 1, 2, 3, \dots, n$. $n = 2$ is the minimalistic scenario which can generate two tree level neutrino masses required to explain neutrino oscillation data. For the general case, with n right-handed neutrinos, the relevant part of the Lagrangian is given as

$$-\mathcal{L} = \sum_{a=1}^3 \sum_{b=1}^n Y_\nu^{ab} \bar{L}_{aL} \tilde{H} N_{bR} + \frac{1}{2} \sum_{b,b'=1}^n M_R^{bb'} \bar{N}_{bR}^c N_{b'R} + H.c., \quad (1.26)$$

where H is the SM Higgs doublet and \tilde{H} is defined as $\tilde{H} = i\sigma_2 H^*$. The second term in Eq. 1.26 is the Majorana mass term while the first term gives the Dirac mass as the Higgs field develops vacuum expectation value (VEV), $\langle H \rangle \rightarrow \frac{v}{\sqrt{2}}$ after the electroweak symmetry breaking. Finally, the full neutrino mass matrix can be expressed as,

$$\mathcal{M}_\nu = \begin{pmatrix} 0 & M_D \\ M_D^T & M_R \end{pmatrix} \quad (1.27)$$

where, $M_D = \frac{Y_\nu v}{\sqrt{2}}$ is the Dirac mass matrix. The $n \times n$ right-handed neutrino Majorana mass matrix M_R is independent of the electroweak scale as this is invariant under the gauge $SU(3)_c \times SU(2)_L \times U(1)_Y$ and hence can be large $M_R \gg v$, implying $|\frac{M_D}{M_R}| \ll 1$. In this limit, the neutrino mass matrix can be block diagonalized by the unitary matrix \mathbb{L}

as

$$\mathbb{L}^\dagger \begin{pmatrix} 0 & M_D \\ M_D^T & M_R \end{pmatrix} \mathbb{L}^* = \begin{pmatrix} m_\nu^{diag} & 0 \\ 0 & M_N^{diag} \end{pmatrix}, \quad (1.28)$$

where the mass eigenvalues m_ν^{diag} and M_N^{diag} are given by

$$m_\nu^{diag} \approx -M_D M_R^{-1} M_D^T, \quad M_N^{diag} \approx M_R, \quad (1.29)$$

and the unitary matrix \mathbb{L} can be parameterized as

$$\mathbb{L} = \begin{pmatrix} U_{3 \times 3} & V_{3 \times n} \\ X_{n \times 3} & Y_{n \times n} \end{pmatrix} \quad (1.30)$$

Hence, in this model, flavor eigenstates $\nu_{\ell L}$ can be written in terms of the mass eigenstates as,

$$\nu_{\ell L} = \sum_{m=1}^3 U_{\ell m} \nu_{mL} + \sum_{m'=4}^{3+n} V_{\ell m'} N_{m'L}^c, \quad \text{with } UU^\dagger + VV^\dagger = 1. \quad (1.31)$$

As a result of this mixing the charged and neutral currents are now modified. Now the charged current and neutral current interactions of the leptons in the basis of mass eigenstates are given by

$$\begin{aligned} \mathcal{L}_\ell^{CC} &= -\frac{g}{\sqrt{2}} W_\mu^+ \left(\sum_{\ell=e}^{\tau} \sum_{m=1}^3 U_{\ell m}^* \bar{\nu}_m \gamma^\mu P_L \ell + \sum_{\ell=e}^{\tau} \sum_{m'=4}^{3+n} V_{\ell m'}^* \bar{N}_{m'}^c \gamma^\mu P_L \ell \right) + h.c., \\ \mathcal{L}_\ell^{NC} &= -\frac{g}{2\cos\theta_W} Z_\mu \left(\sum_{\ell=e}^{\tau} \sum_{m=1}^3 U_{\ell m}^* \bar{\nu}_m \gamma^\mu P_L \nu_\ell + \sum_{\ell=e}^{\tau} \sum_{m'=4}^{3+n} V_{\ell m'}^* \bar{N}_{m'}^c \gamma^\mu P_L \nu_\ell \right) + h.c. \\ &= -\frac{g}{2\cos\theta_W} Z_\mu \left(\sum_{m_1, m_2=1}^3 (U^\dagger U)_{m_1 m_2} \bar{\nu}_{m_1} \gamma^\mu P_L \nu_{m_2} + \sum_{m'_1, m'_2=4}^{3+n} (V^\dagger V)_{m'_1 m'_2} \bar{N}_{m'_1}^c \gamma^\mu P_L N_{m'_2}^c \right) \\ &\quad - \frac{g}{2\cos\theta_W} Z_\mu \left(\sum_{m_1=1}^3 \sum_{m'_2=4}^{3+n} (U^\dagger V)_{m_1 m'_2} \bar{\nu}_{m_1} \gamma^\mu P_L N_{m'_2}^c + h.c. \right) \end{aligned} \quad (1.32)$$

where $P_L = \frac{(1-\gamma_5)}{2}$, ψ^c is the charged conjugate, g is the $SU(2)_L$ gauge coupling. The diagonalized majorana mass terms for the neutrinos can be written as:

$$\mathcal{L}_m^\nu = -\frac{1}{2} \left(\sum_{m=1}^3 m_m^\nu \overline{\nu_{mL}} \nu_{mR}^c + \sum_{m'=4}^{3+n} m_{m'}^N \overline{N_{m'L}^c} N_{m'R} \right) + h.c., \quad (1.33)$$

1.2.2 Left-Right Symmetric Model

The minimal Left Right Symmetric Model is based on the gauge group $SU(3)_c \times SU(2)_L \times SU(2)_R \times U(1)_{B-L}$ [100–102], with the fermions assigned in the doublet representation of $SU(2)_L$ and $SU(2)_R$. In addition to the particle content of the Standard Model (SM), the model contains three right handed Majorana neutrinos N_R , and the additional gauge bosons W_R and Z' . The electric charge Q and the third components of weak isospins I_{3L} and I_{3R} are related as $Q = I_{3L} + I_{3R} + (B - L)/2$. The scalar sector of this model consists of the bi-doublet Φ and the Higgs triplets Δ_L and Δ_R , where the Higgs states have the following representations: $\Phi(\mathbf{1}, \mathbf{2}, \mathbf{2}, 0)$, $\Delta_L(1, 3, 1, +2)$ and $\Delta_R(1, 1, 3, +2)$. The bi-doublet, being neutral under $B - L$ gauge group is not sufficient to break this gauge symmetry. Hence, additional Higgs triplet fields are required. The Higgs field Δ_R takes vacuum expectation value v_R and breaks $SU(2)_R \times U(1)_{B-L}$ down to the group $U(1)_Y$ of SM.

In the Yukawa sector, the bi-doublet couples to the fermion bilinears $\bar{Q}_L Q_R$ and $\bar{\psi}_L \psi_R$, and gives masses to quarks and leptons through the spontaneous symmetry breaking, where its VEVs are denoted as: $\langle \Phi \rangle = \text{diag}(\kappa_1, \kappa_2) / \sqrt{2}$. On the other hand, the Higgs triplet Δ_R couples with the right handed neutrinos N_R and generates the Majorana mass of heavy neutrinos during the symmetry breaking. While the heavy neutrino N_R contributes to the light neutrino mass generation via Type-I seesaw mass [22–24, 26], the triplet Higgs Δ_L generates the Majorana mass of light neutrinos via Type-II seesaw [103, 104]. The VEV of Φ field breaks the SM gauge group $SU(2)_L \times U(1)_Y$ to $U(1)_Q$. Hence, the different VEVs of bi-doublets and triplets follow the hierarchy $v_L \ll \kappa_{1,2} \ll v_R$.

The Yukawa Lagrangian, that generates the lepton masses have the following form:

$$-\mathcal{L}_Y = h\bar{\psi}_L\Phi\psi_R + \tilde{h}\bar{\psi}_L\tilde{\Phi}\psi_R + f_L\psi_L^\top Ci\tau_2\Delta_L\psi_L + f_R\psi_R^\top Ci\tau_2\Delta_R\psi_R + \text{H.c.} \quad (1.34)$$

In the above C is the charge-conjugation matrix, $C = i\gamma_2\gamma_0$, and $\tilde{\Phi} = \tau_2\Phi^*\tau_2$, with τ_2 being the second Pauli matrix, and γ_μ the Dirac matrices. Upon symmetry breaking, this gives rise to the following light-heavy mass matrix,

$$\mathcal{M}_\nu = \begin{pmatrix} M_L & M_D \\ M_D^\top & M_R \end{pmatrix}. \quad (1.35)$$

In the seesaw approximation [22, 26, 103], this leads to the following light neutrino mass matrix (up to $\mathcal{O}(M_R^{-2})$) [105],

$$\begin{aligned} M_\nu &\simeq M_L - M_D M_R^{-1} M_D^\top - \left(\frac{1}{2} M_D M_R^{-1} M_R^{-1*} M_D^\dagger M_L + \text{HC}\right) \\ &= \sqrt{2}v_L f_L - \frac{\kappa^2}{\sqrt{2}v_R} h_D f_R^{-1} h_D^\top - \left(\frac{\kappa^2}{2\sqrt{2}v_R^2 v_L} h_D f_R^{-1} f_R^{-1*} h_D^\dagger f_L + h.c.\right), \end{aligned} \quad (1.36)$$

where $\kappa = \sqrt{\kappa_1^2 + \kappa_2^2}$, Dirac mass $M_D = h_{DK} = \frac{1}{\sqrt{2}}(\kappa_1 h + \kappa_2 \tilde{h})$, and $M_L = \sqrt{2}v_L f_L$, $M_R = \sqrt{2}v_R f_R$. The mass matrix given in Eq. (1.35), can be diagonalized by a 6×6 unitary matrix, as follows:

$$\mathcal{V}^\top \mathcal{M}_\nu \mathcal{V} = \begin{pmatrix} \tilde{M}_\nu & \mathbf{0} \\ \mathbf{0} & \tilde{M}_R \end{pmatrix} \quad (1.37)$$

where $\tilde{M}_\nu = \text{diag}(m_1, m_2, m_3)$, $\tilde{M}_R = \text{diag}(M_1, M_2, M_3)$. Upto $\mathcal{O}(M_R^{-2})$, the mixing matrix \mathcal{V} has the following form,

$$\mathcal{V} \sim \begin{pmatrix} \mathbf{1} - \frac{1}{2}\zeta^* \zeta^\top & \zeta^* + \zeta'^* \\ -\zeta^\top - \zeta'^\top & \mathbf{1} - \frac{1}{2}\zeta^\top \zeta^* \end{pmatrix} \begin{pmatrix} U_\nu & \mathbf{0} \\ \mathbf{0} & V_R \end{pmatrix}. \quad (1.38)$$

In the above, the expansion parameter ζ has the following form $\zeta = M_D M_R^{-1}$, and $\zeta'^* = M_L^\dagger M_D M_R^{-1} M_R^{-1*}$. For $M_L \rightarrow 0$, $\zeta' \rightarrow 0$. The order parameter is defined as, $\theta \equiv \|\zeta\| = \sqrt{\text{Tr}(\zeta^\dagger \zeta)}$. In the subsequent analysis, we denote the mixing matrix as

$$\mathcal{V} = \begin{pmatrix} U & S \\ T & V \end{pmatrix} = \begin{pmatrix} \left(1 - \frac{\theta^2}{2}\right) U_\nu & \theta V_R \\ -\theta U_\nu & \left(1 - \frac{1}{2}\theta^2\right) V_R \end{pmatrix} \quad (1.39)$$

where $\theta = \sqrt{\frac{m_\nu}{m_N}}$.

Gauge Sector and Charged Current Lagrangian

In addition to the SM gauge bosons, this model consists of a right handed charged gauge boson, W_R and an additional neutral gauge boson, Z' . The SM gauge boson W_L and W_R mix with each other, with the mixing

$$\xi \simeq \frac{\kappa_1 \kappa_2}{v_R^2} \simeq \frac{2\kappa_2}{\kappa_1} \left(\frac{M_{W_L}}{M_{W_R}} \right)^2. \quad (1.40)$$

In the limit of small mixing $\xi \ll 1$, the physical masses are

$$M_{W_1} \simeq M_{W_L} \simeq \frac{g}{2}\kappa, \quad M_{W_2} \simeq M_{W_R} \simeq \frac{g}{\sqrt{2}}v_R, \quad (1.41)$$

where, $g \equiv g_L = g_R$ and $M_{Z'} \sim 1.7M_{W_R}$. In our choice of Left-Right model, we assume discrete parity as a symmetry. The charged current Lagrangian for the quarks have the following forms:

$$\mathcal{L}_{CC}^q = \frac{g}{\sqrt{2}} \sum_{i,j} \bar{u}_i V_{ij}^{\text{CKM}} W_{L\mu}^+ \gamma^\mu P_L d_j + \frac{g}{\sqrt{2}} \sum_{i,j} \bar{u}_i V_{ij}^{\text{R-CKM}'} W_{R\mu}^+ \gamma^\mu P_R d_j + \text{H.c.}, \quad (1.42)$$

where $i = (u, c, t)$ correspond to the up type quarks and $j = (d, s, b)$ represent the down type quarks. In our subsequent analysis, we consider $V^{\text{R-CKM}'}$ to be proportional to V^{CKM} with the proportionality factor $\beta \sim \mathcal{O}(1)$. The charged current Lagrangian for the lepton-

neutrino has the following form,

$$\begin{aligned} \mathcal{L}_{CC}^{\ell} = & \frac{g}{\sqrt{2}} \sum_{i,j} \bar{\ell}_{L_i} W_{L\mu}^- \gamma^{\mu} P_L (U_{ij} \nu_{L_j} + S_{ij} N_j^c) + \frac{g}{\sqrt{2}} \sum_{i,j} \bar{\ell}_{R_i} W_{R\mu}^- \gamma^{\mu} P_R (V_{ij}^* N_j + T_{ij}^* \nu_L^c) \\ & + \text{H.c.} \end{aligned} \quad (1.43)$$

Note that, both the masses of the RH neutrino and W_R gauge boson, are proportional to the $SU(2)_R$ breaking scale. However, while the W_R mass and the right handed current are dictated with the gauge coupling $g_R = g$, the RH neutrino mass M_N is governed by the Yukawa coupling f_R , therefore allowing the possibility to have a large hierarchy between W_R and N masses. For sufficiently small M_N and TeV scale W_R , this can give large contribution in meson decays.

The neutral currents which will also contribute in some of the decay channels of the right handed neutrino, are given below: [106, 107]

$$\mathcal{L}_{NC} = \frac{g_L}{\cos\theta_w} (Z_{\mu} J_Z^{\mu} + \frac{\cos^2\theta_w}{\sqrt{\cos 2\theta_w}} Z'_{\mu} J_{Z'}^{\mu}) \quad (1.44)$$

where,

$$J_Z^{\mu} = \sum_i \bar{f} \gamma^{\mu} (T_L^3 P_L - Q \sin^2\theta_w) f, \quad (1.45)$$

$$J_{Z'}^{\mu} = \sum_i \bar{f} \gamma^{\mu} (T_R^3 P_R - \tan^2\theta_w (Q - T_{3L}^3)) f. \quad (1.46)$$

The explicit interaction terms with the leptons and neutrinos are given in [106].

1.3 Existing bounds on mixing angles

As in this thesis we have studied the bounds on mixing angle for various mass ranges of RH neutrinos N , it is good to give a brief overview of the existing bound on mixing angles

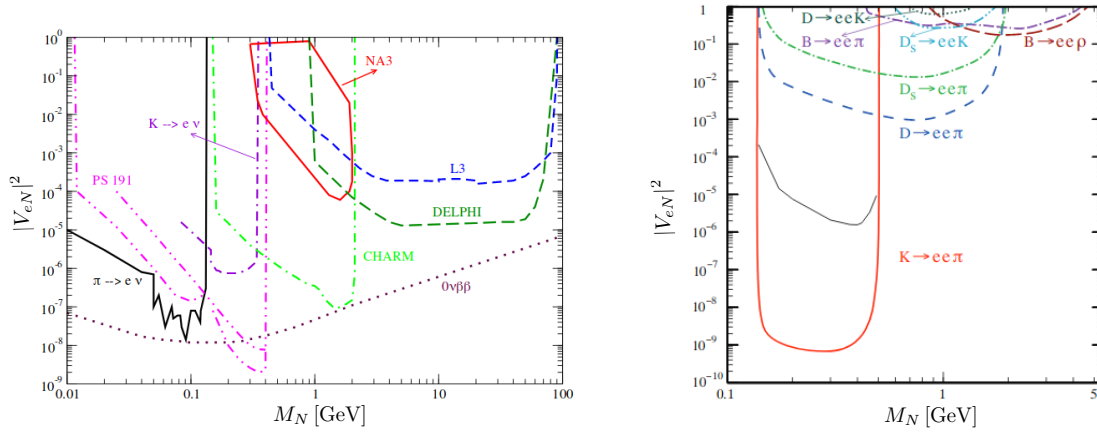


Figure 1.1: Left: Bounds on the mixing angle $|V_{eN}|^2$ as a function of RH neutrino mass M_N in the mass range 10 MeV-100 GeV. The bounds are from peak searches ($K \rightarrow e\nu$, $\pi \rightarrow e\nu$) and from the following experiments: PS191, NA3, CHARM, DELPHI, L3. The region above the contour lines are excluded. The dotted maroon contour is for neutrinoless double beta decay experiment. Right: Excluded region on $|V_{eN}|^2$ versus M_N from meson decays $M_1 \rightarrow ee\pi$. The thin black line is for $K \rightarrow ee\pi$ meson decay with including N decay probability inside the detector.

for our interested mass ranges of N . The results of this section are based on the following Refs. [2, 63, 108].

The bounds on the mixing angles $|V_{eN}|^2$ ($|V_{\mu N}|^2$) exists from the peak searches $\pi \rightarrow e(\mu)\nu$ and $K \rightarrow e(\mu)\nu$ [109]. The other limits on $|V_{eN}|^2$ ($|V_{\mu N}|^2$) are found in decay searches from beam dump experiments like PS191 [110], NA3 [111], CHARM [112] (PS191, NA3, BEBC [113], FMMF [114], NuTeV [115] and CHARMII [116]) which assumes the production of N in meson decays and look for visible channels. We also have limits on $|V_{eN}|^2$ ($|V_{\mu N}|^2$) analysing the data from DELPHI [117] and L3 [118] detectors by looking for N for Z -boson decays. We have shown all these limits together for mixing angle $|V_{eN}|^2$ and $|V_{\mu N}|^2$ in the left panel of Fig. 1.1 and 1.2 respectively.

For the case of mixing angle $|V_{\tau N}|^2$, the limits comes from searches of N decays. We have shown the results in Fig. 1.3. CHARM and NOMAD [119] bounds comes from the assumption that the N is produced via D and τ decays. As earlier, the DELPHI bound assumes N production in Z -boson decays.

Also in the literature, there are quite a few studies on the mixing angles bounds from the three body LNV meson decays $M_1^- \rightarrow \ell_1^- \ell_2^- \pi^+$ and tau decays $\tau^- \rightarrow \ell^- \pi^+ \pi^+$. From the

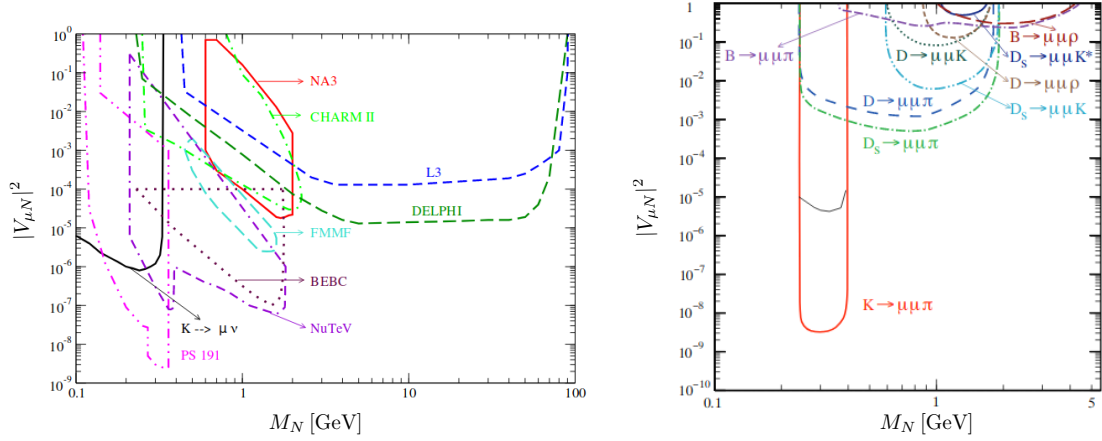


Figure 1.2: Left: Bounds on the mixing angle $|V_{\mu N}|^2$ as a function of RH neutrino mass M_N in the mass range 10 MeV-100 GeV. Again the bounds are from peak searches ($\pi \rightarrow \mu\nu$, $K \rightarrow \mu\nu$) and from the visible decay products in N decays in PS191, NA3, BEBC, FMMF, NuTeV. We have also shown the bounds from DELPHI and L3 data analysis. Right: Excluded region on $|V_{\mu N}|^2$ versus M_N from meson decays $M_1 \rightarrow \mu\mu\pi$. The thin black line is for $K \rightarrow \mu\mu\pi$ meson decay with including N decay probability inside the detector.

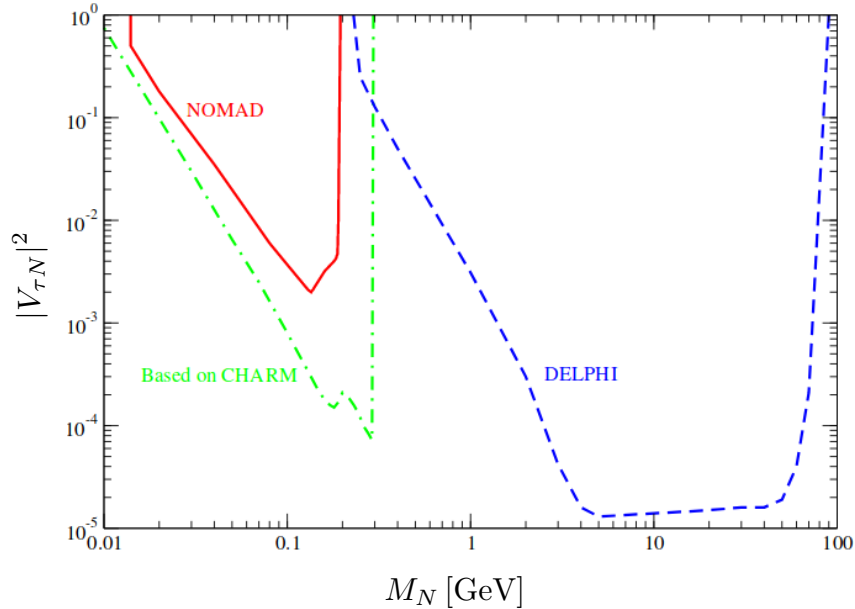


Figure 1.3: Bounds on $|V_{\tau N}|^2$ as a function of RH neutrino mass M_N from the decays of heavy neutrinos in CHARM, NOMAD and DELPHI.

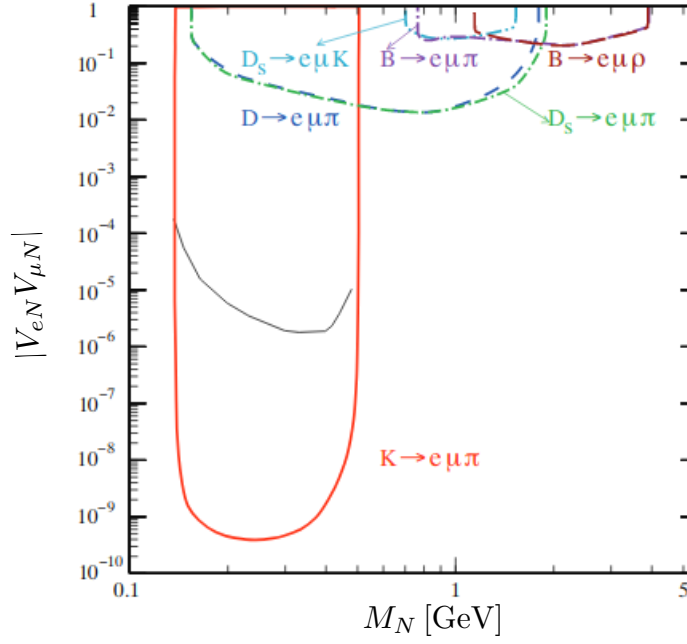


Figure 1.4: The bounds on the mixing angle $|V_{eN}V_{\mu N}|$ versus M_N from the meson decays $M_1 \rightarrow \mu\pi$. The thin black line is for $K \rightarrow e\mu\pi$ meson decay with including N decay probability inside the detector

experimental limit on the branching ratios of these decay modes, it is possible to derive tight constraints on the limit of the mixing angles. We have shown the limits on $|V_{eN}|^2$ and $|V_{\mu N}|^2$ in the right panel of Fig. 1.1 and 1.2 respectively. For mixing angle $|V_{eN}V_{\mu N}|$, $|V_{eN}V_{\tau N}|$ and $|V_{\mu N}V_{\tau N}|$, the limits are shown in Fig. 1.4 and 1.5.

We would like to point out that inclusion of N decay probability inside the detector makes these limits significantly weaker. We have included the RH neutrino decay probability in our analysis. Also note that, in Fig. 1.3, there is no bound for the mixing angle in the mass range 2-3 GeV. We have shown in our thesis that studying the meson decay $B_c \rightarrow \tau\tau\pi$, we can set limit on $|V_{\tau N}|^2$ in this mass range.

For heavy neutrino mass range, the limit exists on $|V_{eN}|^2$ from Electroweak precision data [120] which obtains the bound on $|V_{eN}|^2$ as 1.681×10^{-3} at the 95% CL. For the mass range up to $M_N = 959$ GeV, existing strong bound comes from the GERDA [121] $0\nu\beta\beta$ study which sets bound on $|V_{eN}|^2 \sim \mathcal{O}(10^{-6})$ at 95% CL.

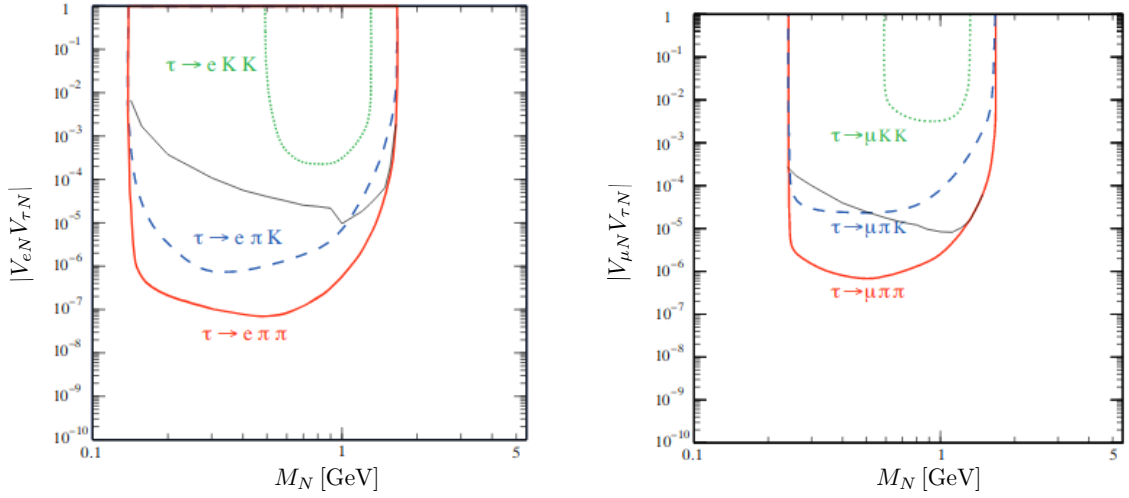


Figure 1.5: Bounds on $|V_{eN}V_{\tau N}|$ and $|V_{\mu N}V_{\tau N}|$ versus M_N from $\tau \rightarrow e(\mu)\pi\pi$, $\tau \rightarrow e(\mu)\pi K$ and $\tau \rightarrow e(\mu)KK$ decays. The effect of the probability of N decay inside the detector is shown by thin black line.

1.4 Outline of the thesis

In chapter 2, we study few lepton-number violating ($\Delta L = 2$) decay modes of B_c meson to $B_s^0 \ell_1^- \ell_2^- \pi^+$, $J/\psi \ell_1^- \ell_2^- \pi^+$, $B_c \rightarrow \ell_1^- \ell_2^- \pi^+$ which can only be induced by a Majorana neutrino. We evaluate these decay modes in the context of type-I seesaw model with the assumption that only one right-handed neutrino is present in the mass range (100 MeV-6 GeV). From non observations of these decay we obtain tight constraints on the mixing angles of the heavy Majorana neutrino mass eigenstate N , with light flavour neutrinos from upper limits of the branching fractions.

In chapter 3, we study few three body LNV meson decays $M_1^+ \rightarrow \ell_1^+ \ell_2^+ \pi^-$ ($M_1 = B, D, D_s, K$) in the context of minimal left right symmetric model. In particular, we calculate the expected number of signal events for these decay modes in ongoing and future experiments like NA62, LHCb, Belle II, SHiP, FCC-ee. When calculating the signal events, we also include the probability factor of N to decay inside the detector for each of the experiments. Finally, we derive constraints on the mass of the right handed charged gauge boson as a function of RH neutrino mass M_N .

In chapter 4, we study the prospect of discovering RH neutrino through LQ productions at the proposed e^-p collider like LHeC. We consider a particular type of scalar LQ \tilde{R}_2 , which can couple with RH neutrinos. At LHeC, LQ can be resonantly produced and decay to RH neutrinos. Further decays of RH neutrinos can give plethora of final states. We present a detailed collider analysis and discuss the discovery prospects of some of these final states.

In chapter 5, we study the discovery potential of very heavy RH neutrinos using fatjet signature. We first calculate the production cross sections for the RH neutrinos at the LHeC (jN_1) and linear collider ($N_1\nu_e$) at various center of mass energies. Very heavy RH neutrinos dominantly decays to ℓW or $h\nu$ modes and can sufficiently boost the W , h such that its hadronic decay modes can form a fatjet. In particular, we study $e + j_1 + J$ and $e + J + p_T^{\text{miss}}$, $J_b + p_T^{\text{miss}}$ at the LHeC and linear collider respectively using detailed cut based analyses.

In chapter 6, we summarize the results obtained in the thesis.

2 Favoured B_c Decay modes to search for a Majorana neutrino

In the literature, there are various three body LNV meson decays proposed to search for Majorana neutrinos [2, 108]. While various B , B_s and B_c meson decay modes have already been suggested, here we propose a few additional B_c decay modes that may perhaps be preferable for Majorana neutrino searches. The B_c mesons are unique, in being the only states consisting of two heavy quarks of different flavours ($b\bar{c}$ for B_c^-). The weak decay of the b quark will be Cabibbo suppressed, for both $b \rightarrow c$, (λ^2 suppressed) and $b \rightarrow u$ (λ^3 suppressed) transitions. However the $c \rightarrow s$ decay will be a Cabibbo favoured transition. Hence, the mode $B_c^- \rightarrow \bar{B}_s^0 \ell_1^- \ell_2^- \pi^+$ is expected to have a larger branching fraction than the other rare lepton number violating decay modes of bottom mesons considered so far. Further, for a heavy neutrino in the mass range $\sim (0.1 - 0.9)$ GeV, it is kinematically possible for it to be produced as an intermediate on mass shell state, resulting in an additional resonance enhancement of the transition rate. Note that below 0.1 GeV tight constraints already exist on $|V_{eN}|^2$ from pion decay.

The $B_c^- \rightarrow \bar{B}_s^0 \pi^-$ mode has already been observed by LHCb [122]. B_c decays to other hadronic modes have also been observed by ATLAS [123] and CMS [124], hence in addition to LHCb, ATLAS and CMS may also be able to perform the search for Majorana neutrinos via this B_c decay mode. In the proton-proton collisions at the Large Hadron Collider, B_c mesons are expected to be mainly produced through the gluon-gluon fusion

process $gg \rightarrow B_c^- + \bar{b} + c$ [125, 126]. Hence, the production cross-section would be expected to increase in the 13/14 TeV run substantially. This, along with the luminosity of the order of few fb^{-1} in Run II, leads one to believe that searches for this rare LNV B_c decay modes may be feasible.

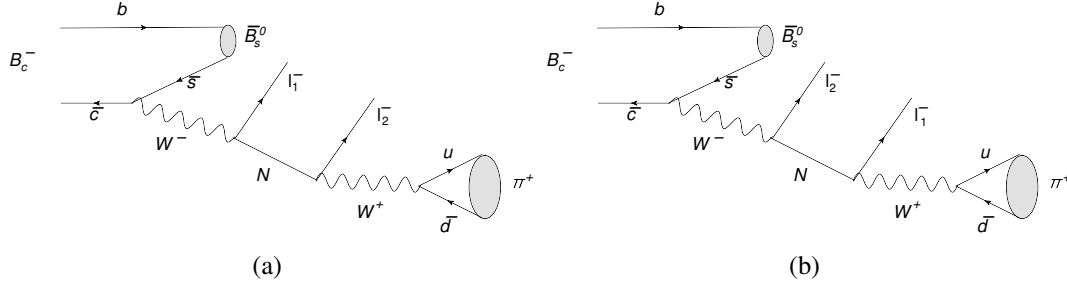
In Sec. 2.2, the four-body decay rate for $B_c^- \rightarrow \bar{B}_s^0 \ell_1^- \ell_2^- \pi^+$ mode is evaluated and the expected upper limits on branching ratios for these modes are used to obtain bounds on the mixings of the heavy neutrino with the light flavoured ones. In Sec. 2.3, the modes $B_c^- \rightarrow J/\psi \ell_1^- \ell_2^- \pi^+$ and $B_c^- \rightarrow \pi^+ \ell_1^- \ell_2^-$ are discussed. We find that although these modes are not Cabibbo favoured, but the ease of reconstruction of the final states for these modes results in tighter possible upper limits for the branching fractions and in addition the phase space enhancement helps in obtaining tighter exclusion curves for the mixing elements.

2.1 Model

In sec. 1.2.1, we have given the formalism for the extension of the SM to include arbitrary number of right handed singlets. In principle there can be any number of right-handed neutrinos but we will consider here only one right-handed neutrino and we denote by $V_{\ell N}$ the mixing coefficient between the standard flavour neutrino $\nu_\ell (\ell = e, \mu, \tau)$ and the heavy mass eigenstate N. The charged and neutral current in this case can be written as

$$\begin{aligned} \mathcal{L}_\ell^{CC} &= -\frac{g}{\sqrt{2}} W_\mu^+ \left(\sum_{\ell=e}^{\tau} \sum_{m=1}^3 U_{\ell m}^* \bar{\nu}_m \gamma^\mu P_L \ell + \sum_{\ell=e}^{\tau} V_{\ell N}^* \bar{N}_m^c \gamma^\mu P_L \ell \right) + h.c., \\ \mathcal{L}_\ell^{NC} &= -\frac{g}{2 \cos \theta_W} Z_\mu \left(\sum_{\ell=e}^{\tau} \sum_{m=1}^3 U_{\ell m}^* \bar{\nu}_m \gamma^\mu P_L \nu_\ell + \sum_{\ell=e}^{\tau} V_{\ell N}^* \bar{N}_m^c \gamma^\mu P_L \nu_\ell \right) + h.c., \end{aligned} \quad (2.1)$$

We take a phenomenological approach regarding the mass and mixing elements of the heavy singlet neutrino, taking them to be free parameters, constrained only by experimental observations.

Figure 2.1: Feynman diagrams for the decay $B_c^- \rightarrow \bar{B}_s^0 \ell_1^- \ell_2^- \pi^+$.

2.2 $B_c^- \rightarrow \bar{B}_s^0 \ell_1^- \ell_2^- \pi^+$ Decays

Evaluation of the four-body decay rate

For the four-body decay $B_c^-(p) \rightarrow \bar{B}_s^0(k_1) \ell_1^-(k_2) \ell_2^-(k_3) \pi^+(k_4)$, where $\ell_1, \ell_2 = e, \mu$, only s-channel diagrams shown in Fig.2.1 contribute. Hence, the Majorana neutrino N that induces this LNV process can appear as an intermediate on mass shell state, leading to an enhancement of the decay rate. Note that the second diagram(Fig.2.1(b)) arises from the exchange of the two leptons. We assume that there is only one Majorana neutrino, that lies in the range, between $\sim (0.1 - 0.9)$ GeV that kinematically allows it to be on mass shell. Moreover, being much heavier than the active light neutrinos, the cosmological and LEP bounds would imply that such a neutrino would have to be necessarily an electroweak gauge singlet or sterile.

The decay amplitude for the processes depicted in Fig.2.1 can be expressed as,

$$i\mathcal{M} = (\mathcal{M}_{lep})_{\beta\mu} (\mathcal{M}_{had})^{\beta\mu}, \quad (2.2)$$

where we can write the leptonic part as,

$$(\mathcal{M}_{lep})_{\beta\mu} = \frac{\sqrt{2}G_F V_{\ell_1 N}^* V_{\ell_2 N} m_N}{(p - k_1 - k_2)^2 - m_N^2 + im_N \Gamma_N} \bar{u}(k_3) \gamma_\beta \gamma_\mu P_{RV}(k_2) + (k_2 \leftrightarrow k_3, \ell_1 \leftrightarrow \ell_2), \quad (2.3)$$

where G_F is the Fermi coupling constant, $V_{\ell_i N}$ ($i=1, 2$) are the mixing elements between the neutrino of flavour state ν_{ℓ_i} and mass eigenstate N and Γ_N is the total decay width of the heavy neutrino N , obtained by summing over all accessible final states. The hadronic tensor is a product of a transition matrix element of B_c to B_s , and a matrix element for the production of a pion:

$$(\mathcal{M}_{had})^{\beta\mu} = \frac{G_F}{\sqrt{2}} V_{cs} V_{ud} \langle \bar{B}_s^0(k_1) | \bar{s} \gamma^\mu (1 - \gamma_5) c | B_c^-(p) \rangle \langle \pi^+(k_4) | \bar{u} \gamma^\beta (1 - \gamma_5) d | 0 \rangle, \quad (2.4)$$

where V_{cs} , V_{ud} are the Cabibbo-Kobayashi-Maskawa (CKM) matrix elements. The above two hadronic matrix elements can be written as,

$$\begin{aligned} \langle \bar{B}_s^0(k_1) | \bar{s} \gamma^\mu c | B_c^-(p) \rangle &= (F_+(q^2)(p+k_1)^\mu + F_-(q^2)(p-k_1)^\mu), \\ \langle \pi^+(k_4) | \bar{u} \gamma^\beta \gamma_5 d | 0 \rangle &= i f_\pi k_4^\beta, \end{aligned} \quad (2.5)$$

where $F_+(q^2)$, $F_-(q^2)$ ($q \equiv p - k_1$) are the momentum transfer squared dependent B_c^- to \bar{B}_s^0 transition form factors and f_π is the decay constant of pion. In terms of these form factors and decay constant, we can write the amplitude \mathcal{M} as,

$$\begin{aligned} \mathcal{M} &= \frac{G_F^2 V_{cs} V_{ud} V_{\ell_1 N}^* V_{\ell_2 N} f_\pi}{(p-k_1-k_2)^2 - m_N^2 + im_N \Gamma_N} (F_+(q^2)(p+k_1)^\mu + F_-(q^2)(p-k_1)^\mu) \\ &\bar{u}(k_3) \gamma_\beta \gamma_\mu (1 + \gamma_5) \nu(k_2) k_4^\beta + (k_2 \rightarrow k_3, \ell_1 \leftrightarrow \ell_2). \end{aligned} \quad (2.6)$$

The form factors for $B_c^- \rightarrow \bar{B}_s^0$ have been calculated in the framework of 3-point QCD sum rule in Ref. [127, 128]. The q^2 dependence takes a simple pole form:

$$F_+(q^2) = \frac{F_+(0)}{1 - \frac{q^2}{M_p^2}}, \quad F_-(q^2) = \frac{F_-(0)}{1 - \frac{q^2}{M_p^2}}, \quad (2.7)$$

where $F_+(0) = 1.3$ and $F_-(0) = -5.8$, and $M_p = 1.7 \div 1.8$ GeV. The accuracy of the sum rules used is determined by the variation of various parameters. It is claimed in [127] that these variations result in $\frac{\delta F}{F} \simeq 5\%$. To avoid this theoretical uncertainty and model

dependence in the form factors, we recommend that the form factors should be determined experimentally by measurement of the semileptonic mode, $B_c^- \rightarrow \bar{B}_s^0 \mu^- \bar{\nu}_\mu$. Alternately, perhaps lattice estimation of the form factors may also be possible.

Although the heavy sterile neutrino N is a SM singlet, it can decay via charged current and neutral current interactions, due to its mixing with the active neutrinos as is evident from the Lagrangian (2.1). The total decay width Γ_N is given by:

$$\begin{aligned} \Gamma_N = & \sum_{\ell', P^0} \Gamma^{\nu_{\ell'} P^0} + \sum_{\ell', V^0} \Gamma^{\nu_{\ell'} V^0} + \sum_{\ell, P} 2\Gamma^{\ell^- P^+} + \sum_{\ell, V} 2\Gamma^{\ell^- V^+} \\ & + \sum_{\bar{\ell}_1, \bar{\ell}_2 (\bar{\ell}_1 \neq \bar{\ell}_2)} 2\Gamma^{\bar{\ell}_1 \bar{\ell}_2 \nu_{\bar{\ell}_2}} + \sum_{\ell', \ell'_2} \Gamma^{\nu_{\ell'} \ell'_2 \ell'_2} + \sum_{\ell'} \Gamma^{\nu_{\ell'} \nu_{\bar{\ell}'}}. \end{aligned} \quad (2.8)$$

In the mass range, which permits the heavy neutrino to be resonantly produced in the decay mode $B_c^- \rightarrow \bar{B}_s^0 \ell_1^- \ell_2^- \pi^+$ the leptons $\ell, \bar{\ell}_1, \bar{\ell}_2, \ell'_2$ can be e or μ , while ℓ' can be e, μ or τ , charged pseudoscalars (P^+) that can contribute are π^+ and K^+ , while π^0 and η are the contributing neutral pseudoscalars (P^0), the charged vector mesons (V^+) will include ρ^+ and K^{*+} and the neutral vector mesons (V^0) that need to be included are ρ^0 and ω . The detailed expressions for the decay rates for each of these channels can be found in Ref. [2, 63].

For the case of $B_c^- \rightarrow J/\psi \ell_1^- \ell_2^- \pi^+$ allowed mass range of m_N is (0.1 – 3) GeV. This will allow the additional charged pseudoscalar mesons: D^+, D_s^+ and charged vector mesons: D^{*+}, D_s^{*+} to contribute, provided ℓ is either e or μ ; for $\ell = \tau$ the mesons can only be $\pi^+, K^+, \rho^+, K^{*+}$. Additional contributing neutral pseudoscalar mesons are: η' and η_c while, ϕ and J/ψ are the heavier neutral vector mesons that can also be produced in the decays of N . $\bar{\ell}_1$ or $\bar{\ell}_2$ can now also be a τ .

For the case of $B_c^- \rightarrow \ell_1^- \ell_2^- \pi^+$ the allowed mass range in which N can be resonantly produced is (0.1 – 6) GeV. Charged pseudoscalar meson B^+ and vector meson B^{*+} will also contribute now for $\ell = e, \mu$. For $\ell = \tau$, the additional accompanying mesons will be $D^+, D_s^+, D^{*+}, D_s^{*+}$. Also, ℓ'_2 can also be τ .

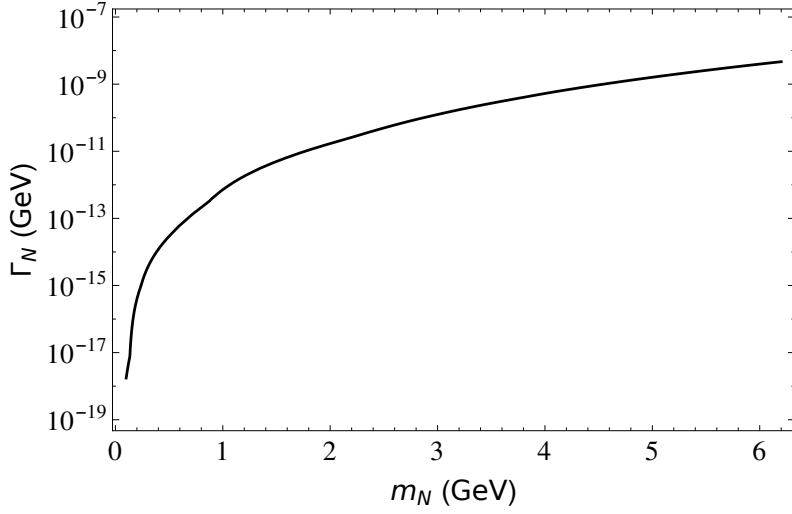


Figure 2.2: Heavy neutrino decay width, Γ_N as a function of the mass m_N when the magnitude of all the mixing angles $|V_{\ell N}| = 1$ ($\ell = e, \mu, \tau$). A bigger range for m_N is chosen than that which allows a resonant enhancement of the $B_c^- \rightarrow \bar{B}_s^0 \ell_1^- \ell_2^- \pi^+$ decay, so as to include the larger values of m_N that will be permitted by the other B_c decay modes to be discussed in Sec. 2.3.

We have re-evaluated Γ_N using the meson masses and decay constants from Ref. [129], in the relevant mass range for the B_c decay modes considered here and write it in the form,

$$\Gamma_N = a_e(m_N) |V_{eN}|^2 + a_\mu(m_N) |V_{\mu N}|^2 + a_\tau(m_N) |V_{\tau N}|^2, \quad (2.9)$$

where, a_e , a_μ and a_τ are functions of the Majorana neutrino mass and hence will differ from mode to mode. In Fig. 2.2, we plot the decay width Γ_N as function of mass m_N , for the mixings $|V_{eN}| = |V_{\mu N}| = |V_{\tau N}| = 1$.

For the mass range of our interest, Γ_N is very small, $\mathcal{O}(10^{-17} - 10^{-8})$ GeV, if the mixing $|V_{eN}|^2 = |V_{\mu N}|^2 = |V_{\tau N}|^2 = 1$ and even smaller for more realistic values of these mixing angles. The small width of N will imply that the heavy neutrino may travel outside the detector before decaying and the resulting decay products may not be visible. We will discuss this issue further in Sec. 2.3. The narrow decay width of N allows the two propagators for N , in equation (2.6) to be written as,

$$\frac{1}{(p_N^2 - m_N^2)^2 + m_N^2 \Gamma_N^2} \simeq \frac{\pi}{m_N \Gamma_N} \delta(p_N^2 - m_N^2). \quad (2.10)$$

Moreover, in the narrow width approximation the two channels contribute as a sum to the total decay width, as the interference term is negligible.

Most of the earlier studies of LNV meson and tau decays have focused on three-body decays. A few more recent phenomenological studies [90, 130–133] of four-body LNV processes have also been performed, including an experimental search through the mode $B^- \rightarrow D^0 \pi^+ \mu^- \mu^-$ by LHCb [134]. The particular four-body B_c decay mode being considered here has the advantage of being Cabibbo favored and hence enhanced.

To calculate the four-body phase space required for evaluating the decay rate $\Gamma(B_c^-(p) \rightarrow \bar{B}_s^0(k_1) \ell_1^-(k_2) \ell_2^-(k_3) \pi^+(k_4)) = \frac{1}{2m} \int d_4(ps) |\mathcal{M}|^2$, the final particles can be partitioned into two subsystems X_{12} and X_{34} , each of which subsequently decays into a two-body state. Hence, the four-body phase space integral is decomposed into a product of three two-body phase space integrals:

$$d_4(ps) = d_2(ps \ B_c^- \rightarrow X_{12} X_{34}) d_2(ps \ X_{12} \rightarrow k_1 k_2) d_2(ps \ X_{34} \rightarrow k_3 k_4) dM_{12}^2 dM_{34}^2, \quad (2.11)$$

where $X_{12} = (k_1 + k_2)$, $X_{34} = (k_3 + k_4)$, $X_{12}^2 = M_{12}^2$ and $X_{34}^2 = M_{34}^2$, $p^2 = m^2$ and $k_i^2 = m_i^2$.

The four-body phase space therefore takes the form,

$$d_4(ps) = \frac{1}{n!} \frac{1}{(4\pi)^6} \frac{1}{4} \lambda^{\frac{1}{2}} \left(1, \frac{M_{12}^2}{m^2}, \frac{M_{34}^2}{m^2} \right) \lambda^{\frac{1}{2}} \left(1, \frac{m_1^2}{M_{12}^2}, \frac{m_2^2}{M_{12}^2} \right) \lambda^{\frac{1}{2}} \left(1, \frac{m_3^2}{M_{34}^2}, \frac{m_4^2}{M_{34}^2} \right) dM_{12}^2 dM_{34}^2 d\cos\theta_{12} d\cos\theta_{34} d\phi, \quad (2.12)$$

where m , m_1 , m_2 , m_3 , and m_4 are the masses of B_c^- , \bar{B}_s^0 , ℓ_1 , ℓ_2 and π^+ respectively, $\lambda(x, y, z) = x^2 + y^2 + z^2 - 2xy - 2xz - 2yz$, and $n = 2$ for identical leptons in the final state, otherwise $n = 1$. $\theta_{12}(\theta_{34})$ is the angle in the $\vec{X}_{12}(\vec{X}_{34})$ rest frame between the three momentum $\vec{k}_1(\vec{k}_3)$ and the line of flight of $\vec{X}_{12}(\vec{X}_{34})$ in the B_c rest frame. The angle ϕ is the angle between the normals to the planes defined in the B_c rest frame by the $\bar{B}_s^0 \ell_1$ pair and the $\ell_2 \pi^+$ pair. This is depicted in the four-body kinematics diagram in

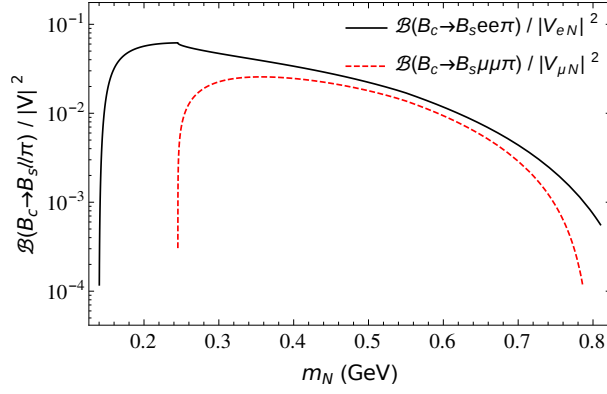


Figure 2.3: $\frac{\mathcal{B}(B_c^- \rightarrow \bar{B}_s^0 \ell^- \ell^- \pi^+)}{|V_{\ell N}|^2}$, where, $\ell = e, \mu$. The theoretical calculation uses Γ_N obtained with the assumption $|V_{eN}| \sim |V_{\mu N}| \sim |V_{\tau N}|$.

the appendix A. The four momenta k_1, k_2 (k_3, k_4) are first evaluated in the $X_{12}^{\vec{X}_{34}}$ rest frame. To finally evaluate the decay rate in the B_c rest frame, it is assumed that $X_{12}^{\vec{X}_{34}}$ moves in the $+\hat{z}$ direction and $X_{34}^{\vec{X}_{12}}$ in the $-\hat{z}$ direction and the resultant boosted explicit form of all the four momenta in the B_c^- rest frame are also given in the appendix A.

Alternately, rather than calculating the full 4-body kinematics to evaluate the decay rate, the narrow width approximation can be used to evaluate the decay rate as a product of a 3-body decay rate and the branching ratio for decay of N to a 2-body mode, as specified below:

$$\Gamma(B_c^- \rightarrow \bar{B}_s^0 \ell_1^- \ell_2^- \pi^+) \approx \Gamma(B_c^- \rightarrow \bar{B}_s^0 \ell_1^- N) \cdot \frac{\Gamma(N \rightarrow \ell_2^- \pi^+)}{\Gamma_N}. \quad (2.13)$$

In Fig. 2.3, we show the curves corresponding to $\frac{\mathcal{B}(B_c^- \rightarrow \bar{B}_s^0 e^- e^- \pi^+)}{|V_{eN}|^2}$ and $\frac{\mathcal{B}(B_c^- \rightarrow \bar{B}_s^0 \mu^- \mu^- \pi^+)}{|V_{\mu N}|^2}$, as a function of the heavy neutrino mass, m_N . The regions below the curves are theoretically allowed. For this calculation, Γ_N is evaluated, under the assumption that has been frequently used in the literature [2, 63], $|V_{eN}| \sim |V_{\mu N}| \sim |V_{\tau N}|$.

Bounds on Mixing angles using upper limits on the Branching ratios for $B_c^- \rightarrow \bar{B}_s^0 \ell_1^- \ell_2^- \pi^+$ Decays

Using the matrix element in eqn.(2.6) and the narrow width approximation, eqn.(2.10) the LNV branching ratios can be written as:

$$\begin{aligned} \mathcal{B} \left(B_c^- \rightarrow \bar{B}_s^0 e^- e^- \pi^+ \right) &= G_{ee} (m_N) \frac{|V_{eN}|^4}{\Gamma_N}, \\ \mathcal{B} \left(B_c^- \rightarrow \bar{B}_s^0 \mu^- \mu^- \pi^+ \right) &= G_{\mu\mu} (m_N) \frac{|V_{\mu N}|^4}{\Gamma_N}, \end{aligned} \quad (2.14)$$

where, G_{ee} and $G_{\mu\mu}$ are functions of the Majorana mass and depend on the explicit matrix element and phase space for each of the processes. When both the like sign dileptons in Fig.2.1 are not of the same flavour, then the process is not only lepton number violating but also lepton flavour violating. If the two vertices of N production and decay can be separated, then the two processes, $B_c^- \rightarrow \bar{B}_s^0 e^- N$ followed by $N \rightarrow \mu^- \pi^+$ and $B_c^- \rightarrow \bar{B}_s^0 \mu^- N$ followed by $N \rightarrow e^- \pi^+$ can be distinguished. Assuming this separation, we may write:

$$\begin{aligned} \mathcal{B} \left(B_c^- \rightarrow \bar{B}_s^0 e^- \mu^- \pi^+ \right) &= G_{e\mu} (m_N) \frac{|V_{eN}|^2 |V_{\mu N}|^2}{\Gamma_N}, \\ \mathcal{B} \left(B_c^- \rightarrow \bar{B}_s^0 \mu^- e^- \pi^+ \right) &= G_{\mu e} (m_N) \frac{|V_{eN}|^2 |V_{\mu N}|^2}{\Gamma_N}, \end{aligned} \quad (2.15)$$

where, we use the notation that the first lepton is produced along with the N , while the second lepton is produced in the decay of N ; $G_{e\mu}$ ($G_{\mu e}$) are again functions of the Majorana mass and vary with the explicit matrix element and phase space for each of the processes. Now, defining,

$$\begin{aligned} F_{ee} &\equiv \frac{\mathcal{B}^{exp} \left(B_c^- \rightarrow \bar{B}_s^0 e^- e^- \pi^+ \right)}{G_{ee} (m_N)}, \quad F_{\mu\mu} \equiv \frac{\mathcal{B}^{exp} \left(B_c^- \rightarrow \bar{B}_s^0 \mu^- \mu^- \pi^+ \right)}{G_{\mu\mu} (m_N)}, \\ F_{e\mu} &\equiv \frac{\mathcal{B}^{exp} \left(B_c^- \rightarrow \bar{B}_s^0 e^- \mu^- \pi^+ \right)}{G_{e\mu} (m_N)}, \quad F_{\mu e} \equiv \frac{\mathcal{B}^{exp} \left(B_c^- \rightarrow \bar{B}_s^0 \mu^- e^- \pi^+ \right)}{G_{\mu e} (m_N)}, \end{aligned} \quad (2.16)$$

where \mathcal{B}^{exp} are the expected experimental upper limits of the Branching ratios, we can obtain the constraints:

$$\frac{|V_{eN}|^4}{\Gamma_N} < F_{ee}, \quad \frac{|V_{\mu N}|^4}{\Gamma_N} < F_{\mu\mu}, \quad \frac{|V_{eN}|^2|V_{\mu N}|^2}{\Gamma_N} < F_{e\mu}/F_{\mu e}. \quad (2.17)$$

The upper limits on the \mathcal{B}^{exp} in eqn.(2.17) can be very simply translated into the upper limits on, $|V_{eN}|^2$, $|V_{\mu N}|^2$, $|V_{eN}V_{\mu N}|$ under the assumption, $|V_{eN}| \sim |V_{\mu N}| \sim |V_{\tau N}|$ in Γ_N . This leads eqn.(2.17) to result in the constraints,

$$\begin{aligned} |V_{eN}|^2 &< F_{ee} (a_e(m_N) + a_\mu(m_N) + a_\tau(m_N)); \quad |V_{\mu N}|^2 < F_{\mu\mu} (a_e(m_N) + a_\mu(m_N) + a_\tau(m_N)); \\ |V_{eN}V_{\mu N}| &< F_{e\mu}/F_{\mu e} (a_e(m_N) + a_\mu(m_N) + a_\tau(m_N)). \end{aligned} \quad (2.18)$$

According to Ref. [135] at the LHC with $\sqrt{s} = 14$ TeV, the beam luminosity and production cross-section will be high enough that the rate of producing B_c events can be $10^8 - 10^9$ per year. A crude estimate [136] using the measured [137] ratio of production cross section times branching fractions between the $B_c^+ \rightarrow J/\Psi\pi^+$ and $B^+ \rightarrow J/\Psi K^+$ decays at $\sqrt{s} = 8$ TeV, indicates $\sim \mathcal{O}(10^9 - 10^{10})$ B_c events with 10 fb^{-1} luminosity at 13/14 TeV. Ultimately, the production cross-section will be directly measured by LHCb at $\sqrt{s} = 13/14$ TeV and will be known more precisely. In any case the large number of B_c events will make a search for the proposed rare LNV B_c decays feasible. Even if these decay modes are not seen, one may naively estimate that it may be possible to set upper limits on the branching ratios of $\sim \mathcal{O}(10^{-7} - 10^{-9})$. However, since the final B_s meson needs to be reconstructed via its prominent decay modes, either $B_s \rightarrow J/\psi(\mu\mu)\phi(KK)$ or $B_s \rightarrow D_s(KK\pi)\pi$, with $\mathcal{B}(B_s \rightarrow J/\psi\phi) \times \mathcal{B}(J/\psi \rightarrow \mu\mu) \times \mathcal{B}(\phi \rightarrow KK) \sim \mathcal{O}(10^{-5})$; $\mathcal{B}(B_s \rightarrow D_s\pi) \times \mathcal{B}(D_s \rightarrow KK\pi) \sim \mathcal{O}(10^{-4})$, upper limits on $\mathcal{B}(B_c^- \rightarrow \bar{B}_s^0 \ell_1^- \ell_2^- \pi^+)$ of only $\sim \mathcal{O}(10^{-5} - 10^{-4})$ may be feasible. These limits are just indicative, exact realistic limits will only be determined by the experimental collaboration, after incorporating the detection, reconstruction efficiencies of all the final particles. Of course, tighter limits

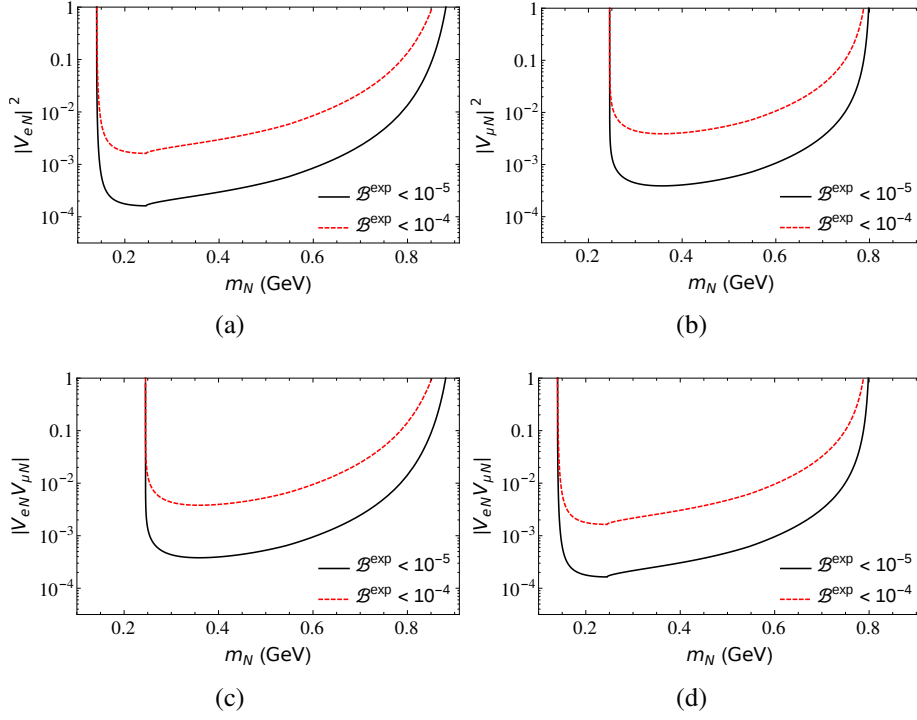


Figure 2.4: Exclusion curves for the mixing element $|V_{eN}|^2$, $|V_{\mu N}|^2$ and $|V_{eN}V_{\mu N}|$ corresponding to the different expected upper limits for branching ratio of the decay modes $B_c^- \rightarrow \bar{B}_s^0 e^- e^- \pi^+$, $\bar{B}_s^0 \mu^- \mu^- \pi^+$, $\bar{B}_s^0 e^- e \mu^- \pi^+$. In Γ_N , we are using the assumption, $|V_{eN}| \sim |V_{\mu N}| \sim |V_{\tau N}|$.

would be possible at future colliders.

In Fig. 2.4, we show the exclusion curves corresponding to the constraints on the mixing angles $|V_{eN}|^2$, $|V_{\mu N}|^2$, $|V_{eN}V_{\mu N}|$ given in eqn.(2.18), for possible upper limits on the \mathcal{B}^{exp} ($B_c^- \rightarrow \bar{B}_s^0 \ell_1^- \ell_2^- \pi^+$), of 10^{-4} and 10^{-5} .

For the lepton flavour violating case, $\ell_1 \neq \ell_2$, the mass difference of e and μ results in a slight difference in the mass range allowed for N (for its resonant production) for the two cases: when the electron is produced along with the Majorana neutrino N , while muon arises from the decay of N , or vice versa. Hence, in Fig.2.4 we present the exclusion curves for these two cases separately. If the separation of the vertices is not easily feasible, one can just add the results of the two cases in the overlapping kinematic range. Using the upper limit on the branching fractions, $\mathcal{B}^{exp} (B_c^- \rightarrow \bar{B}_s^0 \ell_1^- \ell_2^- \pi^+) \sim 10^{-5}$, the bounds on the mixing angles obtained for $\sim (0.1 < m_N < 0.9)$ GeV, are slightly tighter than those

from other heavy meson decays considered in [2, 63]. Only the constraints from K meson visible 3-body decays are tighter, but for the mass range of $\sim 0.35 < m_N < 0.90$ GeV, our exclusion limits are either tighter or compatible with the earlier constraints. A comparison of our exclusion plots against that shown in a recent analysis on global constraints on a heavy neutrino [138], again shows that these bounds could provide very tight constraints in a small range of m_N , beyond that excluded only by peak searches in K meson decays, which is otherwise so far unconstrained. ¹

The reasons for this improved sensitivity are that the meson decay modes considered in the literature so far have been mostly 3-body decay modes involving the annihilation of the initial meson and the weak annihilation vertex of all heavy mesons (except D_s) suffers from Cabibbo suppression. This reduces the coefficient of the mixing elements in the decay rates, resulting in looser constraints. Hence, in spite of the mild phase space suppression this 4-body mode can result in improved exclusion limits for the mixing angles of the heavy Majorana neutrino with the light flavour neutrinos. With a larger sample of B_c events, possible at future high energy colliders, much stronger upper limits on the branching ratios would be possible, which would result in more stringent constraints on the mixing elements.

2.3 Other B_c Decay Modes

Although the modes $B_c^- \rightarrow \bar{B}_s^0 \ell_1^- \ell_2^- \pi^+$, are expected to have a larger branching ratios due to the Cabibbo enhancement, however, as pointed out in the last section, the reconstruction of the \bar{B}_s^0 results in a penalty of $\sim \mathcal{O}(10^{-4})$, implying that with the limited number B_c events at LHCb even in the 13/14 TeV run, upper limits on the branching ratios for these modes, smaller than 10^{-5} may not be feasible. In fact, for the modes $B_c^- \rightarrow J/\psi \ell_1^- \ell_2^- \pi^+$ which are Cabibbo suppressed, but where the reconstruction of J/ψ only results in a

¹We wish to point out that our constraints cannot be directly compared with that in Ref. [138], as their conservative constraints are independent of the heavy neutrino decay products.

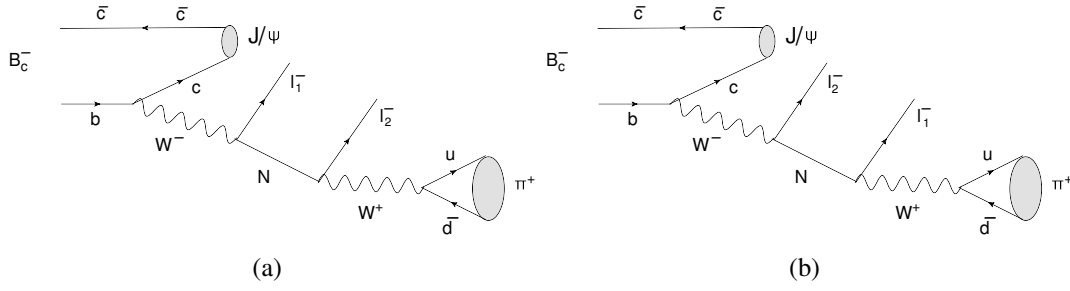


Figure 2.5: Feynman diagrams for the decay $B_c^- \rightarrow J/\psi \ell_1^- \ell_2^- \pi^+$.

suppression factor of $\sim \mathcal{O}(10^{-2})$, tighter upper limits on the branching fraction $\sim \mathcal{O}(10^{-7})$ may be achievable, provided the final leptons are electrons or muons. If one of the final leptons is a tau, the upper limit may be less tighter $\sim \mathcal{O}(10^{-6})$. Also, while LHCb has already searched for Majorana neutrinos via the mode $B^- \rightarrow \pi^+ \mu^- \mu^-$, perhaps a search through the mode $B_c^- \rightarrow \pi^+ \mu^- \mu^-$ may provide tighter constraints on the mixing angles.

2.3.1 $B_c^- \rightarrow J/\psi \ell_1^- \ell_2^- \pi^+$

The diagrams contributing to this decay mode are shown in Fig. 2.5.

The leptonic tensor in the amplitude will have the same form as that in eqn.(2.3), while the hadronic tensor can be written as:

$$(\mathcal{M}_{had})^{\beta\mu} = \frac{G_F}{\sqrt{2}} V_{cb} V_{ud} \langle J/\psi(k_1) | \bar{b} \gamma^\mu (1 - \gamma_5) c | B_c^-(p) \rangle \langle \pi^+(k_4) | \bar{u} \gamma^\beta (1 - \gamma_5) d | 0 \rangle, \quad (2.19)$$

Here, the hadronic matrix element of the weak current in the $B_c^- \rightarrow J/\psi$ transition in terms of the vector and axial-vector form factors is given by,

$$\begin{aligned} \langle J/\psi(k_1) | \mathcal{J}^\mu | B_c^-(p) \rangle = & (-F_V \epsilon^{\mu\nu\alpha\beta} \epsilon_\nu^* Q_\alpha q_\beta + iF_0^A \epsilon^{*\mu} + iF_+^A (\epsilon^* \cdot p) Q^\mu \\ & + iF_-^A (\epsilon^* \cdot p) q^\mu), \end{aligned} \quad (2.20)$$

where, $Q = p + k_1$, $q = p - k_1$, and ϵ is the polarization vector of the J/ψ meson. The form factors, F_V, F_0^A, F_+^A and F_-^A have been estimated using QCD sum rules in Ref. [127],

with the values from zero recoil evolved with the pole dependence:

$$F_i(q^2) = \frac{F_i(0)}{1 - \frac{q^2}{M_{i,pole}^2}}, \quad (2.21)$$

with the numerical values: $F_V(0) = 0.11 \text{ GeV}^{-1}$, $F_0^A = 5.9 \text{ GeV}$, $F_+^A = -0.074 \text{ GeV}^{-1}$ and $F_-^A = 0.12 \text{ GeV}^{-1}$; while the pole mass used in each of the vector/axial-vector form factors for $B_c \rightarrow \bar{c}c$ is 4.5 GeV . We evaluate the four-body decay rate for this mode using the procedure analogous to that followed for the $B_c^- \rightarrow \bar{B}_s^0 \ell_1^- \ell_2^- \pi^+$ decay mode, i.e., using the narrow width approximation for N and the phase space given in eqn.(2.12). Of course, due to the presence of larger number of form factors, the matrix element mod-squared appears more complicated. The bounds on the mixing elements are also derived in a similar fashion, using constraints similar to that given in eqn.(2.18), with the corresponding parameters appropriately defined in terms of the theoretical branching fractions and the experimental upper limits for the $B_c^- \rightarrow J/\psi \ell_1^- \ell_2^- \pi^+$ mode. Note however, that the mass difference between that of B_c and J/ψ will allow neutrino masses up to over 3 GeV to be on shell. This not only allows us to constrain $|V_{eN}|^2$, $|V_{\mu N}|^2$ and $|V_{eN}V_{\mu N}|$ over a bigger mass range, but exclusion curves for $|V_{eN}V_{\tau N}|$, $|V_{\mu N}V_{\tau N}|$ can also be provided for heavy neutrino masses beyond the region probed via tau decays.

2.3.2 $B_c^- \rightarrow \pi^+ \ell_1^- \ell_2^-$

While the number of B_c events at LHCb are expected to be smaller than the number of B^\pm events, still this mode being less suppressed with respect to $B^- \rightarrow \pi^+ \ell_1^- \ell_2^-$, could possibly result in tighter constraints on the mixing angles. The diagrams contributing to this process are shown in Figs. 2.6. Apart from the s-channel diagram (a), there is also a t-channel diagram, where the off-shell heavy neutrino contributes. However, since this diagram is highly suppressed due to CKM suppression, as well as due to absence of resonant enhancement, we only include the dominant contribution of Fig. 2.6(a) (including

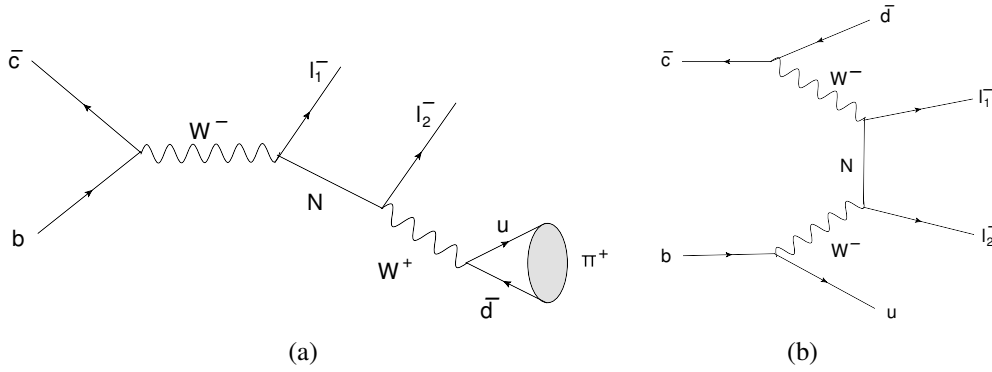


Figure 2.6: Feynman diagrams for the decay $B_c^- \rightarrow \pi^+ \ell_1^- \ell_2^-$.

that for the two leptons exchanged). The large mass difference between that of B_c and π meson allows both final leptons to be taus also. With only pion and electrons/muons as the final state particles, this mode should be easy to reconstruct, however, for the case of one or both of the leptons being a tau, the reconstruction will involve accounting for the tau branching fraction to the final state through which it is seen. The even wider range allowed for the heavy neutrino mass, also allows upper limit on $|V_{\tau N}|^2$, which is unconstrained by any of the τ or other meson decays.

In Fig. 2.7 (a), (b) and (c) we show the exclusion curves for $|V_{eN}|^2$, $|V_{\mu N}|^2$ and $|V_{eN}V_{\mu N}|$ respectively, obtained from the expected upper limits of $\mathcal{B}(B_c^- \rightarrow J/\psi \ell_1^- \ell_2^- \pi^+) \sim 10^{-7}$ and $\mathcal{B}(B_c^- \rightarrow \pi^+ \ell_1^- \ell_2^-) \sim 10^{-9}$ ($\ell_1, \ell_2 = e$ or μ), at LHCb with $\sim 10^{10}$ B_c events.

If one or both of the leptons is a tau, then it's reconstruction would lead to looser upper limits on the branching fraction. Fig. 2.8(a) shows the exclusion curves for $|V_{eN}V_{\tau N}|$, while that for $|V_{\mu N}V_{\tau N}|$ are displayed in Fig. 2.8(b), corresponding to the upper limits: $\mathcal{B}(B_c^- \rightarrow J/\psi \ell_1^- \ell_2^- \pi^+) \sim 10^{-6}$ and $\mathcal{B}(B_c^- \rightarrow \ell_1^- \ell_2^- \pi^+) \sim 10^{-8}$ when, ℓ_1^- or ℓ_2^- is a τ^- . Fig. 2.8(c) shows the exclusion curve for $|V_{\tau N}|^2$ corresponding to an upper limit of $\mathcal{B}(B_c^- \rightarrow \pi^+ \tau^- \tau^-) \sim 10^{-7}$. Note that $|V_{\tau N}|^2$ is very loosely constrained, with some limits from CHARM [139, 140], NOMAD [141] and DELPHI [142] collaborations, but with the mass range of $\sim (0.3 - 5.0)$ GeV almost unconstrained. ² The $B_c^- \rightarrow \pi^+ \tau^- \tau^-$ mode

²Ref. [143] suggests that the large data sets of the B factories may be able to place stringent limits for

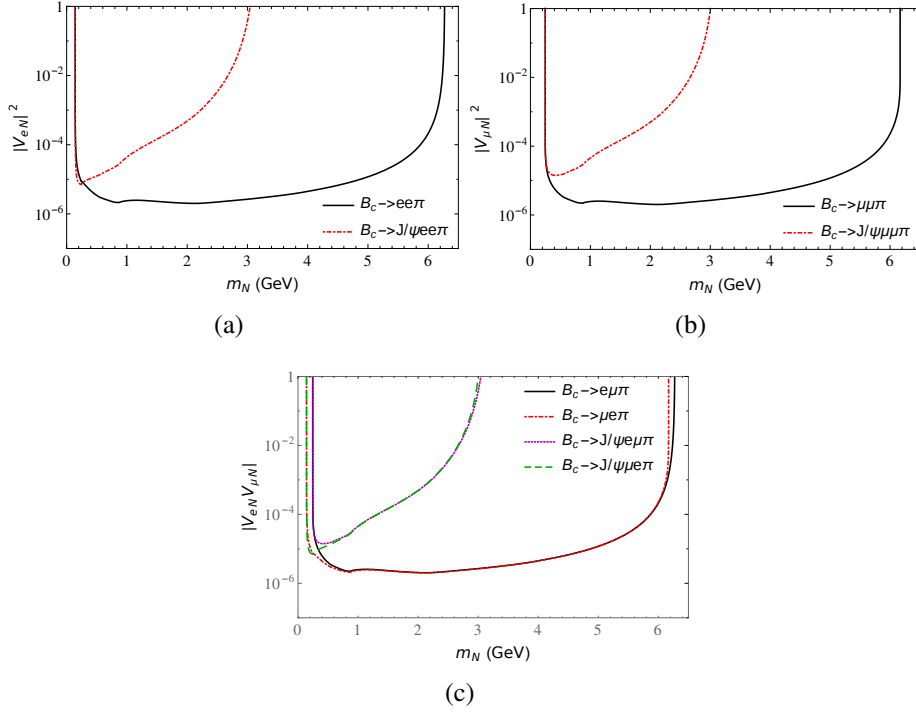


Figure 2.7: Exclusion curves for the mixing element $|V_{\ell_1 N} V_{\ell_2 N}|$ from upper limits for the branching fraction $\mathcal{B}(B_c^- \rightarrow J/\psi \ell_1^- \ell_2^- \pi^+) \sim 10^{-7}$ and $\mathcal{B}(B_c^- \rightarrow \pi^+ \ell_1^- \ell_2^-) \sim 10^{-9}$. Notation regarding the ordering of the leptons is the same as that described in Sec. 2.2

partially fills up this gap in providing exclusion limits in part of this range. In each of the above studies the Majorana sterile neutrino produced in the B_c decay is assumed to propagate as a real particle and then decay after a certain distance from the production point. In the exclusion limits obtained on the mixing elements above, we assumed an idealized detector, where this distance lies within the detector length and hence the probability of this production and decay of the heavy neutrino within the detector is unity. In practice one may need to introduce a more realistic probability factor, which could possibly weaken the constraints on the mixing elements. Estimation of this effect will depend on the specific experimental set up, the momenta carried by the heavy neutrino which would depend on that of the decaying B_c meson etc. Hence this can be properly incorporated only by the respective experimental collaborations in their data analysis. In fact, LHCb has indeed accounted for this in their analysis of a few LNV B decay modes, for a Majorana neutrino of mass of 2 – 3 GeV [134]. However, in order to observe these decay modes,

$100 \text{ MeV} \leq M_N \leq 1.2 \text{ GeV}$.

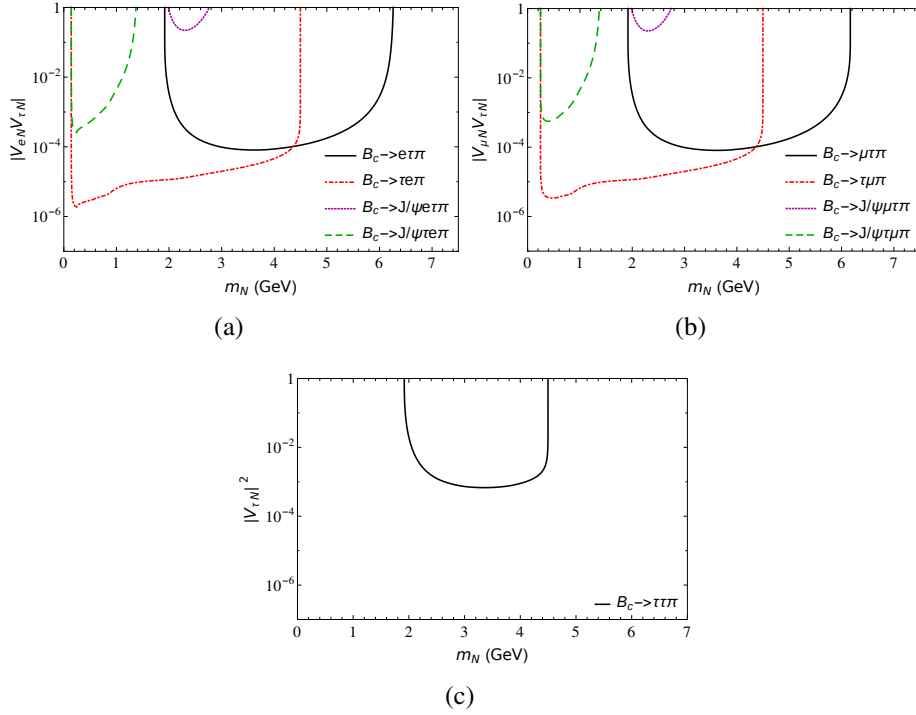


Figure 2.8: Exclusion curves for the mixing element $|V_{\ell_1 N} V_{\ell_2 N}|$. For (a), one of the leptons is an electron while the second one is a tau; the upper limits used are: $\mathcal{B}(B_c^- \rightarrow J/\psi \ell_1^- \ell_2^- \pi^+) \sim 10^{-6}$, $\mathcal{B}(B_c^- \rightarrow \pi^+ \ell_1^- \ell_2^-) \sim 10^{-8}$, (b) corresponds to the case of one muon and one tau, again using the upper limits: $\mathcal{B}(B_c^- \rightarrow J/\psi \ell_1^- \ell_2^- \pi^+) \sim 10^{-6}$, $\mathcal{B}(B_c^- \rightarrow \pi^+ \ell_1^- \ell_2^-) \sim 10^{-8}$ and for (c), both final leptons are taus and the expected upper limit for $\mathcal{B}(B_c^- \rightarrow \pi^+ \ell_1^- \ell_2^-) \sim 10^{-7}$.

heavy neutrinos should decay inside the detector and this finite detector size corrections make these limits significantly weaker. Assuming the detector length is 10 m, obtained limits on the mixing angle $|V_{eN}|^2 \sim (10^{-4}, 10^{-5}, 10^{-6})$ for the mode $B_c^- \rightarrow \overline{B_s^0} \ell_1^- \ell_2^- \pi^+$, $B_c^- \rightarrow J/\psi \ell_1^- \ell_2^- \pi^+$ and $B_c^- \rightarrow \pi^+ \ell_1^- \ell_2^-$ respectively, are only valid if the mass of N is above 0.6, 1.4 and 2.2 GeV.

2.4 Summary

We propose several B_c decay modes for Majorana neutrino searches. The B_c meson is unique in being the only meson with two heavy quarks of different flavour, allowing weak decays not only of the b quark but also the c quark. The b quark decays are always Cabibbo suppressed, with λ^2 or λ^3 suppression for $b \rightarrow c$ or $b \rightarrow u$ transitions respec-

tively. The charm quark decay on the other hand can be Cabibbo favoured. Hence the amplitude for $B_c^- \rightarrow \bar{B}_s^0 \ell_1^- \ell_2^- \pi^+$, ($\ell_1, \ell_2 = e, \mu$) decays can be enhanced. These four-body decay modes involve transition form factors rather than decay constants that appear in case of annihilation of the decaying meson, as is the case for the 3-body meson decays extensively studied for Majorana neutrino searches in the literature. To avoid model dependence and theoretical uncertainties, we suggest that these form factors be measured using the semileptonic mode, $B_c^- \rightarrow \bar{B}_s^0 \mu^- \bar{\nu}$. For a Majorana neutrino that lies in the mass range that allows it to be on the mass shell, there is also a resonant enhancement of the process. A search for Majorana neutrinos via these rare modes which are expected to have larger branching fractions, appears more feasible. Even a non-observation can result in exclusion curves for the mixing angles of the heavy Majorana singlet with the flavour eigenstates, corresponding to possible upper limits for the branching fractions. These constraints are mostly tighter than those obtained from other heavy meson decay modes in earlier studies and the mass range probed lies beyond the range with stringent constraints from experimental bounds on three-body Kaon LNV decays.

In spite of the Cabibbo enhancement for the $B_c^- \rightarrow \bar{B}_s^0 \ell_1^- \ell_2^- \pi^+$ modes, the reconstruction of the B_s leads one to expect less stringent upper limits for these modes compared to that for $B_c^- \rightarrow J/\psi \ell_1^- \ell_2^- \pi^+$ modes where the J/ψ can be reconstructed more easily via the $\mu^+ \mu^-$ mode. Similarly the reconstruction of the $B_c^- \rightarrow \pi^+ \ell_1^- \ell_2^-$ mode would be less demanding. This along with the phase space enhancement of the latter two modes may result in much tighter (by almost an order of magnitude) exclusion curves for the mixing elements, $|V_{eN}|^2$, $|V_{\mu N}|^2$, $|V_{eN} V_{\mu N}|$. Further, for $|V_{eN} V_{\tau N}|$, $|V_{\mu N} V_{\tau N}|$, on which bounds exist only from tau decays, exclusion curves for masses upto about 6 GeV can be provided. Also, upper limits for $|V_{\tau N}|^2$ can be obtained in the mass range (0.3 – 5.0) GeV, where it is so far unconstrained.

3 Constraints on Right Handed Gauge Boson Mass from LNV meson decays

One of the most attractive framework to explain the small light neutrino masses is the Minimal Left-Right Symmetry Model (MLRSM) [100–102]. The model offers several novel features including high scale parity symmetry, Majorana mass of the light and heavy neutrinos, explanation of parity violation in SM, existence of the right handed current etc. The light neutrino masses in this model are generated from dimension-five lepton number violating (LNV) operator [98] that violates lepton number by two units and hence their Majorana nature can be confirmed by observing the distinctive LNV signal at experiments, such as neutrinoless double beta decay ($0\nu\beta\beta$). Additionally, the LNV signature can also be tested at colliders from direct searches [144–148], as well as through indirect searches from meson and tau decays [2, 3, 149, 150]. While the light neutrinos can give dominant contribution in $0\nu\beta\beta$, the LNV searches at collider and meson decays are however not sensitive to such small eV mass scale. Hence, a positive result in the latter experiments will non-arguably prove the existence of lepton number violating BSM states.

Right handed Majorana neutrinos with mass in the hundreds of MeV-few GeV range, can be produced as an intermediate on mass shell state, resulting in a resonance enhancement

of the LNV meson decay rates. The detailed study of these is the main objective of this chapter. We have described the model in sec. 1.2.2. We follow a most generic approach, taking into account all the contributions arising from right handed, left handed currents, as well as their combinations. We obtain constraints on the mass of W_R that may be feasible from a number of ongoing and future experimental searches of meson decay modes with like sign dileptons, such as $K \rightarrow \ell\ell\pi$, $D_s \rightarrow \ell\ell\pi$, $D \rightarrow \ell\ell\pi$ and $B \rightarrow \ell\ell\pi$. The huge number of D_s meson decays expected in the SHiP experiment will result in the most stringent constraint on W_R mass.

3.1 Imprint of Majorana Signature in Meson Decays

In the simplest LRSM, the heavy neutrinos N_i are Majorana, that inherently carry lepton number violation. Together with the gauge bosons W_R , or even with W_L , they can mediate the lepton number violating meson decays, $M_1^+(p) \rightarrow \ell_1^+(k_1)\ell_2^+(k_2)M_2^-(k_3)$, where M_1 is a pseudoscalar, while M_2 can be a pseudoscalar or a vector meson. We assume that there are three RH neutrinos with masses in the 100 MeV – 5 GeV range, that contribute in these meson decays. The Feynman diagrams for these decays are shown in Figs 3.1 and 3.2. The different contributions are mediated through $W_L - N_i - W_L$ (Fig. 3.1(a)), while those in Fig. 3.1(b) and Fig. 3.1(c) are mediated by $W_L - N_i - W_R$ and $W_R - N_i - W_L$, respectively. All these contributions depend on the active-sterile neutrino mixing $S_{\ell_j N_i}$ and the RH neutrino mixing $V_{\ell_j N_i}$, while the diagram shown in Fig. 3.1(d), is mediated with $W_R - N_i - W_R$, and depends on $V_{\ell_j N_i}$.

The diagram in Fig. 3.2 (and a similar diagram with two W_L 's, as well as the diagrams with doubly charged Higgs triplets exchange) will give a small contribution, as this is not a s-channel resonance production diagram. In addition, there can also be additional diagrams with $W_L - W_R$ mixing in one of the legs. These however, will be small compared to the diagrams discussed above, as these come with a further suppression factor of $\tan \xi$,

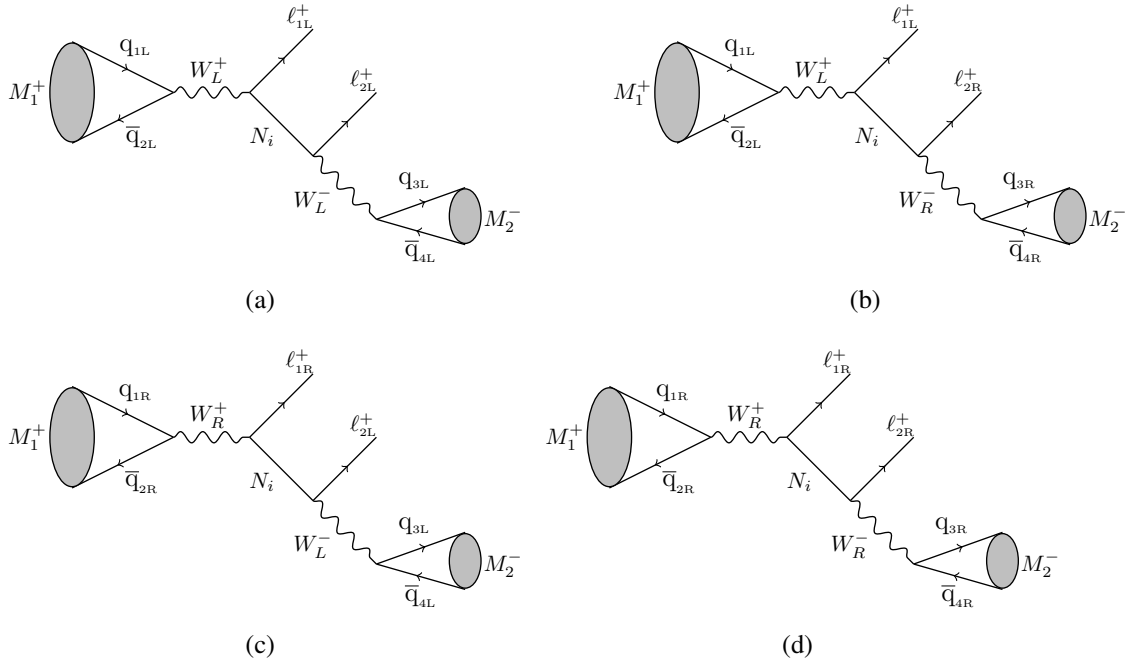


Figure 3.1: The Feynman diagrams for the lepton number violating meson decays. These processes produce resonance enhancement. See text for details.

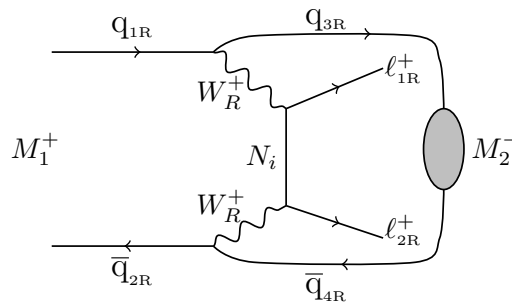


Figure 3.2: The t-channel diagram for the lepton number violating meson decay. See text for details.

due to the $W_L - W_R$ mixing. Hence, we do not consider these in our analysis. Further, note that, the contributions from light neutrino exchange will be negligibly small as they will not be resonantly enhanced.

Below, we explicitly write the amplitudes for the LNV decays of pseudoscalar mesons to a final pseudoscalar as well as to a vector meson. For each of these decays, the LL , RR , LR and RL contributions are a sum of two terms, where the second term is obtained by interchanging the momenta k_1 with k_2 of the 2 leptons, as well as interchanging the leptonic mixing elements. Hence for decay to a pseudoscalar meson we may write,

$$\mathcal{M}_{h_1 h_2}^P = \mathcal{M}_{1h_1 h_2}^P + \mathcal{M}_{2h_1 h_2}^P$$

where, $h_1 h_2$ can be of different chiralities LL, RR, LR, RL .

$$\mathcal{M}_{1LL}^P = A \sum_i M_{N_i} (S_{\ell_1 N_i}^* S_{\ell_2 N_i}^*) \frac{\bar{u}(k_2) \not{k}_3 \not{p} (1 - \gamma_5) v(k_1)}{(p - k_1)^2 - M_{N_i}^2 + i M_{N_i} \Gamma_{N_i}}, \quad (3.1)$$

$$\mathcal{M}_{1RR}^P = A \sum_i M_{N_i} \left(\frac{M_{W_L}^4}{M_{W_R}^4} \right) (V_{\ell_1 N_i} V_{\ell_2 N_i}) \frac{\bar{u}(k_2) \not{k}_3 \not{p} (1 + \gamma_5) v(k_1)}{(p - k_1)^2 - M_{N_i}^2 + i M_{N_i} \Gamma_{N_i}}, \quad (3.2)$$

where $A = G_F^2 V_{M_1}^{CKM} V_{M_2}^{CKM} f_{M_1} f_{M_2}$, k_3 and p are the four momentums of M_2^+ and M_1^- mesons. The LR and RL contributions are

$$\mathcal{M}_{1LR}^P = A \sum_i \left(\frac{M_{W_L}^2}{M_{W_R}^2} \right) (S_{\ell_1 N_i}^* V_{\ell_2 N_i}) \frac{\bar{u}(k_2) \not{k}_3 (\not{p} - \not{k}_1) \not{p} (1 - \gamma_5) v(k_1)}{(p - k_1)^2 - M_{N_i}^2 + i M_{N_i} \Gamma_{N_i}}, \quad (3.3)$$

$$\mathcal{M}_{1RL}^P = A \sum_i \left(\frac{M_{W_L}^2}{M_{W_R}^2} \right) (V_{\ell_1 N_i} S_{\ell_2 N_i}^*) \frac{\bar{u}(k_2) \not{k}_3 (\not{p} - \not{k}_1) \not{p} (1 + \gamma_5) v(k_1)}{(p - k_1)^2 - M_{N_i}^2 + i M_{N_i} \Gamma_{N_i}}. \quad (3.4)$$

In the above, the decay rate Γ^P is

$$\Gamma^P (M_1 \rightarrow \ell_1 \ell_2 M_2) = \frac{1}{n!} \left(\left| \mathcal{M}_{LL}^P + \mathcal{M}_{RR}^P + \mathcal{M}_{LR}^P + \mathcal{M}_{RL}^P \right|^2 \right) d_3(PS), \quad (3.5)$$

In Eqs.(3.1)- (3.4), G_F is the Fermi coupling constant, $V_{\ell_j N_i}$ are the elements of the mixing matrix for N_i , $S_{\ell_j N_i}$ are the elements between the neutrino of flavor state ν_{ℓ_j} and mass eigenstate N_i , $V_{M_1}^{CKM}$, $V_{M_2}^{CKM}$ are the Cabbibo-Kobayashi-Maskawa (CKM) matrix elements at the annihilation (creation) vertex of the meson $M_1(M_2)$, f_{M_1} , f_{M_2} are the decay constants of M_1 , M_2 respectively. We use the values $f_D = 0.204$ GeV, $f_{D_s} = 0.258$ GeV, $f_K = 0.156$ GeV and $f_B = 0.188$ GeV [129]. M_{N_i} , Γ_{N_i} are the mass and decay width of the heavy neutrino N_i . In Eq.(3.5), $n = 2$ for identical final leptons, otherwise $n = 1$.

3.2 Total Decay Width of the heavy Majorana neutrino N

If the mass of N_i lies in the range $0.140 \text{ GeV} < M_{N_i} < 5.3 \text{ GeV}$, it can be produced as an intermediate on mass shell state in the lepton number violating meson decay modes being considered. We compute the total width of N_i including all possible decay channels, that are listed below. We consider only tree level diagrams for the computation. The explicit expressions of the partial decay widths are given in the Appendix B. In addition to the SM gauge bosons W_L , Z , the gauge bosons W_R , Z' will also contribute in the following two and three body decays of RH neutrinos via charged current and neutral current interactions.

- RH neutrino decays to a charged pseudoscalar meson: $N_i \rightarrow \ell^- P^+$, where $\ell = e, \mu, \tau$ and $P^+ = \pi^+, K^+, D^+, D_s^+$.
- RH neutrino decays to a neutral pseudoscalar meson: $N_i \rightarrow \nu_\ell P^0$, where ν_ℓ are the flavor eigenstates ν_e, ν_μ, ν_τ and $P^0 = \pi^0, \eta, \eta', \eta_c$.

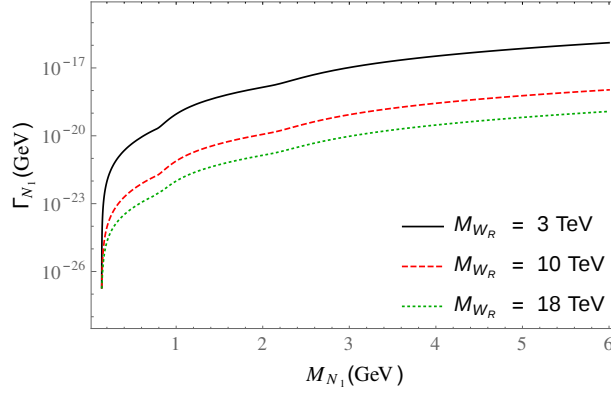


Figure 3.3: The total decay width of the heavy neutrino N_1 .

- RH neutrino decays to a charged vector meson: $N_i \rightarrow \ell^- V^+$, where $\ell = e, \mu, \tau$ and $V^+ = \rho^+, K^{*+}, D^{*+}, D_s^{*+}$.
- RH neutrino decays to neutral vector meson: $N_i \rightarrow \nu_\ell V^0$, where $\nu_\ell = \nu_e, \nu_\mu, \nu_\tau$ and $V^0 = \rho^0, \omega, \phi, J/\psi$.

Three body leptonic decays of N_i

- $N_i \rightarrow \ell_1^- \ell_2^+ \nu_{\ell_2}$, where $\ell_1, \ell_2 = e, \mu, \tau, \ell_1 \neq \ell_2$.
- $N_i \rightarrow \nu_{\ell_1} \ell_2^- \ell_2^+$, where $\ell_1, \ell_2 = e, \mu, \tau$.
- $N_i \rightarrow \nu_{\ell_1} \nu \bar{\nu}$, where $\nu_{\ell_1} = \nu_e, \nu_\mu, \nu_\tau$.

The total decay width of heavy majorana neutrino N_i is given by

$$\begin{aligned} \Gamma_{N_i} = & \sum_{\ell, P} 2\Gamma^{\ell P} + \sum_{\ell, P} \Gamma^{\nu_\ell P} + \sum_{\ell, V} 2\Gamma^{\ell V} + \sum_{\ell, V} \Gamma^{\nu_\ell V} \\ & + \sum_{\ell_1, \ell_2 (\ell_1 \neq \ell_2)} 2\Gamma^{\ell_1 \ell_2 \nu_{\ell_2}} + \sum_{\ell_1, \ell_2} \Gamma^{\nu_{\ell_1} \ell_2 \ell_2} + \sum_{\nu_{\ell_1}} \Gamma^{\nu_{\ell_1} \nu \bar{\nu}}. \end{aligned} \quad (3.6)$$

As each of N_i are Majorana, they can also decay to the charge conjugate of the decay modes $N_i \rightarrow \ell^- P^+$, $N_i \rightarrow \ell^- V^+$, $N_i \rightarrow \ell_1^- \ell_2^+ \nu_{\ell_2}$ with the same partial width, resulting in a 2 factor associated with these widths. In deriving the above relations, we neglect the

contributions from the small mixing between $W_L - W_R$ and $Z - Z'$. We show the total decay width of the heavy neutrino N in Fig. 3.3 for different choices of W_R masses. In our analysis we consider the following mixing texture:

- $U_\nu = U_{\text{PMNS}}$.
- $V_R = I$,

i.e., the RH neutrinos N_i 's are in the mass basis. The numerical values of the elements of the PMNS mixing matrix are taken from Ref. [20].

3.3 Limit on M_{W_R} from ongoing and future experiments in presence of heavy Majorana neutrinos

We consider the LNV signatures from decay modes $M_1^+ \rightarrow \ell^+ \ell^+ M_2^-$. As stated before, the contributions from LL diagram depends on mixing angle S , RL, LR diagrams depend on the active-sterile neutrino mixing S and V , whereas the RR contribution depends on the RH mixing matrix V . The active-sterile mixing from Eq. (1.39) is $S = \theta V_R$. Without loss of generality, one can approximate $\theta \sim \sqrt{\frac{m_\nu}{M_N}}$, where m_ν and M_N are the light and RH neutrino masses, in accordance with the seesaw condition.

The sensitivity reach for the above LNV decay modes in a particular experiment depends on the number of the parent mesons M_1 's produced ($N_{M_1^+}$), their momentum (\vec{p}_{M_1}) and the branching ratio for these mesons to the LNV modes. Assuming the parent meson M_1 decays at rest, the expected number of signal events is [151]:

$$\begin{aligned}
 N_{event} &= 2N_{M_1^+} \text{Br} \left(M_1^+ \rightarrow \ell^+ \ell^+ M_2^- \right) \mathcal{P}_N, \\
 &\approx 2N_{M_1^+} \text{Br} \left(M_1^+ \rightarrow \ell^+ N_i \right) \frac{\Gamma(N_i \rightarrow \ell^+ M_2^-)}{\Gamma_{N_i}} \mathcal{P}_N,
 \end{aligned} \tag{3.7}$$

where for $\ell = e$, $N_i = N_1$ and for $\ell = \mu$, $N_i = N_2$, the factor 2 is due to inclusion of the charge conjugate process of $M_1^+ \rightarrow \ell^+ N_i$ and \mathcal{P}_N , is the probability of the RH neutrino N_i to decay within a detector of the length L_D given by:

$$\mathcal{P}_N = \left[1 - \exp\left(-\frac{M_{N_i} \Gamma_{N_i} L_D}{p_{N_i}^*}\right) \right].$$

In the above, $p_{N_i}^* = \frac{m_{M_1}}{2} \lambda^{\frac{1}{2}}\left(1, \frac{m_\ell^2}{m_{M_1}^2}, \frac{M_{N_i}^2}{m_{M_1}^2}\right)$ is the momentum of N_i in M_1 rest frame. For the meson M_1 produced with fixed boost $\vec{\beta}$, the energy of N_i is then given by,

$$E_{N_i} = E_{N_i}^* \left(\gamma + \frac{p_{N_i}^*}{E_{N_i}^*} \sqrt{\gamma^2 - 1} \cos \theta_{N_i}^* \right),$$

where $E_{N_i}^*$, $p_{N_i}^*$ are the energy and momentum of N_i in rest frame of M_1 and $\gamma = \frac{E_{M_1}}{m_{M_1}}$. $\theta_{N_i}^*$ is the emission angle of particle N_i in the rest frame of M_1 , which is measured from the boost direction $\vec{\beta}$. The energy E_{N_i} of the N_i in the boosted M_1 frame lies within the range,

$$E_{N_i} \in (E_{N_i}^-, E_{N_i}^+) = \left[(\gamma E_{N_i}^* - p_{N_i}^* \sqrt{\gamma^2 - 1}), (\gamma E_{N_i}^* + p_{N_i}^* \sqrt{\gamma^2 - 1}) \right]$$

Hence, the energy distribution of N_i follows a flat distribution as

$$f(E_{N_i}) = \frac{1}{E_{N_i}^+ - E_{N_i}^-} = \frac{1}{2p_{N_i}^* \sqrt{\gamma^2 - 1}},$$

The signal event for $M_1^+ \rightarrow \ell^+ \ell^+ M_2^-$ in the lab-frame is:

$$N_{event} \approx 2N_{M_1^+} \int_{E_{N_i}^-}^{E_{N_i}^+} dE_{N_i} \text{Br}(M_1^+ \rightarrow \ell^+ N_i) \frac{m_{M_1}}{2p_{N_i}^* |\vec{p}_{M_1}|} \frac{\Gamma(N_i \rightarrow \ell^+ M_2^-)}{\Gamma_{N_i}} \mathcal{P}'_N, \quad (3.8)$$

where $\mathcal{P}'_N = \left[1 - \exp\left(-\frac{M_{N_i} \Gamma_{N_i} L_D}{\sqrt{E_{N_i}^2 - M_{N_i}^2}}\right) \right]$, is the probability of N_i to decay within the detector length L_D , after taking into account the boost factor. Since the LNV decays will be rare, the expected number of events for these processes can be assumed to follow a Pois-

son distribution. Using the method of Feldman and Cousins, we get the average upper limit on the number of events at 95% C.L., assuming zero background events and no true signal event to be $N_{event} = 3.09$ [152].

Note that the theoretical estimates of the number of events (given in Eqs. (3.7) or (3.8), corresponding to decay of parent meson at rest or in flight respectively) are functions of the mass parameters M_{N_i} and M_{W_R} . If Majorana neutrinos having a mass such that they can be produced as an on shell intermediate state in the LNV meson decay processes exist, then, equating the numerical upper limit on the number of events to the theoretical expressions, results in constraints on M_{W_R} , corresponding to specific M_{N_i} values for each of the following experiments.

NA62

NA62 is an ongoing experiment at CERN that will produce a large number of K^+ mesons [153]. The primary SPS 400 GeV proton beam, aims on a target, producing a secondary high intensity hadron beam with an optimum content of K^+ ($\approx 6\%$). The expected number of K^+ decays in the fiducial volume is 4.5×10^{12} per year. Assuming three years of running, $N_{K^+} = 1.35 \times 10^{13}$. The detector length $L_D \approx 170$ m and the produced K^+ mesons will decay in flight, carrying a momentum of 75 GeV. Non-observation of signal events for the decay mode $K^+ \rightarrow \ell^+ \ell^+ \pi^-$ at NA62 can be used to set limits on M_{W_R} for $M_{N_i} \sim 0.350$ GeV. Using Eq. (3.8), we derive the 95% C.L limit on M_{W_R} for different M_{N_i} values, shown in Fig. 3.4(a) for the case of decay to like sign di-electrons. From this ee channel, for a heavy Majorana neutrino mass $M_{N_1} \approx 0.38$ GeV, the RH gauge boson mass can be constrained to be $M_{W_R} > 4.6$ TeV. For the $\mu\mu$ channel, for heavy neutrino mass $M_{N_2} \approx 0.35$ GeV, a limit of $M_{W_R} > 4.3$ TeV can be obtained and is shown in Fig. 3.5(a).

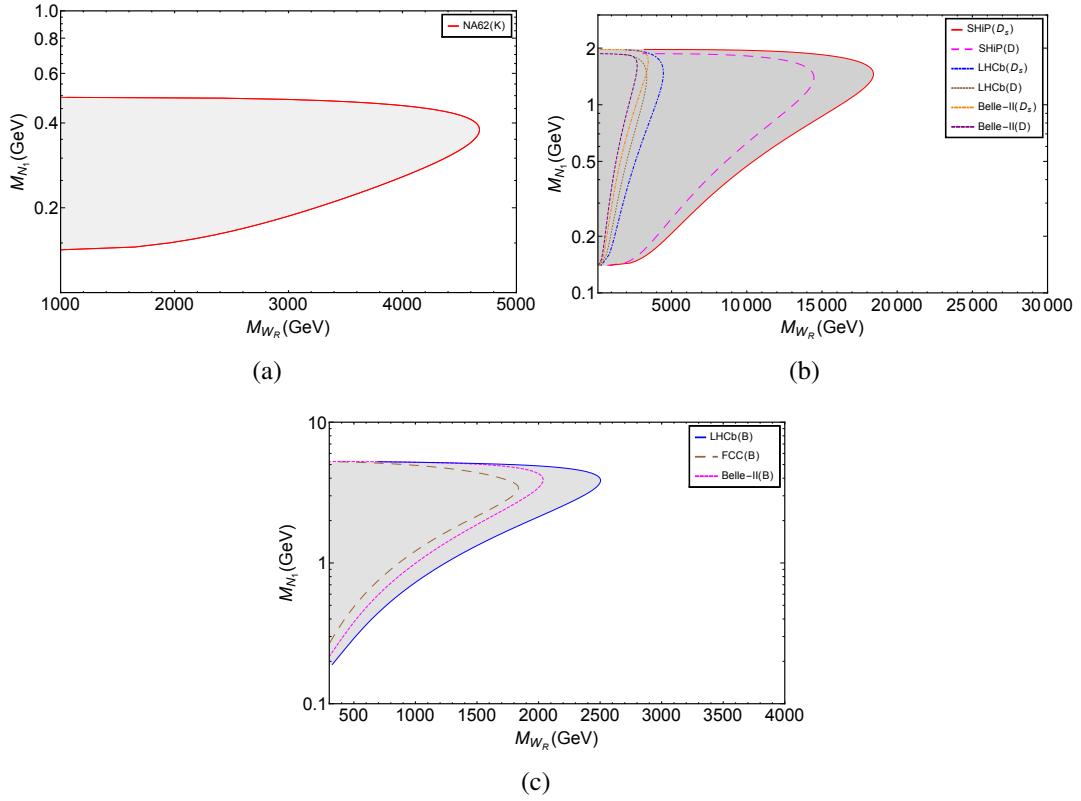


Figure 3.4: Constraints on the RH gauge boson M_{W_R} mass, corresponding to a heavy neutrino M_N , that could be resonantly produced in lepton number violating decays of (a) K , (b) D, D_s and (c) B mesons. The shaded region to the left of the curves corresponding to expected limits from searches at different ongoing and future experiments will be ruled out in the absence of LNV meson decays with like sign di-electrons.

Belle II

The asymmetric SuperKEKB facility is designed to collide electron and positron beams such that the centre of mass energy is in the region of the Υ resonances. An upgrade of Belle, the newly completed Belle II detector is expected to collect data samples corresponding to an integrated luminosity of 50 ab^{-1} by the end of 2024 [154]. The expected number of charged $B\bar{B}$ pairs to be produced at 50 ab^{-1} is 5.5×10^{10} [129, 155]. In addition, a large sample of charged D, D_s mesons will also be accessible, with $N_{D^+} = 3.4 \times 10^{10}$ and $N_{D_s^+} = 10^{10}$ [155]. A direct search for heavy Majorana neutrinos in B-meson decays was performed by the Belle collaboration using a data sample that contained 772×10^6 $B\bar{B}$ pairs (at 711 fb^{-1}) [156]. At KEKB as well as superKEKB, the energies of the e^+ , e^- beams are sufficiently low so that the momentum of the produced B mesons as well as that for the charmed mesons will not be appreciable and the suppression from high momentum of the decaying mesons in the number of events will be absent. Using the much larger expected number of mesons to be produced at Belle II ($N_{D^+}, N_{D_s^+}, N_{B^+}$) with the detector length $L_D = 1.5 \text{ m}$, we calculate the expected number of signal events for the LNV decays of these mesons using Eq. (3.7). In Fig. 3.4(b),(c) and Fig. 3.5(b),(c) we show the limits on M_{W_R} and M_{N_i} that will arise, if no events for the LNV $D^+, D_s^+, B^+ \rightarrow \ell^+ \ell^+ \pi^-$ decays are observed. Note that, among the different decay modes, the most stringent limit $M_{W_R} \geq 3.4 \text{ TeV}$ for heavy Majorana neutrino mass $M_{N_{1,2}} \simeq 1.7 \text{ GeV}$ can come from D_s meson decays, which are Cabibbo favoured modes.

LHCb

The LHCb detector is a forward spectrometer at the Large Hadron Collider (LHC) at CERN. During run 1, the LHCb detector collected data at $\sqrt{s} = 7 \text{ TeV}$ with integrated luminosity of 3 fb^{-1} . During run 2, LHCb will collect additional 5 fb^{-1} at $\sqrt{s} = 13 \text{ TeV}$. A search for heavy Majorana neutrinos in B meson decays had been performed by the

LHCb collaboration using the 7 TeV data [157]. The cross-section for producing B, D and D_s mesons at $\sqrt{s} = 13$ TeV within the LHCb acceptance ($2 < \eta < 5$) are $154 \mu\text{b}$, $1000 \mu\text{b}$ and $460 \mu\text{b}$ respectively [158, 159]. Hence, in run 2 with 5 fb^{-1} , expected number of B, D and D_s mesons are, $N_{B^+} = 7.7 \times 10^{11}$, $N_{D^+} = 5 \times 10^{12}$ and $N_{D_s^+} = 2.3 \times 10^{12}$. The produced B and D mesons will decay in flight, carrying a momentum of order of 100 GeV in forward direction [160]. We take the detector length $L_D \approx 20$ m. The tightest constraint expected from LHCb are also from D_s decays, $M_{W_R} \geq 4.4$ TeV for heavy Majorana neutrino mass $M_{N_1} \approx 1.5$ GeV, while for a heavier neutrino, $M_{N_1} \approx 3.8$ GeV, the constraint is weaker, $M_{W_R} \geq 2.5$ TeV.

FCC-ee

The Future Circular Collider (FCC-ee) [161] will collect multi- ab^{-1} integrated luminosities for e^+e^- collisions at c.m.energy $\sqrt{s} \approx 91$ GeV. The expected number of Z-bosons is $10^{12} - 10^{13}$. The number of charged B mesons from Z decays can be estimated as,

$$N_{B^+} = N_Z \times \text{Br}(Z \rightarrow b\bar{b}) \times f_u,$$

where $N_Z \sim 10^{13}$, $\text{Br}(Z \rightarrow b\bar{b}) = 0.1512$ [162], $f_u = 0.410$ [163] is the fraction of B^+ from \bar{b} quark in Z decay. The B mesons produced at FCC-ee will have an energy distribution peaked at $E_{B^+} = \frac{M_Z}{2}$. Hence we can calculate the number of signal events using Eq. (3.8), where the detector length is taken to be, $L_D = 2$ m. At FCC, for a heavy Majorana neutrino of mass $M_{N_{1,2}} \approx 3.9$ GeV, RH gauge boson mass upto $M_{W_R} \approx 2$ TeV can be excluded using the decay modes $B^+ \rightarrow \ell^+\ell^+\pi^-$.

SHiP

The SHiP experiment is a newly proposed general purpose fixed target facility at the CERN SPS accelerator [164]. A 400 GeV proton beam will be dumped on a heavy target

in order to produce 2×10^{20} proton-target interactions in five years. One of the goals of the experiment is to use decays of charmed mesons to search for heavy sterile neutrinos using the decay mode $D_s^+/D^+ \rightarrow \ell^+\ell^+\pi^-$. The number of charmed meson pairs that are expected to be produced in this experiment can be estimated as [165],

$$N_{meson} = X_{c\bar{c}} \times N_{POT} \times \mathcal{R},$$

where $X_{c\bar{c}}$ is the $c\bar{c}$ production rate, $N_{POT} = 2 \times 10^{20}$ is the number of proton-target interaction. The relative abundances \mathcal{R} of charmed mesons, such as, D and D_s are 30% and 8% respectively. Hence, the expected number of D and D_s mesons are $N_{D^+} = 1.02 \times 10^{17}$ and $N_{D_s^+} = 2.72 \times 10^{16}$ respectively. This very high intensity of the charmed mesons will permit the absence of LNV D_s meson decay mode at SHiP, to set tight constraints on the mass of RH gauge boson, $M_{W_R} > 18.4$ TeV ($M_{W_R} > 17.4$ TeV) for heavy Majorana neutrino mass $M_{N_1} \simeq 1.46$ GeV ($M_{N_2} \simeq 1.43$ GeV). The detector length is taken to be, $L_D = 60$ m. For the 400 GeV CNGS proton beam on target, the expected momentum of the produced charmed mesons is ~ 58 GeV [166]. The result for the constraints on M_{W_R} are shown in Fig. 3.4(b) and Fig. 3.5(b). Similar constraint was obtained from the LNV D_s meson decay at SHiP in Ref. [167].

From Fig. 3.4 and Fig. 3.5 it is evident that the most stringent limit in the $M_N \sim 1$ GeV range will be provided by SHiP with the $D_s/D \rightarrow \ell^+\ell^+\pi^-$ decay mode. In the relatively higher mass range $M_N \sim 4$ GeV, stringent limit can be obtained by FCC-ee, Belle-II and LHCb experiments. Besides, the ongoing NA62 can give constraint $M_{W_R} > 4.6$ TeV ($M_{N_1} \sim 0.38$ GeV), which is competitive with the collider bounds from LHC. Note that our numerical constraints on M_{W_R} for various experiments are obtained assuming idealized detectors with 100% detection, reconstruction efficiencies etc. The realistic constraints (expected to be weaker) will only be feasible through searches by the experimental collaborations, incorporating all these corrections.

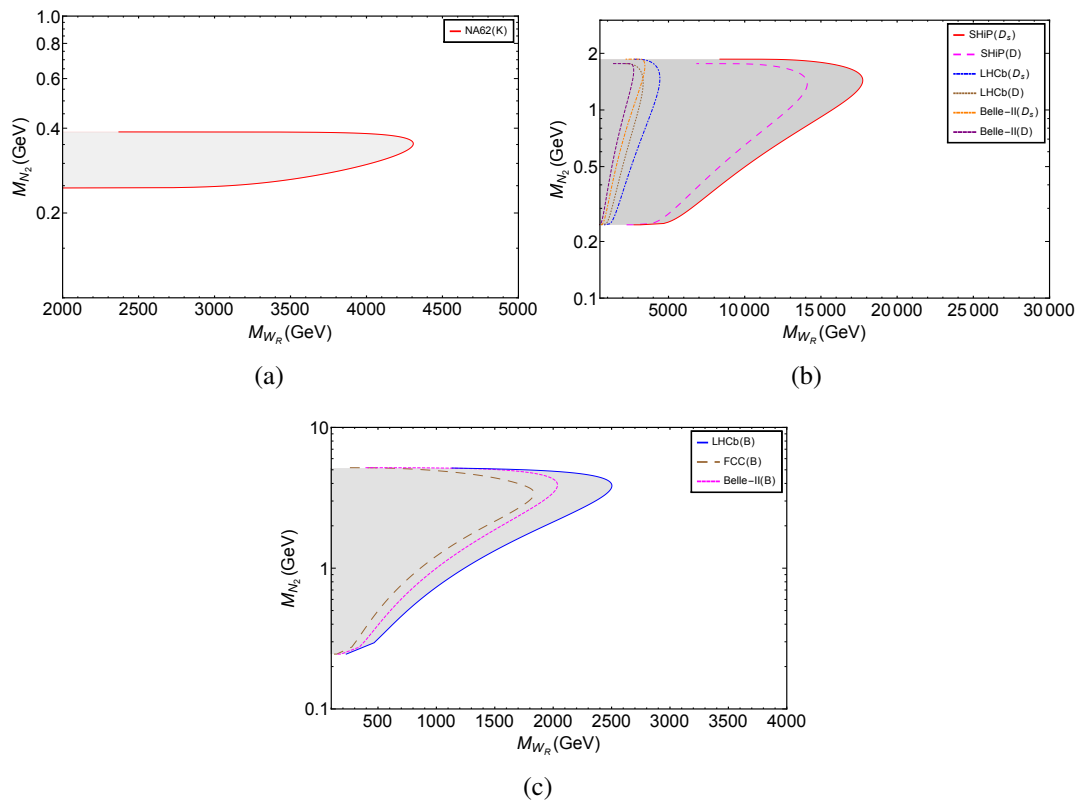


Figure 3.5: Same as Fig. 3.4, except that the limits corresponding to searches at different ongoing and future experiments with like sign dimuons are shown.

3.4 Comparison with Existing constraints from other experiments

A constraint on M_{W_R} mass, $M_{W_R} > 2.5$ TeV was obtained in Ref [168], by calculating the K meson mass difference in a minimal Left-Right symmetric model. In addition to the meson decay searches, there are other direct and indirect searches that constrain the mass of heavy neutrino N and M_{W_R} . In particular, direct collider searches, such as, LHC dijet searches for W' [169], the same sign dilepton searches [146, 147] and indirect searches, such as, $0\nu\beta\beta$ and LFV $\mu \rightarrow e\gamma$, give stringent constraints on the masses of the gauge boson W_R and heavy neutrino N . Assuming a 75% branching ratio of $W_R \rightarrow jj$, the 13 TeV ATLAS dijet search ruled out the W_R mass upto 2.9 TeV [169]. For W_R that couples to two light generation of quarks through CKM type mixing, the branching ratios to of $W_R \rightarrow jj$ is 60% [145]. The limit will be comparable with the reported limit from ATLAS. On the other hand, the search for same-sign dilepton at LHC is only relevant for heavy neutrino mass M_N in the 100 GeV-TeV range. The 95% C.L limit from ATLAS 8 TeV search on the M_{W_R} reaches 2.9 TeV [147, 170]. For all the mediators M_{W_R} and M_N in the TeV-few hundred GeV mass range, the LHC same sign lepton search is more constraining than $0\nu\beta\beta$ [171]. The latter is sensitive to a wide range of heavy neutrino N and RH gauge boson W_R masses. The tightest bound from $0\nu\beta\beta$ $M_{W_R} > 9 - 10$ TeV is applicable for $M_N \sim 0.1$ GeV [170]. The meson decays, on the other hand, are sensitive in constraining the low mass region of RH neutrino of mass between few hundred MeV to few GeV. The ongoing experiment NA62 can constrain $M_{W_R} > 4.6$ TeV ($M_{N_1} \sim 0.38$ GeV), that will be more stringent than the limit provided by LHC-dijet search. The other future experiments, such as, SHiP can allow upto a very large mass $M_{W_R} > 18.4$ TeV ($M_{N_1} \sim 1.46$ GeV).

3.5 Summary

We evaluate the lepton number violating meson decays $M_1 \rightarrow \ell^+ \ell^+ M_2$ within the framework of a Left-Right symmetric model. The right handed Majorana neutrinos of masses in the $\sim (100 \text{ MeV} - 6 \text{ GeV})$ range, can result in a resonant enhancement of these processes. These neutrinos along with the left handed and right handed gauge bosons mediate these processes, with contributions from $W_R - N_i - W_R$, $W_L - N_i - W_L$, $W_R - N_i - W_L$ and $W_L - N_i - W_R$ exchanges. If Majorana neutrinos in this low mass range (\sim upto few GeV), exist, then, non-observation of the LNV meson decays at the various ongoing and future experiments will result in constraints on the RH gauge boson M_{W_R} , corresponding to the Majorana neutrino mass M_{N_i} . The ongoing experiment NA62 can provide the limit $M_{W_R} > 4.6 \text{ TeV} (M_{N_1} \sim 0.38 \text{ GeV})$, that is more stringent than the present collider constraint on W_R . The future experiment, such as SHiP will be sensitive upto a very large mass $M_{W_R} > 18.4 \text{ TeV} (M_{N_1} \sim 1.46 \text{ GeV})$ which will be tighter than any collider constraint but will correspond to a low value of M_N . The meson decays are sensitive for low mass right handed neutrinos (in the few 100 MeV-few GeV range) and are complementary to LHC (sensitive to few hundred GeV to TeV mass neutrinos).

4 Probing Leptoquark and Heavy Neutrino at LHeC

In this chapter we explore leptoquark production and decay for the \tilde{R}_2 class of models at the proposed e^-p collider LHeC, planned to operate with 150 GeV electron and 7 TeV proton beams.

Leptoquarks (LQs) are hypothetical particles, which make leptons couple directly to quarks and vice versa [100, 172, 173]. In the Pati-Salam model, they emerged from the unification of quarks and leptons [174]. They also exist in grand unification theories based on SU(5) [175] and SO(10) [176–180]. They are also expected to exist at TeV scale in extended technicolour models [181–184]. LQs can be either of scalar or vector nature. Using the SM representation of quarks and leptons, all possible LQ states can be classified, with six scalar and six vector LQ multiplets under the SM gauge group [185]. Among the different classes, the scalar LQ \tilde{R}_2 is interesting, as it is one of the multiplets that allows for matter stability [186]. Moreover, it also couples to right handed neutrinos (RH neutrinos). A substantial rise in the production cross section of the RH neutrinos is feasible in the presence of LQs. This has been explored recently for LHC in [187] for inverse seesaw, where a number of final states have been analysed in detail. Leptoquark models have also been tested recently for fitting the IceCube events [188]. For the heavy neutrino searches at LHeC in inverse seesaw model, see [189] and for the LNV signal at LHeC, see [190]. Similar studies for heavy neutrino searches also been carried out

in [191, 192].

The scalar leptoquark \tilde{R}_2 transforms as $(3, 2, \frac{1}{6})$ under the SM gauge group $SU(3)_c \times SU(2)_L \times U(1)_Y$. For the RH neutrino, we adopt a model independent framework. The colour charge of the LQ will enable in its copious production at LHC. Moreover, at e^-p colliders like LHeC, they can be resonantly produced. The LHeC is a proposed e^-p collider in the TeV regime after HERA, supposed to be built in the LHC tunnel [193]. LHeC will use a newly built electron beam of 60 GeV, up to possibly 150 GeV, to collide with the intense 7 TeV proton beam of the LHC. LHeC is expected to operate with 100 fb^{-1} integrated luminosity, and is complementary to the pp collider LHC [194]. The RH neutrino, being coupled to the LQ, can be produced from LQ decay. The decay of LQ into a lepton and a jet, and the decay of RH neutrino in different SM states give rise to a plethora of model signatures, that we study in detail.

4.1 Model

We consider the scalar LQ \tilde{R}_2 , which in the presence of the RH neutrinos N_R , has additional interaction [172, 173, 185],

$$\mathcal{L} = -Y_{ij} \bar{d}_R^i \tilde{R}_2^a \epsilon^{ab} L_L^{j,b} + Z_{ij} \bar{Q}_L^{i,a} \tilde{R}_2^a N_R^j + h.c., \quad (4.1)$$

where $i, j = 1, 2, 3$ are flavor indices and $a, b = 1, 2$ are $SU(2)_L$ indices. We assume that there are three right-chiral neutrinos N_R^j ($j = 1, 2, 3$), Y_{ij} and Z_{ij} are the elements of arbitrary complex 3×3 Yukawa coupling matrices. Note that, \tilde{R}_2 comprises two LQs. One has $Q = \frac{2}{3}$, and the other has $Q = -\frac{1}{3}$. Upon expansion, the Lagrangian becomes

$$\begin{aligned} \mathcal{L} = & -Y_{ij} \bar{d}_R^i e_L^j \tilde{R}_2^{2/3} + (YU_{\text{PMNS}})_{ij} \bar{d}_R^i \nu_L^j \tilde{R}_2^{-1/3} + (V_{\text{CKM}}Z)_{ij} \bar{u}_L^i N_R^j \tilde{R}_2^{2/3} \\ & + Z_{ij} \bar{d}_L^i N_R^j \tilde{R}_2^{-1/3} + h.c., \end{aligned} \quad (4.2)$$

where the superscript of LQ fields denotes electric charge of a given $SU(2)_L$ doublet component of \tilde{R}_2 , U_{PMNS} and V_{CKM} are Pontecorvo-Maki-Nakagawa-Sakata (PMNS) and Cabibbo-Kobayashi-Maskawa (CKM) matrices.

The charged current and neutral current interactions of the RH neutrinos are parametrized in a model independent way as follows,

$$\begin{aligned} -\mathcal{L}_{CC} &= \frac{g}{\sqrt{2}} W_\mu^- \bar{\ell} \gamma^\mu P_L V_{\ell j} N_R^j + \text{H.c.}, \\ -\mathcal{L}_{NC} &= \frac{g}{2 \cos \theta_w} Z_\mu \left\{ (U_{\text{PMNS}}^\dagger V)_{ij} \bar{\nu}_i \gamma^\mu P_L N_R^j + \text{H.c.} \right\} \end{aligned} \quad (4.3)$$

The interaction of the heavy neutrinos with Higgs has the following form:

$$-\mathcal{L}_H = \frac{g M_j}{4 M_W} H \left\{ (U_{\text{PMNS}}^\dagger V)_{ij} \bar{\nu}_i P_R N_R^j + \text{H.c.} \right\} \quad (4.4)$$

In the above $P_{L/R} = (1 \mp \gamma^5)/2$ is the left/right-chirality projection operator, and V is the mixing matrix through which light neutrinos mix with the RH neutrinos.

For the RH neutrino, coupled with LQ, we do not assume any particular model. Instead, we are interested in different frameworks of RH neutrinos, that can lead to large active-sterile mixing, so that the heavy neutrinos decay inside the detector. It is widely known, that a number of different frameworks can generate large active-sterile mixing, including inverse and linear seesaw [93–96], extended seesaw [195–197], cancellation framework [99]. In the inverse seesaw, light SM neutrino masses are extremely tiny, owing to the small lepton number violating parameter of the model. The active-sterile neutrino mixing is not constrained from light neutrino masses in this model. Active-sterile mixing up to $\mathcal{O}(10^{-2})$ is allowed from experimental data [198–203]. In extended seesaw, or double seesaw [204], the RH neutrino gets mass due to seesaw, and light neutrino masses are generated due to two-fold seesaw. In other frameworks, such as, cancellation, small light neutrino masses are generated due to cancellation between different RH neutrino contributions in the mass matrix [99]. The active-sterile mixing is yet un-

constrained from neutrino data. In all the above mentioned frameworks, owing to the charged current and neutral current interactions as well as the interaction with the Higgs, specified above in Eqs.4.3 and 4.4, the RH neutrino N can decay to a number of SM particles, including $l^\pm W^\mp$, νZ , and νH . The branching ratio of these three decays is $\text{Br}(N \rightarrow lW) : \text{Br}(N \rightarrow \nu Z) : \text{Br}(N \rightarrow \nu H) \simeq 0.6 : 0.3 : 0.1$, once RH neutrino mass becomes larger than the Higgs mass $M_N > M_H$ and $M_N < 200 \text{ GeV}$ [2, 75].

In the following sections, we first consider the resonant production of LQ and its decay to a lepton and jet. We next consider the production of heavy neutrinos from LQ decay, and discuss the discovery prospect of the LQ in a number of channels. As mentioned before, we consider the prompt decays of heavy neutrino for the analysis of the RH neutrino signature, that occurs due to large active-sterile neutrino mixing. We compare between the usual charged current (CC) production of heavy neutrinos vs the alternate production from LQ decay. We show that the production from LQ decay dominates over the CC production mode by order of magnitude for active-sterile mixing $V \lesssim 10^{-2}$.

4.2 Constraints on Leptoquark Couplings

The couplings of the LQs to fermions are constrained by low energy precision observables such as atomic parity violation, Kaon decays etc. We assume that the Yukawa coupling matrix elements, $Y_{ij} = \delta_{ij} Y_{ii}$ and $Z_{ij} = \delta_{ij} Z_{ii}$, where, $i, j = 1, 2, 3$. Hence the LQ couples exclusively to a lepton and a quark of the same generation, although it can have non-zero couplings to fermions of more than one generation.

LQs have been searched for and studied in the context of e^+e^- [205, 206], ep [207, 208], $p\bar{p}$ [209, 210], and pp [211, 212] colliders. The present tightest bounds are from the LHC [1, 213–216]. LHC has studied the process $pp \rightarrow LQ \bar{L}Q \rightarrow \ell j \ell j$ for LQs of first, second and third generations. Non-observation of any new physics at the LHC has ruled out LQs of masses up to 1.1 TeV at 95% C.L for the LQ decaying to $e j$ with 100%

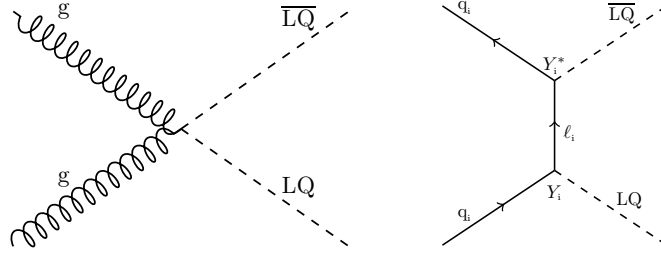


Figure 4.1: Left panel: Feynman diagram for the gluon-initiated LQ pair-production process at LHC. Right panel: the same, but for the quark-initiated processes.

branching ratio [1]. For second generation, the bound is even more stringent $M_{LQ} > 1.5$ TeV at 95% C.L [216]. For third generation, the bound is $M_{LQ} > 900$ GeV at 95% C.L [215].

At LHC, numerous QCD diagrams contribute to the LQ pair production. For illustration, we show only one representative gluon initiated diagram in the left panel of Fig. 4.1. However, with non-zero Yukawa couplings, significantly large contribution to the LQ pair production may arise through a single t channel diagram (see the right panel of Fig. 4.1). The pair production cross-section at LHC can be parametrised as [217],

$$\sigma_{\text{pair}}(Y_{ii}, M_{LQ}) = a_0(M_{LQ}) + a_2(M_{LQ})|Y_{ii}|^2 + a_4(M_{LQ})|Y_{ii}|^4, \quad (4.5)$$

where the three terms correspond to the QCD pair production, an interference term and t-channel production. In Fig. 4.2, we show the variation of LQ pair production cross-section with the Yukawa coupling Y_{11} .

For small Yukawa coupling Y_{11} , LQ pair production is mostly governed by QCD, as can be seen from the straight line upto $Y_{11} \sim 0.5$ in Fig. 4.2. For intermediate Yukawa couplings there exists a region with negative interference between QCD diagrams and the t-channel diagram where the total cross section decreases [217], resulting in the mild dip in the cross-section for coupling beyond 0.5, that is seen in Fig. 4.2. For large Yukawa coupling Y_{ii} , the t-channel process dominates and significantly enhances the cross-section. The right panel of Fig. 4.2 shows the limit on the first-generation scalar LQ pair-production

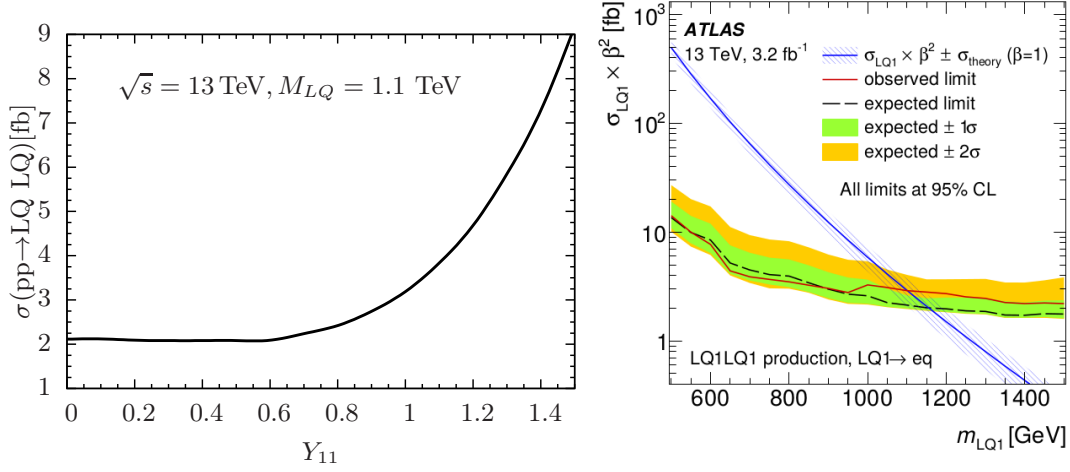
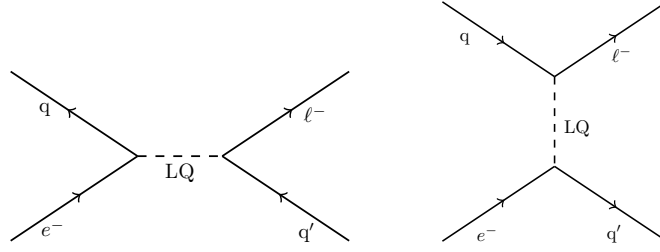


Figure 4.2: Left panel: variation of the production cross-section with Yukawa coupling for $\sqrt{s} = 13$ TeV. Right panel: limit on scalar LQ pair-production time branching fraction to eq final state as a function of mass for first-generation LQs. The yellow and green bands represent the 2σ and 1σ expected limits. The NLO prediction is shown in blue curve with uncertainty due to choice of PDF set and renormalisation/factorisation scale [1].

times the branching fraction to ej final state as a function of the mass. For the branching fraction $LQ \rightarrow ej$ as 100%, the bound on the pair-production of LQ becomes $\sigma(pp \rightarrow LQLQ) \lesssim 3$ fb, for LQ mass 1.1 TeV. Comparing the left and right panel of Fig. 4.2, one can see that the limit on the cross section for a LQ of mass 1.1 TeV, will be inconsistent with a Yukawa coupling larger than 1.

It is obvious from Eq. 4.1, that for the LQ to have 100% branching ratio in the $LQ \rightarrow ej$ decay mode, the coupling Z needs to be zero. Allowing non-zero value for coupling Z will open up new decay modes, such as $\bar{l}N$ for LQ, and hence will lower the stringent bound on LQs. We however, adopt a conservative approach, and in order to be consistent with the LHC results for first generation of LQ, throughout our study, we consider $M_{LQ} \geq 1.1$ TeV. Additionally, we also keep both the couplings non-zero.

The present bound on coupling Y from atomic parity violation are $Y_{de} < 0.34 \left(\frac{M_{LQ}}{1TeV}\right)$, $Y_{ue} < 0.36 \left(\frac{M_{LQ}}{1TeV}\right)$ [217]. These bounds are extracted under the assumption that only one of the two contributions is present at a given moment. These bounds allow large coupling for larger mass of LQ, and place a stringent constraint for lighter LQ.

Figure 4.3: Feynman diagram for $e^-p \rightarrow \ell j$.

The most stringent bound on the diagonal couplings of $\tilde{R}_2^{\frac{2}{3}}$ comes from LFV decay mode $K_L \rightarrow \mu^- e^+$, as this is a tree level process. Following Refs. [217, 218], the bound is given by, $|Y_{s\mu}Y_{de}^*| < 2.1 \times 10^{-5} \left(\frac{M_{LQ}}{1TeV}\right)^2$. In order to satisfy both the APV and LFV constraints, for $Y_{de} \sim \mathcal{O}(0.1)$, the other coupling $Y_{s\mu}$ has to be tiny. We consider $Y_{s\mu}$ to be zero and a large value (0.3) for Y_{de} to get large production cross-section of LQ at LHeC.

We discuss the production of a LQ, and its decay to different final states in the next section, for the benchmark points, that are in agreement with the described constraints.

4.3 Leptoquark Production and Its Decays

At e^-p colliders, scalar LQs can be resonantly produced through s-channel process as shown in the left panel of Fig. 4.3, and decay to a lepton and a jet. In addition, LQ can also be a t-channel mediator for the process $e^-p \rightarrow l^- j$, that we consider in our analysis (shown in the right panel of Fig. 4.3).

The production cross-section of a LQ at LHeC, as well as that for both the single and pair production at LHC, are shown in Fig. 4.4 for varying LQ mass. Clearly, the LHeC cross-section is more than both the pair-production, as well as, the single production of LQ associated with a charged lepton at LHC. The higher LQ production cross-section as well as the lower background at LHeC will allow more precise studies for probing LQ and RH neutrinos. Once produced, the LQ can decay into a number of final states, including, a) a quark-lepton pair that gives rise to single charged lepton and a light jet, b) a light jet

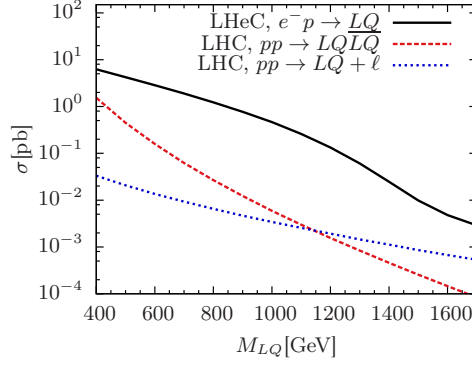


Figure 4.4: Comparison of the cross section for LQ production at LHC and at LHeC. The c.m.energy for LHC is $\sqrt{s} = 13$ TeV. For LHeC, we use electron beam of 150 GeV and proton beam of 7 TeV, respectively. The coupling Y_{de} has been varied as $0.3 \frac{M_{LQ}}{1 \text{ TeV}}$, in agreement with the APV constraints.

Benchmarks	$M_{N_{1,2,3}}$	Y	Z	Process	$\sigma(\text{fb})$
BP1	(150, 1000, 1000)	(0.3, 0, 0)	(0, 0, 0)	ℓj	221
BP2	(150, 1000, 1000)	(0.3, 0, 0)	(1, 0, 0)	$j N_1$	242
BP3	(1000, 1000, 150)	(0.3, 0, 0)	(0, 0, 1)	$\bar{\nu} N_3$	222

Table 4.1: Benchmark parameters and production cross-section for ℓj , $j N_1$ and $\bar{\nu} N_3$ at LHeC with electron and proton beam energy 150 GeV and 7 TeV respectively. LQ mass is considered as 1.1 TeV.

and a heavy neutrino, and c) a top quark accompanied with a heavy neutrino. These heavy neutrinos appearing from the decays of the LQ can again be more easily probed at LHeC through its decay products. Note that, for all these processes, the LQ can also mediate as t -channel mediator. For b) and c), there is also t -channel contribution from W gauge boson mediator, but significantly smaller for the active-sterile mixing $V \lesssim 10^{-2}$. We give numerical estimates in Section. 4.5. However, during computation (in Fig. 4.5 and for the collider analysis), we consider all the contributions together.

For our computations, the LQ mass has been set to 1.1 TeV. We choose three benchmark points, with the three heavy neutrino masses and the LQ couplings, Y_{ii} and Z_{ii} chosen such that they are consistent with all the constraints mentioned in Sec. 4.2, as well as with the neutrino oscillation data [189]. These parameters for the benchmark points have been specified in Table 4.1. The production cross-section for these three processes at LHeC, with electron and proton beam energies of 150 GeV and 7 TeV respectively, are also

shown in Fig. 4.5 as a function of the couplings.

The general expression for the two body decay of a scalar LQ to $\ell_i q$ and $N_i q$ final states are given by,

$$\Gamma(LQ \rightarrow \ell_i q) = \frac{|Y_{ii}|^2}{16\pi M_{LQ}^3} \lambda^{\frac{1}{2}}(M_{LQ}^2, m_{\ell_i}^2, m_q^2) (M_{LQ}^2 - m_{\ell_i}^2 - m_q^2) \quad (4.6)$$

$$\Gamma(LQ \rightarrow N_i q) = \frac{|Z_{ii}|^2}{16\pi M_{LQ}^3} \lambda^{\frac{1}{2}}(M_{LQ}^2, M_{N_i}^2, m_q^2) (M_{LQ}^2 - M_{N_i}^2 - m_q^2) \quad (4.7)$$

In the massless limit of leptons and quarks, the branching ratios are given by,

$$\beta(LQ \rightarrow \ell_i q) = \frac{|Y_{ii}|^2}{\sum_i (|Y_{ii}|^2 + |Z_{ii}|^2)} \quad \text{and} \quad \beta(LQ \rightarrow N_i q) = \frac{|Z_{ii}|^2}{\sum_i (|Y_{ii}|^2 + |Z_{ii}|^2)} \quad (4.8)$$

At an $e^- p$ collider LQs can be resonantly produced, followed by their decay. Hence, we can write the cross section approximately as,

$$\sigma(e^- p \rightarrow \ell_i q \text{ or } N_i q) \approx \sigma(e^- p \rightarrow LQ) \cdot \beta(LQ \rightarrow \ell_i q \text{ or } N_i q). \quad (4.9)$$

As can be seen, from Eq. (4.8), with increasing coupling Z_{11} the branching ratio of $\sigma(e^- p \rightarrow j N_1)$ increases, while $\sigma(e^- p \rightarrow l j)$ decreases. This results in larger cross-section for $\sigma(e^- p \rightarrow j N_1)$ for larger Z_{11} . Cross section for the other channel $e^- p \rightarrow \bar{l} N_3$ is also large for large value of Z_{33} . The values of the cross-section in fb, for three benchmark points are given in the last column of Table. 4.1. As can be seen, the production cross-section at LHeC is fairly large, approximately $\sigma \sim 221 - 242$ fb for the chosen benchmark points. As we will show in the next section, folded with branching ratios of heavy neutrino, top quark, the total cross-section for the different final states will be sizeable.

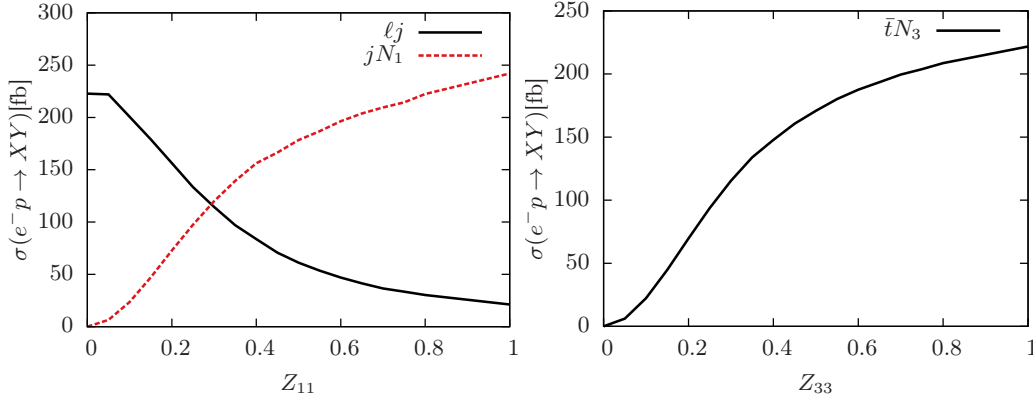


Figure 4.5: Production cross-section for l^j , jN_1 and lN_3 at LHeC with varying coupling Z_{11} . We have considered 150 GeV electron beam colliding with 7 TeV Proton beam. The LQ mass has been set to 1.1 TeV. For l^j, jN_1 , the coupling $Y_{11} = 0.3$, Z_{11} is varying and for lN_3 production, the coupling $Y_{11} = 0.3$, Z_{33} is varying, rest of the Yukawa couplings have been set to zero.

4.4 Collider Analysis

We implemented the model in FeynRules [219], generated the model files for MadGraph5 (v2_5_5) [220] to calculate the parton level cross-section for signals and background. For the collider simulation part, we passed the MadGraph generated parton level events to PYTHIA (v6.4.28) [221], where subsequent decay, initial state radiation, final state radiation and hadronisation have been carried out. The jets are reconstructed by anti- κ_t algorithm [222] implemented in Fastjet package [223] with radius parameter $R = 0.4$. For the analysis of signal and background events we use the following set of basic cuts,

1. Electrons and muons in the final state should have the following transverse momentum and pseudo-rapidity $p_T^\ell > 20 \text{ GeV}$, $|\eta^\ell| < 2.5$.
2. Jets are ordered in p_T , jets should have $p_T^j > 40 \text{ GeV}$ and $|\eta^j| < 2.5$.
3. Photons are counted if $p_T^\gamma > 10 \text{ GeV}$ and $|\eta^\gamma| < 2.5$.
4. Jets should be separated by $\Delta R_{jj} > 0.5$.
5. Leptons should be separated by $\Delta R_{\ell\ell} > 0.2$.
6. Leptons and photons isolation $\Delta R_{\ell\gamma} > 0.2$.
7. Jets and leptons should be separated by $\Delta R_{\ell j} > 0.4$.
8. Hadronic activity within a cone of radius 0.3 around a lepton must be limited to

$\Sigma p_T^{\text{hadron}} < 0.2p_T^\ell$, where p_T^ℓ is the transverse momentum of lepton within the specified cone.

Due to the initial and final state radiations, additional jets will be present in the final states considered. For the inverse seesaw framework, lepton number violation (LNV) is dictated by the parameter μ_X , that is negligibly small. Therefore, the cross-section for LNV di-lepton final states will be suppressed. For the framework where light neutrino masses are generated as a result of cancellation, sizable lepton number violation can however be present. Below, we adopt a conservative approach, and only consider lepton number conserving signatures. A number of signatures, including single lepton and multi-jet, di-lepton associated with multi-jet and missing energy, and multi-lepton associated with missing energy and b -jet have been analysed in the subsequent sections.

4.5 Signals and Background

Signal I : $\ell^- + \mathbf{n}$ -jets ($1 \leq \mathbf{n} \leq 2$)

The single-lepton associated with jet is the easiest channel to probe LQ. LQ, once produced resonantly, can directly decay to a charged-lepton and a jet. Additionally, the t -channel contribution, as shown in Fig. 4.3 will also be present. Therefore, the parton level final state is $\ell^- + \mathbf{n}$ -jets ($\mathbf{n} = 1$). Additional jets will be present due to ISR, FSR. We demand the final state should contain ℓ^- and number of jets $1 \leq \mathbf{n}\text{-jets} \leq 2$. The main backgrounds arise from SM process, such as, $e^-p \rightarrow \ell^-j, \ell^-jj$, that are significantly larger as compared to the signal. From Tab. 4.2, the signal cross-section is 220 fb, while the background cross-section is 3×10^6 fb. We use a number of cuts on different kinematic variables to reduce the background.

In Fig. 4.6 we have shown the transverse momentum of the leading lepton, leading and subleading jet, as well as the invariant mass distribution of the leading jet and leading

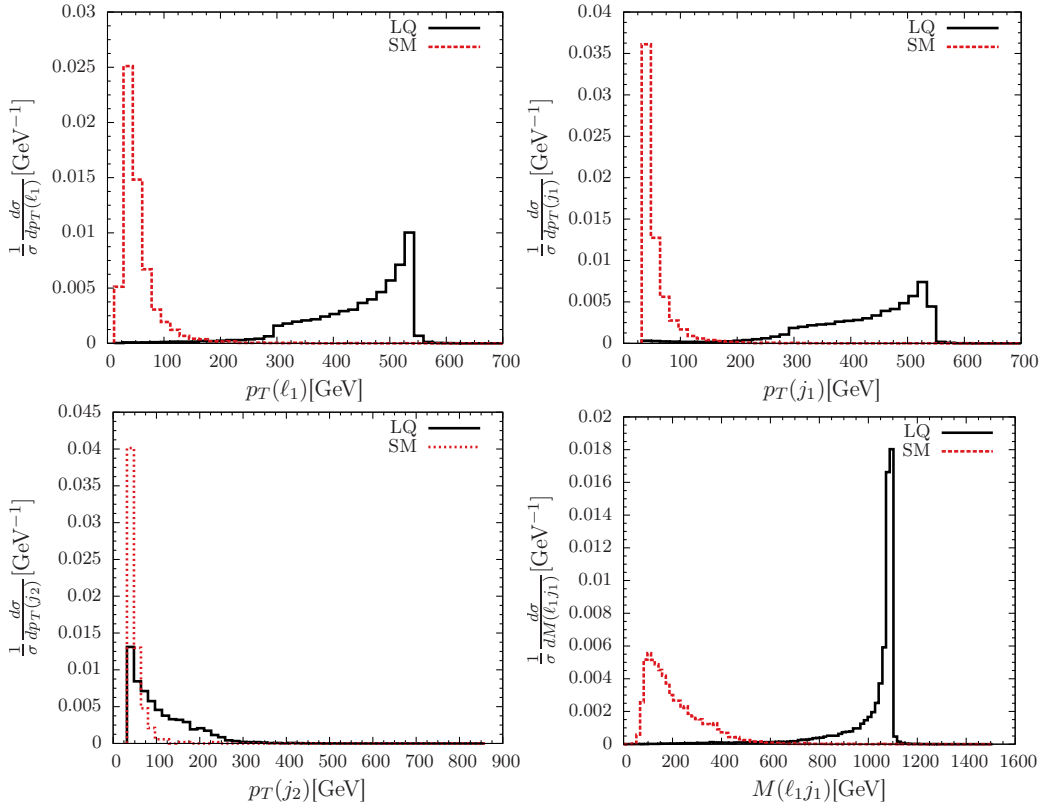


Figure 4.6: Distribution of transverse momentum p_T of leading lepton, leading and sub leading jet p_T distribution, and invariant mass distribution of leading lepton and leading jet for the final state $\ell^- + n$ -jets ($1 \leq n \leq 2$).

lepton, both for the signal and background. Evidently, for a very heavy LQ, a high- p_T cut on leading jet or lepton, and LQ invariant mass-cut will reduce SM background drastically.

In Table. 4.2, we have shown how we can reduce the SM background to zero using p_T cut - $p_T^{\ell^-} (> 400\text{GeV})$ on leading lepton and invariant mass cut - $|M_{LQ} - M_{\ell_1 j_1}| \leq 100\text{GeV}$ simultaneously after using the basic sets of cuts mentioned in the previous section.

Cuts	Final States	Signal (fb)	Background (fb)
No cuts	$\ell^- + n$ -jets ($1 \leq n \leq 2$)	220	2.96×10^6
Basic cuts	$\ell^- + n$ -jets ($1 \leq n \leq 2$)	159	4.08×10^5
Leading lepton p_T cut	+ $p_T^{\ell^-} (> 400\text{GeV})$	118	178
LQ invariant mass cut	+ $ M_{LQ} - M_{\ell_1 j_1} \leq 100\text{GeV}$	101	0

Table 4.2: Signal and Background cross-sections for the final state $\ell^- + n$ -jets ($1 \leq n \leq 2$) after different cuts. BP1 has been used for this final state.

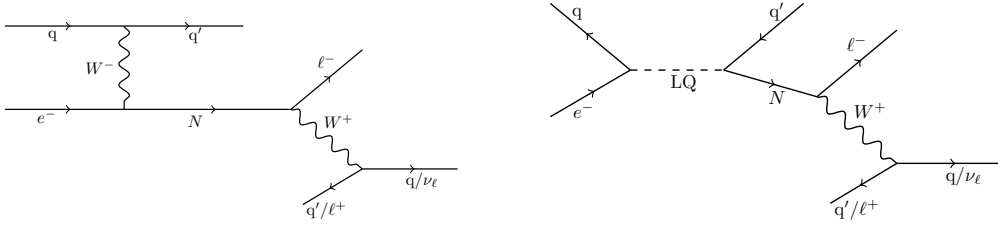


Figure 4.7: Feynman diagram for various final states from $e^- p \rightarrow j N$. For this case, t-channel LQ mediated diagram can also contribute.

Signal II

If the coupling Z_{ij} is non-zero, the LQ can also decay to RH neutrino and a jet, as shown in the right panel of Fig. 4.7. The considered final state, can also arise from the t-channel W exchange diagram as shown in left panel of Fig. 4.7. For active-sterile mixing $V \sim 10^{-2} - 10^{-3}$, the contribution from LQ however dominates. For example, with the BP2, the CC production cross section is ≈ 12.7 fb, while the production cross section from LQ decay is ≈ 240 fb.

The subsequent decays of RH neutrino, followed by hadronic and leptonic decays of gauge bosons gives rise to a number of partonic states, that we list below.

1. $\ell^- + n\text{-jets}$ ($n = 3$) (For hadronic decays of W^+).
2. $\ell^- + \ell^+ + n\text{-jets}$ ($n = 1$) + \cancel{E}_T (For leptonic decays of W^+).

$\ell^- + n\text{-jets}$ ($n \geq 3$)

For the case of the hadronic decays of the charged gauge boson, we demand a charged lepton and at least three jets as final state. The invariant mass of the three jets and the charged lepton must be equal to that of the mass of the LQ. Hence a cut on the invariant mass distribution allows the separation of the signal from the background. For the background we generate $e^- p \rightarrow \ell^- + n\text{-jets}$ upto $n = 3$. The distribution is given in the top left panel of Fig. 4.8. Additionally, the leading jet that is directly generated from LQ

decay has a very high transverse momentum (see Fig. 4.8). Therefore, a large cut on the transverse momentum of the leading jet reduces the background. As can be seen from Table. 4.3, the large p_T cut on the leading jet itself reduces the background by $\mathcal{O}(10^4)$. Further reduction in background is achieved though a cut on the invariant mass distribution of the heavy neutrino. Stringent cuts, such as, the cuts on the invariant mass of the LQ and the heavy neutrino make the background negligibly small.

Cuts	Final States	Signal (fb)	Background (fb)
No cuts	$\ell^- + n\text{-jets}(n \geq 3)$	24.8	2.99×10^6
Basic cuts	$\ell^- + n\text{-jets}(n \geq 3)$	7.65	2.9×10^3
Leading Jet p_T cut	$+p_T^{j_1} (> 200\text{GeV})$	6.56	180
LQ invariant mass cut	$+ M_{LQ} - M_{\ell_1 j_1 j_2 j_3} \leq 100\text{GeV}$	3.65	60
N invariant mass cut	$+ M_{N_1} - M_{\ell_1 j_a j_b} \leq 30\text{GeV}$	3.08	0

Table 4.3: Signal and Background cross-sections for the final state $\ell^- + n\text{-jets} (n \geq 3)$ with cuts. BP2 has been used for this final state.

$\ell^- \ell^+ + n\text{-jets} (n \geq 1) + \cancel{E}_T$

For the scenario, when charged gauge boson produced in the decay of RH neutrino, decays leptonically, the signal will have 2 opposite sign charged leptons, jets (one or more) and missing energy. The dominant SM background comes from the processes like $e^- p \rightarrow \ell^- \ell^+ j \nu_\ell$ and $e^- p \rightarrow \ell^- \ell^+ j j \nu_\ell$. The reduction of the background in this case is achieved by applying proper cuts on the missing energy, transverse momentum of leading jet and effective mass M_{EFF} . The M_{EFF} variable is defined as,

$$M_{EFF} = \sum_i p_{T_i}^j + \sum_i p_{T_i}^\ell + \cancel{E}_T,$$

where $p_{T_i}^j, p_{T_i}^\ell$ are the transverse momentum of the jet and lepton, and \cancel{E}_T is the missing transverse energy. We expect a hard distribution for M_{EFF} , since the p_T of the lepton and jets coming mostly from resonantly produced LQ (as the t-channel contribution is small) is significantly large. The peak of the M_{EFF} shifts towards higher values with increasing LQ mass.

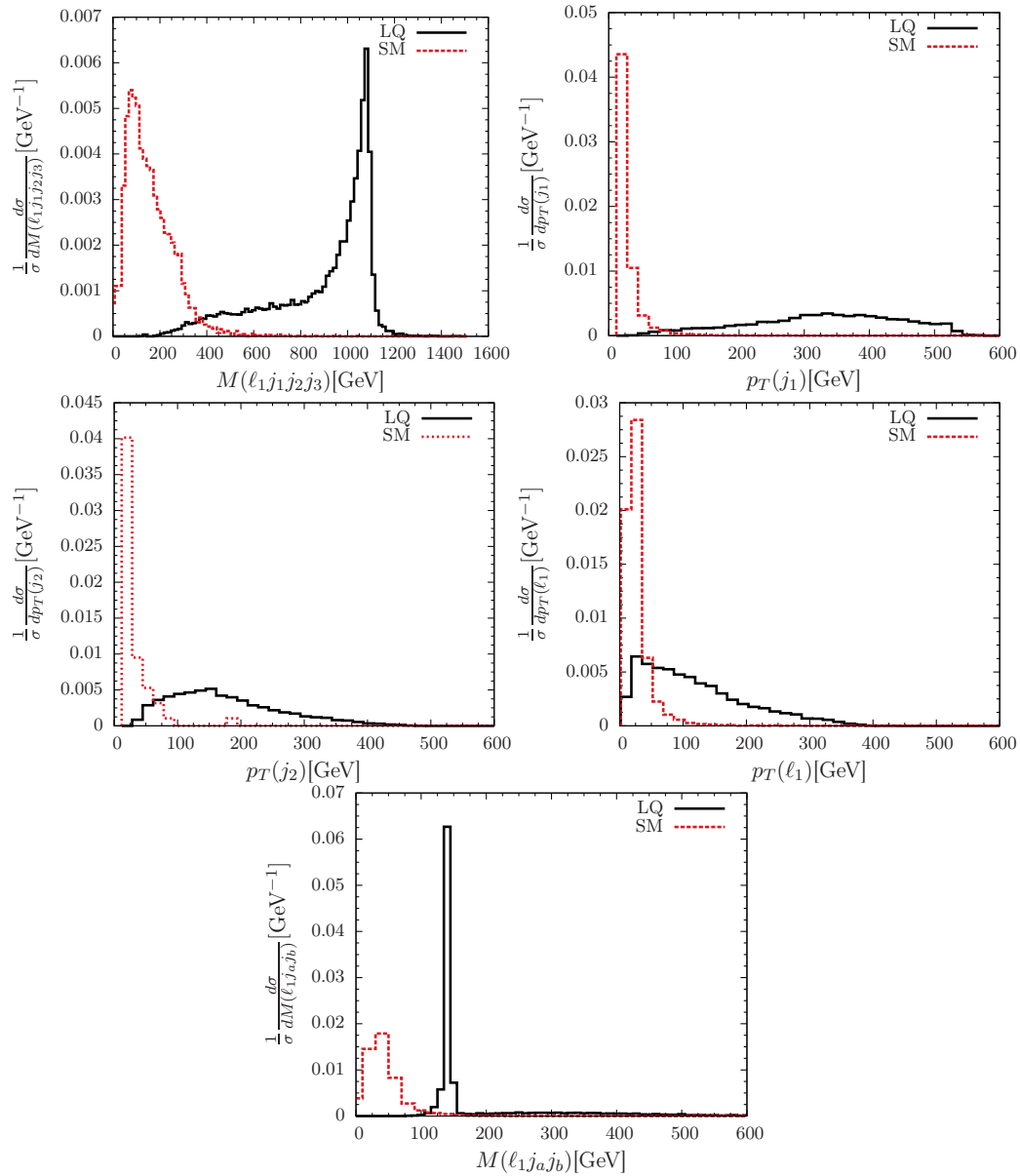


Figure 4.8: Invariant Mass distribution of LQ, p_T distribution of leading, sub leading jet, and of leading lepton. We also show the invariant mass distribution of N for the final state $\ell^- + n\text{-jets}$ ($n \geq 3$).

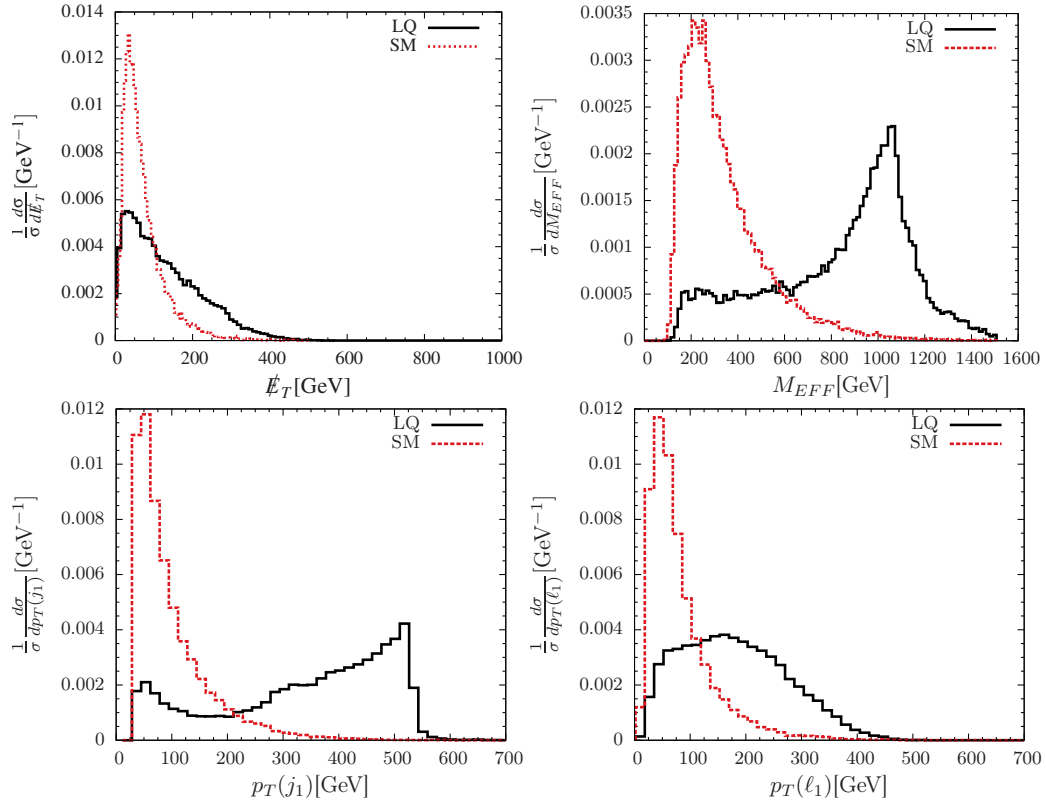


Figure 4.9: Missing transverse energy distribution, M_{EFF} distribution, p_T distribution of leading jet, and leading lepton for the final state $\ell^-\ell^+ + n\text{-jets} (n \geq 1) + \cancel{E}_T$.

We have shown in Fig. 4.9 the missing energy \cancel{E}_T , M_{EFF} , leading jet and leading lepton p_T distributions. The effect of different cuts on the signal and background cross-sections are given in Table. 4.4.

Cuts	Final States	Signal (fb)	Background (fb)
No cuts	$\ell^-\ell^+ + n\text{-jets} (n \geq 1) + \cancel{E}_T$	11.2	5.22×10^2
Basic cuts	$\ell^-\ell^+ + n\text{-jets} (n \geq 1) + \cancel{E}_T$	7.84	258
Missing energy cut	$\ell^-\ell^+ + n\text{-jets} (n \geq 1) + \cancel{E}_T (> 100\text{GeV})$	4.26	57.5
Leading Jet p_T cut	$+p_T^{j_1} (> 300\text{GeV})$	3.24	3.73
M_{EFF} cuts	$+M_{EFF} (> 500\text{GeV})$	2.88	2.54

Table 4.4: Signal and Background cross-section after various cuts for the final state $\ell^-\ell^+ + n\text{-jets} (n \geq 1) + \cancel{E}_T$. BP2 has been used for this final state.

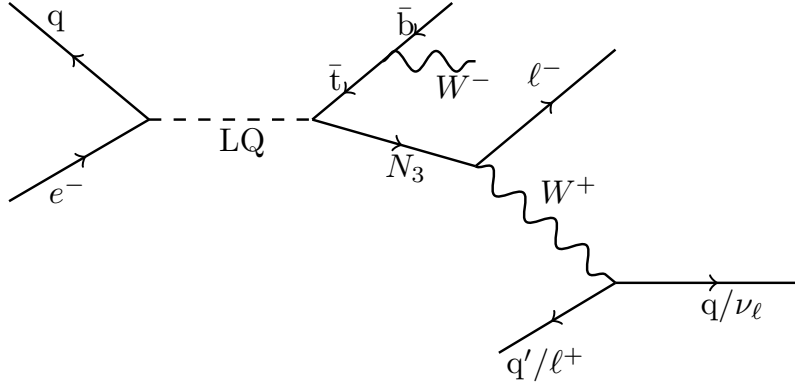


Figure 4.10: Feynman diagram for various final states from $e^- p \rightarrow \bar{t} N_3$. For this case also, the t-channel mediated diagram with gauge boson and LQ will contribute.

Signal III

For the LQ mass more than $M_N + M_t$, it can further decay to $\bar{t} N_3$, that enables a final state with large lepton or large jet multiplicity. The large lepton multiplicity is promising due to suppressed SM background.

For the $\bar{t} N_3$ production channel, considering subsequent decays of N_3 and \bar{t} , where N_3 is assumed to decay to $\tau^\pm W^\mp$, following final states at parton-level are possible:

- (1) $\bar{b} \ell^- \tau^- \ell^+ + \cancel{E}_T$ (For leptonic decays of both the W bosons, $W^- \rightarrow \ell^- \nu$, $W^+ \rightarrow \ell^+ \nu$),
- (2) $\bar{b} \ell^- \tau^- + n\text{-jets (n = 2)} + \cancel{E}_T$ (For the W boson decays, $W^- \rightarrow \ell^- \nu$ and $W^+ \rightarrow jj$),
- (3) $\bar{b} \tau^- \ell^+ + n\text{-jets (n = 2)} + \cancel{E}_T$ (For the W boson decays, $W^- \rightarrow jj$ and $W^+ \rightarrow \ell^+ \nu$),
- (4) $\bar{b} \tau^- + n\text{-jets (n = 4)}$ (For the W boson decays, $W^- \rightarrow jj$ and $W^+ \rightarrow jj$).

We do not consider the last final states in our study because of very small cross-section and very large SM background due to large jet multiplicity.

$$\bar{b} \ell^- \tau^- \ell^+ + \cancel{E}_T$$

For the final states involving τ and b , tagging can reduce the SM background significantly. We consider the p_T for the b and τ jets, as $p_T > 40$ GeV. In this work, we adopt a minimalistic approach and consider a flat 75% efficiency for b -tagging and 60% efficiency for τ -tagging. Similar to the previous case, the M_{EFF} distribution is hard due to the large

Cuts	Final States	Signal (fb)	Background (fb)
No cuts	$\bar{b}\ell^-\tau^-\ell^+ + \cancel{E}_T$	1.57	0.323
Basic cuts	$\bar{b}\ell^-\tau^-\ell^+ + \cancel{E}_T$	0.83	7.51×10^{-3}
Missing energy cut	$\bar{b}\ell^-\tau^-\ell^+ + \cancel{E}_T(> 100\text{GeV})$	0.502	4.46×10^{-3}
Leading Jet p_T cut	$+p_T^{j_1}(> 100\text{GeV})$	0.476	2.16×10^{-3}
M_{EFF} cuts, b and τ tagging	$+M_{EFF}(> 500\text{GeV})$	0.21	7.7×10^{-4}

Table 4.5: Signal and Background cross-section after various cuts for the final state $\bar{b}\ell^-\tau^-\ell^+ + \cancel{E}_T$. BP3 has been used for this final state.

Cuts	Final States	Signal (fb)	Background (fb)
No cuts	$\bar{b}\ell^-\tau^- + \text{n-jets} (n \geq 2) + \cancel{E}_T$	3.54	0.729
Basic cuts	$\bar{b}\ell^-\tau^- + \text{n-jets} (n \geq 2) + \cancel{E}_T$	1.457	2.18×10^{-2}
Missing energy cut	$\bar{b}\ell^-\tau^- + \text{n-jets} (n \geq 2) + \cancel{E}_T(> 100\text{GeV})$	1.277	1.344×10^{-2}
Leading Jet p_T cut	$+p_T^{j_1}(> 100\text{GeV})$	1.226	7.65×10^{-3}
M_{EFF} cuts, b and τ tagging	$+M_{EFF}(> 500\text{GeV})$	0.522	2.4×10^{-3}

Table 4.6: Signal and Background cross-section after various cuts for the final state $\bar{b}\ell^-\tau^- + \text{n-jets} (n \geq 2) + \cancel{E}_T$. BP3 has been used for this final state.

missing energy and large transverse momenta of final state particles. For this signal, the most dominant SM background comes from the process $\bar{t}\ell^-W^+$, $\bar{t}Z\nu$ and $\bar{t}h\nu$ with $\bar{t} \rightarrow \bar{b}\tau^-\nu$, $W^+ \rightarrow \ell^+\nu$, $Z \rightarrow \ell^+\ell^-$, and $h \rightarrow \ell^+\ell^-$. After applying the basic cuts only, SM background drops significantly. In addition, we use missing energy \cancel{E}_T , leading jet p_T and M_{EFF} distribution to further reduce the SM background.

$$\bar{b}\ell^-\tau^- + \text{n-jets} (n \geq 2) + \cancel{E}_T$$

For this case, due to large jet multiplicity, SM background is greater than the previous signal and the background mainly comes from the process $\bar{t}\ell^-W^+$. However, using missing energy \cancel{E}_T , cuts on leading jet p_T and M_{EFF} distribution, the SM background can be reduced significantly.

$$\bar{b}\ell^+\tau^- + \text{n-jets} (n \geq 2) + \cancel{E}_T$$

For this final state, SM background is actually negligibly small at e^-p collider for the beam energies considered.

Cuts	Final States	Signal (fb)	Background (fb)
No cuts	$\bar{b}\ell^+\tau^- + \text{n-jets } (n \geq 2) + \cancel{E}_T$	4.07	0
Basic cuts, b and τ tagging	$\bar{b}\ell^+\tau^- + \text{n-jets } (n \geq 2) + \cancel{E}_T$	1.83	0

Table 4.7: Signal and Background cross-section after various cuts for the final state $\bar{b}\ell^+\tau^- + \text{n-jets } (n \geq 2) + \cancel{E}_T$. BP3 has been used for this final state.

Final States	1.1 TeV	1.2 TeV	1.3 TeV	1.4 TeV	1.5 TeV	1.6 TeV	1.7 TeV
$\ell^- + \text{n-jets } (1 \leq n \leq 2)$	101	47.53	18.37	6.148	2.04	0.82	0.42
$\ell^- + \text{n-jets } (n \geq 3)$	3.08	1.98	0.83	0.47	0.322	0.24	0.18
$\bar{b}\ell^+\tau^- + \text{n-jets } (n \geq 2) + \cancel{E}_T$	1.83	0.74	0.29	0.12	0.06	0.03	0.02

Table 4.8: Cross-sections (in fb) after all the cuts as a function of LQ mass.

4.6 Signal Strength for Higher LQ Mass

Bound on LQs parameter space is expected to improve in future with increasing luminosity at LHC. Hence, we repeat our study for higher LQ masses. Though for higher LQ mass, we can allow for large yukawa coupling, we use the same coupling as for 1.1 TeV LQ mass to compare our result for different LQ masses. Using the same set of cuts for each final states as we did for LQ mass 1.1 TeV, we have calculated the cross-section for LQ mass of 1.2, 1.3, ... upto 1.7 TeV. The partonic cross-sections and the effect of different cuts is shown in Table. 4.8 and 4.9.

Zero Background Case

First, we consider only final states for which the SM background is zero or can be reduced to zero using invariant mass cut of LQ and RH neutrinos. The SM background is practically zero, for final state, $\bar{b}\ell^+\tau^- + \text{n-jets } (n \geq 2) + \cancel{E}_T$. For the final state, $\ell^- + \text{n-jets } (1 \leq n \leq 2)$, using p_T^ℓ cut and LQ invariant mass cut (for corresponding LQ mass), the SM background can be reduced to zero.

Similarly, for the final state, $\ell^- + \text{n-jets } (n \geq 3)$, selection cut on p_T^j , along with on LQ invariant mass, and invariant mass of RH neutrino can make the SM background negligibly small. The results are given in Table. 4.8. We have also shown the cross section

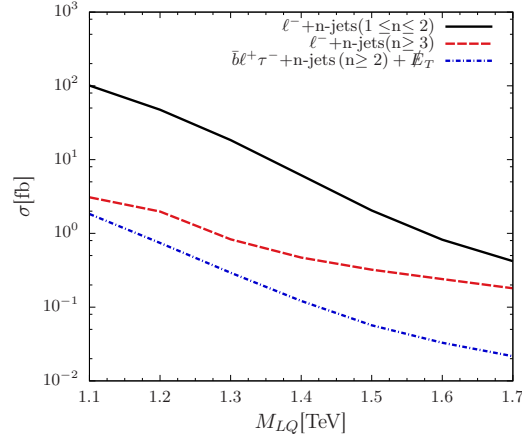


Figure 4.11: Signal cross-section as a function of LQ mass for different final states.

as a function of LQ masses in Fig. 4.11. As can be seen, the cross-section for the $\ell^- + n\text{-jets}(1 \leq n \leq 2)$ channel is the largest, varies $10^2 - 0.42$ fb for a wide range of LQ mass. With 100 fb^{-1} luminosity, this predicts 10^4 number of events at LHeC. The other channel with jet multiplicity ($n \geq 3$) also offers a large cross-section, and large number of events $\mathcal{O}(10^2)$.

Non-Zero Background Case

For the final states, $\ell^- + n\text{-jets}(1 \leq n \leq 2)$ and $\ell^- + n\text{-jets}(n \geq 3)$, the SM background is non zero if we do not use the invariant mass of LQ and RH neutrino. Since, the LQ and RH neutrino masses are unknown, we do not implement the mass cut, rather in this section show the cross-sections with a very generic sets of cuts. Assuming LQ mass to be more than 1 TeV, all the other cuts which we considered can be easily applied. For the above two final states we applied cuts only on p_T^ℓ and p_T^j . For final states, $\ell^- \ell^+ + n\text{-jets}(n \geq 1) + \cancel{E}_T$, $\bar{b}\ell^- \tau^- \ell^+ + \cancel{E}_T$ and $\bar{b}\ell^- \tau^- + n\text{-jets}(n \geq 2) + \cancel{E}_T$ we used the same cuts as in Tables. 4.4, 4.5 and 4.6 respectively.

We show the signal cross section and statistical significance with integrated luminosity of 100 fb^{-1} in Fig. 4.12. We also show the required luminosity to achieve 3σ and 5σ statistical significance in Fig. 4.13. The statistical significance has been calculated using

Final States	1.1 TeV	1.2 TeV	1.3 TeV	1.4 TeV	1.5 TeV	1.6 TeV	1.7 TeV
$\ell^- + n\text{-jets}(1 \leq n \leq 2)$	118	57	23	8	2.8	1.16	0.62
$\ell^- + n\text{-jets}(n \geq 3)$	6.56	2.36	1	0.5	0.32	0.23	0.18
$\ell^- \ell^+ + n\text{-jets}(n \geq 1) + \cancel{E}_T$	2.88	1.38	0.57	0.23	0.102	0.057	0.039
$\bar{b} \ell^- \tau^- \ell^+ + \cancel{E}_T$	0.21	0.08	0.03	0.012	0.007	0.003	0.0018
$\bar{b} \ell^- \tau^- + n\text{-jets}(n \geq 2) + \cancel{E}_T$	0.522	0.175	0.063	0.025	0.013	0.008	0.006

Table 4.9: Cross-sections in fb, after all the cuts (except invariant LQ and right handed neutrinos mass cut) as a function of LQ mass. Backgrounds are same as for 1.1 TeV, as the beam energies are same.

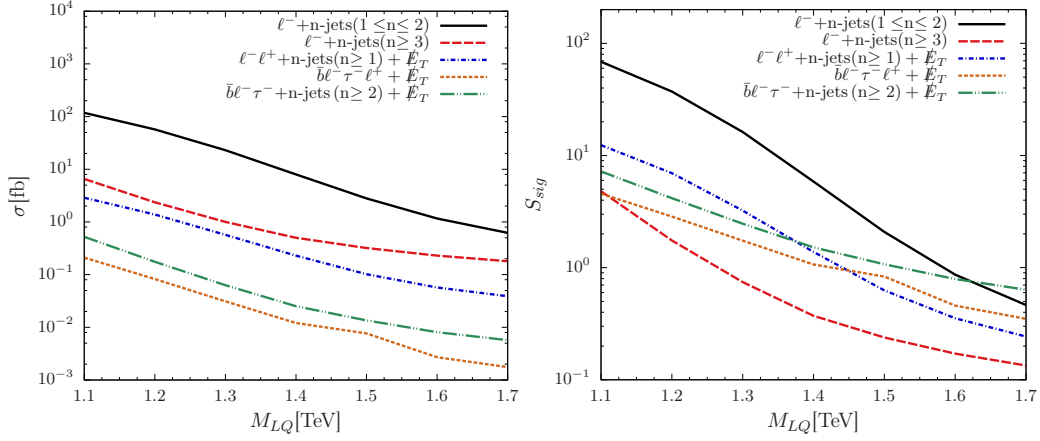


Figure 4.12: Left panel: The signal cross-section as a function of LQ mass for different final states. Right panel: the significance with 100 fb^{-1} luminosity.

the following expression:

$$S_{sig} = \frac{S}{\sqrt{S+B}}, \quad (4.10)$$

where, S and B denote the number of signal and background events, respectively.

4.7 Results

We discuss the discovery prospect of LQ in the mass range 1.1-1.7 TeV at LHeC. We have shown the significance for different final states with integrated luminosity 100 fb^{-1} and 1000 fb^{-1} for each LQ mass in the range 1.1-1.7 TeV in Table.4.10. The channel $\ell^- + n\text{-jets}(1 \leq n \leq 2)$ is the most promising. For the final states $\ell^- + n\text{-jets}(1 \leq n \leq 2)$, even with integrated luminosity 2 fb^{-1} , the statistical significance is 9.69σ for the LQ of mass 1.1 TeV.

Final States	1.1 TeV		1.2 TeV		1.3 TeV		1.4 TeV		1.5 TeV		1.6 TeV		1.7 TeV	
$\ell^- + n\text{-jets}(1 \leq n \leq 2)$	68	217	37	117	16	51	6	19	2	7	0.87	2.74	0.46	1.46
$\ell^- + n\text{-jets}(n \geq 3)$	4.8	15	1.74	5.5	0.74	2.35	0.37	1.17	0.24	0.75	0.23	0.54	0.13	0.42
$\ell^- \ell^+ + n\text{-jets}(n \geq 1) + \cancel{E}_T$	12	39	7	22	3.2	10	1.4	4.4	0.62	1.98	0.35	1.12	0.24	0.76
$\bar{b} \ell^- \tau^- \ell^+ + \cancel{E}_T$	4.5	14.4	2.8	8.9	1.7	5.4	1.06	3.3	0.8	2.5	0.5	1.5	0.35	1.12
$\bar{b} \ell^- \tau^- + n\text{-jets}(n \geq 2) + \cancel{E}_T$	7.2	22	4.15	13	2.46	7.8	1.5	4.77	1.04	3.3	0.78	2.48	0.65	2.1

Table 4.10: Significance for different final states with integrated luminosity $\mathcal{L} = 100 \text{ fb}^{-1}$ (1st column corresponding to each LQ mass) and $\mathcal{L} = 1000 \text{ fb}^{-1}$ (2nd column corresponding to each LQ mass) respectively for the LQ mass range [1.1-1.7]TeV.

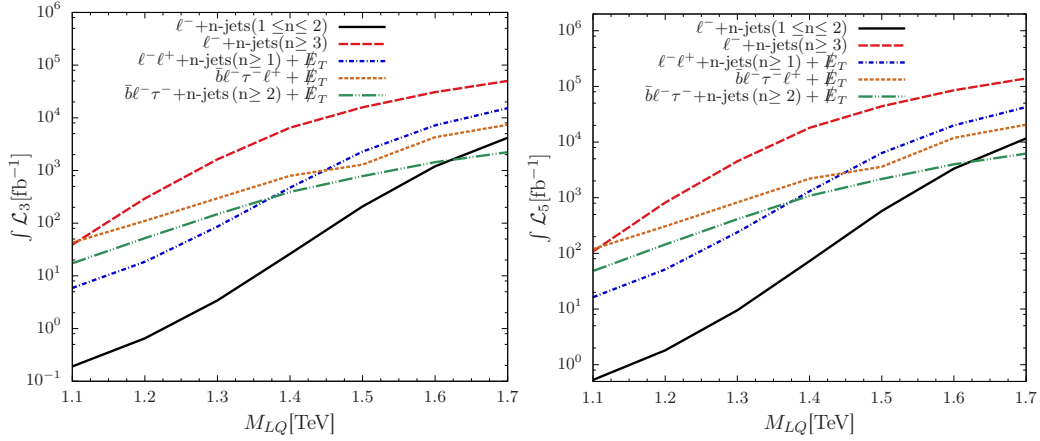


Figure 4.13: The required luminosity to achieve 3σ (left panel) and 5σ (right panel) for different final states.

For final states $\ell^- + n\text{-jets}(n \geq 3)$ and $\ell^- \ell^+ + n\text{-jets}(n \geq 1) + \cancel{E}_T$, statistical significance drastically decreases with higher LQ masses. Similarly for the final states $\bar{b} \ell^- \tau^- \ell^+ + \cancel{E}_T$ and $\bar{b} \ell^- \tau^- + n\text{-jets}(n \geq 2) + \cancel{E}_T$, in spite of small SM background, as the signal cross section is itself small for higher LQ masses, its difficult to observe these final state for higher LQ masses.

4.8 Summary

We study the discovery prospect of \tilde{R}_2 class of LQ model at LHeC. The model contains two LQs with $Q = \frac{2}{3}$, and $Q = -\frac{1}{3}$. LQ with $Q = \frac{2}{3}$ can be copiously produced at LHeC, due to its interaction with the electron and down type quark. We study the production and its decay to different final states, including a lepton and a jet, a jet and a RH neutrino, and RH neutrino and a top quark. The typical production cross-section for

$e^- p \rightarrow lj, jN_1, \bar{l}N_3$ are 221, 242, 222 fb for $M_{LQ} = 1.1$ TeV, $M_{N_{1,3}} = 150$ GeV, and the couplings $Y_{11} = 0.3, Z_{33} = 1$. The produced RH neutrino further decays and give a plethora of model signatures. For the RH neutrinos, we adopt a model independent framework, and a large active-sterile mixing to ensure its decay within the detector. For the LQs, the higher production cross-section as well as the lower backgrounds at LHeC result in a much higher statistical significance for few of the signals studied.

We have analysed a number of final states, including $\ell^- + n$ -jets ($1 \leq n \leq 2$), $\ell^\pm + n$ -jets ($n \geq 3$), $\ell^\pm \ell^\mp + n$ -jets ($n \geq 1$) + \cancel{E}_T , $\bar{b}\ell^- \tau^- \ell^+ + \cancel{E}_T$, $\bar{b}\ell^- \tau^- + n$ -jets ($n \geq 2$) + \cancel{E}_T , $\bar{b}\ell^+ \tau^- + n$ -jets ($n \geq 2$) + \cancel{E}_T . Among these, the model signature $\ell^- + n$ -jets ($1 \leq n \leq 2$) arises due to the direct decay of LQ to a lepton and a jet. All the other final states arise due to the decay of LQ to a RH neutrino and a light jet, or to a RH neutrino and top quark, with successive decays of RH neutrino, and t quark into SM states.

We find that, among all the above mentioned final states, $\ell^- + n$ -jets ($1 \leq n \leq 2$) has the highest discovery prospect even after giving a generic set of cuts. A LQ of mass upto 1.4 TeV in this channel can be discovered at more than 5σ C.L. with 100 fb^{-1} of data. The LQs will also result in the enhancement of the RH neutrino production in association with a light jet, or with top quark. If at LHeC the electron beam is polarized, the right handed neutrino- light jet production cross-section can substantially increase [189, 190]. We find that among all the final states $\ell^- + n$ -jets ($n \geq 3$), and $\bar{b}\ell^+ \tau^- + n$ -jets ($n \geq 2$) + \cancel{E}_T are the most optimal, after implementing the selection cuts judiciously. With 100 fb^{-1} integrated luminosity, for LQ mass 1.1 TeV, the expected number of events for the final states $\ell^- + n$ -jets ($n \geq 3$), and $\bar{b}\ell^+ \tau^- + n$ -jets ($n \geq 2$) + \cancel{E}_T are 10^4 and 180 respectively.

5 Probing right handed neutrinos using fat jet signatures

The inclusion of heavy neutral leptons (right-handed neutrinos) to the Standard Model (SM) particle content is one of the best motivated ways to account for the observed neutrino masses and flavor mixing. The modification of the charged and neutral currents from active-sterile mixing of the neutral leptons can provide novel signatures which can be tested at the future collider experiments. In this chapter, we explore the discovery prospect of a very heavy right handed neutrino to probe such extensions at the future collider experiments like Large Hadron electron Collider (LHeC) and linear collider. We consider the production of the heavy neutrino via the t and s -channel processes and its subsequent decays into the semi-leptonic final states. We specifically focus on the scenario where the gauge boson produced from heavy neutrino decay is highly boosted, leading to a fat-jet. We study the bounds on the sterile neutrino properties from several past experiments and compare with our results.

1. We study the prospect of discovery of RHNs at LHeC considering the boosted objects for the first time. In the LHeC we concentrate on the lepton number violating (LNV) and lepton number conserving (LNC) channels to produce the RHN in association with a jet (j_1). Hence the RHN will decay into the dominant ℓW and the W will decay into a pair of jets. The daughter W coming from the heavy RHN will be boosted and its hadronic decay products, jets, of the W will be collimated such that they can form a fat jet (J). Hence a

signal sample of $\ell + j_1 + J$ can be studied thoroughly at this collider. In this process people have mostly studied the lepton number conserving channel where as the lepton number violating will be potentially background free. However, for clarity we study the combined channel and the corresponding SM backgrounds. We consider two scenarios at the LHeC where the electron and proton beams will have 60 GeV and 7 TeV energies where the center of mass energy becomes $\sqrt{s} = 1.3$ TeV. We have also considered another center of mass energy at the $\sqrt{s} = 1.8$ TeV where the proton beam energy is raised up to the 13.5 TeV. For both of the colliders we consider the luminosity at 1 ab^{-1} . Here the RHN is a first generation RHN (N_1) and ℓ is electron (e). Finally we study up to 3 ab^{-1} luminosity.

2. At the linear collider the production of the RHNs is occurring from the s - and t - channel processes in association with a SM light neutrino (ν). We consider the linear collider at two different center of mass energies, such as $\sqrt{s} = 1$ TeV and $\sqrt{s} = 3$ TeV which can probe up to a high mass of the RHNs such as 900 GeV (at the 1 TeV linear collider) and 2.9 TeV (at the 3 TeV linear collider) due to the almost constant cross section for the $N\nu$ production. For both of the center of mass energies we consider 1 ab^{-1} luminosity. Finally we study up to 3 (5) ab^{-1} luminosity for the 1 (3) TeV linear collider.

3. At this mass scale, the RHNs will be produced at rest, however, the daughter particles can be sufficiently boosted. We consider $N \rightarrow \ell W, W \rightarrow jj$ and $N \rightarrow h\nu, h \rightarrow b\bar{b}$ modes at the linear collider where h is the SM Higgs boson. If the RHN is sufficiently heavy, such the, $M_N \geq 400$ GeV, the W and h can be boosted because M_W and $M_h \ll \frac{M_N}{2}$. As a result W and h will produce a fat jet (J) and a fat b jet (J_b) respectively. Therefore the signal will be $\ell + J$ plus missing momentum and J_b plus missing momentum in the W and h modes respectively at the linear collider. Therefore studying the signals and the backgrounds for each process we put the bounds in the mass- mixing plane of the RHNs.

4. We want to comment that studying $e^-e^+ \rightarrow N_2\nu_\mu/N_3\nu_\tau$ mode in the Z mediated s -channel will be interesting where $N_2(N_3)$ will be the second (third) generation RHN. Studying the signal events and the corresponding SM backgrounds one can also calculate the limits on the mixing angles involved in these processes. Such a process will be proportional to $|V_{\mu N}|^2$ ($|V_{\tau N}|^2$). In these processes the signal will be $\mu(\tau) + jj$ plus missing momentum followed by the decay of $N_2(N_3) \rightarrow \mu jj(\tau jj)$. One can also calculate the bounds on the mass-mixing plane for different significances. A boosted analysis could be interesting, however, a non-boosted study might be more useful as the cross-section goes down with the rise in collider energy in these processes. Such signals can also be studied if the RHNs can decay through the LFV modes, such as $e^-e^+ \rightarrow N\nu_e, N \rightarrow \mu W, W \rightarrow jj$, however, $\mu \rightarrow e\gamma$ process will make this process highly constrained due to the strong limit $Br(\mu^+ \rightarrow e^+\gamma) < 4.2 \times 10^{-13}$ at the 90% C. L. [224]. The corresponding limits on τ are weaker [225, 226]. Such final states have been studied in [227] for $M_N = 150$ GeV, a high mass test with using boosted object will be interesting in future. A comprehensive LHC study has been performed in [228].

5. The RHN produced at the linear collider may decay in to another interesting mode, namely, $N \rightarrow Z\nu, Z \rightarrow b\bar{b}$. Which can be another interesting channel where boosted objects can be stated. However, precision measurements at the Z -boson resonance using electron-positron colliding beams at LEP experiment strongly constrains Z boson current, and hence, $Zb\bar{b}$ coupling. This channel also suffers from larger QCD background compared to the leptonic decay of Z boson, and hence, leptonic decay of Z boson has better discovery prospect for this particular mode of RHN decay. On the other hand, SM Higgs, h , mostly decays ($\sim 60\%$) to $b\bar{b}$ due to large $hb\bar{b}$ coupling. Due to this, we focus on the Higgs decay mode of RHN, $N \rightarrow h\nu, h \rightarrow b\bar{b}$ to study the fat jet signature. We mainly focus on the first two items.

This chapter is organised as follows. in Sec. 5.1, we calculate the production cross sections of heavy neutrino at different colliders. In Sec.5.2 we discuss the complete collider

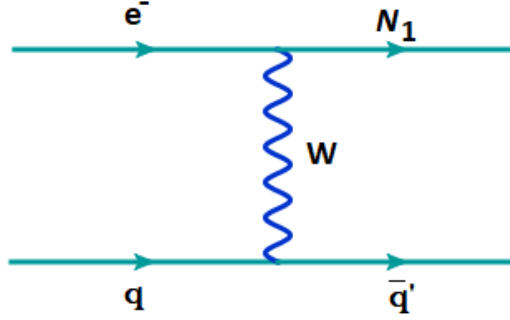


Figure 5.1: Production process, $ep \rightarrow N_1 j_1$, of the RHN at the LHeC through a t channel W boson exchange.

study. In Sec. 5.3 we calculate the bounds on the mixing angles and compare them with the existing results.

5.1 Heavy neutrino production

5.1.1 Production cross section at LHeC

The LHeC can produce the RHN in the process $e p \rightarrow N_1 j_1$ through the t -channel exchanging the W boson. In this case the first generation RHN (N_1) will be produced. The corresponding Feynman diagram is given in Fig. 5.1. The total differential production cross section for this process is calculated as

$$\frac{d\hat{\sigma}_{LHeC}}{d\cos\theta} = |V_{eN_1}|^2 \frac{3.89 \times 10^8}{32\pi} 3 \times \frac{1}{3} \left(\frac{1}{2}\right)^2 \left(\frac{M_{inv}^2 - M_N^2}{M_N^2}\right) \times \frac{256 C_\ell^2 C_q^2 \left(\frac{M_{inv}^2 - M_N^2}{4}\right)}{\left[M_N^2 - 2\left\{\frac{M_{inv}^2}{4}(1 - \cos\theta)\right\} + \frac{M_{inv}^2}{4}(1 + \cos\theta)\right]^2 + \Gamma_W^2 M_W^2} \quad (5.1)$$

where $\sqrt{\hat{s}} = M_{inv}$ and $C_\ell = C_q = \frac{g}{2^{\frac{3}{2}}}$. Performing the integration over $\cos\theta$ between $[-1, 1]$ we find the cross section as $\hat{\sigma}_{LHeC}$ and finally convoluting the PDF (CTEQ5M)

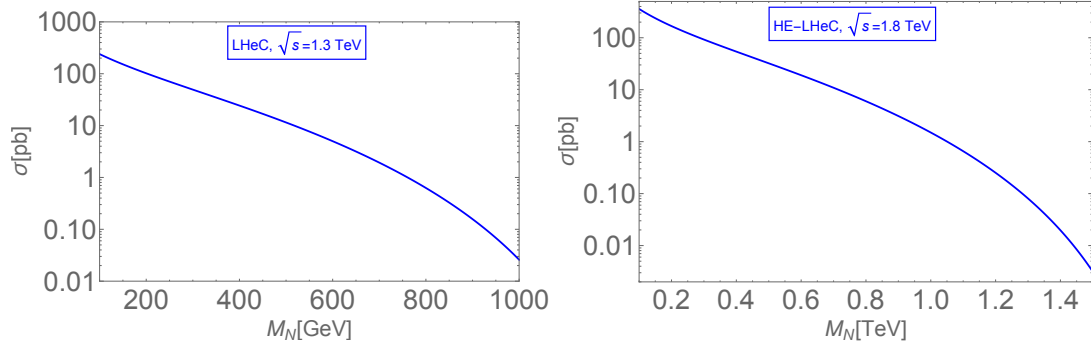


Figure 5.2: RHN production cross section at the LHeC considering $e p \rightarrow N_1 j$ process for the $e p$ collider at $\sqrt{s} = 1.3$ TeV (LHeC, left panel) and $\sqrt{s} = 1.8$ TeV (HE-LHeC, right panel).



Figure 5.3: RHN production processes at the linear collider. The left panel is the dominant t channel process and the right panel is s channel process to produce the $e^+e^- \rightarrow N_1\nu_1$. To produce $N_2\nu_2$ and $N_3\nu_3$, the Z mediated s channel process will act.

[229] we get the total cross section as

$$\sigma = \sum_i \int_{\frac{M^2}{E_{CM}^2}}^1 dx q_i(x, \sqrt{x}E_{CM}) \hat{\sigma}_{LHeC}(\sqrt{x}E_{CM}) \quad (5.2)$$

where E_{CM} is the center of mass energy of the LHeC and i runs over the quark flavors. For different center of mass energies E will be different. In Fig. 5.2 we plot the total production cross sections of N_1 at the three different collider energies such as $\sqrt{s} = 1.3$ TeV (LHeC) and $\sqrt{s} = 1.8$ TeV (High Energy LHeC (HE-LHeC)) respectively. The cross section in Fig. 5.2 is normalized by the square of the mixing $|V_{eN_1}|^2$ to correspond the maximum value for a fixed M_N .

5.1.2 Production cross section at linear collider

The linear collider can produce the heavy neutrino in the process $e^+e^- \rightarrow \bar{\nu}_1 N_1$ through t and s -channels exchanging the W and Z bosons, respectively. The corresponding Feynman diagrams are given in Fig. 5.3. The total differential production cross section for this process is calculated as

$$\begin{aligned} \frac{d\sigma_{ILC}}{d\cos\theta} &= |V_{eN_1}|^2 (3.89 \times 10^8 \text{ pb}) \times \frac{\beta}{32\pi} \frac{s + M_N^2}{s} \left(\frac{1}{2}\right)^2 \\ &\times \left[\frac{16C_1^2 C_2^2 (s^2 - M_N^4) (1 + \cos\theta)(1 + \beta \cos\theta)}{(M_N^2 - \frac{s - M_N^2}{2}(1 - \beta \cos\theta) - M_W^2)^2 + M_W^2 \Gamma_W^2} \right. \\ &+ \frac{(4(C_{A_e}^2 + C_{V_e}^2)(C_{A_\nu}^2 + C_{V_\nu}^2)(1 + \beta \cos^2\theta) + 16C_{A_e} C_{V_e} C_{A_\nu} C_{V_\nu} (1 + \beta) \cos\theta) (s^2 - M_N^4)}{(s - M_Z^2)^2 + M_Z^2 \Gamma_Z^2} \\ &- 32C_1^2 C_{A_e}^2 (s^2 - M_N^4) (1 + \cos\theta)(1 + \beta \cos\theta) \\ &\left. \times \frac{\left(M_N^2 - \frac{s - M_N^2}{2}(1 - \beta \cos\theta) - M_W^2\right) (s - M_Z^2) + M_W M_Z \Gamma_W \Gamma_Z}{((M_N^2 - \frac{s - M_N^2}{2}(1 - \beta \cos\theta) - M_W^2)^2 + M_W^2 \Gamma_W^2)((s - M_Z^2)^2 + M_Z^2 \Gamma_Z^2)} \right], \quad (5.3) \end{aligned}$$

where $\beta = (s - M_N^2)/(s + M_N^2)$,

$$\begin{aligned} C_1 &= -C_2 = \frac{g}{2\sqrt{2}}, \quad C_{A_\nu} = C_{V_\nu} = \frac{g}{4\cos\theta_w}, \\ C_{A_e} &= \frac{g}{2\cos\theta_w} \left(-\frac{1}{2} + 2\sin^2\theta_w\right), \quad C_{V_e} = -\frac{g}{4\cos\theta_w}. \quad (5.4) \end{aligned}$$

The total production cross section for the process $e^+e^- \rightarrow \bar{\nu}_1 N_1$ from the t and s channel processes at the linear collider at different center of mass energies are shown in Fig. 5.4. The s channel Z mediated process can produce the second (third) generation of RHNs, $N_2(N_3)$ in association with $\nu_2(\nu_3)$. The cross sections for different center of mass energies have been given in Fig. 5.5. The cross section in this mode decreases with the increase in the center of mass energy. Such modes can reach up to a cross section of 1 pb for $M_N = 100$ GeV at $\sqrt{s} = 250$ GeV. Consider the leading decay mode of the RHN into

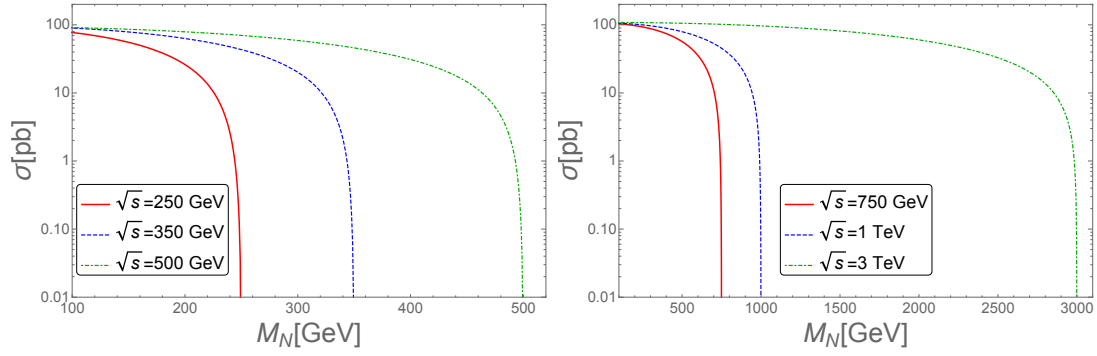


Figure 5.4: RHN production cross section at the linear collider considering $e^+e^- \rightarrow N_1\nu_1$ process at the different center of mass energies.

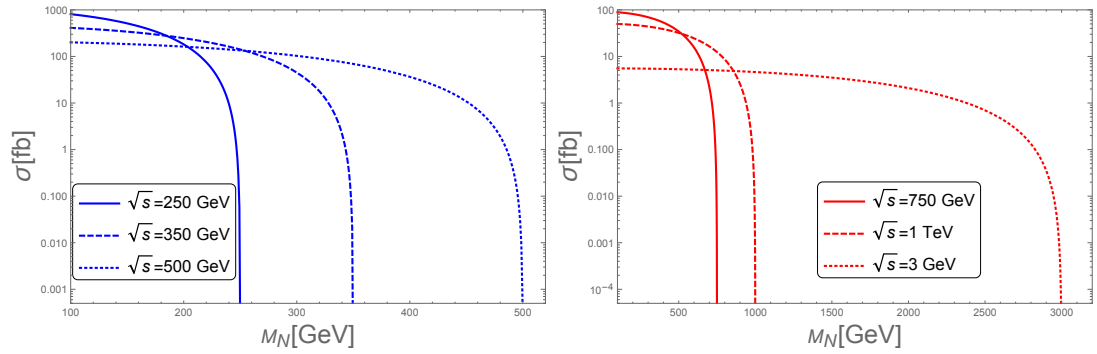


Figure 5.5: RHN production cross section at the linear collider considering $e^+e^- \rightarrow N_2\nu_2$ ($N_3\nu_3$) process at the different center of mass energies from the s channel Z boson exchange.

W and ℓ (μ, τ) followed by the hadronic decay of the W could be interesting to probe the corresponding mixing angles. The cross sections in Figs. 5.4 and 5.5 are normalized by the square of the mixing $|V_{eN_1}|^2$ to correspond the maximum value for a fixed M_N .

5.2 Collider Analysis

We implement our model in FeynRules [219], generate the UFO file of the model for MadGraph5 [220] to calculate the signals and the backgrounds. Further we use PYTHIA6 [221] for LHeC and PYTHIA8 [230] for the linear colliders, where subsequent decay, initial state radiation, final state radiation and hadronisation have been carried out. We prefer the hadronic decay mode of the W where the jets can be collimated so that we can call it a fat-jet (J). Such a topology is very powerful to discriminate the signal from

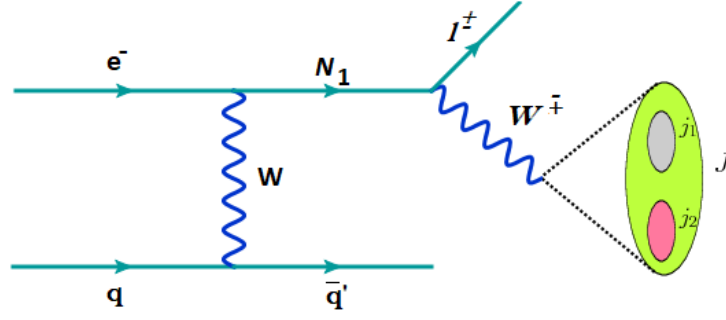


Figure 5.6: $e + J + j_1$ final state at the LHeC and HE-LHeC.

the SM backgrounds. We perform the detector simulation using DELPHES version 3.4.1 [231]. The detector card for the LHeC has been used from [232]. We use the ILD card for the linear collider. In our analysis the jets are reconstructed by Cambridge-Aachen algorithm [233, 234] implemented in Fastjet package [223, 235] with the radius parameter as $R = 0.8$.

We study the production of the first generation RHN (N_1) and its subsequent leading decay mode ($e p \rightarrow N_1 j_1, N_1 \rightarrow W e, W \rightarrow J$) at the LHeC with $\sqrt{s} = 1.3$ TeV and 1.8 TeV center of mass energies. The corresponding Feynman diagram is given in Fig. 5.6. We also study the RHN production at the linear collider (International Linear Collider, ILC) at $\sqrt{s} = 1$ TeV and CLIC at $\sqrt{s} = 3$ TeV collider energies. However, for simplicity we will use the term linear collider unanimously. At the linear collider we consider two sets of signals after the production of the RHN, such that, $e^+ e^- \rightarrow N_1 \nu, N_1 \rightarrow W e, W \rightarrow J$ and $e^+ e^- \rightarrow N_1 \nu, N_1 \rightarrow h \nu, h \rightarrow J_b$ where J_b is a fat b -jet coming from the boosted SM Higgs decay in the dominant mode. For the two types of colliders we consider 1000 fb^{-1} luminosity. The corresponding Feynman diagrams are given in Fig. 5.7. For the analysis of signal and background events we use the following set of basic cuts,

1. Electrons in the final state should have the following transverse momentum (p_T^e) and pseudo-rapidity ($|\eta^e|$) as $p_T^e > 10 \text{ GeV}, |\eta^e| < 2.5$.
2. Jets are ordered in p_T , jets should have $p_T^j > 10 \text{ GeV}$ and $|\eta^j| < 2.5$.
3. Photons are counted if $p_T^\gamma > 10 \text{ GeV}$ and $|\eta^\gamma| < 2.5$.
4. Leptons should be separated by $\Delta R_{\ell\ell} > 0.2$.

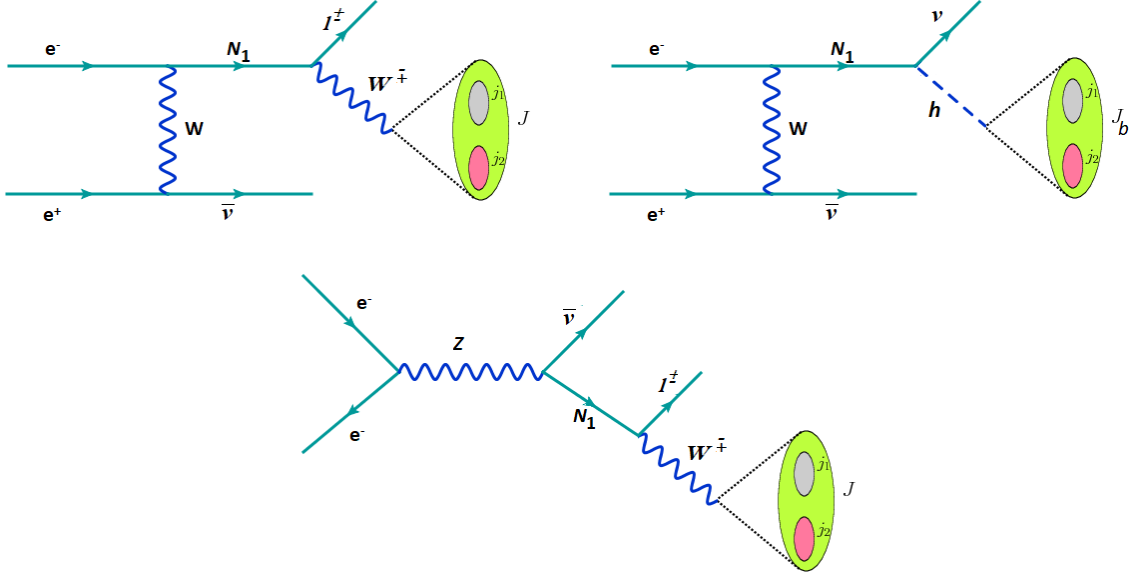


Figure 5.7: $e + J + p_T^{miss}$ and $J_b + p_T^{miss}$ final states at the linear colliders.

5. The leptons and photons are separated by $\Delta R_{\ell\gamma} > 0.3$.
6. The jets and leptons should be separated by $\Delta R_{\ell j} > 0.3$.
7. Fat Jet is constructed with radius parameter $R = 0.8$.

5.2.1 LHeC analysis for the signal $e^- p \rightarrow j N_1 \rightarrow e^\pm + J + j_1$

Producing N_1 at the LHeC and followed by its decay into leading mode to study the boosted objects, we consider the final state $e^\pm + J + j_1$. In this case we have two different processes, one is them is the $e^+ + J + j_1$ and the other one is $e^- + J + j_1$. The first one is the Lepton Number Violating (LNV) channel and the second one is the Lepton Number Conserving (LNC). At the time of showing the results we combine LNV and LNC channels to obtain the final state as $e^\pm + J + j_1$.

The LNV signal is almost background free until some e^+ +jets events appear from some radiations, however, that effect will be negligible. Therefore for completeness we include the LNC channel where the leading SM backgrounds will come from $e^- jjj$, $e^- jj$ and $e^- j$ including initial state and final state radiations. For completeness we include both

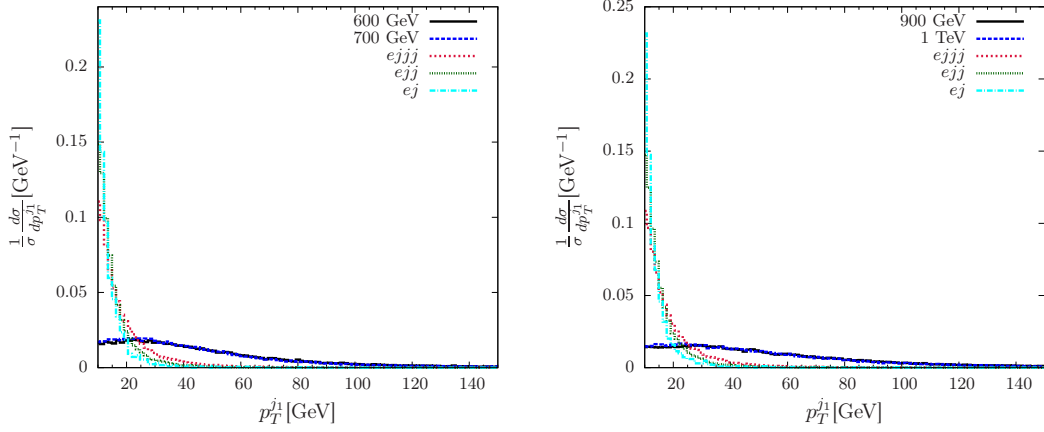


Figure 5.8: Transverse momentum distribution of the associated jet (p_T^{j1}) from the signal and background events for $M_N = 600$ GeV and 700 GeV at the $\sqrt{s} = 1.3$ TeV LHeC (left panel) and $M_N = 900$ GeV and 1 TeV at the $\sqrt{s} = 1.8$ TeV LHeC (right panel).

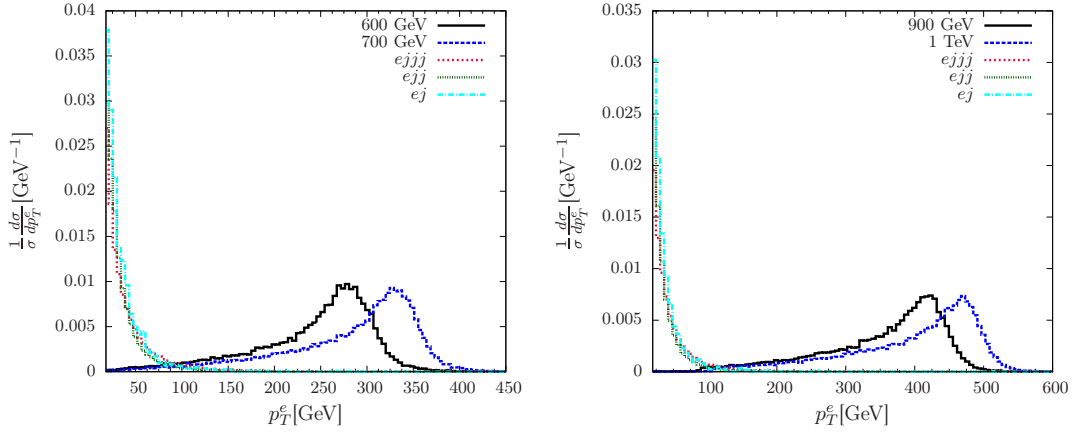


Figure 5.9: Transverse momentum distribution of the electron (p_T^e) from the signal and background events for $M_N = 600$ GeV and 700 GeV at the $\sqrt{s} = 1.3$ TeV LHeC (left panel) and $M_N = 900$ GeV and 1 TeV at the $\sqrt{s} = 1.8$ TeV HE-LHeC (right panel).

of the LNV and LNC channels. Further we use the fat-jet algorithm to reduce the SM backgrounds. We have shown the distributions of the transverse momentum of the leading jet (p_T^{j1}), lepton (p_T^e) and fat-jet (p_T^J) in Figs.5.8-5.10. The fat-jet mass distribution (M_J) has been shown in Figs.5.11. The invariant mass distribution of the lepton and fat-jet system (M_{eJ}) has been shown in Fig. 5.12. We have also compared the signals with the corresponding SM backgrounds. As a sample we consider $M_N = 600$ GeV and 700 GeV for $\sqrt{s} = 1.3$ TeV LHeC and $M_N = 900$ GeV, 1 TeV at $\sqrt{s} = 1.8$ TeV HE-LHeC as shown in Figs.5.8-5.12. We have chosen $M_N = 400$ GeV- 900 GeV for the 1.3 TeV

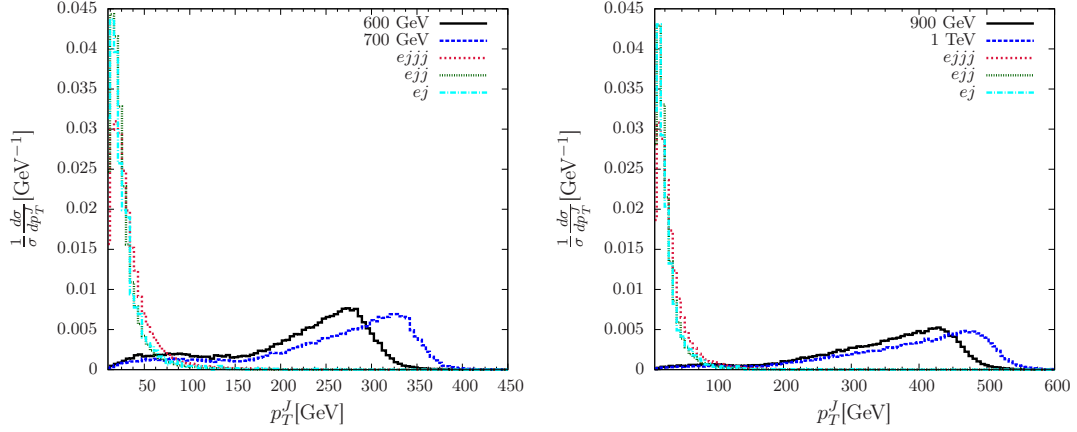


Figure 5.10: Transverse momentum distribution of the fat jet (p_T^J) from the signal and background events for $M_N = 600$ GeV and 700 GeV at the $\sqrt{s} = 1.3$ TeV LHeC (left panel) and $M_N = 900$ GeV and 1 TeV at the $\sqrt{s} = 1.8$ TeV HE-LHeC (right panel).

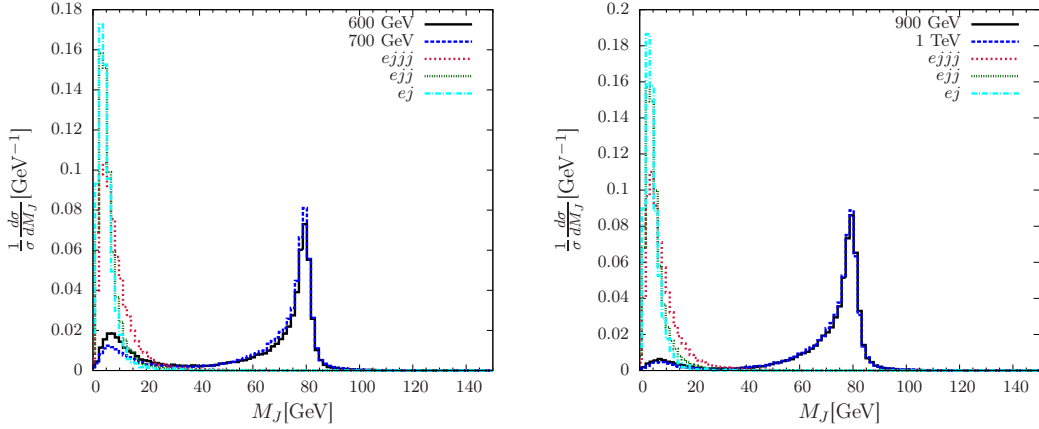


Figure 5.11: Jet mass (M_J) distribution of the fat jet from the signal and background events for $M_N = 600$ GeV and 700 GeV at the $\sqrt{s} = 1.3$ TeV LHeC (left panel) and $M_N = 900$ GeV and 1 TeV at the $\sqrt{s} = 1.8$ TeV HE-LHeC (right panel).

LHeC and $M_N = 800$ GeV- 1.5 TeV for the 1.8 TeV HE-LHeC. As benchmark points we have chosen $M_N = 600$ GeV, 700 GeV at the 1.3 TeV LHeC and $M_N = 900$ GeV, 1.0 TeV at the 1.8 TeV HE-LHeC after the basic cuts. In view of the distributions in Figs.5.8-5.12, we have used the following advanced selection cuts to reduce the backgrounds:

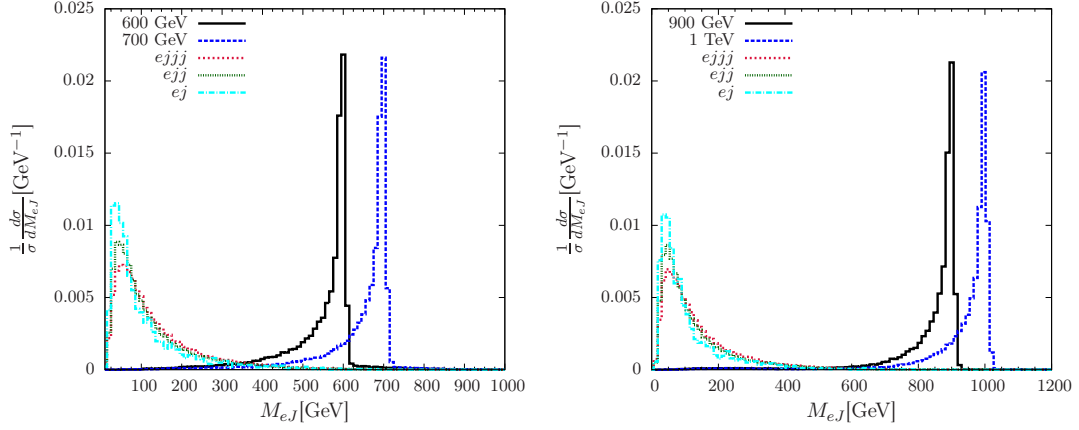


Figure 5.12: Invariant mass distribution of the fat jet and electron system (M_{eJ}) from the signal and background events for $M_N = 600$ GeV and 700 GeV at the $\sqrt{s} = 1.3$ TeV LHeC (left panel) and $M_N = 900$ GeV and 1 TeV at the $\sqrt{s} = 1.8$ TeV HE-LHeC (right panel).

Advanced cuts for $M_N = 400$ GeV -900 GeV at the $\sqrt{s} = 1.3$ TeV LHeC after the detector simulation

1. Transverse momentum for lepton and jet, $p_T^{e^\pm} > 50$ GeV.
2. Transverse momentum for fat-jet $p_T^J > 175$ GeV.
3. Fat-jet mass $M_J > 70$ GeV.
4. Invariant mass window of e^\pm and fat-jet J , $|M_{eJ} - M_N| \leq 20$ GeV.

We have noticed that $M_J > 70$ GeV cuts out the low energy peaks ($M_J \leq 25$ GeV) which come from the hadronic activity of the low energy jets. Similarly, the p_T^J and p_T^e cuts are also very effective. Due to the presence of the RHN, these distributions from the signal will be in the high values than the SM backgrounds. Therefore selecting such cuts at high values, as we have done here, will be extremely useful to reduce the SM backgrounds.

We have noticed that ej background can completely be reduced with the application of the kinematic cuts on p_T^e , p_T^J and M_J . It is difficult to obtain a fat jet from this process because the t channel exchange of the Z boson and photon will contribute to this process, however, the other low-energy jets may come from the radiations at the initial and final states. These jets do not help to make the fat jets sufficiently energetic. Therefore $p_T^J > 175$ GeV ($p_T^J > 400$ GeV) at the LHeC (HE-LHeC) are very useful. Similarly the $ejjj$ is the irreducible

Cuts	Signal		Background		Total
	$M_{N_1} = 600$ GeV	$M_{N_1} = 700$ GeV	$ejjj$	ejj	
Basic Cuts	645,860	261,254	70,029,800	189,689,000	259,718,800
$p_T^J > 175$ GeV	476,640	214,520	295,658	338,720	634,378
$M_J > 70$ GeV	356,350	160,017	35,244	17,520	52,764
$p_T^e > 50$ GeV	356,126	159,918	33,286	17,520	50,806
$ M_{eJ} - M_N \leq 20$ GeV	304,457	129,690	7	1	8

Table 5.1: Cut flow of the signal and background events for the final state $e^\pm + J + j_1$ for $M_N = 600$ GeV and 700 GeV with $\sqrt{s} = 1.3$ TeV LHeC where the signal events are normalized by the square of the mixing.

Cuts	Signal		Background		Total
	$M_{N_1} = 900$ GeV	$M_{N_1} = 1$ TeV	$ejjj$	ejj	
Basic Cuts	427,311	207,015	108,243,000	273,410,000	381,653,000
$p_T^J > 400$ GeV	158,694	110,289	12,225	12,450	24,675
$M_J > 70$ GeV	145,558	96,787	4,596	4,150	8,746
$p_T^e > 250$ GeV	144,997	96,487	4,596	4,150	8,746
$ M_{eJ} - M_N \leq 20$ GeV	119,659	71,490	3	1	4

Table 5.2: Cut flow of the signal and background events for the final state $e^\pm + J + j_1$ for $M_N = 900$ GeV and 1.0 TeV with $\sqrt{s} = 1.8$ TeV HE-LHeC where the signal events are normalized by the square of the mixing.

background in this case which will contribute most among the backgrounds. Whereas ejj is the second leading background in this case. However, both of these backgrounds can be reduced using the invariant mass cut of the RHN. As the RHN will decay according to $N \rightarrow eJ$, therefore the invariant mass of the eJ system with an window of 20 GeV ($|M_{eJ} - M_N| \leq 20$ GeV) will be extremely useful to reduce the backgrounds further in these colliders. In Tab. 5.1 we have given the two benchmark scenarios at the 1.3 TeV LHeC where the signal events are normalized by the square of the mixing.

Advanced cuts for $M_N = 800$ GeV – 1.5 TeV at the $\sqrt{s} = 1.8$ TeV HE-LHeC after the detector simulation

1. Transverse momentum for lepton, $p_T^{e^\pm} > 250$ GeV.
2. Transverse momentum for fat-jet $p_T^J > 400$ GeV.
3. Fat-jet mass $M_J > 70$ GeV.
4. Invariant mass window of e^\pm and fat-jet J , $|M_{eJ} - M_N| \leq 20$ GeV.

We have chosen $M_N = 900$ GeV and 1 TeV at the $\sqrt{s} = 1.8$ TeV HE-LHeC. The corresponding signals normalized by the square of the mixing and the SM backgrounds are listed in Tab. 5.2. Due to the heavier mass range of the RHN, we have chosen stronger cuts for the transverse momenta of the electron and fat-jet which became useful to reduce the backgrounds.

5.2.2 Linear collider analysis for the signal $e^\pm + J + p_T^{miss}$

In linear collider we study $e^\pm + J + p_T^{miss}$ signal from the leading decay mode of the RHN at the 1 TeV and 3 TeV center of mass energy. The corresponding distributions for two benchmark points for $M_N = 500$ GeV, 800 GeV at $\sqrt{s} = 1$ TeV and $M_N = 800$ GeV, 2 TeV at $\sqrt{s} = 3$ TeV linear colliders are given in Figs.5.13-5.17 after the basic cuts. We perform a complete cut based analysis for the signal and the SM backgrounds. In this process we have $\nu_e eW$ as the leading background whereas WW , ZZ and $t\bar{t}$ are other important backgrounds. We have shown the missing momentum (p_T^{miss}), transverse momenta of

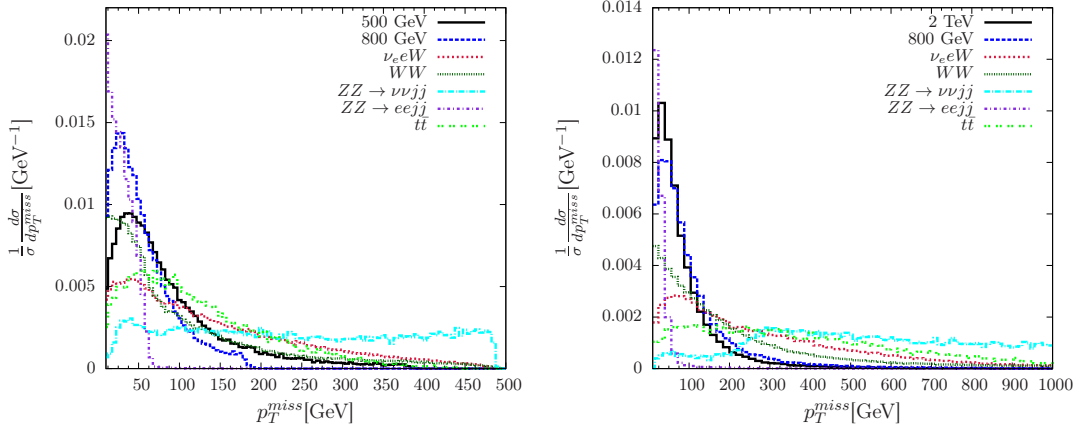


Figure 5.13: Missing momentum distribution of the signal and background events for $M_N = 500$ GeV and 800 GeV at the $\sqrt{s} = 1$ TeV (left panel) and $M_N = 800$ GeV and 2 TeV at the $\sqrt{s} = 3$ TeV (right panel) linear colliders.

the electron p_T^e and fat-jet p_T^J in Figs. 5.13-5.15 for the linear colliders. The fat-jet mass M_J distribution has been shown in Fig. 5.16. We construct the polar angle variable in Fig. 5.17 for the electron (fat jet), $\cos \theta_e$ ($\cos \theta_J$) where $\theta_{e(J)} = \tan^{-1} \left[\frac{p_T^{e(J)}}{p_z^{e(J)}} \right]$, where $p_z^{e(J)}$

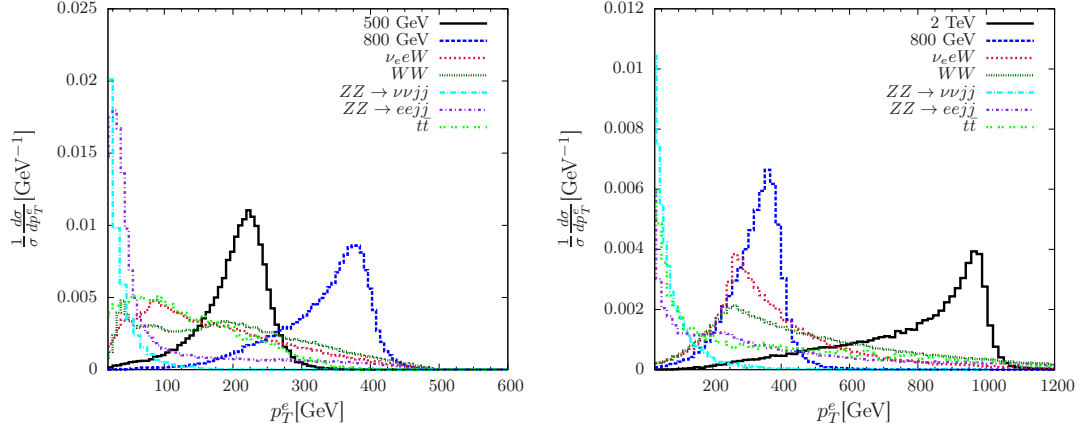


Figure 5.14: Transverse momentum distribution of the electron (p_T^e) from the signal and background events for $M_N = 500$ GeV and 800 GeV at the $\sqrt{s} = 1$ TeV (left panel) and $M_N = 800$ GeV and 2 TeV at the $\sqrt{s} = 3$ TeV (right panel) linear colliders.

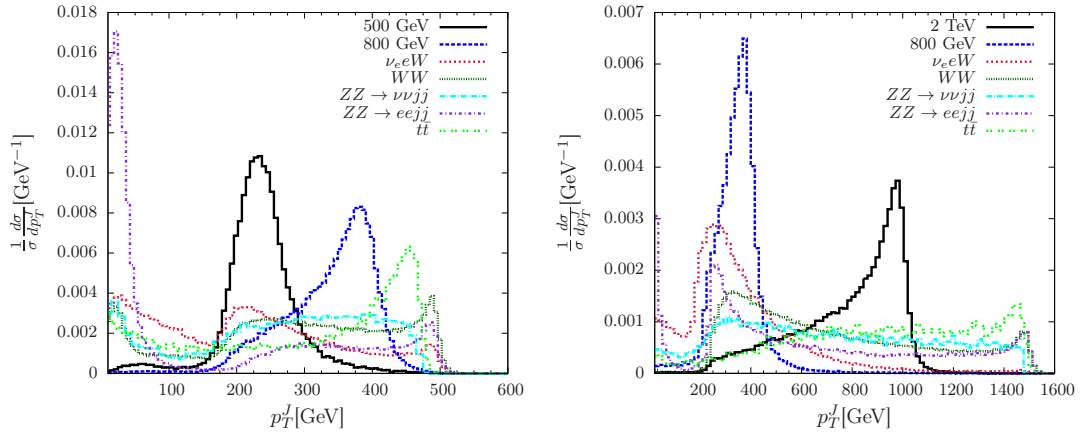


Figure 5.15: Transverse momentum distribution of the fat jet (p_T^J) from the signal and background events for $M_N = 500$ GeV and 800 GeV at the $\sqrt{s} = 1$ TeV (left panel) and $M_N = 800$ GeV and 2 TeV at the $\sqrt{s} = 3$ TeV linear colliders.

is the z component of the three momentum of the electron (fat jet). This is a very effective cut which reduces the SM background significantly. In view of these distributions, we have used the following advanced selection cuts to reduce the backgrounds:

Advanced cuts for $M_N = 400$ GeV- 900 GeV at the $\sqrt{s} = 1$ TeV linear collider after the detector simulation

1. Transverse momentum for fat-jet $p_T^J > 150$ GeV for M_N mass range 400 GeV- 600 GeV and $p_T^J > 250$ GeV for M_N mass range 700 GeV- 900 GeV.

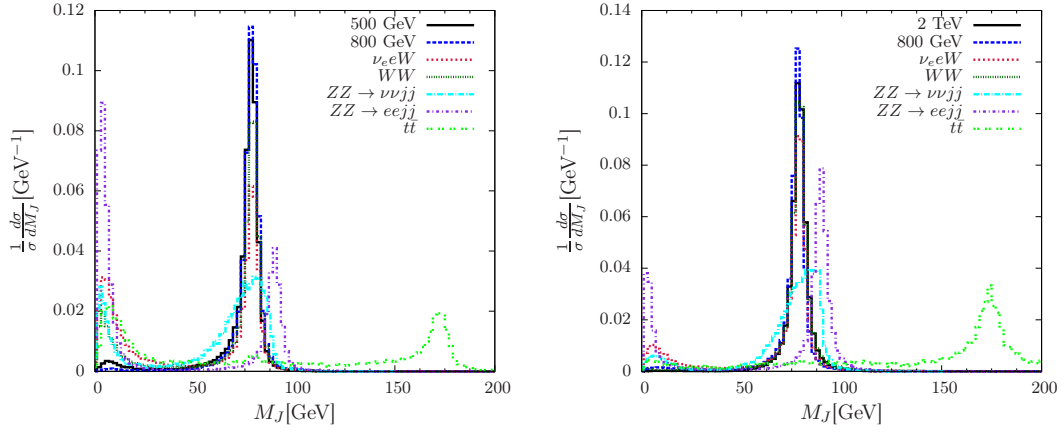


Figure 5.16: Jet mass (M_J) distribution of the fat jet from the signal and background events for $M_N = 500$ GeV and 800 GeV at the $\sqrt{s} = 1$ TeV (left panel) and $M_N = 800$ GeV and 2 TeV at the $\sqrt{s} = 3$ TeV (right panel) linear colliders.

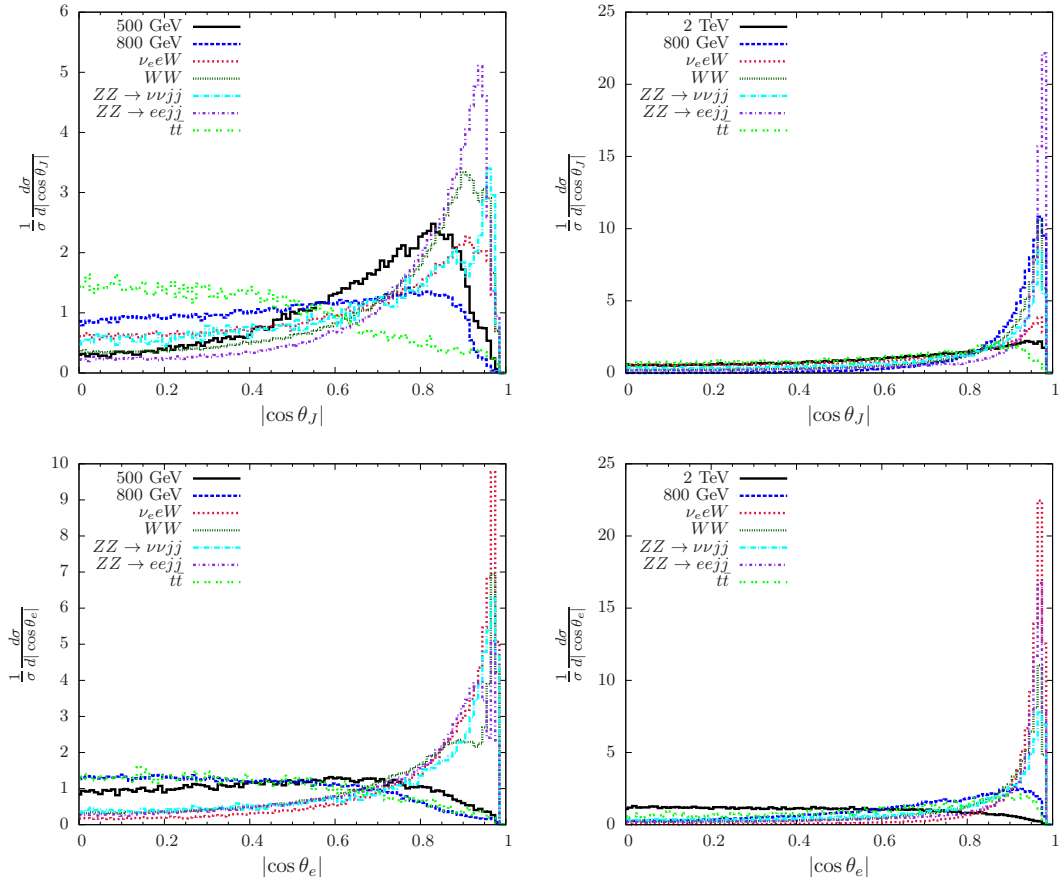


Figure 5.17: $\cos \theta_{J(e)}$ distributions for the $J(e)$ in the first row (second row) for the 1 TeV (left column) and 3 TeV (right column) linear colliders.

Cuts	Signal	Background				Total
		$\nu_e e W$	WW	ZZ	$t\bar{t}$	
Basic Cuts	12,996,200	201,586	72,244	7,200	4,300	285,330
$ \cos \theta_J \leq 0.85$	12,789,800	148,802	44,910	3,800	4,100	201,600
$ \cos \theta_e \leq 0.85$	12,671,800	79,008	40,574	2,800	3,900	126,280
$p_T^J > 150$ GeV	12,308,300	70,669	40,490	2,300	3,200	116,660
$M_J > 70$ GeV	10,923,100	62,303	37,043	2,100	2,300	103,700
$p_T^\ell > 100$ GeV	10,714,500	57,076	33,488	1,400	1,530	93,400

Table 5.3: Cut flow for the signal and background events for the final state $e^\pm + J + p_T^{miss}$ for $M_N = 500$ GeV at the $\sqrt{s} = 1$ TeV linear collider. The signal events are normalized by the square of the mixing.

Cuts	Signal	Background				Total
		$\nu_e e W$	WW	ZZ	$t\bar{t}$	
Basic Cuts	8,684,990	201,586	72,244	7,200	4,300	285,330
$ \cos \theta_J \leq 0.85$	8,649,570	148,802	44,910	3,800	4,100	201,600
$ \cos \theta_e \leq 0.85$	8,618,420	79,008	40,574	2,800	3,900	126,280
$p_T^J > 250$ GeV	7,681,440	59,001	40,329	2,303	2,720	104,354
$M_J > 70$ GeV	7,176,280	53,990	36,997	2,187	2,282	95,437
$p_T^\ell > 200$ GeV	7,080,200	38,729	26,208	942	613	66,493

Table 5.4: Cut flow for the signal and background events for the final state $e^\pm + J + p_T^{miss}$ for $M_N = 800$ GeV at the $\sqrt{s} = 1$ TeV linear collider. The signal events are normalized by the square of the mixing.

2. Transverse momentum for leading lepton $p_T^{e^\pm} > 100$ GeV for M_N mass range 400 GeV-600 GeV and $p_T^{e^\pm} > 200$ GeV for M_N mass range 700 GeV-900 GeV.
3. Polar angle of lepton and fat-jet $|\cos \theta_e| < 0.85$, $|\cos \theta_J| < 0.85$.
4. Fat-jet mass $M_J > 70$ GeV.

We have tested $M_N = 400$ GeV to 900 GeV at the $\sqrt{s} = 1$ TeV at the linear collider. Hence we consider two benchmark points at the $\sqrt{s} = 1$ TeV linear collider such as $M_N = 500$ GeV and 800 GeV. The cut flow for the $\sqrt{s} = 1$ TeV are given in the Tabs. 5.3 and 5.4 respectively. We have noticed that $\cos \theta_{e(J)}$ is a very important kinematic variable and setting $|\cos \theta_{e(J)}| < 0.85$ puts a very strong cut for the SM backgrounds. The $M_J > 70$ GeV is also effective to cut out the low mass peaks ($1 \text{ GeV} \leq M_J \leq 25 \text{ GeV}$) from the low energy jets.

Cuts	Signal	Background				Total
		$\nu_e e W$	WW	ZZ	$t\bar{t}$	
Basic Cuts	21,789,900	193,533	12,135	1,361	271	207,301
$ \cos \theta_J \leq 0.85$	13,599,300	126,980	4,766	406	215	132,367
$ \cos \theta_e \leq 0.85$	12,163,300	21,110	4,609	390	195	26,304
$p_T^J > 250$ GeV	12,083,500	18,619	4,607	390	189	23,807
$M_J > 70$ GeV	11,287,000	17,442	4,411	385	176	22,416
$p_T^\ell > 200$ GeV	11,094,300	16,915	4,108	343	104	21,470

Table 5.5: Cut flow for the signal and background events for the final state $e^\pm + J + p_T^{miss}$ for $M_N = 800$ GeV at the $\sqrt{s} = 3$ TeV linear collider. The signal events are normalized by the square of the mixing.

Advanced cuts for $M_N = 700$ GeV-2.9 TeV at the $\sqrt{s} = 3$ TeV linear collider after the detector simulation

1. Transverse momentum for fat-jet $p_T^J > 250$ GeV for the M_N mass range 700 GeV-900 GeV and $p_T^J > 400$ GeV for M_N mass range 1 – 2.9 TeV.
2. Transverse momentum for leading lepton $p_T^{e^\pm} > 200$ GeV for M_N mass range 700–900 GeV and $p_T^{e^\pm} > 250$ GeV for M_N mass range 1 – 2.9 TeV.
3. Polar angle of lepton and fat-jet $|\cos \theta_e| < 0.85$, $|\cos \theta_J| < 0.85$.
4. Fat-jet mass $M_J > 70$ GeV.

We have tested $M_N = 700$ GeV to 2.9 TeV at the $\sqrt{s} = 3$ TeV at the linear collider. Hence we consider two benchmark points at the $\sqrt{s} = 3$ TeV linear collider such as $M_N = 800$ GeV and 2 TeV. The cut flow for the benchmark points at the $\sqrt{s} = 3$ TeV are given in the Tabs. 5.5 and 5.6 respectively. At the 3 TeV we see almost the same behavior for the kinematic variables as we noticed at the 1 TeV case except the p_T distributions of the electron and fat jet. At this point we must mention that the backgrounds like ZZ and $t\bar{t}$ can have more than one lepton in the final state which has been efficiently vetoed to reduce the effect.

Cuts	Signal	Background				Total
		$\nu_e e W$	WW	ZZ	$t\bar{t}$	
Basic Cuts	13,822,500	193,533	12,135	1,382	271	207,322
$ \cos \theta_J \leq 0.85$	12,701,600	126,980	4,766	412	215	132,374
$ \cos \theta_e \leq 0.85$	12,647,200	21,110	4,609	396	195	26,310
$p_T^J > 400$ GeV	12,611,000	15,737	4,605	396	184	20,923
$M_J > 70$ GeV	12,015,600	14,889	4,410	391	175	19,865
$p_T^\ell > 250$ GeV	11,987,000	14,184	4,010	336	10	18,630

Table 5.6: Cut flow for the signal and background events for the final state $e^\pm + J + p_T^{miss}$ for $M_N = 2$ TeV at the $\sqrt{s} = 3$ TeV linear collider. The signal events are normalized by the square of the mixing.

5.2.3 Linear collider analysis for the signal $J_b + p_T^{miss}$

Considering the $N \rightarrow h\nu, h \rightarrow J_b$ mode at the linear collider we obtain the $J_b + p_T^{miss}$ final state. For this final state the dominant SM backgrounds come from the processes $h\nu_\ell\bar{\nu}_\ell$ and $Z\nu_\ell\bar{\nu}_\ell$. Backgrounds can also come from the intermediate processes ZZ and ZH . We have generated the background events combining all these processes in MadGraph for our analysis. In Figs.5.18, 5.19 and 5.20, we plot the missing momentum (p_T^{miss}),

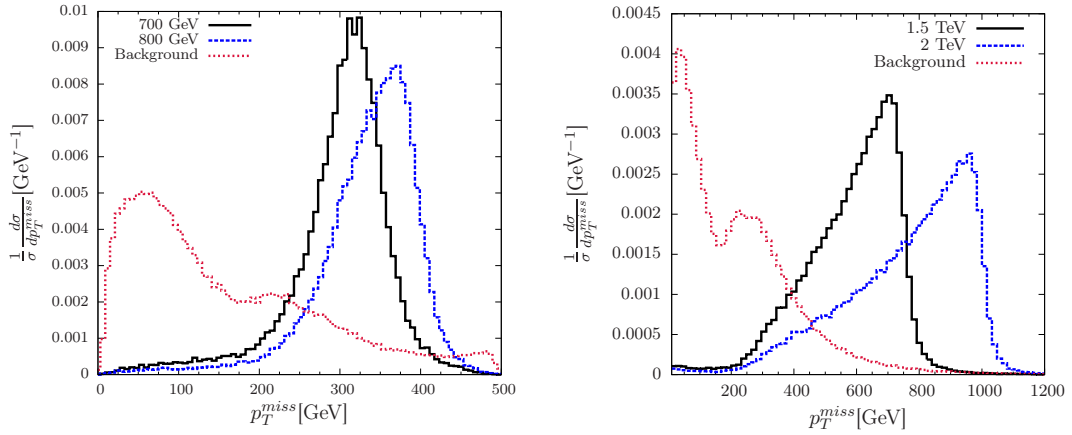


Figure 5.18: p_T^{miss} distribution of the signal and background events for $M_N = 700$ GeV and 800 GeV at the $\sqrt{s} = 1$ TeV (left panel) and $M_N = 1.5$ TeV and 2 TeV at the $\sqrt{s} = 3$ TeV (right panel) linear colliders.

transverse momentum of the fat-b jet $p_T^{J_b}$ and jet mass of the fat-b jet (M_{J_b}) distributions for $M_N = 700$ GeV and 800 GeV at the $\sqrt{s} = 1$ TeV linear collider and $M_N = 1.5$ TeV and 2 TeV at the $\sqrt{s} = 3$ TeV linear collider. In view of these distributions, we have used

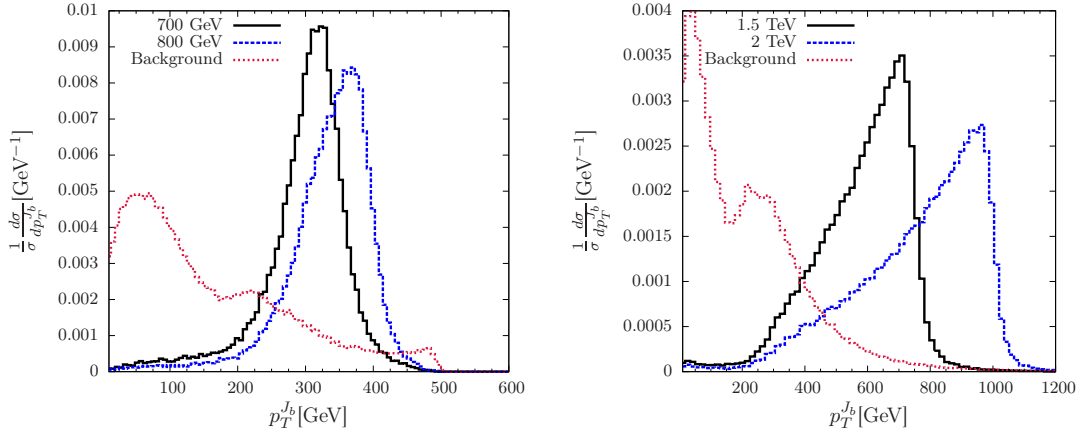


Figure 5.19: Transverse momentum distribution of J_b ($p_T^{J_b}$) from the signal and background events for $M_N = 700$ GeV and 800 GeV at the $\sqrt{s} = 1$ TeV (left panel) and $M_N = 1.5$ TeV and 2 TeV at the $\sqrt{s} = 3$ TeV (right panel) linear colliders.

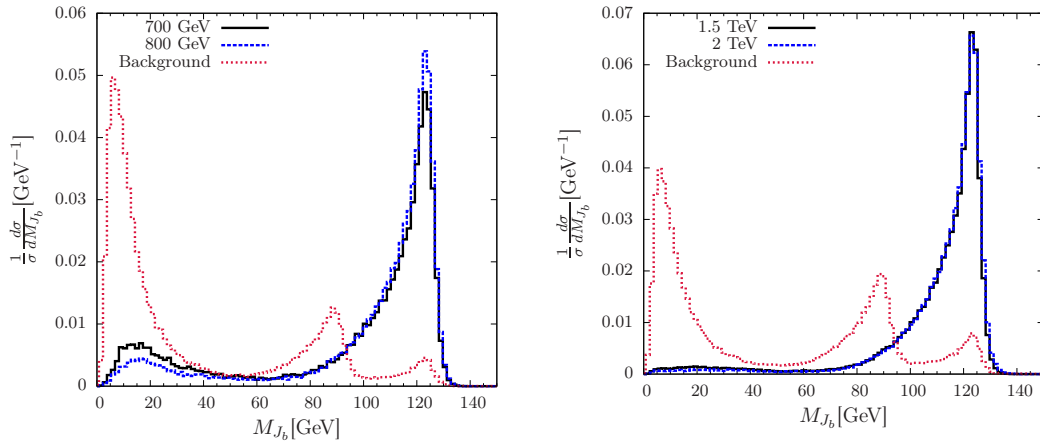


Figure 5.20: Fat b-Jet mass (M_{J_b}) distribution from the signal and background events for $M_N = 700$ GeV and 800 GeV at the $\sqrt{s} = 1$ TeV (left panel) and $M_N = 1.5$ TeV and 2 TeV at the $\sqrt{s} = 3$ TeV (right panel) linear colliders.

the following advanced selection cuts to reduce the SM background:

Advanced cuts for $M_N = 400$ GeV- 900 GeV at the $\sqrt{s} = 1$ TeV linear collider after the detector simulation

1. Transverse momentum for J_b , $p_T^{J_b} > 250$ GeV.
2. Fat-b mass, $M_{J_b} > 115$ GeV.
3. Missing energy, $p_T^{miss} > 150$ GeV.

We consider two benchmark points such as $M_N = 700$ GeV and 800 GeV at the 1 TeV

Cuts	Signal		Background
	$M_N = 700$ GeV	$M_N = 800$ GeV	
Basic Cuts	1,288,150	1,248,340	19,300
$p_T^{miss} > 150$ GeV	1,239,440	1,223,480	8,373
$p_T^{J_b} > 250$ GeV	1,100,790	1,153,650	4,239
$M_{J_b} > 115$ GeV	609,330	661,258	855

Table 5.7: Cut flow for the signal and background events for the final state $J_b + p_T^{miss}$ for $M_N = 700$ GeV and 800 GeV at the $\sqrt{s} = 1$ TeV linear collider. The signal events are normalized by the square of the mixing.

linear collider to produce the boosted Higgs from RHNs. The cut flow has been shown in Tab. 5.7. The b-jets are coming from the SM h as the M_{J_b} distribution peaks at the Higgs mass for the signal at the linear colliders. As a result $M_{J_b} > 115$ GeV sets a strong cut on the SM backgrounds.

Advanced cuts for the $M_N = 1$ TeV -2.9 TeV for the $\sqrt{s} = 3$ TeV linear collider after the detector simulation

1. Transverse momentum for fat-b (J_b), $p_T^{J_b} > 350$ GeV.
2. Fat-b mass, $M_{J_b} > 115$ GeV.
3. Missing energy, $p_T^{miss} > 175$ GeV.

We consider two benchmark points such as $M_N = 1.5$ TeV and 2 TeV at the 3 TeV linear collider for the boosted Higgs production from the RHN. The cut flow has been shown in Tab. 5.8. The b-jets are coming from the SM h as the M_{J_b} distribution peaks at the Higgs mass for the signal at the linear colliders. As a result $M_{J_b} > 115$ GeV sets a strong cut on the SM backgrounds. We also consider a strong $p_T^{J_b} > 350$ GeV cut for the high mass RHNs at the 3 TeV collider. In this work, we adopt a minimalistic approach and consider a flat 70% tagging efficiency for each of the daughter b jets coming from the Higgs decay.

Cuts	Signal		Background
	$M_N = 1.5 \text{ TeV}$	$M_N = 2 \text{ TeV}$	
Basic Cuts	5,077,160	4,043,130	74,245
$p_T^{miss} > 175 \text{ GeV}$	5,005,240	4,011,420	39,231
$p_T^{J_b} > 350 \text{ GeV}$	4,731,550	3,902,490	15,327
$M_{J_b} > 115 \text{ GeV}$	2,961,620	2,479,960	3,740

Table 5.8: Cut flow for the signal and background events for the final state $J_b + p_T^{miss}$ for $M_N = 1.5 \text{ TeV}$ and 2 TeV at the $\sqrt{s} = 3 \text{ TeV}$ linear collider. The signal events are normalized by the square of the mixing.

5.3 Current bounds

The bounds on the light-heavy neutrino mixing for the electron flavor comes from a variety of searches. As we are interested on the RHN of mass $M_N \geq 100 \text{ GeV}$, therefore we will compare our results with such bounds which are important for that mass range. The Electroweak Precision Data (EWPD) bounds have been calculated in [120, 236, 237] which obtains the bound on $|V_{eN}|^2$ as 1.681×10^{-3} at the 95% C. L., the LEP2 [238], calculated at the 95% C.L., bounds are rather weaker except $M_N = 108 \text{ GeV}$ where it touches the EWPD line. The strongest bounds are coming from the GERDA [121] $0\nu 2\beta$ study where the limits as calculated in [148] up to $M_N = 959 \text{ GeV}$. The lepton universality limits from [138] set bounds on $|V_{eN}|^2$ at 6.232×10^{-4} up to $M_N = 1 \text{ TeV}$ at the 95% C. L. These bounds are plotted in Figs. 5.21 -5.26.

Apart from the above mentioned indirect searches, the recent collider searches for the LHC also set bounds $|V_{eN}|^2$ at the $\sqrt{s} = 8 \text{ TeV}$ at 95% C. L. from same dilepton plus dijet search. The bounds on $|V_{eN}|^2$ from ATLAS (ATLAS8- ee) [147] and CMS (CMS8 - ee) [199] are obtained at 23.3 fb^{-1} and 19.7 fb^{-1} luminosities respectively for the $e^\pm e^\pm + 2j$ sample. The ATLAS limit is weaker than the CMS limits for $100 \text{ GeV} \leq M_N \leq 500 \text{ GeV}$. The LHC has also published the recent results at $\sqrt{s} = 13 \text{ TeV}$ with 35.9 fb^{-1} luminosity which set stronger bounds on $|V_{eN}|^2$ than the previous direct searches for $100 \text{ GeV} \leq M_N \leq 500 \text{ GeV}$. The bounds on $|V_{eN}|^2$ from the $e^\pm e^\pm + 2j$ signal in CMS (CMS13- ee) [201] and from trilepton search at CMS (CMS13- 3ℓ) [200] are also

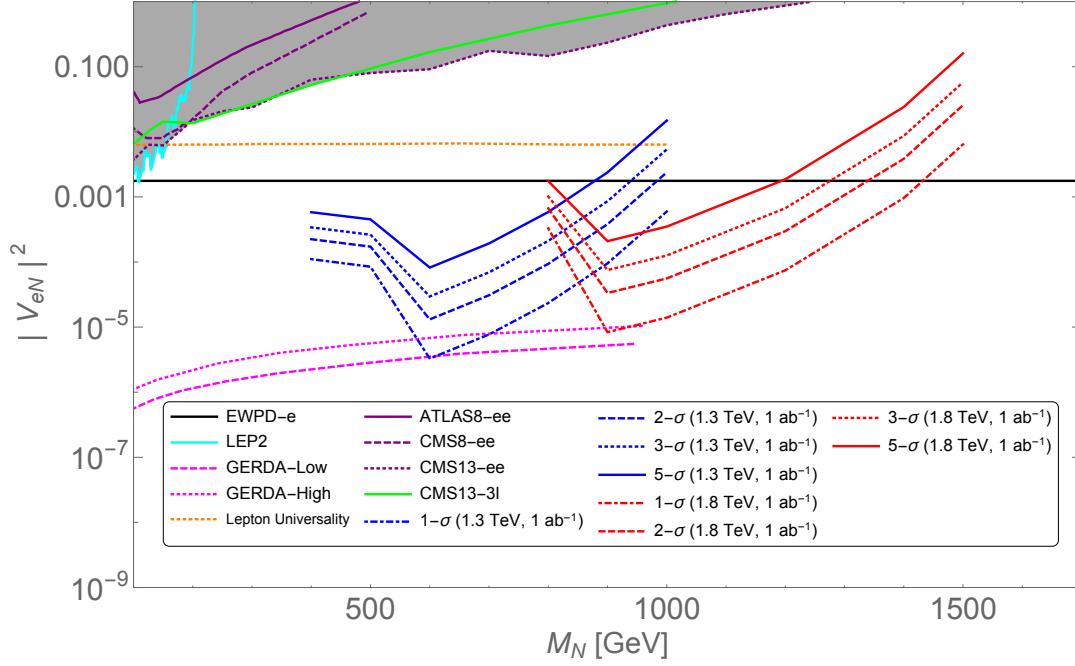


Figure 5.21: The prospective upper limits on $|V_{eN}|^2$ at the 1.3 TeV LHeC (blue band) and 1.8 TeV HE-LHeC (red band) at the 1 ab^{-1} luminosity compared to EWPD, LEP2, GERDA, ATLAS (ATLAS8- ee), CMS (CMS8- ee) at the 8 TeV LHC, 13 TeV CMS search for $e^\pm e^\pm + 2j$ (CMS13- ee) and 13 TeV CMS search for 3ℓ (CMS13- ee) respectively.

competitive, however, weaker than the EWPD for $100 \text{ GeV} \leq M_N \leq 1.2 \text{ TeV}$. These limits are also plotted in Figs. 5.21 -5.26.

We have explored that at the LHeC with $\sqrt{s} = 1.3 \text{ TeV}$ collider energy and 1 ab^{-1} luminosity, the bound on $|V_{eN}|^2$ for $M_N = 600 \text{ GeV}$ with $1\text{-}\sigma$ C.L. is better than the $0\nu 2\beta$ limit from GERDA-low where as $M_N \geq 959 \text{ GeV}$ at $1\text{-}\sigma$ limit can be probed better than the GERDA-low and high limit [121, 148]. The GERDA limits are stronger for the M_N benchmarks we have studied. The results have been shown in Fig. 5.21. In the same figure we show the bounds obtained from the HE-LHeC with $\sqrt{s} = 1.8 \text{ TeV}$ collider energy and 1 ab^{-1} luminosity. In this case the current GERDA bounds are stronger up to $M_N = 959 \text{ GeV}$ [121, 148]. At the HE-LHeC RHN up to $M_N = 1.2 \text{ TeV}$ can be probed at $5\text{-}\sigma$ and these bounds could be stronger than the limits obtained from the EWPD-e limit [120, 236, 237]. The improved scenario at the 3 ab^{-1} luminosity for the LHeC and HE-LHeC are shown in Figs. 5.22.

At the linear collider we have explored two sets of signals. one is the $e + J + p_T^{\text{miss}}$ and

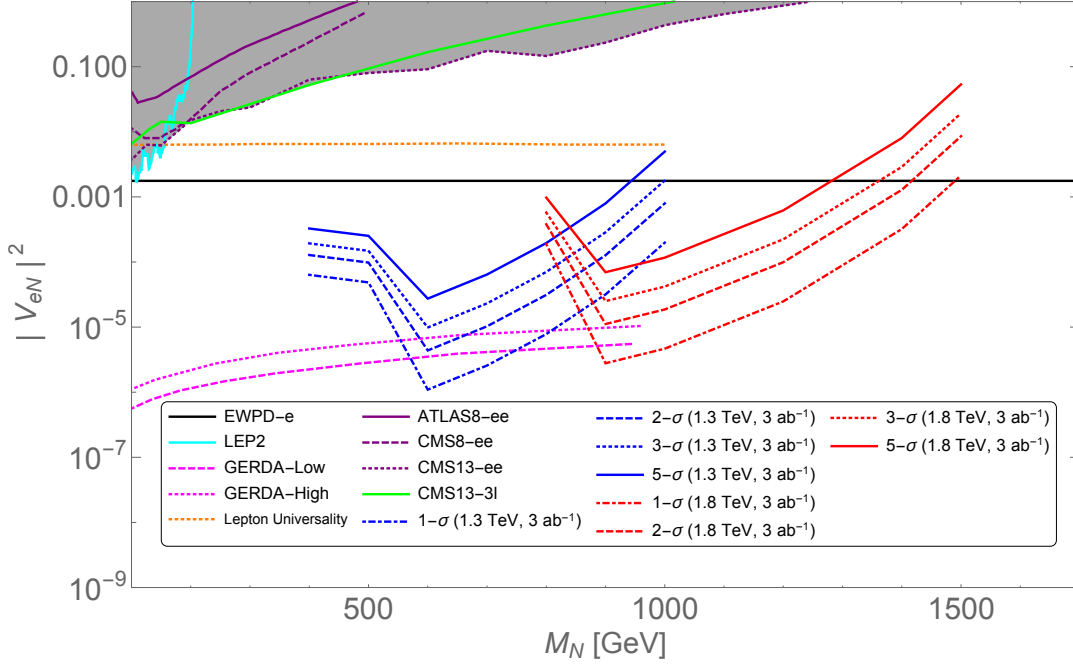


Figure 5.22: Same as Fig. 5.21 with 3 ab^{-1} luminosity at the 1.3 TeV LHeC and 1.8 TeV HE-LHeC.

the other one is $J_b + p_T^{miss}$. Using $e + J + p_T^{miss}$ signal at the 1 TeV linear collider we have probed RHNs between $400 \text{ GeV} \leq M_N \leq 900 \text{ GeV}$ at $5\text{-}\sigma$ but the $0\nu 2\beta$ limit from GERDA [148] is stronger than this result for $M_N \leq 959 \text{ GeV}$, however, the bounds on $|V_{eN}|^2$ for the RHNs heavier than 1 TeV can be probed at $5\text{-}\sigma$ significance or more at the linear collider with the 3 TeV center of mass energy. In this case apart from the fat jet properties, the polar angle cut for the leptons worked nicely. The results are shown in Fig. 5.23. We have also studied the linear colliders at 1(3) TeV center of mass energy with 3(5) ab^{-1} luminosity. We can find the improved results in Fig. 5.24. Using the $J_b + p_T^{miss}$ signal we did a complementarity check where $M_N \geq 1 \text{ TeV}$ can be probed better than GERDA [148] at $5\text{-}\sigma$ significance or more at the 3 TeV linear collider. The linear collider can probe $|V_{eN}|^2$ down to $\mathcal{O}(10^{-5})$ for $M_N = 1.35 \text{ TeV}$ at 3 TeV, however, compared to this the bounds obtained at the 1 TeV linear collider are weaker. The corresponding bounds at the $\sqrt{s} = 1 \text{ TeV}$ and 3 TeV linear collider are plotted in Figs. 5.23 and 5.25. The red (blue) band represents the bounds on $|V_{eN}|^2$ at 1 TeV (3 TeV) linear collider at different confidence levels. Comparing the bounds between the final states $e + J + p_T^{miss}$

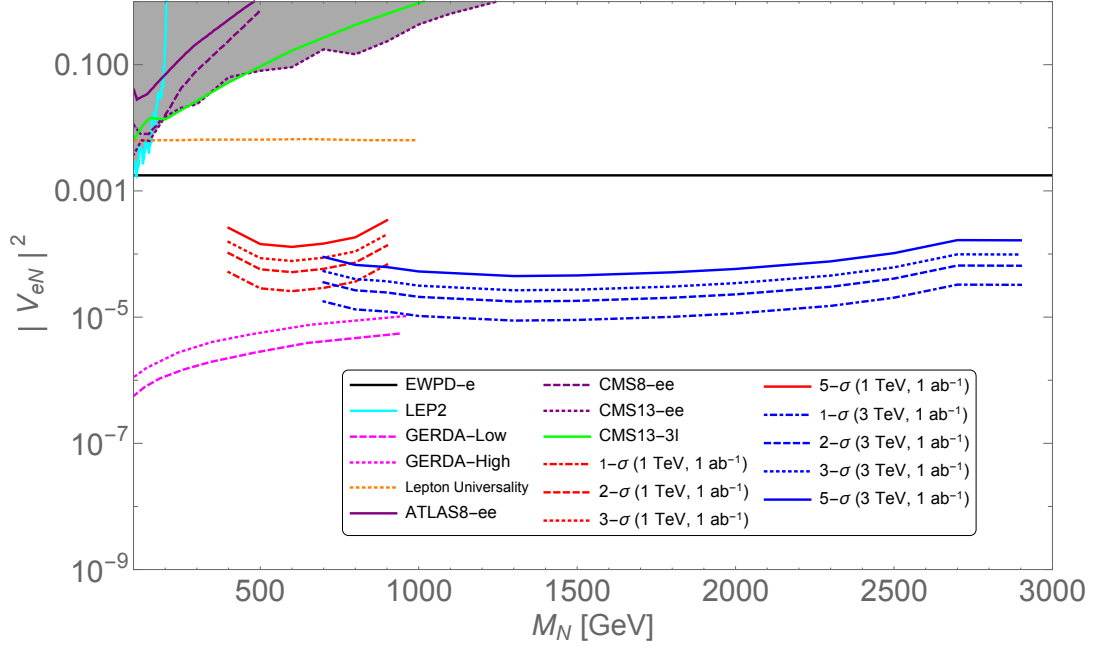


Figure 5.23: The prospective upper limits on $|V_{eN}|^2$ at the 1 TeV (red band) and 3 TeV (blue band) linear colliders at the 1 ab^{-1} luminosity for $e + J + p_T^{miss}$ signal compared to EWPd, LEP2, GERDA, ATLAS (ATLAS8- ee), CMS (CMS8 - ee) at the 8 TeV LHC, 13 TeV CMS search for $e^\pm e^\pm + 2j$ (CMS13- ee) and 13 TeV CMS search for 3ℓ (CMS13- ee) respectively.

and $J_b + p_T^{miss}$ we find that the former one puts slightly stronger limits on $|V_{eN}|^2$. The results are shown in Fig. 5.25. We have also studied the linear colliders at 1(3) TeV center of mass energy with 3(5) ab^{-1} luminosity. We can find the improved results in Fig. 5.26. Finally we comment that our results at the linear collider are stronger than the limits obtained from the EWPd-e [120, 236, 237] throughout the study.

5.4 Summary

We have studied the RHNs which can be responsible for the generation of the tiny light neutrino masses. We have calculated the production cross sections for the RHNs at the LHeC and linear collider at various center of mass energies and have tested the discovery prospects of these RHNs. We have chosen $\sqrt{s} = 1.3 \text{ TeV}$ and 1.8 TeV for the LHeC and $\sqrt{s} = 1 \text{ TeV}$ and 3 TeV for the linear collider. We have considered the sufficiently heavy mass range of the RHNs. These RHNs can decay dominantly into ℓW mode. A

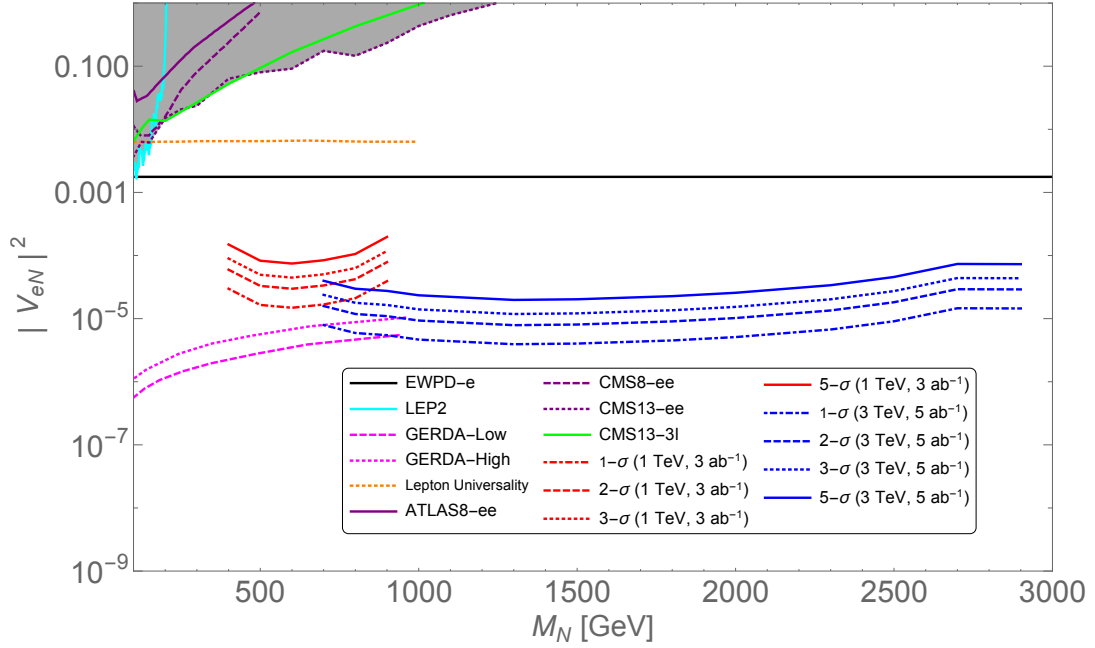


Figure 5.24: Same as Fig. 5.23 with 3(5) ab^{-1} luminosity at the 1(3) TeV linear collider.

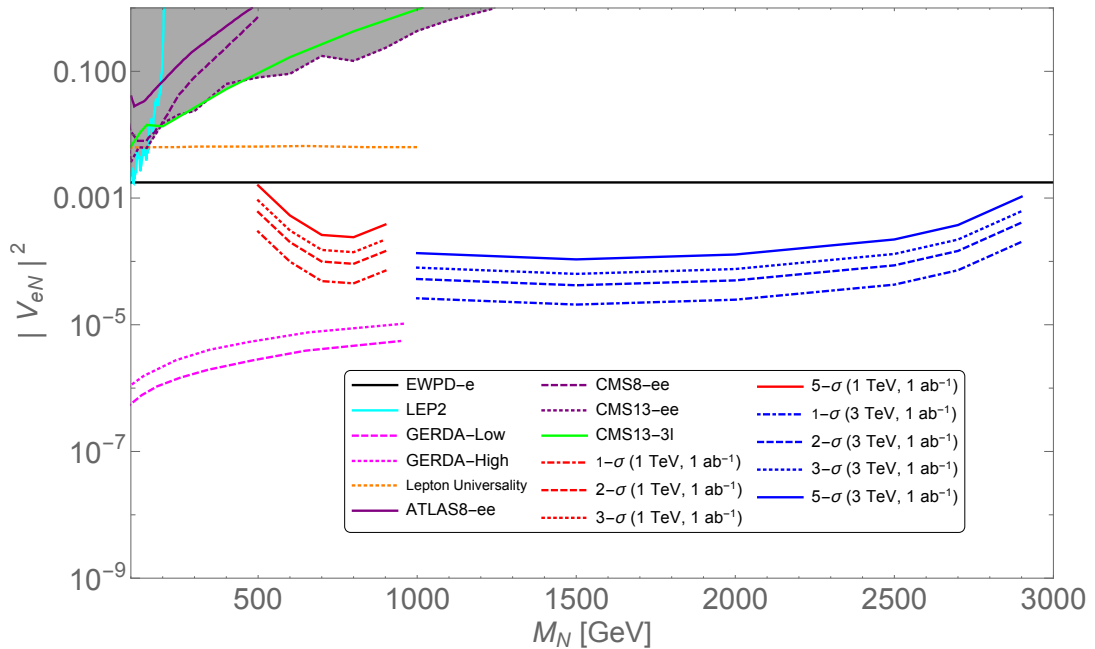


Figure 5.25: The prospective upper limits on $|V_{eN}|^2$ at the 1 TeV (red band) and 3 TeV (blue band) linear colliders at the 1 ab^{-1} luminosity for $J_b + p_T^{miss}$ signal compared to EWPD, LEP2, GERDA, ATLAS (ATLAS8- ee), CMS (CMS8 - ee) at the 8 TeV LHC, 13 TeV CMS search for $e^\pm e^\pm + 2j$ (CMS13- ee) and 13 TeV CMS search for 3ℓ (CMS13- ee) respectively.

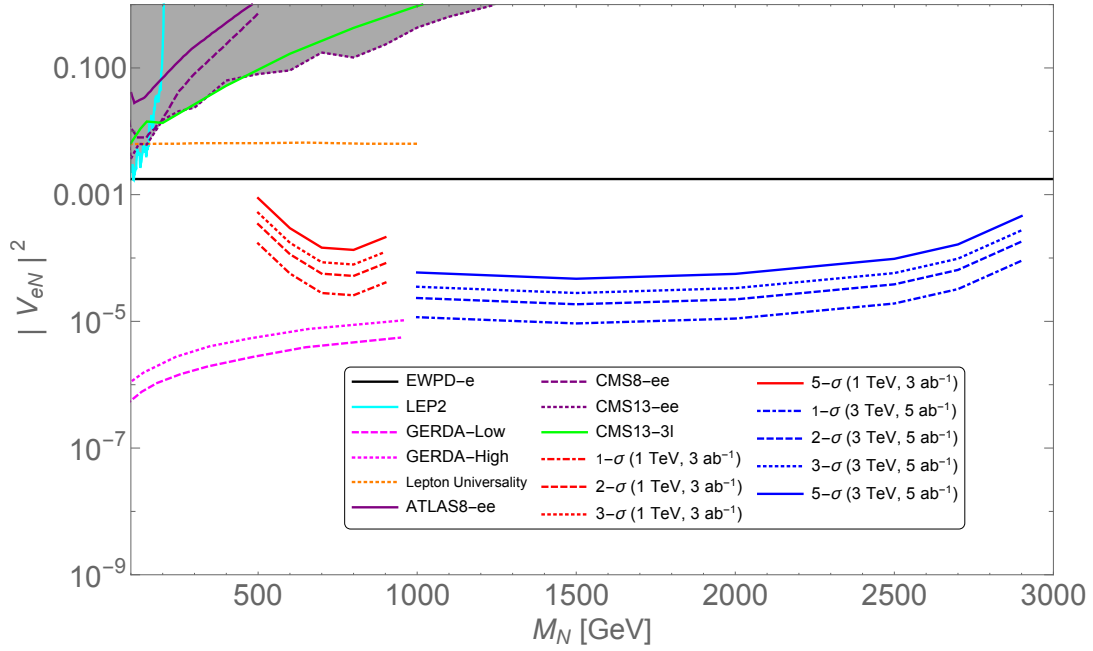


Figure 5.26: Same as Fig. 5.25 with 3(5) ab^{-1} luminosity at the 1(3) TeV linear collider.

massive RHN can sufficiently boost the W such that its hadronic decay modes can form a fat-jet. Therefore we study $e + j_1 + J$ and $e + J + p_T^{miss}$ at the LHeC and linear collider respectively. Similarly we consider another interesting mode $N \rightarrow h\nu, h \rightarrow b\bar{b}$ where a boosted SM Higgs can produce a fat b-jet and test the $J_b + p_T^{miss}$ final state at the linear collider. Simulating the events and passing through the selection cuts for the different colliders we calculate the bounds on $|V_{eN}|^2$ at different luminosities and compare with the existing bounds. We conclude that $M_N \geq 959$ GeV can be successfully probed at the 1.8 TeV at the at 5- σ C. L. with 1 ab^{-1} and 3 ab^{-1} luminosities respectively. Whereas $M_N \leq 2.9$ TeV can be probed at the 3 TeV linear collider with more than 5- σ C.L using the $e + J + p_T^{miss}$ signal. A complementary signal of $J_b + p_T^{miss}$ can be useful, too but this is weaker than the bounds obtained by the $e + J + p_T^{miss}$ final state.

6 Conclusions and Outlook

The neutrino mass mechanism is still unknown. There are many possible models proposed in the literature, some of which have been discussed in this thesis. Different models predict different mass ranges of sterile neutrinos. We have concentrated on models in which sterile neutrinos are Majorana, although there are many neutrino mass models with Dirac sterile neutrinos also.

In this thesis, we study in detail few three and four body LNV meson decays in the context of type-I seesaw and MLRSM. From non-observation of these decay modes, we derive constraints on active-sterile neutrino mixing angles or on the right handed gauge boson mass M_{W_R} , as function of sterile neutrino mass M_N in the mass range 100 MeV - 6 GeV. We obtain tight exclusion curves for the mixing elements $|V_{eN}|^2$, $|V_{\mu N}|^2$, $|V_{eN}V_{\mu N}|$. We further obtain exclusion curves for $|V_{eN}V_{\tau N}|$, $|V_{\mu N}V_{\tau N}|$, on which bounds exist only from tau decays. Most importantly we derive upper limits for $|V_{\tau N}|^2$ in the mass range (0.3-5) GeV, where it had been so far unconstrained. We find that the ongoing experiment NA62 can provide the limit $M_{W_R} > 4.6$ TeV corresponding to $M_{N_1} \sim 0.38$ GeV), which is tighter than the present collider constraint on W_R . We also find that the future experiment SHiP will result in a far more stringent bound $M_{W_R} > 18.4$ TeV for $M_N \sim 1.46$ GeV, than other existing bounds from collider and neutrinoless double beta decay searches.

We also study heavy neutrino production through a scalar LQ \tilde{R}_2 at the proposed a ep col-

luder LHeC and study many possible final states emerging from the decay of this heavy neutrino using cut based analyses. As the heavy neutrino production in this model is independent of mixing angle, the production cross-section is large and greatly improves the discovery potential of heavy neutrinos. We find that final state $\ell^- + n\text{-jets}$ ($1 \leq n \leq 2$) has the highest discovery prospect and a LQ mass upto 1.4 TeV can be discovered at more than 5σ C.L. with 100 fb^{-1} data. Among all the final states, which are coming from the channel jN_1 , the final states $\ell^- + n\text{-jets}$ ($n \geq 3$) and $\bar{b}\ell^+\tau^- + n\text{-jets}$ ($n \geq 2$) are the most optimal.

Finally, we study the discovery prospects of very heavy RHNs using fatjet signature at LHeC and linear collider. The gauge boson W or the Higgs boson h produced from very heavy RHNs is highly boosted and as a result the hadronic decay products will be highly collimated to give a fatjet. We show that using the fatjet high p_T and mass distributions we can significantly reduce the SM background which enhances the discovery prospects of these heavy RHNs. We find that the final state $e + j_1 + J$ at HE-LHeC and $e + J + p_T^{\text{miss}}$ at the linear collider, can give stronger limits on the mixing angle $|V_{eN}|^2$ than the limits obtained from the EWPD-e limit for the mass range $1 \text{ TeV} \leq M_N \leq 1.2 \text{ TeV}$ and $1 \text{ TeV} \leq M_N \leq 2.9 \text{ TeV}$ respectively.

It is important to discover whether neutrinos are Majorana or Dirac fermions and the absolute scale of neutrino masses. The possible clue can come from the $0\nu\beta\beta$ and from the cosmological observations. Nature of neutrinos and the absolute scale of neutrino masses will determine the direction of neutrino mass model building and the scale of new physics. Searches for sterile neutrinos including majorana sterile neutrinos need to be performed at all possible scales, as their discovery may provide hints of the new physics responsible for neutrino mass generation. The LNV meson decays are sensitive for the searches of low mass right handed neutrinos (in the few 100 MeV-few GeV range) and

are complementary to collider searches which are sensitive to few hundred GeV to TeV mass neutrinos. One can expect to observe these meson decays at experiments like NA62, SHiP, LHCb, FCC-ee and Belle-II due to large number of mesons production. For the mass range of 100 GeV or beyond, RH neutrinos can be searched for more easily at the proposed e^+e^- (ILC) or e^-p (LHeC) colliders compared to pp and $p\bar{p}$ colliders, due to smaller background.

Appendices

A Kinematics of four-body decay

$$B_c^- \rightarrow \bar{B}_s^0 \ell_1^- \ell_2^- \pi^+$$

To describe the kinematics of four-body decays, five independent variables are required. We choose the independent variables to be, M_{12}^2 , M_{34}^2 , θ_{12} , θ_{34} and ϕ , which for the processes, $B_c^-(p) \rightarrow \bar{B}_s^0(k_1)\ell_1^-(k_2)\ell_2^-(k_3)\pi^+(k_4)$ or $B_c^-(p) \rightarrow J/\psi(k_1)\ell_1^-(k_2)\ell_2^-(k_3)\pi^+(k_4)$ are defined as:

$$M_{12}^2 = (k_1 + k_2)^2 ; \quad M_{34}^2 = (k_3 + k_4)^2 ; \quad \cos\theta_{12} = \frac{\hat{v} \cdot \vec{k}_1}{|\vec{k}_1|} ; \quad \cos\theta_{34} = \frac{-\hat{v} \cdot \vec{k}_3}{|\vec{k}_3|}, \quad (\text{A.1})$$

$\bar{B}_s^0(J/\psi)\ell_1$ and $\ell_2\pi^+$ pair goes back to back in the B_c rest frame and we define the direction of $\bar{B}_s^0(J/\psi)\ell_1$ as \hat{v} and direction of $\ell_2\pi^+$ as $-\hat{v}$. ϕ is the angle between the normals to the planes defined in the B_c rest frame by the $\bar{B}_s^0(J/\psi)\ell_1$ pair and the $\ell_2\pi^+$ pair. The ranges of the angular variables are $0 \leq \theta_{12} \leq \pi$, $0 \leq \theta_{34} \leq \pi$, and $-\pi \leq \phi \leq \pi$. To evaluate the decay rate for the 4-body LNV $B_c^- \rightarrow \bar{B}_s^0\ell_1^-\ell_2^-\pi^+$ mode, the mod squared of the matrix element specified in eqn. (2.6) is expressed in terms of the dot products of the momenta

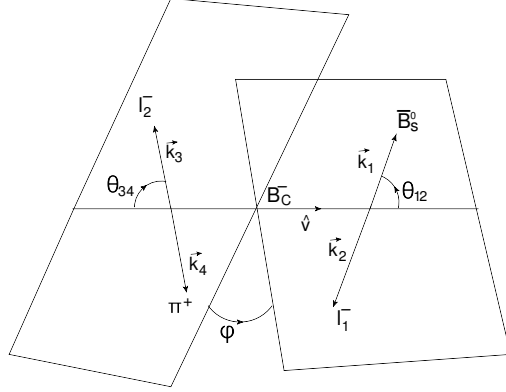


Figure A.1: Kinematics of four-body decays $B_c^- \rightarrow \bar{B}_s^0 \ell_1^- \ell_2^- \pi^+$ in the B_c rest frame.

of the final state particles as:

$$\begin{aligned}
& \sum |\mathcal{M}|^2 = G_F^4 m_N^2 |V_{cs}|^2 |V_{ud}|^2 |V_{\ell_1 N} V_{\ell_2 N}|^2 f_\pi^2 \frac{\pi}{m_N \Gamma_N} \delta(p_N^2 - m_N^2) \\
& (8(F_+^2 + 2F_+ F_- + F_-^2)(m_4^2 m^2(k_2 \cdot k_3) - 2m^2(k_2 \cdot k_4)(k_3 \cdot k_4) + 4(k_2 \cdot p)(k_3 \cdot k_4)(k_4 \cdot p) \\
& - 2m_4^2(k_2 \cdot p)(k_3 \cdot p)) + 8(F_+^2 - 2F_+ F_- + F_-^2)(m_4^2 m_1^2(k_2 \cdot k_3) - 2m_1^2(k_2 \cdot k_4)(k_3 \cdot k_4) \\
& + 4(k_1 \cdot k_2)(k_3 \cdot k_4)(k_4 \cdot k_1) - 2m_4^2(k_1 \cdot k_2)(k_1 \cdot k_3)) + 16(F_+^2 - F_-^2)(m_4^2(k_2 \cdot k_3)(p \cdot k_1) \\
& - 2(k_2 \cdot k_4)(k_3 \cdot k_4)(p \cdot k_1) + 2(p \cdot k_2)(k_3 \cdot k_4)(k_1 \cdot k_4) - m_4^2(p \cdot k_2)(k_1 \cdot k_3) + 2(k_1 \cdot k_2)(k_3 \cdot k_4) \\
& (p \cdot k_4) - m_4^2(k_1 \cdot k_2)(p \cdot k_3))) + (k_2 \leftrightarrow k_3, m_2 \leftrightarrow m_3) . \tag{A.2}
\end{aligned}$$

Following are the explicit form of the four momenta of the final state particles $\bar{B}_s^0(k_1)$, $\ell_1^-(k_2)$, $\ell_2^-(k_3)$ and $\pi^+(k_4)$ in the B_c rest frame,

$$p = [m, 0, 0, 0]; \quad (\text{A.3})$$

$$\begin{aligned} k_1^\mu = & \left[\frac{\sqrt{M_{12}^2 + X^2}}{2M_{12}^2} (M_{12}^2 + m_1^2 - m_2^2) + \frac{X}{2} \cos(\theta_{12}) \lambda^{\frac{1}{2}} \left(1, \frac{m_1^2}{M_{12}^2}, \frac{m_2^2}{M_{12}^2} \right), \right. \\ & \frac{1}{2} M_{12} \lambda^{\frac{1}{2}} \left(1, \frac{m_1^2}{M_{12}^2}, \frac{m_2^2}{M_{12}^2} \right) \sin(\theta_{12}), 0, \frac{1}{2} \sqrt{M_1^2 + X^2} \cos(\theta_{12}) \\ & \left. \lambda^{\frac{1}{2}} \left(1, \frac{m_1^2}{M_{12}^2}, \frac{m_2^2}{M_{12}^2} \right) + \frac{X}{2M_{12}^2} (M_{12}^2 + m_1^2 - m_2^2) \right]; \end{aligned} \quad (\text{A.4})$$

$$\begin{aligned} k_2^\mu = & \left[\frac{\sqrt{M_{12}^2 + X^2}}{2M_{12}^2} (M_{12}^2 + m_2^2 - m_1^2) - \frac{X}{2} \cos(\theta_{12}) \lambda^{\frac{1}{2}} \left(1, \frac{m_1^2}{M_{12}^2}, \frac{m_2^2}{M_{12}^2} \right), \right. \\ & - \frac{1}{2} M_{12} \lambda^{\frac{1}{2}} \left(1, \frac{m_1^2}{M_{12}^2}, \frac{m_2^2}{M_{12}^2} \right) \sin(\theta_{12}), 0, -\frac{1}{2} \sqrt{M_{12}^2 + X^2} \cos(\theta_{12}) \\ & \left. \lambda^{\frac{1}{2}} \left(1, \frac{m_1^2}{M_{12}^2}, \frac{m_2^2}{M_{12}^2} \right) + \frac{X}{2M_{12}^2} (M_{12}^2 + m_2^2 - m_1^2) \right]; \end{aligned} \quad (\text{A.5})$$

$$\begin{aligned} k_3^\mu = & \left[\frac{\sqrt{M_{34}^2 + X^2}}{2M_{34}^2} (M_{34}^2 + m_3^2 - m_4^2) - \frac{X}{2} \cos(\theta_{34}) \lambda^{\frac{1}{2}} \left(1, \frac{m_3^2}{M_{34}^2}, \frac{m_4^2}{M_{34}^2} \right), \right. \\ & \frac{1}{2} M_{34} \lambda^{\frac{1}{2}} \left(1, \frac{m_3^2}{M_{34}^2}, \frac{m_4^2}{M_{34}^2} \right) \sin(\theta_{34}) \cos(\phi), \frac{1}{2} M_{34} \lambda^{\frac{1}{2}} \left(1, \frac{m_3^2}{M_{34}^2}, \frac{m_4^2}{M_{34}^2} \right) \sin(\theta_{34}) \sin(\phi), \\ & \left. \frac{1}{2} \sqrt{M_{34}^2 + X^2} \cos(\theta_{34}) \lambda^{\frac{1}{2}} \left(1, \frac{m_3^2}{M_{34}^2}, \frac{m_4^2}{M_{34}^2} \right) - \frac{X}{2M_{34}^2} (M_{34}^2 + m_3^2 - m_4^2) \right]; \end{aligned} \quad (\text{A.6})$$

$$\begin{aligned} k_4^\mu = & \left[\frac{\sqrt{M_{34}^2 + X^2}}{2M_{34}^2} (M_{34}^2 + m_4^2 - m_3^2) + \frac{X}{2} \cos(\theta_{34}) \lambda^{\frac{1}{2}} \left(1, \frac{m_3^2}{M_{34}^2}, \frac{m_4^2}{M_{34}^2} \right), \right. \\ & - \frac{1}{2} M_{34} \lambda^{\frac{1}{2}} \left(1, \frac{m_3^2}{M_{34}^2}, \frac{m_4^2}{M_{34}^2} \right) \sin(\theta_{34}) \cos(\phi), -\frac{1}{2} M_{34} \lambda^{\frac{1}{2}} \left(1, \frac{m_3^2}{M_{34}^2}, \frac{m_4^2}{M_{34}^2} \right) \sin(\theta_{34}) \sin(\phi), \\ & \left. - \frac{1}{2} \sqrt{M_{34}^2 + X^2} \cos(\theta_{34}) \lambda^{\frac{1}{2}} \left(1, \frac{m_3^2}{M_{34}^2}, \frac{m_4^2}{M_{34}^2} \right) - \frac{X}{2M_{34}^2} (M_{34}^2 + m_4^2 - m_3^2) \right]; \end{aligned} \quad (\text{A.7})$$

where $X = \frac{1}{2} \lambda^{\frac{1}{2}} \left(1, \frac{M_{12}^2}{m^2}, \frac{M_{34}^2}{m^2} \right)$. The results for $B_c^- \rightarrow J/\psi \ell_1^- \ell_2^- \pi^+$ are obtained in an analogous way, although they are a bit more complicated due to the additional form factors involved in the pseudoscalar to vector meson transition.

B Partial decay widths of RH neutrino N_i in LRSM

The different partial decay widths of the RH neutrinos N_i are

$$\begin{aligned}
\Gamma(N_j \rightarrow \ell^- P^+) &= \frac{G_F^2 M_{N_j}^3}{16\pi} f_P^2 |V_{q\bar{q}'}|^2 \left(|S_{\ell_1 N_j}|^2 F_P(x_\ell, x_P) + |V_{\ell_1 N_j}|^2 \xi_1^4 F_P(x_\ell, x_P) \right. \\
&\quad \left. + 4Re[S_{\ell_1 N_j} V_{\ell_1 N_j}] \xi_1^2 x_\ell x_P^2 \lambda^{\frac{1}{2}}(1, x_\ell^2, x_P^2) \right); \\
\Gamma(N_j \rightarrow \ell^- V^+) &= \frac{G_F^2 M_{N_j}^3}{16\pi} f_V^2 |V_{q\bar{q}'}|^2 \left(|S_{\ell_1 N_j}|^2 F_V(x_\ell, x_V) + |V_{\ell_1 N_j}|^2 \xi_1^4 F_V(x_\ell, x_V) \right. \\
&\quad \left. - 12Re[S_{\ell_1 N_j} V_{\ell_1 N_j}] \xi_1^2 x_\ell x_V^2 \lambda^{\frac{1}{2}}(1, x_\ell^2, x_V^2) \right); \\
\Gamma(N_j \rightarrow \nu_\ell P^0) &= \frac{G_F^2 M_{N_j}^3}{4\pi} f_P^2 \sum_i |U_{\ell i}|^2 |S_{\ell_1 N_j}|^2 \left(K_P^2 + K_P'^2 \xi_2^4 - 2K_P K_P' \xi_2^2 \right) F_P(x_{\nu_\ell}, x_P); \\
\Gamma(N_j \rightarrow \nu_\ell V^0) &= \frac{G_F^2 M_{N_j}^3}{4\pi} f_V^2 \sum_i |U_{\ell i}|^2 |S_{\ell_1 N_j}|^2 \left(K_V^2 + K_V'^2 \xi_2^4 - 2K_V K_V' \xi_2^2 \right) F_V(x_{\nu_\ell}, x_P);
\end{aligned}$$

In the above, f_P and f_V are the decay constants for the pseudoscalar and vector mesons respectively. The values used for these are taken from PDG [129].

$$\begin{aligned}
\Gamma(N_j \rightarrow \ell_1^- \ell_2^+ \nu_{\ell_2}) &= \frac{G_F^2 M_{N_j}^5}{16\pi^3} \left(|S_{\ell_1 N_j}|^2 \sum_i |U_{\ell_2 i}|^2 I_1(x_{\ell_1}, x_{\nu_{\ell_2}}, x_{\ell_2}) + |V_{\ell_1 N_j}|^2 \sum_i |T_{\ell_2 i}|^2 \xi_1^4 \right. \\
&\quad \left. I_1(x_{\ell_1}, x_{\nu_{\ell_2}}, x_{\ell_2}) - 8Re(S_{\ell_1 N_j}^* V_{\ell_1 N_j}^* \sum_i U_{\ell_2 i} T_{\ell_2 i}) \xi_1^2 I_3(x_{\ell_1}, x_{\nu_{\ell_2}}, x_{\ell_2}) \right);
\end{aligned}$$

$$\begin{aligned}
\Gamma(N_j \rightarrow \nu_{\ell_2} \ell_2^- \ell_2^+) &= \frac{G_F^2 M_{N_j}^5}{16\pi^3} \left(|S_{\ell_2 N_j}|^2 \sum_i |U_{\ell_2 i}|^2 \left[I_1(x_{\nu_{\ell_2}}, x_{\ell_2}, x_{\ell_2}) + 2((g_V^\ell)^2 + (g_A^\ell)^2) \right. \right. \\
&I_1(x_{\nu_{\ell_2}}, x_{\ell_2}, x_{\ell_2}) + 2((g_V^\ell)^2 - (g_A^\ell)^2) I_2(x_{\nu_{\ell_2}}, x_{\ell_2}, x_{\ell_2}) + 2((g_V^\ell)^2 + (g_A^\ell)^2) \xi_2^4 \\
&I_1(x_{\nu_{\ell_2}}, x_{\ell_2}, x_{\ell_2}) + 2((g_V^\ell)^2 - (g_A^\ell)^2) \xi_2^4 I_2(x_{\nu_{\ell_2}}, x_{\ell_2}, x_{\ell_2}) - 4\xi_2^2((g_V^\ell g_V^\ell + g_A^\ell g_A^\ell) \\
&I_1(x_{\nu_{\ell_2}}, x_{\ell_2}, x_{\ell_2}) + (g_V^\ell g_V^\ell - g_A^\ell g_A^\ell) I_2(x_{\nu_{\ell_2}}, x_{\ell_2}, x_{\ell_2})) \left. \right] + |V_{\ell_2 N_j}|^2 \sum_i |T_{\ell_2 i}|^2 \xi_1^4 \\
&I_1(x_{\nu_{\ell_2}}, x_{\ell_2}, x_{\ell_2}) - 8\text{Re}[S_{\ell_2 N_j}^* V_{\ell_2 N_j}^* \sum_i U_{\ell_2 i} T_{\ell_2 i}] \xi_1^2 I_3(x_{\ell_2}, x_{\nu_{\ell_2}}, x_{\ell_2}) + 2\text{Re}[|S_{\ell_2 N_j}|^2 \sum_i |U_{\ell_2 i}|^2] \\
&\left[\xi_2^2 (g_A^\ell - g_V^\ell) I_1(x_{\nu_{\ell_2}}, x_{\ell_2}, x_{\ell_2}) - \xi_2^2 (g_A^\ell + g_V^\ell) I_2(x_{\nu_{\ell_2}}, x_{\ell_2}, x_{\ell_2}) - (g_A^\ell - g_V^\ell) I_1(x_{\nu_{\ell_2}}, x_{\ell_2}, x_{\ell_2}) \right. \\
&+ (g_A^\ell + g_V^\ell) I_2(x_{\nu_{\ell_2}}, x_{\ell_2}, x_{\ell_2}) \left. \right] - 8\text{Re}[S_{\ell_2 N_j} V_{\ell_2 N_j} \sum_i U_{\ell_2 i}^* T_{\ell_2 i}^*] \xi_1^2 \left[(g_V^\ell - g_A^\ell) \xi_2^2 I_3(x_{\nu_{\ell_2}}, x_{\ell_2}, x_{\ell_2}) \right. \\
&+ \frac{1}{4} (g_V^\ell + g_A^\ell) \xi_2^2 I_4(x_{\ell_2}, x_{\ell_2}, x_{\nu_{\ell_2}}) + (g_V^\ell - g_A^\ell) I_3(x_{\nu_{\ell_2}}, x_{\ell_2}, x_{\ell_2}) + \frac{1}{4} (g_V^\ell + g_A^\ell) \\
&I_4(x_{\ell_2}, x_{\ell_2}, x_{\nu_{\ell_2}}) \left. \right] \Bigg);
\end{aligned}$$

$$\begin{aligned}
\Gamma(N_j \rightarrow \nu_{\ell_1} \ell_2^- \ell_2^+) &= \frac{G_F^2 M_{N_j}^5}{8\pi^3} |S_{\ell_1 N_j}|^2 \sum_i |U_{\ell_1 i}|^2 \left[((g_V^\ell)^2 + (g_A^\ell)^2) I_1(x_{\nu_{\ell_1}}, x_{\ell_2}, x_{\ell_2}) \right. \\
&+ ((g_V^\ell)^2 - (g_A^\ell)^2) I_2(x_{\nu_{\ell_1}}, x_{\ell_2}, x_{\ell_2}) + ((g_V^\ell)^2 + (g_A^\ell)^2) \xi_2^4 I_1(x_{\nu_{\ell_1}}, x_{\ell_2}, x_{\ell_2}) \\
&+ ((g_V^\ell)^2 - (g_A^\ell)^2) \xi_2^4 I_2(x_{\nu_{\ell_1}}, x_{\ell_2}, x_{\ell_2}) - 2\xi_2^2 [(g_V^\ell g_V^\ell + g_A^\ell g_A^\ell) I_1(x_{\nu_{\ell_1}}, x_{\ell_2}, x_{\ell_2}) + (g_V^\ell g_V^\ell - g_A^\ell g_A^\ell) \\
&I_2(x_{\nu_{\ell_1}}, x_{\ell_2}, x_{\ell_2}) \left. \right].
\end{aligned}$$

In the above decay mode $\ell_1 \neq \ell_2$.

$$\Gamma(N_j \rightarrow \nu_\ell \nu \bar{\nu}) = \frac{G_F^2 M_{N_j}^5}{192\pi^3} |S_{\ell N_j}|^2 \sum_i |U_{\ell i}|^2 \left(1 - \sin^2 \theta_w \xi_2^2 \right)^2,$$

where $\xi_1 = \frac{M_{WL}}{M_{WR}}$, $\xi_2 = \frac{M_Z}{M_{Z'}}$, $x_i = \frac{m_i}{M_N}$ with $m_i = m_\ell, m_{P^0}, m_{V^0}, m_{P^+}, m_V^+$. The kinematical function are given by,

$$I_1(x, y, z) = \int_{(x+y)^2}^{(1-z)^2} \frac{ds}{s} (s - x^2 - y^2)(1 + z^2 - s) \lambda^{\frac{1}{2}}(s, x^2, y^2) \lambda^{\frac{1}{2}}(1, s, z^2);$$

$$I_2(x, y, z) = yz \int_{(y+z)^2}^{(1-x)^2} \frac{ds}{s} (1 + x^2 - s) \lambda^{\frac{1}{2}}(s, y^2, z^2) \lambda^{\frac{1}{2}}(1, s, x^2);$$

$$I_3(x, y, z) = xyz \int_{(x+y)^2}^{(1-z)^2} \frac{ds}{s} \lambda^{\frac{1}{2}}(s, x^2, y^2) \lambda^{\frac{1}{2}}(1, s, z^2);$$

$$I_4(x, y, z) = z \int_{(x+y)^2}^{(1-z)^2} \frac{ds}{s} \lambda^{\frac{1}{2}}(s, x^2, y^2) \lambda^{\frac{1}{2}}(1, s, z^2);$$

$$F_P(x, y) = ((1 + x^2)(1 + x^2 - y^2) - 4x^2) \lambda^{\frac{1}{2}}(1, x^2, y^2);$$

$$F_V(x, y) = ((1 - x^2)^2 + (1 + x^2)y^2 - 2y^4) \lambda^{\frac{1}{2}}(1, x^2, y^2).$$

Neutral current couplings of leptons are given by,

$$g_V^\ell = -\frac{1}{4} + \sin^2\theta_w, \quad g_A^\ell = \frac{1}{4},$$

$$g_V^{\prime\ell} = -\frac{1}{4} + \sin^2\theta_w, \quad g_A^{\prime\ell} = -\frac{1}{4} + \frac{1}{2}\sin^2\theta_w.$$

Neutral current coupling of pseudoscalar mesons are given by,

$$K_{\pi^0} = -\frac{1}{2\sqrt{2}}, \quad K'_{\pi^0} = \frac{1}{\sqrt{2}}(\frac{1}{2} - \sin^2\theta_w),$$

$$K_\eta = -\frac{1}{2\sqrt{6}}, \quad K'_\eta = \frac{1}{\sqrt{6}}(\frac{1}{2} - \sin^2\theta_w),$$

$$K_{\eta'} = \frac{1}{4\sqrt{3}}, \quad K'_{\eta'} = \frac{1}{\sqrt{3}}(-\frac{1}{4} + \frac{1}{2}\sin^2\theta_w),$$

$$K_{\eta_c} = -\frac{1}{4}, \quad K'_{\eta_c} = (\frac{1}{4} - \frac{1}{2}\sin^2\theta_w),$$

Neutral current coupling of vector mesons are given by,

$$K_{\rho^0} = \frac{1}{\sqrt{2}}(\frac{1}{2} - \sin^2\theta_w),$$

$$K_{\omega} = -\frac{1}{3\sqrt{2}}\sin^2\theta_w,$$

$$K_{\phi} = (-\frac{1}{4} + \frac{1}{3}\sin^2\theta_w),$$

$$K_{J/\psi} = (\frac{1}{4} - \frac{2}{3}\sin^2\theta_w).$$

Bibliography

- [1] **ATLAS** Collaboration, M. Aaboud *et al.*, *Search for scalar leptoquarks in pp collisions at $\sqrt{s} = 13$ TeV with the ATLAS experiment*, *New J. Phys.* **18** no. 9, (2016) 093016, [arXiv:1605.06035 \[hep-ex\]](#).
- [2] A. Atre, T. Han, S. Pascoli, and B. Zhang, *The Search for Heavy Majorana Neutrinos*, *JHEP* **05** (2009) 030, [arXiv:0901.3589 \[hep-ph\]](#).
- [3] S. Mandal and N. Sinha, *Favoured B_c Decay modes to search for a Majorana neutrino*, *Phys. Rev.* **D94** no. 3, (2016) 033001, [arXiv:1602.09112 \[hep-ph\]](#).
- [4] S. Mandal, M. Mitra, and N. Sinha, *Constraining the right-handed gauge boson mass from lepton number violating meson decays in a low scale left-right model*, *Phys. Rev.* **D96** no. 3, (2017) 035023, [arXiv:1705.01932 \[hep-ph\]](#).
- [5] G. Senjanovic and R. N. Mohapatra, *Exact Left-Right Symmetry and Spontaneous Violation of Parity*, *Phys. Rev.* **D12** (1975) 1502.
- [6] S. Mandal, M. Mitra, and N. Sinha, *Probing leptoquarks and heavy neutrinos at the LHeC*, *Phys. Rev.* **D98** no. 9, (2018) 095004, [arXiv:1807.06455 \[hep-ph\]](#).
- [7] J. C. Pati and A. Salam, *Unified Lepton-Hadron Symmetry and a Gauge Theory of the Basic Interactions*, *Phys. Rev.* **D8** (1973) 1240–1251.

- [8] A. Das, S. Jana, S. Mandal, and S. Nandi, *Probing right handed neutrinos at the LHeC and lepton colliders using fat jet signatures*, *Phys. Rev.* **D99** no. 5, (2019) 055030, [arXiv:1811.04291 \[hep-ph\]](#).
- [9] **Super-Kamiokande** Collaboration, Y. Fukuda *et al.*, *Evidence for oscillation of atmospheric neutrinos*, *Phys. Rev. Lett.* **81** (1998) 1562–1567, [arXiv:hep-ex/9807003 \[hep-ex\]](#).
- [10] **Super-Kamiokande** Collaboration, S. Fukuda *et al.*, *Constraints on neutrino oscillations using 1258 days of Super-Kamiokande solar neutrino data*, *Phys. Rev. Lett.* **86** (2001) 5656–5660, [arXiv:hep-ex/0103033 \[hep-ex\]](#).
- [11] **Super-Kamiokande** Collaboration, S. Fukuda *et al.*, *Determination of solar neutrino oscillation parameters using 1496 days of Super-Kamiokande I data*, *Phys. Lett.* **B539** (2002) 179–187, [arXiv:hep-ex/0205075 \[hep-ex\]](#).
- [12] **Super-Kamiokande** Collaboration, Y. Ashie *et al.*, *Evidence for an oscillatory signature in atmospheric neutrino oscillation*, *Phys. Rev. Lett.* **93** (2004) 101801, [arXiv:hep-ex/0404034 \[hep-ex\]](#).
- [13] B. T. Cleveland, T. Daily, R. Davis, Jr., J. R. Distel, K. Lande, C. K. Lee, P. S. Wildenhain, and J. Ullman, *Measurement of the solar electron neutrino flux with the Homestake chlorine detector*, *Astrophys. J.* **496** (1998) 505–526.
- [14] **GALLEX** Collaboration, W. Hampel *et al.*, *GALLEX solar neutrino observations: Results for GALLEX IV*, *Phys. Lett.* **B447** (1999) 127–133.
- [15] **SAGE** Collaboration, J. N. Abdurashitov *et al.*, *Solar neutrino flux measurements by the Soviet-American Gallium Experiment (SAGE) for half the 22 year solar cycle*, *J. Exp. Theor. Phys.* **95** (2002) 181–193, [arXiv:astro-ph/0204245 \[astro-ph\]](#). [*Zh. Eksp. Teor. Fiz.*122,211(2002)].

- [16] SNO Collaboration, Q. R. Ahmad *et al.*, *Measurement of the rate of $\nu_e + d \rightarrow p + p + e^-$ interactions produced by ^8B solar neutrinos at the Sudbury Neutrino Observatory*, *Phys. Rev. Lett.* **87** (2001) 071301, [arXiv:nucl-ex/0106015](#) [nucl-ex].
- [17] SNO Collaboration, Q. R. Ahmad *et al.*, *Direct evidence for neutrino flavor transformation from neutral current interactions in the Sudbury Neutrino Observatory*, *Phys. Rev. Lett.* **89** (2002) 011301, [arXiv:nucl-ex/0204008](#) [nucl-ex].
- [18] SNO Collaboration, S. N. Ahmed *et al.*, *Measurement of the total active B-8 solar neutrino flux at the Sudbury Neutrino Observatory with enhanced neutral current sensitivity*, *Phys. Rev. Lett.* **92** (2004) 181301, [arXiv:nucl-ex/0309004](#) [nucl-ex].
- [19] KamLAND Collaboration, K. Eguchi *et al.*, *First results from KamLAND: Evidence for reactor anti-neutrino disappearance*, *Phys. Rev. Lett.* **90** (2003) 021802, [arXiv:hep-ex/0212021](#) [hep-ex].
- [20] M. C. Gonzalez-Garcia, M. Maltoni, and T. Schwetz, *Global Analyses of Neutrino Oscillation Experiments*, *Nucl. Phys.* **B908** (2016) 199–217, [arXiv:1512.06856](#) [hep-ph].
- [21] Planck Collaboration, P. A. R. Ade *et al.*, *Planck 2015 results. XIII. Cosmological parameters*, *Astron. Astrophys.* **594** (2016) A13, [arXiv:1502.01589](#) [astro-ph.CO].
- [22] P. Minkowski, $\mu \rightarrow e\gamma$ at a Rate of One Out of 10^9 Muon Decays?, *Phys. Lett.* **67B** (1977) 421–428.
- [23] *M. Gell-Mann, P. Ramond and R. Slansky, Supergravity, edited by P. Van Nieuwenhuizen and D. Freedman, North Holland, Amsterdam (1980)*.

- [24] T. Yanagida, in *Proc. of the Workshop on Grand Unified Theory and Baryon Number of the Universe*, KEK, Japan, 1979 .
- [25] P. Ramond, *The Family Group in Grand Unified Theories*, in *International Symposium on Fundamentals of Quantum Theory and Quantum Field Theory Palm Coast, Florida, February 25-March 2, 1979*, pp. 265–280. 1979.
[arXiv:hep-ph/9809459](#) [hep-ph].
- [26] R. N. Mohapatra and G. Senjanovic, *Neutrino Mass and Spontaneous Parity Nonconservation*, *Phys. Rev. Lett.* **44** (1980) 912.
- [27] J. Schechter and J. W. F. Valle, *Neutrino Masses in $SU(2) \times U(1)$ Theories*, *Phys. Rev.* **D22** (1980) 2227.
- [28] J. Schechter and J. W. F. Valle, *Neutrino Decay and Spontaneous Violation of Lepton Number*, *Phys. Rev.* **D25** (1982) 774.
- [29] I. Dorsner and P. Fileviez Perez, *Upper Bound on the Mass of the Type III Seesaw Triplet in an $SU(5)$ Model*, *JHEP* **06** (2007) 029, [arXiv:hep-ph/0612216](#) [hep-ph].
- [30] B. Bajc, M. Nemevsek, and G. Senjanovic, *Probing seesaw at LHC*, *Phys. Rev.* **D76** (2007) 055011, [arXiv:hep-ph/0703080](#) [hep-ph].
- [31] A. de Gouvea, J. Jenkins, and N. Vasudevan, *Neutrino Phenomenology of Very Low-Energy Seesaws*, *Phys. Rev.* **D75** (2007) 013003, [arXiv:hep-ph/0608147](#) [hep-ph].
- [32] A. de Gouvea, *GeV seesaw, accidentally small neutrino masses, and Higgs decays to neutrinos*, [arXiv:0706.1732](#) [hep-ph].
- [33] LSND Collaboration, C. Athanassopoulos *et al.*, *The Liquid scintillator neutrino detector and LAMPF neutrino source*, *Nucl. Instrum. Meth.* **A388** (1997) 149–172, [arXiv:nucl-ex/9605002](#) [nucl-ex].

- [34] J. M. Conrad, W. C. Louis, and M. H. Shaevitz, *The LSND and MiniBooNE Oscillation Searches at High Δm^2* , *Ann. Rev. Nucl. Part. Sci.* **63** (2013) 45–67, [arXiv:1306.6494 \[hep-ex\]](#).
- [35] **MiniBooNE** Collaboration, A. A. Aguilar-Arevalo *et al.*, *A Search for electron neutrino appearance at the $\Delta m^2 \sim 1\text{eV}^2$ scale*, *Phys. Rev. Lett.* **98** (2007) 231801, [arXiv:0704.1500 \[hep-ex\]](#).
- [36] **MiniBooNE** Collaboration, A. A. Aguilar-Arevalo *et al.*, *A Search for Electron Antineutrino Appearance at the $\Delta m^2 \sim 1\text{eV}^2$ Scale*, *Phys. Rev. Lett.* **103** (2009) 111801, [arXiv:0904.1958 \[hep-ex\]](#).
- [37] **MiniBooNE** Collaboration, A. A. Aguilar-Arevalo *et al.*, *Improved Search for $\bar{\nu}_\mu \rightarrow \bar{\nu}_e$ Oscillations in the MiniBooNE Experiment*, *Phys. Rev. Lett.* **110** (2013) 161801, [arXiv:1303.2588 \[hep-ex\]](#).
- [38] **Double Chooz** Collaboration, Y. Abe *et al.*, *Reactor electron antineutrino disappearance in the Double Chooz experiment*, *Phys. Rev.* **D86** (2012) 052008, [arXiv:1207.6632 \[hep-ex\]](#).
- [39] **Daya Bay** Collaboration, F. P. An *et al.*, *Observation of electron-antineutrino disappearance at Daya Bay*, *Phys. Rev. Lett.* **108** (2012) 171803, [arXiv:1203.1669 \[hep-ex\]](#).
- [40] **RENO** Collaboration, J. K. Ahn *et al.*, *Observation of Reactor Electron Antineutrino Disappearance in the RENO Experiment*, *Phys. Rev. Lett.* **108** (2012) 191802, [arXiv:1204.0626 \[hep-ex\]](#).
- [41] S. Dodelson and L. M. Widrow, *Sterile-neutrinos as dark matter*, *Phys. Rev. Lett.* **72** (1994) 17–20, [arXiv:hep-ph/9303287 \[hep-ph\]](#).

- [42] X.-D. Shi and G. M. Fuller, *A New dark matter candidate: Nonthermal sterile neutrinos*, *Phys. Rev. Lett.* **82** (1999) 2832–2835, [arXiv:astro-ph/9810076](#) [[astro-ph](#)].
- [43] K. Abazajian, G. M. Fuller, and M. Patel, *Sterile neutrino hot, warm, and cold dark matter*, *Phys. Rev.* **D64** (2001) 023501, [arXiv:astro-ph/0101524](#) [[astro-ph](#)].
- [44] K. N. Abazajian and G. M. Fuller, *Bulk QCD thermodynamics and sterile neutrino dark matter*, *Phys. Rev.* **D66** (2002) 023526, [arXiv:astro-ph/0204293](#) [[astro-ph](#)].
- [45] G. M. Fuller, A. Kusenko, I. Mocioiu, and S. Pascoli, *Pulsar kicks from a dark-matter sterile neutrino*, *Phys. Rev.* **D68** (2003) 103002, [arXiv:astro-ph/0307267](#) [[astro-ph](#)].
- [46] K. Abazajian, *Production and evolution of perturbations of sterile neutrino dark matter*, *Phys. Rev.* **D73** (2006) 063506, [arXiv:astro-ph/0511630](#) [[astro-ph](#)].
- [47] A. Kusenko, *Sterile neutrinos: The Dark side of the light fermions*, *Phys. Rept.* **481** (2009) 1–28, [arXiv:0906.2968](#) [[hep-ph](#)].
- [48] A. Kusenko, *Detecting sterile dark matter in space*, *Int. J. Mod. Phys.* **D16** (2008) 2325–2335, [arXiv:astro-ph/0608096](#) [[astro-ph](#)].
- [49] T. Asaka, M. Shaposhnikov, and A. Kusenko, *Opening a new window for warm dark matter*, *Phys. Lett.* **B638** (2006) 401–406, [arXiv:hep-ph/0602150](#) [[hep-ph](#)].
- [50] P. L. Biermann and A. Kusenko, *Relic keV sterile neutrinos and reionization*, *Phys. Rev. Lett.* **96** (2006) 091301, [arXiv:astro-ph/0601004](#) [[astro-ph](#)].

- [51] A. Boyarsky, O. Ruchayskiy, and M. Shaposhnikov, *The Role of sterile neutrinos in cosmology and astrophysics*, *Ann. Rev. Nucl. Part. Sci.* **59** (2009) 191–214, [arXiv:0901.0011 \[hep-ph\]](#).
- [52] M. Shaposhnikov and I. Tkachev, *The nuMSM, inflation, and dark matter*, *Phys. Lett.* **B639** (2006) 414–417, [arXiv:hep-ph/0604236 \[hep-ph\]](#).
- [53] H. J. de Vega and N. G. Sanchez, *Model independent analysis of dark matter points to a particle mass at the keV scale*, *Mon. Not. Roy. Astron. Soc.* **404** (2010) 885, [arXiv:0901.0922 \[astro-ph.CO\]](#).
- [54] H. J. de Vega, P. Salucci, and N. G. Sanchez, *The mass of the dark matter particle from theory and observations*, *New Astron.* **17** (2012) 653–666, [arXiv:1004.1908 \[astro-ph.CO\]](#).
- [55] H. J. de Vega and N. G. Sanchez, *Warm dark matter in the galaxies: theoretical and observational progresses. Highlights and conclusions of the chalonge meudon workshop 2011*, [arXiv:1109.3187 \[astro-ph.CO\]](#).
- [56] C. Destri, H. J. de Vega, and N. G. Sanchez, *Fermionic warm dark matter produces galaxy cores in the observed scales because of quantum mechanics*, *New Astron.* **22** (2013) 39–50, [arXiv:1204.3090 \[astro-ph.CO\]](#).
- [57] M. Drewes *et al.*, *A White Paper on keV Sterile Neutrino Dark Matter*, *JCAP* **1701** no. 01, (2017) 025, [arXiv:1602.04816 \[hep-ph\]](#).
- [58] F. S. Queiroz and K. Sinha, *The Poker Face of the Majoron Dark Matter Model: LUX to keV Line*, *Phys. Lett.* **B735** (2014) 69–74, [arXiv:1404.1400 \[hep-ph\]](#).
- [59] G. M. Fuller, A. Kusenko, and K. Petraki, *Heavy sterile neutrinos and supernova explosions*, *Phys. Lett.* **B670** (2009) 281–284, [arXiv:0806.4273 \[astro-ph\]](#).
- [60] R. E. Shrock, *New Tests For, and Bounds On, Neutrino Masses and Lepton Mixing*, *Phys. Lett.* **96B** (1980) 159–164.

- [61] G. Cvetič, C. Dib, S. K. Kang, and C. S. Kim, *Probing Majorana neutrinos in rare K and D , D_s , B , B_c meson decays*, *Phys. Rev.* **D82** (2010) 053010, [arXiv:1005.4282 \[hep-ph\]](#).
- [62] G. Cvetič, C. Dib, and C. S. Kim, *Probing Majorana neutrinos in rare $\pi^+ \rightarrow e^+ e^+ \mu^- \nu$ decays*, *JHEP* **06** (2012) 149, [arXiv:1203.0573 \[hep-ph\]](#).
- [63] J. C. Helo, S. Kovalenko, and I. Schmidt, *Sterile neutrinos in lepton number and lepton flavor violating decays*, *Nucl. Phys.* **B853** (2011) 80–104, [arXiv:1005.1607 \[hep-ph\]](#).
- [64] CLEO Collaboration, Q. He *et al.*, *Search for rare and forbidden decays $D^+ \rightarrow h^+ e^- e^+$* , *Phys. Rev. Lett.* **95** (2005) 221802, [arXiv:hep-ex/0508031 \[hep-ex\]](#).
- [65] CLEO Collaboration, Y. Kubota *et al.*, *The CLEO-II detector*, *Nucl. Instrum. Meth.* **A320** (1992) 66–113.
- [66] CLEO Collaboration, P. Rubin *et al.*, *Search for rare and forbidden decays of charm and charmed-strange mesons to final states $h^+ - e^- + e^+$* , *Phys. Rev.* **D82** (2010) 092007, [arXiv:1009.1606 \[hep-ex\]](#).
- [67] FOCUS Collaboration, J. M. Link *et al.*, *Search for rare and forbidden three body dimuon decays of the charmed mesons D^+ and $D(s)^+$* , *Phys. Lett.* **B572** (2003) 21–31, [arXiv:hep-ex/0306049 \[hep-ex\]](#).
- [68] BaBar Collaboration, J. P. Lees *et al.*, *Searches for Rare or Forbidden Semileptonic Charm Decays*, *Phys. Rev.* **D84** (2011) 072006, [arXiv:1107.4465 \[hep-ex\]](#).
- [69] LHCb Collaboration, R. Aaij *et al.*, *Search for the lepton number violating decays $B^+ \rightarrow \pi^- \mu^+ \mu^+$ and $B^+ \rightarrow K^- \mu^+ \mu^+$* , *Phys. Rev. Lett.* **108** (2012) 101601, [arXiv:1110.0730 \[hep-ex\]](#).

- [70] M. Dittmar, A. Santamaria, M. C. Gonzalez-Garcia, and J. W. F. Valle, *Production Mechanisms and Signatures of Isosinglet Neutral Heavy Leptons in Z^0 Decays*, *Nucl. Phys.* **B332** (1990) 1–19.
- [71] F. del Aguila, J. A. Aguilar-Saavedra, and R. Pittau, *Neutrino physics at large colliders*, *J. Phys. Conf. Ser.* **53** (2006) 506–527, [arXiv:hep-ph/0606198](#) [[hep-ph](#)].
- [72] W. Buchmuller and C. Greub, *Heavy Majorana neutrinos in electron - positron and electron - proton collisions*, *Nucl. Phys.* **B363** (1991) 345–368.
- [73] F. M. L. Almeida, Jr., Y. do Amaral Coutinho, J. A. Martins Simoes, and M. A. B. do Vale, *Neutral heavy lepton production at next high-energy $e^+ e^-$ linear colliders*, *Phys. Rev.* **D63** (2001) 075005, [arXiv:hep-ph/0008201](#) [[hep-ph](#)].
- [74] F. F. Deppisch, P. S. Bhupal Dev, and A. Pilaftsis, *Neutrinos and Collider Physics*, *New J. Phys.* **17** no. 7, (2015) 075019, [arXiv:1502.06541](#) [[hep-ph](#)].
- [75] S. Banerjee, P. S. B. Dev, A. Ibarra, T. Mandal, and M. Mitra, *Prospects of Heavy Neutrino Searches at Future Lepton Colliders*, *Phys. Rev.* **D92** (2015) 075002, [arXiv:1503.05491](#) [[hep-ph](#)].
- [76] S. Bray, J. S. Lee, and A. Pilaftsis, *Heavy Majorana neutrino production at e^- gamma colliders*, *Phys. Lett.* **B628** (2005) 250–261, [arXiv:hep-ph/0508077](#) [[hep-ph](#)].
- [77] W.-Y. Keung and G. Senjanovic, *Majorana Neutrinos and the Production of the Right-handed Charged Gauge Boson*, *Phys. Rev. Lett.* **50** (1983) 1427.
- [78] T.-H. Ho, C.-R. Ching, and Z.-J. Tao, *Production of right-handed gauge boson and heavy Majorana neutrino in SSC*, *Phys. Rev.* **D42** (1990) 2265–2273.
- [79] D. A. Dicus, D. D. Karatas, and P. Roy, *Lepton nonconservation at supercollider energies*, *Phys. Rev.* **D44** (1991) 2033–2037.

- [80] A. Datta, M. Guchait, and D. P. Roy, *Prospect of heavy right-handed neutrino search at SSC / CERN LHC energies*, *Phys. Rev.* **D47** (1993) 961–966, [arXiv:hep-ph/9208228 \[hep-ph\]](#).
- [81] A. Ferrari, J. Collot, M.-L. Andrieux, B. Belhorma, P. de Saintignon, J.-Y. Hostachy, P. Martin, and M. Wielers, *Sensitivity study for new gauge bosons and right-handed Majorana neutrinos in pp collisions at $s = 14\text{-TeV}$* , *Phys. Rev.* **D62** (2000) 013001.
- [82] A. Ali, A. V. Borisov, and N. B. Zamorin, *Majorana neutrinos and same sign dilepton production at LHC and in rare meson decays*, *Eur. Phys. J.* **C21** (2001) 123–132, [arXiv:hep-ph/0104123 \[hep-ph\]](#).
- [83] F. M. L. Almeida, Jr., Y. do Amaral Coutinho, J. A. Martins Simoes, and M. A. B. do Vale, *On a signature for heavy Majorana neutrinos in hadronic collisions*, *Phys. Rev.* **D62** (2000) 075004, [arXiv:hep-ph/0002024 \[hep-ph\]](#).
- [84] T. Han and B. Zhang, *Signatures for Majorana neutrinos at hadron colliders*, *Phys. Rev. Lett.* **97** (2006) 171804, [arXiv:hep-ph/0604064 \[hep-ph\]](#).
- [85] P. S. B. Dev, A. Pilaftsis, and U.-k. Yang, *New Production Mechanism for Heavy Neutrinos at the LHC*, *Phys. Rev. Lett.* **112** no. 8, (2014) 081801, [arXiv:1308.2209 \[hep-ph\]](#).
- [86] A. Das, P. S. Bhupal Dev, and N. Okada, *Direct bounds on electroweak scale pseudo-Dirac neutrinos from $\sqrt{s} = 8\text{ TeV}$ LHC data*, *Phys. Lett.* **B735** (2014) 364–370, [arXiv:1405.0177 \[hep-ph\]](#).
- [87] T. G. Rizzo, *INVERSE NEUTRINOLESS DOUBLE BETA DECAY*, *Phys. Lett.* **116B** (1982) 23–28.
- [88] C. A. Heusch and P. Minkowski, *Lepton flavor violation induced by heavy Majorana neutrinos*, *Nucl. Phys.* **B416** (1994) 3–45.

- [89] S. Bar-Shalom, N. G. Deshpande, G. Eilam, J. Jiang, and A. Soni, *Majorana neutrinos and lepton-number-violating signals in top-quark and W-boson rare decays*, *Phys. Lett.* **B643** (2006) 342–347, [arXiv:hep-ph/0608309](https://arxiv.org/abs/hep-ph/0608309) [hep-ph].
- [90] N. Quintero, G. Lopez Castro, and D. Delepine, *Lepton number violation in top quark and neutral B meson decays*, *Phys. Rev.* **D84** (2011) 096011, [arXiv:1108.6009](https://arxiv.org/abs/1108.6009) [hep-ph]. [Erratum: *Phys. Rev.*D86,079905(2012)].
- [91] S. L. Glashow, *Partial Symmetries of Weak Interactions*, *Nucl. Phys.* **22** (1961) 579–588.
- [92] S. Weinberg, *A Model of Leptons*, *Phys. Rev. Lett.* **19** (1967) 1264–1266.
- [93] R. N. Mohapatra, *Mechanism for understanding small neutrino mass in superstring theories*, *Phys. Rev. Lett.* **56** (Feb, 1986) 561–563. <https://link.aps.org/doi/10.1103/PhysRevLett.56.561>.
- [94] R. N. Mohapatra and J. W. F. Valle, *Neutrino mass and baryon-number nonconservation in superstring models*, *Phys. Rev. D* **34** (Sep, 1986) 1642–1645. <https://link.aps.org/doi/10.1103/PhysRevD.34.1642>.
- [95] M. Malinsky, J. C. Romao, and J. W. F. Valle, *Novel supersymmetric SO(10) seesaw mechanism*, *Phys. Rev. Lett.* **95** (2005) 161801, [arXiv:hep-ph/0506296](https://arxiv.org/abs/hep-ph/0506296) [hep-ph].
- [96] M. Hirsch, S. Morisi, and J. W. F. Valle, *A4-based tri-bimaximal mixing within inverse and linear seesaw schemes*, *Phys. Lett.* **B679** (2009) 454–459, [arXiv:0905.3056](https://arxiv.org/abs/0905.3056) [hep-ph].
- [97] R. N. Mohapatra, S. Nasri, and H.-B. Yu, *Seesaw right handed neutrino as the sterile neutrino for LSND*, *Phys. Rev.* **D72** (2005) 033007, [arXiv:hep-ph/0505021](https://arxiv.org/abs/hep-ph/0505021) [hep-ph].

- [98] S. Weinberg, *Baryon and Lepton Nonconserving Processes*, *Phys. Rev. Lett.* **43** (1979) 1566–1570.
- [99] M. Mitra, G. Senjanovic, and F. Vissani, *Neutrinoless Double Beta Decay and Heavy Sterile Neutrinos*, *Nucl. Phys.* **B856** (2012) 26–73, [arXiv:1108.0004](https://arxiv.org/abs/1108.0004) [hep-ph].
- [100] J. C. Pati and A. Salam, *Lepton Number as the Fourth Color*, *Phys. Rev.* **D10** (1974) 275–289. [Erratum: *Phys. Rev.* **D11**, 703(1975)].
- [101] R. N. Mohapatra and J. C. Pati, *Left-Right Gauge Symmetry and an Isoconjugate Model of CP Violation*, *Phys. Rev.* **D11** (1975) 566–571.
- [102] R. N. Mohapatra and J. C. Pati, *A Natural Left-Right Symmetry*, *Phys. Rev.* **D11** (1975) 2558.
- [103] M. Magg and C. Wetterich, *Neutrino Mass Problem and Gauge Hierarchy*, *Phys. Lett.* **94B** (1980) 61–64.
- [104] G. Lazarides, Q. Shafi, and C. Wetterich, *Proton Lifetime and Fermion Masses in an SO(10) Model*, *Nucl. Phys.* **B181** (1981) 287–300.
- [105] W. Grimus and L. Lavoura, *The Seesaw mechanism at arbitrary order: Disentangling the small scale from the large scale*, *JHEP* **11** (2000) 042, [arXiv:hep-ph/0008179](https://arxiv.org/abs/hep-ph/0008179) [hep-ph].
- [106] V. Tello, *Connections between the high and low energy violation of Lepton and Flavor numbers in the minimal left-right symmetric model*. PhD thesis, SISSA, Trieste, 2012. <http://hdl.handle.net/1963/6272>.
- [107] R. N. Mohapatra and D. P. Sidhu, *Gauge Theories of Weak Interactions with Left-Right Symmetry and the Structure of Neutral Currents*, *Phys. Rev.* **D16** (1977) 2843.

- [108] A. Abada, V. De Romeri, M. Lucente, A. M. Teixeira, and T. Toma, *Effective Majorana mass matrix from tau and pseudoscalar meson lepton number violating decays*, *JHEP* **02** (2018) 169, [arXiv:1712.03984 \[hep-ph\]](#).
- [109] D. I. Britton *et al.*, *Measurement of the $\pi^+ \rightarrow e^+$ neutrino branching ratio*, *Phys. Rev. Lett.* **68** (1992) 3000–3003.
- [110] G. Bernardi *et al.*, *FURTHER LIMITS ON HEAVY NEUTRINO COUPLINGS*, *Phys. Lett.* **B203** (1988) 332–334.
- [111] NA3 Collaboration, J. Badier *et al.*, *Mass and Lifetime Limits on New Longlived Particles in 300-GeV/ π^- Interactions*, *Z. Phys.* **C31** (1986) 21.
- [112] CHARM Collaboration, F. Bergsma *et al.*, *A Search for Decays of Heavy Neutrinos in the Mass Range 0.5-GeV to 2.8-GeV*, *Phys. Lett.* **166B** (1986) 473–478.
- [113] WA66 Collaboration, A. M. Cooper-Sarkar *et al.*, *Search for Heavy Neutrino Decays in the BEBC Beam Dump Experiment*, *Phys. Lett.* **160B** (1985) 207–211.
- [114] FMMF Collaboration, E. Gallas *et al.*, *Search for neutral weakly interacting massive particles in the Fermilab Tevatron wide band neutrino beam*, *Phys. Rev.* **D52** (1995) 6–14.
- [115] NuTeV, E815 Collaboration, A. Vaitaitis *et al.*, *Search for neutral heavy leptons in a high-energy neutrino beam*, *Phys. Rev. Lett.* **83** (1999) 4943–4946, [arXiv:hep-ex/9908011 \[hep-ex\]](#).
- [116] CHARM II Collaboration, P. Vilain *et al.*, *Search for heavy isosinglet neutrinos*, *Phys. Lett.* **B343** (1995) 453–458. [*Phys. Lett.*B351,387(1995)].
- [117] DELPHI Collaboration, P. Abreu *et al.*, *Search for neutral heavy leptons produced in Z decays*, *Z. Phys.* **C74** (1997) 57–71. [Erratum: *Z. Phys.*C75,580(1997)].

- [118] **L3** Collaboration, O. Adriani *et al.*, *Search for isosinglet neutral heavy leptons in Z^0 decays*, *Phys. Lett.* **B295** (1992) 371–382.
- [119] **NOMAD** Collaboration, P. Astier *et al.*, *Search for heavy neutrinos mixing with tau neutrinos*, *Phys. Lett.* **B506** (2001) 27–38, [arXiv:hep-ex/0101041](#) [[hep-ex](#)].
- [120] F. del Aguila, J. de Blas, and M. Perez-Victoria, *Effects of new leptons in Electroweak Precision Data*, *Phys. Rev.* **D78** (2008) 013010, [arXiv:0803.4008](#) [[hep-ph](#)].
- [121] **GERDA** Collaboration, M. Agostini *et al.*, *Results on Neutrinoless Double- β Decay of ^{76}Ge from Phase I of the GERDA Experiment*, *Phys. Rev. Lett.* **111** no. 12, (2013) 122503, [arXiv:1307.4720](#) [[nucl-ex](#)].
- [122] **LHCb** Collaboration, R. Aaij *et al.*, *Observation of the Decay $B_c^+ \rightarrow B_s^0 \pi^+$* , *Phys. Rev. Lett.* **111** no. 18, (2013) 181801, [arXiv:1308.4544](#) [[hep-ex](#)].
- [123] **ATLAS** Collaboration, G. Aad *et al.*, *Study of the $B_c^+ \rightarrow J/\psi D_s^+$ and $B_c^+ \rightarrow J/\psi D_s^{*+}$ decays with the ATLAS detector*, *Eur. Phys. J.* **C76** no. 1, (2016) 4, [arXiv:1507.07099](#) [[hep-ex](#)].
- [124] **CMS** Collaboration, V. Khachatryan *et al.*, *Measurement of the ratio of the production cross sections times branching fractions of $B_c^\pm \rightarrow J/\psi \pi^\pm$ and $B^\pm \rightarrow J/\psi K^\pm$ and $\mathcal{B}(B_c^\pm \rightarrow J/\psi \pi^\pm \pi^\pm \pi^\mp)/\mathcal{B}(B_c^\pm \rightarrow J/\psi \pi^\pm)$ in pp collisions at $\sqrt{s} = 7$ TeV*, *JHEP* **01** (2015) 063, [arXiv:1410.5729](#) [[hep-ex](#)].
- [125] **LHCb** Collaboration, R. Aaij *et al.*, *Measurements of B_c^+ production and mass with the $B_c^+ \rightarrow J/\psi \pi^+$ decay*, *Phys. Rev. Lett.* **109** (2012) 232001, [arXiv:1209.5634](#) [[hep-ex](#)].
- [126] **Quarkonium Working Group** Collaboration, N. Brambilla *et al.*, *Heavy quarkonium physics*, [arXiv:hep-ph/0412158](#) [[hep-ph](#)].

- [127] V. V. Kiselev, A. E. Kovalsky, and A. K. Likhoded, *B_c decays and lifetime in QCD sum rules*, *Nucl. Phys.* **B585** (2000) 353–382, [arXiv:hep-ph/0002127](#) [[hep-ph](#)].
- [128] V. V. Kiselev, *Exclusive decays and lifetime of B_c meson in QCD sum rules*, [arXiv:hep-ph/0211021](#) [[hep-ph](#)].
- [129] **Particle Data Group** Collaboration, K. A. Olive *et al.*, *Review of Particle Physics*, *Chin. Phys.* **C38** (2014) 090001.
- [130] G. Lopez Castro and N. Quintero, *Lepton number violating four-body tau lepton decays*, *Phys. Rev.* **D85** (2012) 076006, [arXiv:1203.0537](#) [[hep-ph](#)]. [Erratum: *Phys. Rev.*D86,079904(2012)].
- [131] H. Yuan, T. Wang, G.-L. Wang, W.-L. Ju, and J.-M. Zhang, *Lepton-number violating four-body decays of heavy mesons*, *JHEP* **08** (2013) 066, [arXiv:1304.3810](#) [[hep-ph](#)].
- [132] H.-R. Dong, F. Feng, and H.-B. Li, *Lepton number violation in D meson decay*, *Chin. Phys.* **C39** no. 1, (2015) 013101, [arXiv:1305.3820](#) [[hep-ph](#)].
- [133] G. Lopez Castro and N. Quintero, *Lepton number violation in tau lepton decays*, *Nucl. Phys. Proc. Suppl.* **253-255** (2014) 12–15, [arXiv:1212.0037](#) [[hep-ph](#)].
- [134] **LHCb** Collaboration, R. Aaij *et al.*, *Searches for Majorana neutrinos in B⁻ decays*, *Phys. Rev.* **D85** (2012) 112004, [arXiv:1201.5600](#) [[hep-ex](#)].
- [135] C.-H. Chang, C. Driouichi, P. Eerola, and X. G. Wu, *BCVEGPY: An Event generator for hadronic production of the B_c meson*, *Comput. Phys. Commun.* **159** (2004) 192–224, [arXiv:hep-ph/0309120](#) [[hep-ph](#)].
- [136] *Our crude estimate is based on private communication with Vanya Belyaev from the LHCb collaboration .*

- [137] **LHCb** Collaboration, R. Aaij *et al.*, *Measurement of B_c^+ production in proton-proton collisions at $\sqrt{s} = 8$ TeV*, *Phys. Rev. Lett.* **114** (2015) 132001, [arXiv:1411.2943 \[hep-ex\]](#).
- [138] A. de Gouvêa and A. Kobach, *Global Constraints on a Heavy Neutrino*, *Phys. Rev.* **D93** no. 3, (2016) 033005, [arXiv:1511.00683 \[hep-ph\]](#).
- [139] **CHARM II** Collaboration, P. Vilain *et al.*, *Search for heavy isosinglet neutrinos*, *Phys. Lett.* **B343** (1995) 453–458. [*Phys. Lett.*B351,387(1995)].
- [140] J. Orloff, A. N. Rozanov, and C. Santoni, *Limits on the mixing of tau neutrino to heavy neutrinos*, *Phys. Lett.* **B550** (2002) 8–15, [arXiv:hep-ph/0208075 \[hep-ph\]](#).
- [141] **NOMAD** Collaboration, P. Astier *et al.*, *Search for heavy neutrinos mixing with tau neutrinos*, *Phys. Lett.* **B506** (2001) 27–38, [arXiv:hep-ex/0101041 \[hep-ex\]](#).
- [142] **DELPHI** Collaboration, P. Abreu *et al.*, *Search for neutral heavy leptons produced in Z decays*, *Z. Phys.* **C74** (1997) 57–71. [Erratum: *Z. Phys.*C75,580(1997)].
- [143] A. Kobach and S. Dobbs, *Heavy Neutrinos and the Kinematics of Tau Decays*, *Phys. Rev.* **D91** no. 5, (2015) 053006, [arXiv:1412.4785 \[hep-ph\]](#).
- [144] W.-Y. Keung and G. Senjanović, *Majorana neutrinos and the production of the right-handed charged gauge boson*, *Phys. Rev. Lett.* **50** (May, 1983) 1427–1430. <https://link.aps.org/doi/10.1103/PhysRevLett.50.1427>.
- [145] M. Mitra, R. Ruiz, D. J. Scott, and M. Spannowsky, *Neutrino Jets from High-Mass W_R Gauge Bosons in TeV-Scale Left-Right Symmetric Models*, *Phys. Rev.* **D94** no. 9, (2016) 095016, [arXiv:1607.03504 \[hep-ph\]](#).

- [146] **CMS** Collaboration, V. Khachatryan *et al.*, *Search for heavy neutrinos and W bosons with right-handed couplings in proton-proton collisions at $\sqrt{s} = 8$ TeV*, *Eur. Phys. J.* **C74** no. 11, (2014) 3149, [arXiv:1407.3683 \[hep-ex\]](#).
- [147] **ATLAS** Collaboration, G. Aad *et al.*, *Search for heavy Majorana neutrinos with the ATLAS detector in pp collisions at $\sqrt{s} = 8$ TeV*, *JHEP* **07** (2015) 162, [arXiv:1506.06020 \[hep-ex\]](#).
- [148] F. F. Deppisch, P. S. Bhupal Dev, and A. Pilaftsis, *Neutrinos and Collider Physics*, *New J. Phys.* **17** no. 7, (2015) 075019, [arXiv:1502.06541 \[hep-ph\]](#).
- [149] G. Cvetič, C. Dib, S. K. Kang, and C. S. Kim, *Probing Majorana neutrinos in rare K and D, D_s, B, B_c meson decays*, *Phys. Rev.* **D82** (2010) 053010, [arXiv:1005.4282 \[hep-ph\]](#).
- [150] **LHCb** Collaboration, R. Aaij *et al.*, *Searches for Majorana neutrinos in B⁻ decays*, *Phys. Rev.* **D85** (2012) 112004, [arXiv:1201.5600 \[hep-ex\]](#).
- [151] T. Asaka and H. Ishida, *Lepton number violation by heavy Majorana neutrino in B decays*, *Phys. Lett.* **B763** (2016) 393–396, [arXiv:1609.06113 \[hep-ph\]](#).
- [152] G. J. Feldman and R. D. Cousins, *A Unified approach to the classical statistical analysis of small signals*, *Phys. Rev.* **D57** (1998) 3873–3889, [arXiv:physics/9711021 \[physics.data-an\]](#).
- [153] <https://na62.web.cern.ch/na62/>.
- [154] *SuperKEKB WEB page*, <http://www-superkekb.kek.jp>.
- [155] *Our estimate is based on private communication with Karim Trabelsi from the Belle collaboration.*
- [156] **Belle** Collaboration, D. Liventsev *et al.*, *Search for heavy neutrinos at Belle*, *Phys. Rev.* **D87** no. 7, (2013) 071102, [arXiv:1301.1105 \[hep-ex\]](#). [Erratum: *Phys. Rev.* **D95**, no. 9, 099903 (2017)].

- [157] **LHCb** Collaboration, R. Aaij *et al.*, *Search for Majorana neutrinos in $B^- \rightarrow \pi^+ \mu^- \mu^-$ decays*, *Phys. Rev. Lett.* **112** no. 13, (2014) 131802, [arXiv:1401.5361 \[hep-ex\]](#).
- [158] **LHCb** Collaboration, R. Aaij *et al.*, *Measurement of the b -quark production cross-section in 7 and 13 TeV pp collisions*, *Phys. Rev. Lett.* **118** no. 5, (2017) 052002, [arXiv:1612.05140 \[hep-ex\]](#). [Erratum: *Phys. Rev. Lett.* 119, no. 16, 169901(2017)].
- [159] **LHCb** Collaboration, R. Aaij *et al.*, *Measurements of prompt charm production cross-sections in pp collisions at $\sqrt{s} = 13$ TeV*, *JHEP* **03** (2016) 159, [arXiv:1510.01707 \[hep-ex\]](#). [Erratum: *JHEP* 05, 074(2017)].
- [160] Marina Artuso, *Talk given at ICHEP 2016 on behalf of LHCb collaboration*, <https://cds.cern.ch/record/2206834/files/LHCb-TALK-2016-222.pdf>.
- [161] *FCC-ee WEB page*, <http://tlep.web.cern.ch>.
- [162] **Particle Data Group** Collaboration, K. A. Olive *et al.*, *Review of Particle Physics*, *Chin. Phys.* **C38** (2014) 090001.
- [163] **Heavy Flavor Averaging Group (HFAG)** Collaboration, Y. Amhis *et al.*, *Averages of b -hadron, c -hadron, and τ -lepton properties as of summer 2014*, [arXiv:1412.7515 \[hep-ex\]](#).
- [164] *SHiP WEB page*, <http://ship.web.cern.ch/ship/>.
- [165] S. Alekhin *et al.*, *A facility to Search for Hidden Particles at the CERN SPS: the SHiP physics case*, *Rept. Prog. Phys.* **79** no. 12, (2016) 124201, [arXiv:1504.04855 \[hep-ph\]](#).
- [166] D. Gorbunov and M. Shaposhnikov, *How to find neutral leptons of the ν MSSM?*, *JHEP* **10** (2007) 015, [arXiv:0705.1729 \[hep-ph\]](#). [Erratum: *JHEP* 11, 101(2013)].

- [167] O. Castillo-Felisola, C. O. Dib, J. C. Helo, S. G. Kovalenko, and S. E. Ortiz, *Left-Right Symmetric Models at the High-Intensity Frontier*, *Phys. Rev.* **D92** no. 1, (2015) 013001, [arXiv:1504.02489 \[hep-ph\]](#).
- [168] A. Maiezza, M. Nemevsek, F. Nesti, and G. Senjanovic, *Left-Right Symmetry at LHC*, *Phys. Rev.* **D82** (2010) 055022, [arXiv:1005.5160 \[hep-ph\]](#).
- [169] ATLAS Collaboration, T. A. collaboration, *Search for New Phenomena in Dijet Events with the ATLAS Detector at $\sqrt{s}=13$ TeV with 2015 and 2016 data*, .
- [170] J. C. Helo and M. Hirsch, *LHC dijet constraints on double beta decay*, *Phys. Rev.* **D92** no. 7, (2015) 073017, [arXiv:1509.00423 \[hep-ph\]](#).
- [171] F. F. Deppisch, M. Hirsch, and H. Pas, *Neutrinoless Double Beta Decay and Physics Beyond the Standard Model*, *J. Phys.* **G39** (2012) 124007, [arXiv:1208.0727 \[hep-ph\]](#).
- [172] W. Buchmuller, R. Ruckl, and D. Wyler, *Leptoquarks in Lepton - Quark Collisions*, *Phys. Lett.* **B191** (1987) 442–448. [Erratum: *Phys. Lett.* **B448**,320(1999)].
- [173] W. Buchmuller and D. Wyler, *Constraints on SU(5) Type Leptoquarks*, *Phys. Lett.* **B177** (1986) 377–382.
- [174] J. C. Pati and A. Salam, *Unified lepton-hadron symmetry and a gauge theory of the basic interactions*, *Phys. Rev. D* **8** (Aug, 1973) 1240–1251. <https://link.aps.org/doi/10.1103/PhysRevD.8.1240>.
- [175] H. Georgi and S. L. Glashow, *Unity of all elementary-particle forces*, *Phys. Rev. Lett.* **32** (Feb, 1974) 438–441. <https://link.aps.org/doi/10.1103/PhysRevLett.32.438>.
- [176] H. Georgi, *The State of the Art?Gauge Theories*, *AIP Conf. Proc.* **23** (1975) 575–582.

- [177] H. Fritzsch and P. Minkowski, *Unified Interactions of Leptons and Hadrons*, *Annals Phys.* **93** (1975) 193–266.
- [178] R. N. Mohapatra and B. Sakita, *SO(2n) Grand Unification in an SU(N) Basis*, *Phys. Rev.* **D21** (1980) 1062.
- [179] F. Wilczek and A. Zee, *Families from Spinors*, *Phys. Rev.* **D25** (1982) 553.
- [180] A. Melfo, A. Ramirez, and G. Senjanovic, *Type II see-saw dominance in SO(10)*, *Phys. Rev.* **D82** (2010) 075014, [arXiv:1005.0834](https://arxiv.org/abs/1005.0834) [hep-ph].
- [181] S. Dimopoulos and L. Susskind, *Mass without scalars*, *Nuclear Physics B* **155** no. 1, (1979) 237 – 252. <http://www.sciencedirect.com/science/article/pii/055032137990364X>.
- [182] S. Dimopoulos, *Technicoloured signatures*, *Nuclear Physics B* **168** no. 1, (1980) 69 – 92. <http://www.sciencedirect.com/science/article/pii/0550321380902771>.
- [183] E. Farhi and L. Susskind, *Technicolour*, *Physics Reports* **74** no. 3, (1981) 277 – 321. <http://www.sciencedirect.com/science/article/pii/0370157381901733>.
- [184] H. Georgi and S. L. Glashow, *Unextended hypercolor and unification*, *Phys. Rev. Lett.* **47** (Nov, 1981) 1511–1513. <https://link.aps.org/doi/10.1103/PhysRevLett.47.1511>.
- [185] I. Doršner, S. Fajfer, A. Greljo, J. F. Kamenik, and N. Košnik, *Physics of leptoquarks in precision experiments and at particle colliders*, *Phys. Rept.* **641** (2016) 1–68, [arXiv:1603.04993](https://arxiv.org/abs/1603.04993) [hep-ph].
- [186] J. M. Arnold, B. Fornal, and M. B. Wise, *Simplified models with baryon number violation but no proton decay*, *Phys. Rev.* **D87** (2013) 075004, [arXiv:1212.4556](https://arxiv.org/abs/1212.4556) [hep-ph].

- [187] D. Das, K. Ghosh, M. Mitra, and S. Mondal, *Probing sterile neutrinos in the framework of inverse seesaw mechanism through leptoquark productions*, *Phys. Rev. D* **97** no. 1, (2018) 015024, [arXiv:1708.06206 \[hep-ph\]](#).
- [188] U. K. Dey, D. Kar, M. Mitra, M. Spannowsky, and A. C. Vincent, *Searching for Leptoquarks at IceCube and the LHC*, [arXiv:1709.02009 \[hep-ph\]](#).
- [189] S. Mondal and S. K. Rai, *Probing the Heavy Neutrinos of Inverse Seesaw Model at the LHeC*, *Phys. Rev. D* **94** no. 3, (2016) 033008, [arXiv:1605.04508 \[hep-ph\]](#).
- [190] S. Mondal and S. K. Rai, *Polarized window for left-right symmetry and a right-handed neutrino at the Large Hadron-Electron Collider*, *Phys. Rev. D* **93** no. 1, (2016) 011702, [arXiv:1510.08632 \[hep-ph\]](#).
- [191] M. Lindner, F. S. Queiroz, W. Rodejohann, and C. E. Yaguna, *Left-Right Symmetry and Lepton Number Violation at the Large Hadron Electron Collider*, *JHEP* **06** (2016) 140, [arXiv:1604.08596 \[hep-ph\]](#).
- [192] S. Antusch, E. Cazzato, and O. Fischer, *Sterile neutrino searches at future e^-e^+ , pp , and e^-p colliders*, *Int. J. Mod. Phys. A* **32** no. 14, (2017) 1750078, [arXiv:1612.02728 \[hep-ph\]](#).
- [193] **LHeC Study Group** Collaboration, J. L. Abelleira Fernandez *et al.*, *A Large Hadron Electron Collider at CERN: Report on the Physics and Design Concepts for Machine and Detector*, *J. Phys. G* **39** (2012) 075001, [arXiv:1206.2913 \[physics.acc-ph\]](#).
- [194] **LHeC Study Group** Collaboration, J. L. Abelleira Fernandez *et al.*, *On the Relation of the LHeC and the LHC*, [arXiv:1211.5102 \[hep-ex\]](#).
- [195] J. Barry, W. Rodejohann, and H. Zhang, *Light Sterile Neutrinos: Models and Phenomenology*, *JHEP* **07** (2011) 091, [arXiv:1105.3911 \[hep-ph\]](#).

- [196] J. Heeck and H. Zhang, *Exotic Charges, Multicomponent Dark Matter and Light Sterile Neutrinos*, *JHEP* **05** (2013) 164, [arXiv:1211.0538 \[hep-ph\]](#).
- [197] S. K. Kang and C. S. Kim, *Extended double seesaw model for neutrino mass spectrum and low scale leptogenesis*, *Phys. Lett.* **B646** (2007) 248–252, [arXiv:hep-ph/0607072 \[hep-ph\]](#).
- [198] ATLAS Collaboration, G. Aad *et al.*, *Search for heavy neutrinos and right-handed W bosons in events with two leptons and jets in pp collisions at $\sqrt{s} = 7$ TeV with the ATLAS detector*, *Eur. Phys. J.* **C72** (2012) 2056, [arXiv:1203.5420 \[hep-ex\]](#).
- [199] CMS Collaboration, V. Khachatryan *et al.*, *Search for heavy Majorana neutrinos in $e^\pm e^\pm + \text{jets}$ and $e^\pm \mu^\pm + \text{jets}$ events in proton-proton collisions at $\sqrt{s} = 8$ TeV*, *JHEP* **04** (2016) 169, [arXiv:1603.02248 \[hep-ex\]](#).
- [200] CMS Collaboration, A. M. Sirunyan *et al.*, *Search for heavy neutral leptons in events with three charged leptons in proton-proton collisions at $\sqrt{s} = 13$ TeV*, *Phys. Rev. Lett.* **120** no. 22, (2018) 221801, [arXiv:1802.02965 \[hep-ex\]](#).
- [201] CMS Collaboration, A. M. Sirunyan *et al.*, *Search for heavy Majorana neutrinos in same-sign dilepton channels in proton-proton collisions at $\sqrt{s} = 13$ TeV*, [arXiv:1806.10905 \[hep-ex\]](#).
- [202] A. Das, *Searching for the minimal Seesaw models at the LHC and beyond*, *Adv. High Energy Phys.* **2018** (2018) 9785318, [arXiv:1803.10940 \[hep-ph\]](#).
- [203] A. Das and N. Okada, *Bounds on heavy Majorana neutrinos in type-I seesaw and implications for collider searches*, *Phys. Lett.* **B774** (2017) 32–40, [arXiv:1702.04668 \[hep-ph\]](#).

- [204] J. Chakraborty, S. Goswami, and A. Raychaudhuri, *An $SO(10)$ model with adjoint fermions for double seesaw neutrino masses*, *Phys. Lett.* **B698** (2011) 265–270, [arXiv:1012.2715 \[hep-ph\]](#).
- [205] **OPAL** Collaboration, G. Abbiendi *et al.*, *Search for leptoquarks in electron photon scattering at $s(ee)^{(1/2)}$ up to 209-GeV at LEP*, *Phys. Lett.* **B526** (2002) 233–246, [arXiv:hep-ex/0112024 \[hep-ex\]](#).
- [206] **OPAL** Collaboration, G. Abbiendi *et al.*, *Search for pair produced leptoquarks in e^+e^- interactions at \sqrt{s} approximately = 189-GeV to 209-GeV*, *Eur. Phys. J.* **C31** (2003) 281–305, [arXiv:hep-ex/0305053 \[hep-ex\]](#).
- [207] **H1** Collaboration, C. Adloff *et al.*, *A Search for leptoquark bosons and lepton flavor violation in e^+p collisions at HERA*, *Eur. Phys. J.* **C11** (1999) 447–471, [arXiv:hep-ex/9907002 \[hep-ex\]](#). [Erratum: *Eur. Phys. J.*C14,553(2000)].
- [208] **ZEUS** Collaboration, H. Abramowicz *et al.*, *Search for first-generation leptoquarks at HERA*, *Phys. Rev.* **D86** (2012) 012005, [arXiv:1205.5179 \[hep-ex\]](#).
- [209] **D0** Collaboration, V. M. Abazov *et al.*, *Search for scalar bottom quarks and third-generation leptoquarks in pp^- collisions at $\sqrt{s} = 1.96$ TeV*, *Phys. Lett.* **B693** (2010) 95–101, [arXiv:1005.2222 \[hep-ex\]](#).
- [210] **D0** Collaboration, V. M. Abazov *et al.*, *Search for first generation leptoquark pair production in the electron + missing energy + jets final state*, *Phys. Rev.* **D84** (2011) 071104, [arXiv:1107.1849 \[hep-ex\]](#).
- [211] **CMS** Collaboration, V. Khachatryan *et al.*, *Search for pair production of first and second generation leptoquarks in proton-proton collisions at $\sqrt{s} = 8$ TeV*, *Phys. Rev.* **D93** no. 3, (2016) 032004, [arXiv:1509.03744 \[hep-ex\]](#).

- [212] **ATLAS** Collaboration, G. Aad *et al.*, *Searches for scalar leptoquarks in pp collisions at $\sqrt{s} = 8$ TeV with the ATLAS detector*, *Eur. Phys. J. C* **76** no. 1, (2016) 5, [arXiv:1508.04735 \[hep-ex\]](#).
- [213] **CMS** Collaboration, A. M. Sirunyan *et al.*, *Search for third-generation scalar leptoquarks and heavy right-handed neutrinos in final states with two tau leptons and two jets in proton-proton collisions at $\sqrt{s} = 13$ TeV*, *JHEP* **07** (2017) 121, [arXiv:1703.03995 \[hep-ex\]](#).
- [214] **CMS** Collaboration, A. M. Sirunyan *et al.*, *Constraints on models of scalar and vector leptoquarks decaying to a quark and a neutrino at $\sqrt{s} = 13$ TeV*, [arXiv:1805.10228 \[hep-ex\]](#).
- [215] **CMS** Collaboration, A. M. Sirunyan *et al.*, *Search for a singly produced third-generation scalar leptoquark decaying to a τ lepton and a bottom quark in proton-proton collisions at $\sqrt{s} = 13$ TeV*, Submitted to: *JHEP* (2018) , [arXiv:1806.03472 \[hep-ex\]](#).
- [216] **ATLAS, CMS** Collaboration, F. Romeo, *Searches for new physics in lepton plus jet final states in ATLAS and CMS*, in *2017 International Workshop on Baryon and Lepton Number Violation: From the Cosmos to the LHC (BLV 2017) Cleveland, Ohio, USA, May 15-18, 2017*. 2017. [arXiv:1709.00229 \[hep-ex\]](#). <https://inspirehep.net/record/1621275/files/arXiv:1709.00229.pdf>.
- [217] I. Dorsner, S. Fajfer, and A. Greljo, *Cornering Scalar Leptoquarks at LHC*, *JHEP* **10** (2014) 154, [arXiv:1406.4831 \[hep-ph\]](#).
- [218] I. Dorsner, J. Drobnak, S. Fajfer, J. F. Kamenik, and N. Kosnik, *Limits on scalar leptoquark interactions and consequences for GUTs*, *JHEP* **11** (2011) 002, [arXiv:1107.5393 \[hep-ph\]](#).

- [219] A. Alloul, N. D. Christensen, C. Degrande, C. Duhr, and B. Fuks, *FeynRules 2.0 - A complete toolbox for tree-level phenomenology*, *Comput. Phys. Commun.* **185** (2014) 2250–2300, [arXiv:1310.1921 \[hep-ph\]](#).
- [220] J. Alwall, R. Frederix, S. Frixione, V. Hirschi, F. Maltoni, O. Mattelaer, H. S. Shao, T. Stelzer, P. Torrielli, and M. Zaro, *The automated computation of tree-level and next-to-leading order differential cross sections, and their matching to parton shower simulations*, *JHEP* **07** (2014) 079, [arXiv:1405.0301 \[hep-ph\]](#).
- [221] T. Sjostrand, S. Mrenna, and P. Z. Skands, *PYTHIA 6.4 Physics and Manual*, *JHEP* **05** (2006) 026, [arXiv:hep-ph/0603175 \[hep-ph\]](#).
- [222] M. Cacciari, G. P. Salam, and G. Soyez, *The Anti- $k(t)$ jet clustering algorithm*, *JHEP* **04** (2008) 063, [arXiv:0802.1189 \[hep-ph\]](#).
- [223] M. Cacciari, G. P. Salam, and G. Soyez, *FastJet User Manual*, *Eur. Phys. J.* **C72** (2012) 1896, [arXiv:1111.6097 \[hep-ph\]](#).
- [224] **MEG** Collaboration, A. M. Baldini *et al.*, *Search for the lepton flavour violating decay $\mu^+ \rightarrow e^+ \gamma$ with the full dataset of the MEG experiment*, *Eur. Phys. J.* **C76** no. 8, (2016) 434, [arXiv:1605.05081 \[hep-ex\]](#).
- [225] **BaBar** Collaboration, B. Aubert *et al.*, *Searches for Lepton Flavor Violation in the Decays $\tau^{+-} \rightarrow e^{+-} \gamma$ and $\tau^{+-} \rightarrow \mu^{+-} \gamma$* , *Phys. Rev. Lett.* **104** (2010) 021802, [arXiv:0908.2381 \[hep-ex\]](#).
- [226] **SuperB** Collaboration, B. O’Leary *et al.*, *SuperB Progress Reports – Physics*, [arXiv:1008.1541 \[hep-ex\]](#).
- [227] T. Saito, M. Asano, K. Fujii, N. Haba, S. Matsumoto, T. Nabeshima, Y. Takubo, H. Yamamoto, and K. Yoshioka, *Extra dimensions and Seesaw Neutrinos at the*

- International Linear Collider*, *Phys. Rev.* **D82** (2010) 093004, [arXiv:1008.2257 \[hep-ph\]](#).
- [228] S. Antusch, E. Cazzato, O. Fischer, A. Hammad, and K. Wang, *Lepton Flavor Violating Dilepton Dijet Signatures from Sterile Neutrinos at Proton Colliders*, *JHEP* **10** (2018) 067, [arXiv:1805.11400 \[hep-ph\]](#).
- [229] J. Pumplin, D. R. Stump, J. Huston, H. L. Lai, P. M. Nadolsky, and W. K. Tung, *New generation of parton distributions with uncertainties from global QCD analysis*, *JHEP* **07** (2002) 012, [arXiv:hep-ph/0201195 \[hep-ph\]](#).
- [230] T. Sjöstrand, S. Ask, J. R. Christiansen, R. Corke, N. Desai, P. Ilten, S. Mrenna, S. Prestel, C. O. Rasmussen, and P. Z. Skands, *An Introduction to PYTHIA 8.2*, *Comput. Phys. Commun.* **191** (2015) 159–177, [arXiv:1410.3012 \[hep-ph\]](#).
- [231] **DELPHES 3** Collaboration, J. de Favereau, C. Delaere, P. Demin, A. Giammanco, V. Lemaître, A. Mertens, and M. Selvaggi, *DELPHES 3, A modular framework for fast simulation of a generic collider experiment*, *JHEP* **02** (2014) 057, [arXiv:1307.6346 \[hep-ex\]](#).
- [232] *Conference talk by O. Fischer, Exotic Higgs Search at Higgs & Top at LHeC*, <https://indico.cern.ch/event/774889/>, *LHeC Card for DELPHES is available from* https://indico.cern.ch/event/774889/contributions/3220312/attachments/1754841/2845678/delphes_card_LHeC_1.0.tcl.
- [233] Y. L. Dokshitzer, G. D. Leder, S. Moretti, and B. R. Webber, *Better jet clustering algorithms*, *JHEP* **08** (1997) 001, [arXiv:hep-ph/9707323 \[hep-ph\]](#).
- [234] M. Wobisch and T. Wengler, *Hadronization corrections to jet cross-sections in deep inelastic scattering*, in *Monte Carlo generators for HERA physics. Proceedings, Workshop, Hamburg, Germany, 1998-1999*, pp. 270–279. 1998. [arXiv:hep-ph/9907280 \[hep-ph\]](#).

- [235] M. Cacciari and G. P. Salam, *Dispelling the N^3 myth for the k_t jet-finder*, *Phys. Lett.* **B641** (2006) 57–61, [arXiv:hep-ph/0512210](#) [hep-ph].
- [236] E. Akhmedov, A. Kartavtsev, M. Lindner, L. Michaels, and J. Smirnov, *Improving Electro-Weak Fits with TeV-scale Sterile Neutrinos*, *JHEP* **05** (2013) 081, [arXiv:1302.1872](#) [hep-ph].
- [237] J. de Blas, *Electroweak limits on physics beyond the Standard Model*, *EPJ Web Conf.* **60** (2013) 19008, [arXiv:1307.6173](#) [hep-ph].
- [238] **L3** Collaboration, P. Achard *et al.*, *Search for heavy isosinglet neutrino in e^+e^- annihilation at LEP*, *Phys. Lett.* **B517** (2001) 67–74, [arXiv:hep-ex/0107014](#) [hep-ex].